Dissertation
submitted to the
Combined Faculty of Mathematics, Engineering and Natural Sciences
of Heidelberg University, Germany
for the degree of
Doctor of Natural Sciences

Put forward by
Dennis Hofmann
born in: Wiesbaden
Oral examination: 10.07.2025

Investigating Air-Water Gas Transfer via Fluorescence Imaging

Referees: Prof. Dr. Bernd Jähne
Prof. Dr. Ulrich Platt

Investigating Air-Water Gas Transfer via Fluorescence Imaging:

This study presents an advanced Fluorescence Imaging technique to make air-water gas exchange dynamics in a wind-wave facility visible up to high wind speeds. Fluorescence is generated by the pH-sensitive dye pyranine, which transitions into its fluorescent alkaline form upon reacting with the invading alkaline trace gas methylamine. A high-intensity laser illumination system combined with a multi-camera setup is implemented at the Heidelberg Aeolotron, enabling high-resolution imaging of fluorescent patterns in gas concentration fields near the water surface. Near-surface turbulent structures such as quasi-streamwise vortices, Langmuir circulations, and microscale wave breaking are identified. A major achievement is the development of a simulation-based method for estimating water-side gas transfer velocities. By modeling one-dimensional mass transport using the Small Eddy Model and comparing simulated fluorescence time series to experimental data, a robust determination of turbulence profiles and gas transfer velocities with uncertainties between 5 % and 20 % is established. Additionally, an algorithm is developed to detect and track microscale wave breaking events, combining structure tensor-based Oriented FAST and Rotated BRIEF detection, cluster analysis, and optical flow techniques. Based on the detected microscale wave breaking statistics, a first quantitative estimate suggests that microscale wave breaking contributes approximately 35 % to 80 % of the total water-side gas transfer velocity within a friction velocity range of $0.3\,\mathrm{cm\,s^{-1}}$ to $0.8\,\mathrm{cm\,s^{-1}}$.

Untersuchung des Luft-Wasser-Gasaustauschs durch Fluoreszenz-Bildgebung:

Die vorliegende Arbeit stellt ein weiterentwickeltes Fluoreszenzbildgebungsverfahren vor, mit dem die Dynamik des Luft-Wasser-Gasaustauschs in einer Wind-Wellen-Anlage bis zu hohen Windgeschwindigkeiten sichtbar gemacht werden kann. Die Fluoreszenz wird durch den pH-sensitiven Farbstoff Pyranin erzeugt, der bei Reaktion mit dem sich lösenden alkalischen Spurengas Methylamin in seine fluoreszierende alkalische Form übergeht. Am Heidelberger Aeolotron wird ein leistungsstarkes Laser-Beleuchtungssystem in Kombination mit einem Multikamera-Setup installiert, das die hochauflösende Bildgebung von Fluoreszenzmustern der Gaskonzentrationsfelder nahe der Wasseroberfläche ermöglicht. Oberflächennahe turbulente Strukturen wie quasistromartige Wirbel, Langmuir-Zirkulationen und Microscale Wave Breaking werden identifiziert. Eine wichtiges Resultat ist die Entwicklung einer simulationsbasierten Methode zur Abschätzung der wasserseitigen Gastransfergeschwindigkeiten. Durch die Modellierung des eindimensionalen Massentransports mit Hilfe des Small-Eddy-Modells und dem Vergleich simulierter Fluoreszenz-Zeitreihen mit experimentellen Daten wird eine robuste Bestimmung von Turbulenzprofilen und Gastransfergeschwindigkeiten mit Unsicherheiten zwischen 5 % und 20 % erreicht. Darüber hinaus wird ein Algorithmus zur Erkennung und Verfolgung von Microscale Wave Breaking-Ereignissen entwickelt, der strukturtensorbasierte Oriented FAST and Rotated BRIEF-Erkennung, Clusteranalyse und optische Flussverfahren kombiniert. Auf der Grundlage der detektierten Microscale Wave Breaking-Statistiken deutet eine erste quantitative Schätzung darauf hin, dass Microscale Wave Breaking etwa 35 % bis 80 % zur gesamten wasserseitigen Gastransfergeschwindigkeit innerhalb eines Schubspannungsgeschwindigkeitsbereichs von $0{,}3\,\mathrm{cm\,s^{-1}}$ bis $0{,}8\,\mathrm{cm\,s^{-1}}$ beiträgt.

Contents

List of Figures

List of Tables

List of Abbreviations

BLI	Boundary Layer Imaging
CL	Craik-Leibovich
LC	Langmuir Circulation
LIF	Laser-Induced Fluorescence
LUT	Lookup Table
MWB	Microscale Wave Breaking
ORB	Oriented FAST and Rotated BRIEF
QSV	Quasi-Streamwise Vortex
RBF	Radial Basis Function

1 Introduction

Global warming is one of the most challenging problems mankind has ever faced. Anthropogenic emissions of greenhouse gases such as carbon dioxide CO_2, nitrous oxide N_2O, and methane CH_4 have destabilized the delicate balance between the Earth's major compartments and led to a disruption of the natural distribution of carbon (Levin & Hesshaimer, 2000). The main consequence of this disturbance is an imbalance in the Earth's radiation budget between incoming solar radiation and outgoing long-wave radiation, resulting in an intensification of the greenhouse effect (IPCC, 2013). Among the different compartments, the ocean plays a pivotal role, covering around 70 % of the Earth's surface and being considered the planet's largest carbon sink for atmospheric CO_2. The continuous exchange of CO_2 between the atmosphere and the ocean mitigates atmospheric CO_2 concentrations while also leading to ocean acidification (Doney et al., 2009) through the ongoing uptake of increasing amounts of carbon. Current estimates suggest that the oceans absorb approximately 25 % of anthropogenic CO_2 emissions (Friedlingstein et al., 2022). However, absorbing CO_2 by the oceans has far-reaching consequences. It not only disrupts marine ecosystems, most visibly through phenomena such as coral bleaching (Anthony et al., 2008), but also changes the ocean's role as a thermal buffer (Rose & Rayborn, 2016). Given the wide-ranging impacts of oceanic CO_2 uptake, a thorough understanding of air-sea gas exchange is essential to improve the predictive accuracy of climate models.

Air-sea gas exchange is governed by a complex interplay of physical, chemical, and biological processes. Among the physical factors, the degree of near-surface turbulence is of decisive importance (Soloviev et al., 2007), as transport is significantly less efficient in the uppermost ocean layers compared to the bulk. This inefficiency is primarily due to the presence of a thin boundary layer, less than 1 mm thick, where molecular diffusion dominates, forming the rate-limiting transport step for gas exchange (Jähne & Haußecker, 1998). Wind is considered the principal driver of near-surface turbulence, acting indirectly through tangential shear stress and wave growth (Jähne, 2019). This input leads to shear-induced small-scale vortices below the surface and, via interaction with surface waves, gives rise to larger-scale flow phenomena such as Langmuir circulations (LCs) (Thorpe, 2004). These circulations have been shown to substantially enhance vertical transport processes, especially under low wind conditions (Veron & Melville, 2001). Additionally, wave breaking further injects turbulent energy and directly disrupts and renews the boundary layer on both large and small scales. Of particular interest is microscale wave breaking (MWB), which has been identified as a major contributor to gas exchange at moderate wind speeds (Zappa et al., 2004). Chemical factors, such as the presence of surfactants or surface films affect gas exchange by contributing to wave damping (Frew et al., 2004). Likewise, biological processes, such as those caused by phytoplankton or microbial communities, can significantly impact exchange dynamics through both biogeochemical and surface-active effects (Wurl et al., 2016).

The complex network of potentially interacting processes controlling air-sea gas exchange is presented in Fig. 1.1. All these processes act on a variety of spatial and temporal scales, complicating an accurate estimation of gas exchange rates.

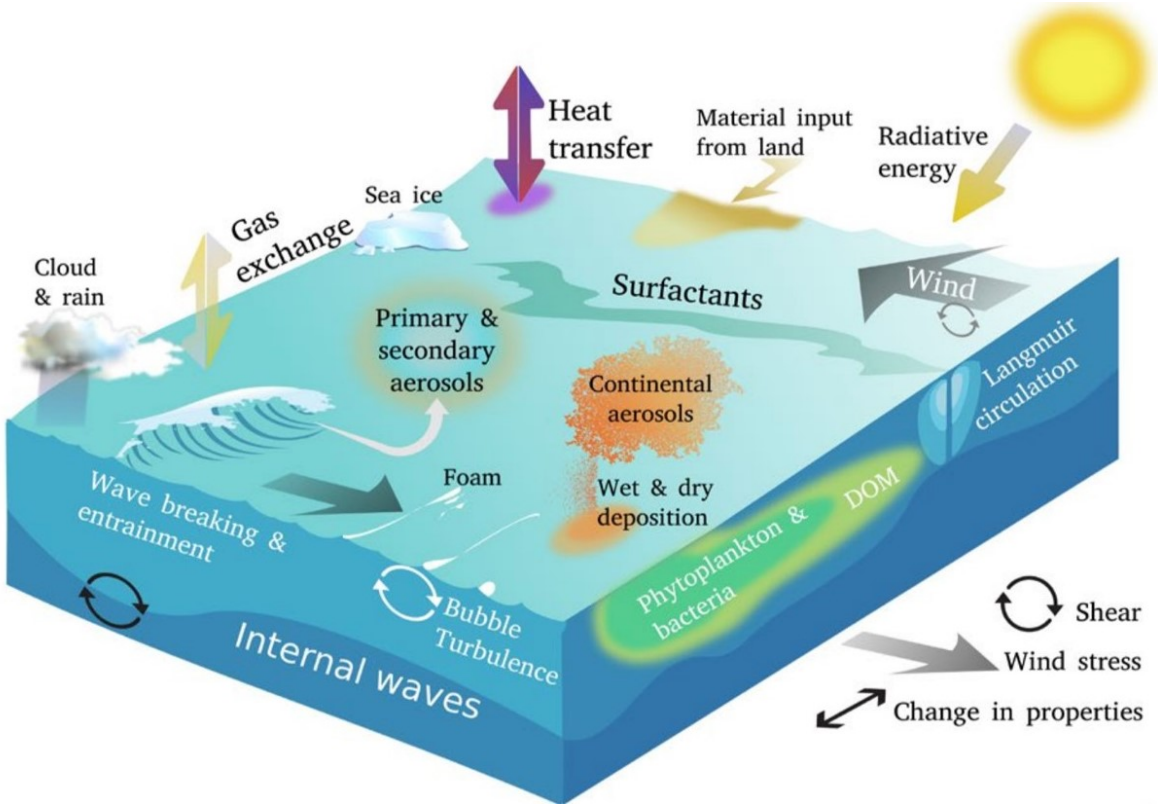

Figure 1.1: Overview of the physical, chemical, and biological factors influencing air-sea gas exchange (Neukermans et al., 2018).

1.1 Air-Sea Gas Exchange Studies

Studies of air-sea gas exchange are frequently carried out as part of field measurements under natural conditions. These either measure the gas fluxes across the air- water interface directly using eddy covariance techniques (Dong et al., 2021) or monitor the concentrations of trace gases in air and water over time (Ho et al., 2011). Both approaches are conceptually linked by the gas transfer velocity k, a key parameter describing the efficiency of gas transport across the air-sea interface. This relates the flux j to a concentration difference Δc via

$$j = k\Delta c. \tag{1.1}$$

The gas transfer velocity represents the central quantity in gas exchange research and is commonly parameterized as a function of wind speed, reflecting the dominant role of wind in the generation of near-surface turbulence. However, there is significant scatter observed in field measurements attributable to various sources of uncertainty (Ford et al., 2024; Wanninkhof et al., 2009; Woolf et al., 2019). At low wind speeds, gas fluxes are minimal, requiring extended integration times to detect

measurable changes in concentration. These longer observation periods increase the likelihood of changing wind and wave conditions, leading to additional variability. At high wind speeds, experimental challenges such as ship stability and sensor limitations limit the reliability of measurements. In consequence, the most robust transfer velocity data are usually found at moderate wind conditions (Jähne, 2019). Besides, field measurements are constrained by their limited spatial and temporal resolution. The integration over large surface areas and long time periods precludes the observation of fine-scale variability in gas exchange. However, it is increasingly recognized that small-scale processes are crucial for understanding the fundamental mechanisms of gas transfer (Garbe et al., 2014; Wanninkhof et al., 2011).

To overcome these limitations, laboratory studies in wind-wave facilities have proven useful. These allow for controlled environments with stable and repeatable wind and wave fields over extended time periods. In addition, laboratory settings facilitate the use of high-resolution, non-invasive imaging techniques that are particularly advantageous for studying the micro-scale structure of gas concentration fields. Among these, infrared thermography is a widely used method for detecting horizontal thermal footprints on water surfaces (Jessup et al., 1997; Schnieders et al., 2013). These exploit heat as a tracer to make the near-surface turbulence visible, whereby the thermal signatures are basically similar to the gas concentration structures (Klein, 2019; Kräuter, 2015). Furthermore, laser-induced fluorescence (LIF) imaging techniques have shown great potential for measuring the vertical profile of gas concentration fields directly (Herlina & Jirka, 2008). This technique detect either the direct fluorescence of gas molecules or the fluorescence response of gas-sensitive dyes (Friedl, 2013; Friman & Jähne, 2019). Nevertheless, with growing wave motion, vertically resolved imaging becomes increasingly difficult. Consequently, recent studies focus on horizontally resolved Fluorescence Imaging of the surface structures as with thermographic techniques. These Fluorescence Imaging techniques provide the opportunity to capture the horizontal microscale structure of the gas exchange. By extending these techniques with imaging systems similar to light field cameras (Wanner & Goldluecke, 2014), e.g. using camera arrays, it is theoretically even possible to realize a 3D reconstruction of concentration fields below the water surface, combining the vertical resolution of LIF with horizontal spatial mapping. However, such 3D reconstructions have not yet been successfully implemented to date. Initial implementations of horizontal gas imaging techniques (Kräuter, 2015; Papst, 2019) are limited in their applicability under strong wind and wave conditions, a gap that the present study aims to fill.

As a preview of the potential of Fluorescence Imaging, Fig. 1.2 shows a representative image of a horizontally resolved gas concentration field at the water surface, recorded in the course of this study. It reveals pronounced microscale heterogeneity that emphasizes the spatial complexity of air-water gas exchange. These visible patterns result from an interplay of different fine-scale processes and exhibit different surface “footprints” depending on the underlying mechanism, such as coherent structures caused by organized turbulent vortices or more irregular features associated with surface renewal by microscale wave breaking. The method thus enables the imaging of surface signatures that can be directly linked to specific transport processes governing gas transfer across the interface. How this kind of high-resolution imaging can be realized experimentally is one of the central topics of this work.

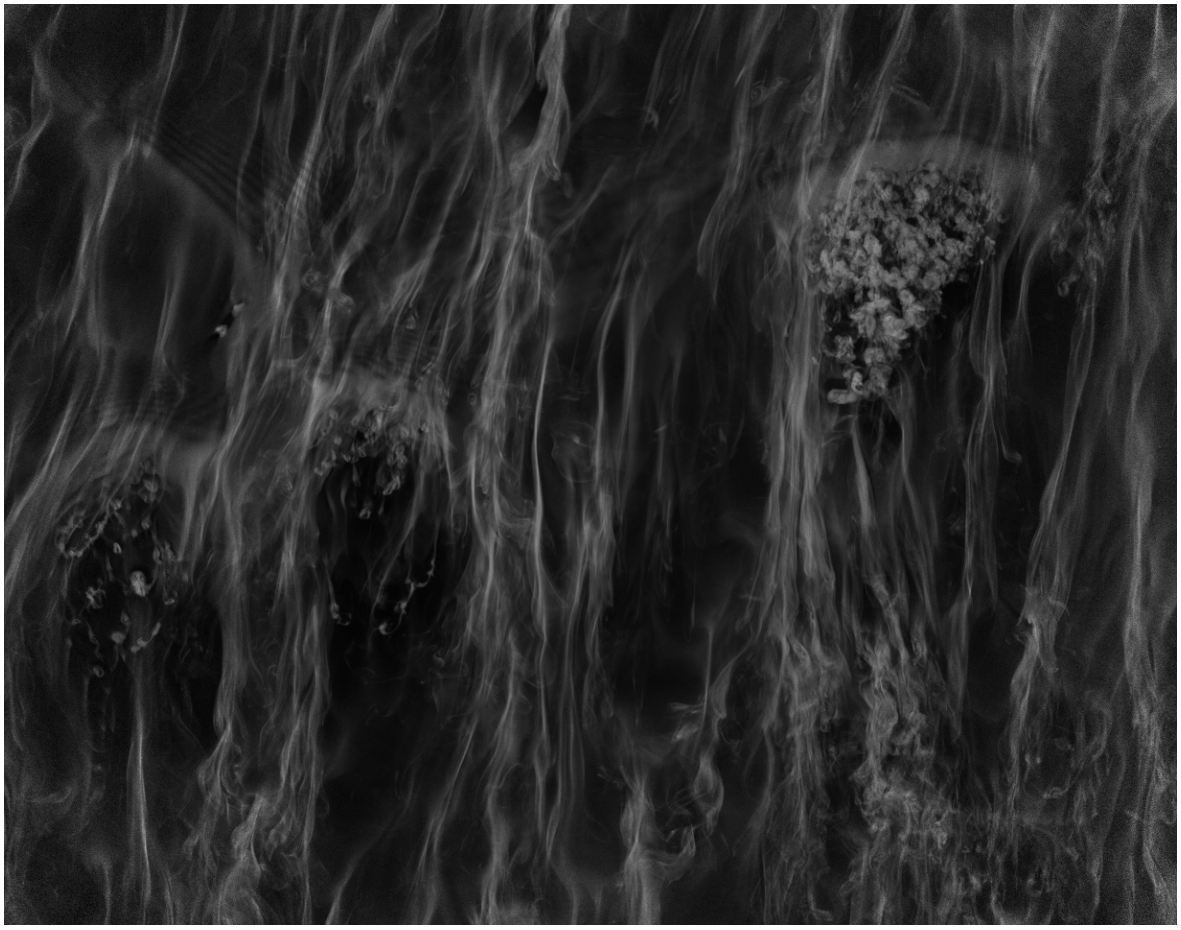

Figure 1.2: Horizontal-resolved Fluorescence Imaging of gas exchange at a water surface. Exemplary image captured in the scope of this work. The image brightness correlates approximately with the gas concentration. The different spatial patterns indicate different gas exchange mechanisms. For example, streak-like patterns emerge as a result of coherent turbulent vortices and turbulent swirls caused by MWB events (top right).

In spite of the obvious challenge of reproducing realistic air-sea interactions in a wind-wave facility, these laboratory studies are more likely to identify the driving mechanisms under controlled conditions and separate their contribution to gas exchange (Jähne, 2019, 2020). In this sense, an upscaling of the results to the conditions at the sea surface would be possible.

1.2 Research Methodology and Scope

This thesis develops and applies a novel fluorescence method for imaging gas concentration fields at the air-water interface. Building upon the method presented by Papst (2019), this study implements major adaptations for use in the Aeolotron, a large-scale, annular wind-wave channel. These enhancements enable the detailed observation of gas exchange processes in spatially and temporally high precision even under high wind speeds and rough surface conditions, thus surpassing the limitations of previous methods.

A comprehensive measurement campaign is conducted, covering the entire range of wind speeds achievable in the Aeolotron, both under steady-state and transient conditions. The campaign further

examines the influence of surface films, variations in surface tension, atmospheric density, and effects of a saltwater model.
While previous studies have provided qualitative observations of near-surface turbulent structures, a major goal of this work is to establish a reliable method to quantitatively derive gas transfer rates from the fluorescence signal captured in image sequences.
Another focus is the detailed investigation of MWB, an important mechanism with characteristic near-surface footprints. For this purpose, a special algorithm for identifying and quantifying MWB events in the image data is developed. A combined analysis of transfer velocities and MWB characteristics is used to assess the contribution of MWB to the overall gas exchange rates.
The presented work is carried out within the framework of a DFG-funded Koselleck project aiming to explore novel experimental insights for quantifying air-sea gas exchange. As part of this broader campaign, complementary measurement techniques are also employed, including infrared thermography and classical mass balance methods. While these techniques provide valuable reference data, this thesis focuses exclusively on the Fluorescence Imaging technique and its outcomes.

1.3 Structure of the Thesis

As an introductory part to the imaging of gas exchange processes, Chapter 2 presents the theoretical principles of transport at the air-water interface, fluorescence response, and necessary image processing techniques. Subsequently, Chapter 3 provides a methodological overview of the Fluorescence Imaging approach, outlines its development, and describes the adaptations made in the context of this study. It also includes the implementation of numerical simulations that serve to validate the methodology and provide a theoretical model of the fluorescence signal behavior. Chapter 4 details the experimental realization of the method, including a comprehensive description of the tailored setup at the Heidelberg Aeolotron and a complete documentation of all gas exchange experiments performed during the measurement campaign. The large volume of image sequences generated during the experiments is preprocessed in Chapter 5. This chapter also presents the processing of additional spectroscopic data sets, which provide further insights into gas concentrations, fluxes, and dye composition. In Chapter 6, the actual image analysis is carried out. This includes an initial qualitative analysis of the near-surface fluorescence patterns, followed by a quantitative evaluation of the fluorescence intensity. In addition, the implementation of the algorithm for detecting MWB is explained. Afterwards, chapter 7 outlines the methodology for deriving gas transfer velocities from the image data. Finally, Chapter 8 shows the results with regard to the gas transfer velocities and establishes a correlation with MWB, as well as discussing the various evaluation methods. Chapter 9 completes the study with a summary and an outlook.

2 Theoretical Background

This chapter establishes a theoretical framework for describing gas exchange between air and water. It begins by exploring the basic fluid dynamic transport equations and their application to an air-water interface. In this context, key concepts such as mass boundary layer and transfer velocity are defined, which serve as a basis for quantifying gas exchange processes. Additionally, important physical phenomena influencing the gas exchange dynamics are presented. To support the methodological approach of this study, the chapter also explains theoretical principles of fluorescence. Finally, it covers essential image processing techniques necessary for analyzing the resulting data.

2.1 Transport Processes in Fluids

Transport processes play a key role in the exchange of substances, heat, and momentum between the various compartments of the Earth. The dominance of specific transport mechanisms depends on the thermodynamic phases of the involved reservoirs. In fluids, these are molecular diffusion, advection, and turbulent flows. While molecular diffusion and turbulence comprise transport processes based on random movements, advection is caused by directed movements.

2.1.1 Molecular Diffusion

The molecular diffusion describes the phenomenon of how particles spread out to compensate a concentration gradient. This is caused by the thermal energy of atoms or molecules, resulting in a fundamental random motion. Here, elastic collisions between the particles lead to changes in direction. Their movement can thus be described by the random walk model (K. Pearson, 1905). On length scales larger than the free path length of the particles, they move in the direction of the concentration gradient. This results in a mass flux from high-concentration regions to low-concentration regions within the medium. According to Fick's Law (Fick, 1855), the flux increases proportionally to the concentration gradient as in

$$\vec{j}_{c,\mathrm{diff}} = -D\nabla c, \tag{2.1}$$

where the diffusion constant or diffusivity D defines a material-dependent parameter. A variety of formulas exist for calculating the diffusion constant from other material and environmental variables. The most common one follows from the Maxwell-Boltzmann distribution of kinetic gas theory with

$$D = \frac{1}{3}ul. \tag{2.2}$$

Thus, diffusion is proportional to the mean velocity u and the mean free path l of the spreading particles. The factor $\frac{1}{3}$ comes into play because the particles propagate to the same extent in all

three spatial dimensions. Since the Maxwell-Boltzmann distribution only holds for ideal gases, Eq. (2.2) specifically describes diffusion in gases. However, the stronger the interaction between the diffusing particles and the surrounding medium, the slower diffusion becomes. In this respect, the Stokes-Einstein relation provides the following expression for the diffusion constant,

$$D = \frac{k_B T}{6\pi\eta r}. \tag{2.3}$$

Its denominator corresponds to Stokes' friction and considers the intermolecular interaction through the dynamic viscosity η of the medium. In addition, the diffusivity depends on the temperature T and the Boltzmann constant k_B, which relates temperature to thermal energy, as well as the particles' hydrodynamic radius r. The term Eq. (2.3) is especially applicable for diffusion in water with low concentrations of the diffusing substance. A more comprehensive discussion of the theoretical calculation of diffusion constants can be found in Cussler (2009). In summary, the diffusion coefficient D depends mainly on the temperature, the size of the diffusing particles, and their interactions with the surrounding medium. This holds true regardless of the underlying theoretical framework.
A more general description of diffusion in terms of a transport equation can be obtained by combining the microscopic behavior of particles with the macroscopic principle of mass conservation. According to this, the temporal change in concentration within a control volume equals the flux across its boundary. By applying Gauss's integral theorem, the continuity equation can be expressed in the following mathematically rigorous form

$$\frac{\partial \rho}{\partial t} + \nabla \cdot \vec{j} = 0. \tag{2.4}$$

It is important to note that this equation is only valid in the absence of sources or sinks within the control volume. When the mass flux is governed solely by diffusion, incorporating Eq. (2.1) into the continuity equation (2.4) yields Fick's second law

$$\frac{\partial c}{\partial t} = D\Delta c. \tag{2.5}$$

This represents the simplest form of a transport equation, where diffusion is the only operative transport mechanism.
Since the diffusion of heat and momentum follows similar physical mechanisms as the diffusion of substances, namely the thermal movement of particles and their mutual interactions, comparable transport equations govern these processes. In the case of heat diffusion, Fourier's law expresses the heat flux $\vec{j}_{h,\mathrm{diff}}$ by

$$\vec{j}_{h,\mathrm{diff}} = -\lambda_h \nabla T, \tag{2.6}$$

with λ_h denoting the thermal conductivity. Mathematically, this is analogous to Fick's first law, but heat diffusion is obviously driven by a temperature gradient. The corresponding transport equation is the heat equation given by

$$\frac{\partial T}{\partial t} = \chi \Delta T, \tag{2.7}$$

where $\chi = \frac{\lambda_h}{c_p \rho}$ represents the temperature diffusivity, and incorporates both λ_h along with the specific heat capacity at constant pressure c_p and fluid density ρ. Momentum diffusion, however, is somewhat more complex due to its vectorial nature, unlike the scalar quantities concentration and heat. Nonetheless, the analysis can be simplified by considering the momentum in the x-direction and its diffusion in the z-direction. The momentum flux $\vec{j}_{m,\text{diff},zx}$ corresponds to the shear stress τ_{zx} of the fluid, which is described by Newton's law as

$$\vec{j}_{m,\text{diff},zx} = \tau_{zx} = -\nu \frac{\partial \rho u_x}{\partial z}. \tag{2.8}$$

Here, ν is the kinematic viscosity, a measure of the internal frictional forces of the fluid. It implies that momentum diffusion perpendicular to the direction of flow is mediated by internal friction within the fluid and driven by a velocity gradient in that direction. The associated momentum transport equation is

$$\frac{\partial \vec{u}}{\partial t} = \nu \Delta \vec{u}, \tag{2.9}$$

which represents the famous Navier-Stokes equation in its simplest form (Roedel & Wagner, 2017).

2.1.2 Advection

Advection is the process by which matter is carried along with the flow of a fluid. In gas exchange close to an air-water interface, advection only plays a limited role as substances are primarily transported along the bulk flow without significant vertical mixing, unlike diffusion or turbulence. In the interest of completeness, we briefly outline how transport equations are extended to include advection. The key addition is to supplement the total flux across the boundary of the control volume in the continuity equation (2.4) by an advective flux $\vec{j}_{\text{adv}}$ alongside the diffusive flux $\vec{j}_{\text{diff}}$. After

$$\vec{j}_{\text{adv}} = \vec{u}\phi, \tag{2.10}$$

the advective flux corresponds to a simple multiplication of the fluid velocity $\vec{u}$ by the transported quantity ϕ. Substituting $\vec{j} = \vec{j}_{\text{adv}} + \vec{j}_{\text{diff}}$ into Eq. (2.4) leads to the following extended transport equations for substances, heat, and momentum

$$\frac{\partial c}{\partial t} + \vec{u} \cdot \nabla c = D \Delta c, \tag{2.11}$$

$$\frac{\partial T}{\partial t} + \vec{u} \cdot \nabla T = \chi \Delta T, \tag{2.12}$$

$$\frac{\partial \vec{u}}{\partial t} + \vec{u} \cdot \nabla \vec{u} = -\frac{1}{\rho} \nabla p + \vec{f} + \nu \Delta \vec{u}. \tag{2.13}$$

It should be noted that the left-hand side of each equation now corresponds to the total derivative of the transported quantities. The total derivative captures both the local rate of change and the advective transport, meaning the flux accounts for diffusion as well as movement with the fluid flow. The momentum transport equation shown here corresponds to the best-known form of the Navier-Stokes equation, which also includes gradients of pressure p and external body forces $\vec{f}$ acting on the fluid

motion. It provides a comprehensive and fundamental description of fluid dynamics (Degreif, 2006).

2.1.3 Turbulence

The term turbulence denotes a complex nonlinear flow behavior of fluids characterized by a chaotic and irregular velocity field. It arises from random, unpredictable fluctuations in the flow velocity. Unfortunately, the exact nature of these velocity fluctuations is one of the unsolved problems of classical physics, which complicates the description of turbulence phenomena immensely. Simply explained, a turbulent motion occurs if the inertial forces of the flow exceed its viscous frictional forces. We can imagine a turbulent flow in the form of eddies. This is the approach of Kolmogorov's theory (Kolmogorov, 1941), which states that a turbulent flow consists of eddies with widely differing sizes. Here, energy is primarily injected at the largest scales and gradually divided into smaller eddies resulting in an energy cascade towards smaller scales. On the smallest scale, the energy is completely dissipated into heat through viscous friction. Kolmogorov defined characteristic length, time, and velocity scales in which dissipation dominates. As a result, this gives an estimate for the size of the smallest turbulent elements.

The key quantity to assess the potential of a flow for turbulence is the so-called Reynolds number. It is defined as

$$Re = \frac{ul}{\nu}, \tag{2.14}$$

where u is the mean flow velocity, l is the characteristic length scale of the dominant flow. Originally established in Reynolds (1883), this dimensionless number is equivalent to the ratio of inertial forces to viscous forces in a flow and allows a prediction to be made whether a flow is laminar or turbulent. Below a critical Reynolds number Re_{crit}, the dissipative forces dominate, causing any emerging turbulent structures to decay immediately. Consequently, this has a stabilizing effect on the flow, which is laminar and stationary in this regime. However, above Re_{crit}, the inertial forces overpower the viscous forces. Here, the statistical fluctuations of the velocity field increase, leading to a destabilization of the flow. In this regime, the flow becomes turbulent and unsteady. Typical values for Re_{crit} range from magnitudes of 10^3 up to 10^5, but depend strongly on the specific conditions of the problem (Schlichting & Gersten, 2006). In particular, the transition range close to the critical Reynolds number between a perfectly laminar flow and a fully developed turbulent flow remains poorly understood and is a subject of ongoing research (Xiao & She, 2019).

Although turbulence is a non-deterministic phenomenon, the stochastic fluctuations can be effectively integrated into transport equations. The most commonly used method to deal with these fluctuations is the Reynolds decomposition. In this approach, the transported quantities concentration c and momentum $\rho\vec{u}$ are split into a time-averaged part and a fluctuating part. Assuming a constant density, this only applies to the velocity for momentum,

$$c = \overline{c} + c', \tag{2.15}$$

$$\vec{u} = \overline{\vec{u}} + \vec{u}'. \tag{2.16}$$

Here, $\overline{c}$ and $\overline{\vec{u}}$ refer to the mean components, while c' and $\vec{u}'$ represent the fluctuating components. The fluctuations c' and $\vec{u}'$ are defined as the deviations from the mean value, implying that the time average of these fluctuations over a sufficiently long time period is inherently zero, i.e. $\overline{c'} = \overline{\vec{u}'} = 0$. Since the focus is on gas exchange, only concentrations and fluid velocities are considered. However, the same assumptions can be made for the temperature in the context of heat transport (Kundu & Cohen, 2008).

By inserting Eqs. (2.15) and (2.16) into the transport equations for mass and momentum and averaging the resulting equations, we obtain

$$\frac{\partial \overline{c}}{\partial t} + \frac{\partial}{\partial x_j}\left(\overline{c} \cdot \overline{u}_j + \overline{c' \cdot u'_j}\right) = D\Delta\overline{c}, \tag{2.17}$$

$$\frac{\partial \overline{u}_i}{\partial t} + \frac{\partial}{\partial x_j}\left(\overline{u}_i \cdot \overline{u}_j + \overline{u'_i \cdot u'_j}\right) = -\frac{1}{\rho}\frac{\partial p}{\partial x_i} + f_i + \nu\Delta\overline{u}_i. \tag{2.18}$$

When averaging these equations over time, all mixed terms containing products of an averaged and a fluctuating component are eliminated, as the temporal mean of the fluctuations vanishes. Consequently, only the products of the averaged variables and the mean of their fluctuation products remain. The first term describes the transport resulting from the mean flow, equivalent to advection, while the second term captures the effect of turbulence on this mean transport. The strength of this turbulence term depends mainly on the correlation between the two fluctuating quantities. If the variables are not correlated, the temporal averaging cancels out these fluctuations. However, if the variables are correlated, the turbulence effect can be significantly large. This correlation is commonly referred to as eddy covariance. In the context of momentum transport, which is inherently three-dimensional, the eddy covariance terms are summarized in the Reynolds stress tensor. More specifically, this two-dimensional tensor contains as elements all covariances between the fluctuating velocity components in the three dimensions, effectively accounting for the complicated interactions within the turbulent flow (Kundu & Cohen, 2008). The equations simplify significantly in the one-dimensional case when focusing only on vertical transport and neglecting the advective term. This assumption is justified because advection is primarily associated with horizontal flows. Consequently, the governing transport equations reduce to

$$\frac{\partial \overline{c}}{\partial t} = \frac{\partial}{\partial z}\left(D\frac{\partial \overline{c}}{\partial z} - \overline{c' \cdot u'_z}\right), \tag{2.19}$$

$$\frac{\partial \overline{u}_x}{\partial t} = \frac{\partial}{\partial z}\left(\nu\frac{\partial \overline{u}_x}{\partial z} - \overline{u'_x \cdot u'_z}\right). \tag{2.20}$$

They resemble the classical diffusion equations (2.5) and (2.9), but with an additional term accounting for turbulence effects. This similarity leads to the idea of describing turbulent transport analogously to diffusive transport. By introducing the turbulent diffusivity K_c and turbulent viscosity K_m, the covariance terms can be reformulated in

$$\overline{c' \cdot u'_z} = -K_c\frac{\partial \overline{c}}{\partial z}, \tag{2.21}$$

$$\overline{u'_x \cdot u'_z} = -K_m\frac{\partial \overline{u}_x}{\partial z}. \tag{2.22}$$

A comparison with Eq. (2.4) yields the following expressions for the vertical mass and momentum flux densities, respectively

$$j_c = -\left(D + K_c(z)\right) \frac{\partial \overline{c}}{\partial z}, \tag{2.23}$$

$$j_m = -\left(\nu + K_m(z)\right) \frac{\partial \overline{u}_x}{\partial z}. \tag{2.24}$$

It is important to note that, unlike molecular diffusivity, turbulent diffusivity is generally a function of depth. The precise vertical profile of turbulence is only well known in certain limiting cases. Nevertheless, it remains one of the most critical parameters for accurately determining the transport of mass, heat, and momentum in turbulent flows (Degreif, 2006; Haußecker, 1996; Roedel & Wagner, 2017).

2.1.4 General Transport Equations

So far, the transport equations considered describe the temporal and spatial change of mass, heat, or momentum in a fluid exclusively by physical mechanisms such as diffusion, advection, and turbulence. Their formulations rely on the continuity equation (2.4), which assumes that any change in the total amount of a quantity within a control volume is caused solely by transport across its boundaries, without internal sources or sinks. In many real systems, however, chemical reactions play an important role, consuming or producing substances within the control volume. Thus, such reactions act as internal sources or sinks resulting in an additional temporal change of the transported substances (Cussler, 2009). To address this, the continuity equation needs to be modified as follows by including a reaction or source term R,

$$\frac{\partial \rho}{\partial t} + \nabla \cdot \vec{j} = R, \tag{2.25}$$

whereby mass conservation is no longer valid. This extension leads directly to a generalized transport equation given by

$$\frac{\partial \overline{c}}{\partial t} + \frac{\partial}{\partial z}\left(\overline{c} \cdot \overline{u}_z + \overline{c' \cdot u'_z}\right) = D\Delta\overline{c} + R, \tag{2.26}$$

which includes the phenomena of diffusion, advection, turbulence, and chemical reactions (Bird et al., 2002). It represents the most comprehensive formulation of mass transport in fluids as used in this work.

2.2 Air-Sea Gas Exchange

After having clarified the basic transport phenomena in fluids, this section addresses how these mediate the exchange of gases at an air-water interface. This requires applying the transport equations to the interfacial conditions by assessing the significance of the transport mechanisms near the interface. In general, gas exchange is influenced by the concentration differences between the air and water phases, as well as the strength of the transport mechanisms (Garbe et al., 2014), as mathematically expressed in Eq. (2.23). Throughout the discussion, the air-water interface is assumed to lie in the x-y plane, and transport is considered only in the z-direction, simplifying the problem to one-dimensional transport equations.

2.2.1 Concept of Boundary Layers

An initial approach to physically describing the gas exchange at an interface between air and water is provided by the concept of boundary layers. In principle, vertical transport of gases is driven by diffusion and turbulence, with turbulence prevailing over diffusion in most cases. However, the situation changes considerably in the vicinity of a boundary that separates air and water. Such an interface is characterized by an abrupt change in physical properties, especially in mass density. Due to this density difference, turbulent eddies are basically unable to penetrate the air-water interface. As turbulent eddies approach the interface, they progressively diminish in size and the intensity of turbulence decreases until it ultimately vanishes at the water surface (Prandtl, 1957). It is this phenomenon that allows the definition of mass boundary layers on both sides of the interface, where diffusion emerges as the primary transport mechanism. Beyond these boundary layers, in the bulk phase, turbulence naturally dominates over diffusion. The intersection between the turbulence depth profile and the constant diffusion determines the extent of the boundary layer and defines its thickness. Typical mass boundary layer thicknesses on the water side range from 10 µm to 350 µm, while on the air side they reach from 150 µm to 1500 µm. Since diffusion is significantly slower than turbulence, these boundary layers represent the bottleneck for gas exchange. Accordingly, the efficiency of gas exchange is mainly controlled by the transport processes taking place in these thin mass boundary layers close to the water surface (Jähne, 2019).

We will now examine how the boundary layers around the air-water interface affect the concentration fields of a transported species. At equilibrium, when the net flux of gas molecules between air and water is zero, the distribution of the gas between the two phases is predicted by its solubility, also known as the Ostwald coefficient. According to Henry's law, this solubility α refers to the ratio of the tracer concentration dissolved in the water phase $c_{w,\mathrm{eq}}$ to that contained in the air phase $c_{a,\mathrm{eq}}$, as shown in

$$\alpha = \frac{c_{w,\mathrm{eq}}}{c_{a,\mathrm{eq}}}. \tag{2.27}$$

As a consequence, the gas concentration profile exhibits a discontinuity, i.e. a step change, at the interface instead of a continuous transition. If the system is disturbed from this thermodynamic equilibrium, a flux across the interface is induced to restore equilibrium. This flux is specified by Eq. (2.23) and remains constant over depth due to mass conservation. If the concentration in the air-side bulk phase $c_{a,b}$ exceeds that in the water-side bulk phase $c_{w,b}$ after $\alpha c_{a,b} > c_{w,b}$, the flux is oriented from the air to the water side, referred to as invasion. Conversely, the flux will be directed from the water to the air phase if $\alpha c_{a,b} < c_{w,b}$ holds, which is called evasion. At the interface itself, the thermodynamic equilibrium is instantaneously established between the surface concentrations in both phases $c_{a,s}$ and $c_{w,s}$, ensuring that the condition

$$c_{w,s} = \alpha c_{a,s} \tag{2.28}$$

is satisfied. As an example, we consider an invasion experiment in which an initial excess of gas in the air side dissolves in the water. Given the typically high solubility $\alpha \gg 1$ of gases used in invasion experiments, it will dissolve more quickly in water at the interface than it is replenished from the air-

side bulk through the air-side mass boundary layer. Thus, the air-side gas concentration at the surface $c_{a,s}$ decreases relative to the air-side bulk concentration $c_{a,b}$. In contrast, on the water side, the gas is transported downwards to the bulk phase more slowly through the aqueous mass boundary layer than it enters from the surface, leading to an accumulation of gas in the vicinity of the interface. As a result, the water-side gas concentration at the surface $c_{w,s}$ increases compared to the bulk concentration $c_{w,b}$ in water. Since transport directly at the interface is solely mediated by diffusion, the following applies to the flux

$$j_c = -D \left.\frac{\partial c}{\partial z}\right|_{z=0}, \tag{2.29}$$

whereas the linear gradients of the concentration profiles in the two phases can be determined from the diffusion constants of the air and water sides. This will become particularly relevant for the calculation of the mass boundary layer thickness. With a constant flux, the system will reach a steady state, whereby the concentration profiles remain stable over time (Papst, 2019). The resulting concentration profile and respective boundary layers arising in the vicinity of the interface are summarized in Fig. 2.1.

Similarly to mass transport, an analogous boundary layer concept can be applied to the transport of heat and momentum. In the case of momentum transport, taking place via molecular viscosity and turbulent viscosity, we find viscous boundary layers forming in both phases close to the air-water interface. Within these layers, molecular viscosity dominates over turbulent effects, meaning that emerging turbulent eddies are too small to contribute effectively to the transport. The thickness of the viscous boundary layer is usually between 250 µm to 3000 µm on the water side and varies from 150 µm to 1500 µm on the air side. Interestingly, the thicknesses of the mass boundary layer and the viscous boundary layer are of the same order of magnitude on the air side, whereas they differ significantly on the water side. This discrepancy arises because the molecular diffusion constant, with typical values of $D_a \approx 10^{-1}\,\mathrm{cm^2\,s^{-1}}$ and $D_w \approx 10^{-5}\,\mathrm{cm^2\,s^{-1}}$ (Yaws, 1995), varies in the two phases to a much greater extent than the viscosity with $\nu_a \approx 1.5 \cdot 10^{-1}\,\mathrm{cm^2\,s^{-1}}$ and $\nu_w \approx 10^{-2}\,\mathrm{cm^2\,s^{-1}}$ (Lide, 2004) of the two media. The reason for this is that momentum transport relies on molecular collisions, which allow efficient transport even in dense fluids. In contrast, mass transport results from diffusion, requiring individual molecules to actively move through the medium. This process is significantly slower in water due to the higher density and increased intermolecular interactions. Hence, momentum is transported more efficiently than mass, particularly on the water side, leading to a relatively thinner mass boundary layer.

The relative thickness of the mass boundary layer compared to the viscous boundary layer is quantified by the Schmidt number, defined as the dimensionless quotient between the kinematic viscosity of water and the molecular diffusion coefficient

$$Sc = \frac{\nu}{D}. \tag{2.30}$$

It serves as a comparative measure of mass and momentum transport and provides important insights into the relative efficiency of these processes. In particular, tracers with high Schmidt numbers show much slower mass transport relative to momentum transport, underscoring the decisive role of the mass boundary layer in limiting gas exchange. Similarly, a turbulent Schmidt number can be defined as the ratio of turbulent viscosity over turbulent diffusivity, characterizing the relationship between

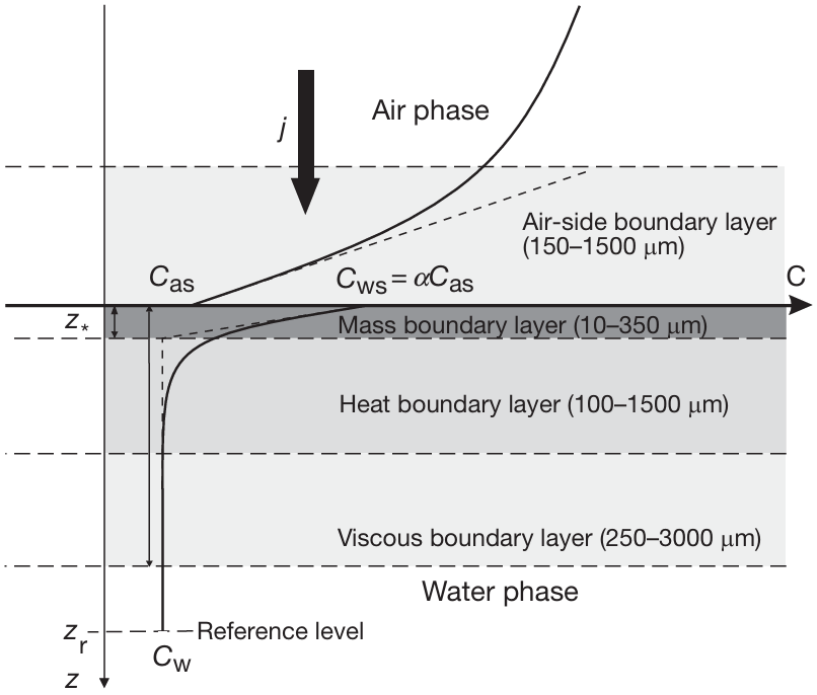

Figure 2.1: Boundary layers for mass and momentum at an air-water interface. The black curve represents the typical steady state concentration profile of a trace gas with solubility $\alpha > 1$ (Jähne, 2019).

turbulent transport mechanisms

$$Sc_{\text{turb}} = \frac{K_m}{K_c}. \tag{2.31}$$

As we will see, the Schmidt number becomes a potential candidate for parameterizing gas exchange at the air-water interface (Jähne & Haußecker, 1998).

2.2.2 Physical Quantification of Gas Exchange

In order to quantify the gas exchange across the air-water interface, two physical parameters have become established: transfer velocity k and transfer resistance R. Both quantities are the reciprocal of each other and are defined as quotients of flux density j and concentration difference Δc between two vertically separated layers (Garbe et al., 2014)

$$k = \frac{j}{\Delta c} = \frac{1}{R}. \tag{2.32}$$

While the transfer velocity refers to the mean velocity at which a gas is transported vertically through an arbitrary layer, the transfer resistance indicates the time required for the gas to pass one unit length of this layer (Jähne, 2019; Kräuter, 2015; Papst, 2019). To link the two quantities to the driving transport mechanisms, we assume a concentration difference between two distinct vertical points. This concentration gradient causes a mass flow according to Eq. (2.23). By rearranging and integrating along the depth, we get the concentration difference as

$$\Delta c = c(z_2) - c(z_1) = -j_c \int_{z_1}^{z_2} \frac{1}{D + K_c(z)}\, dz. \tag{2.33}$$

Finally, inserting into Eq. (2.32) leads to the following elementary expressions for the transfer velocity and the transfer resistance

$$k = -\left(\int_{z_1}^{z_2} \frac{1}{D + K_c(z)}\, dz\right)^{-1} = \frac{1}{R}. \tag{2.34}$$

Here, it is evident that the rate of gas exchange can be calculated solely from knowledge of the molecular and turbulent diffusivities governing the respective transport mechanisms. As discussed in Sec. 2.1.3, the determination of the exact turbulence depth profile poses a major challenge.

Since it is not possible to express the diffusivities across the air and water phases in a continuous form, the transfer velocity and resistances in both phases must be treated separately. This partitioning is feasible due to the additivity of the integral over different arbitrary layers. Thus, the total resistance for mass transfer corresponds to the sum of the transfer resistances in the air and water phases, denoted as R_a and R_w for the air-side and water-side contributions, respectively. It has already been established that the main resistance in each phase is located within their mass boundary layers. Conceptually, this approach is analogous to the addition of resistances in a series connection within an electrical circuit. In addition, resistances of different transport mechanisms add up reciprocally, which is equivalent to a parallel connection in electrical circuits. Due to the discontinuous concentration profile at the air-water interface, the resistances also need to be corrected for the solubility when considering the transport across this interface. This results in two different total resistances depending on the side of consideration, denoted by $R^{\mathrm{a}}_{\mathrm{tot}}$ for the air-side view and $R^{\mathrm{w}}_{\mathrm{tot}}$ for the water-side view, as given by

$$R^{\mathrm{a}}_{\mathrm{tot}} = R_a + \frac{R_w}{\alpha}, \tag{2.35}$$

$$R^{\mathrm{w}}_{\mathrm{tot}} = \alpha R_a + R_w. \tag{2.36}$$

Similarly, the corresponding reciprocal terms apply to the transfer velocity, leading to

$$k^{\mathrm{a}}_{\mathrm{tot}} = \left(\frac{1}{k_a} + \frac{1}{\alpha k_w}\right)^{-1}, \tag{2.37}$$

$$k^{\mathrm{w}}_{\mathrm{tot}} = \left(\frac{\alpha}{k_a} + \frac{1}{k_w}\right)^{-1}. \tag{2.38}$$

These equations summarize to $R^{\mathrm{w}}_{\mathrm{tot}} = \alpha R^{\mathrm{a}}_{\mathrm{tot}}$ and $k^{\mathrm{a}}_{\mathrm{tot}} = \alpha k^{\mathrm{w}}_{\mathrm{tot}}$ indicating that solubility dictates which term dominates the total transfer resistance, and thus identifies which phase controls the gas exchange (Garbe et al., 2014; Jähne, 2019; Liss & Slater, 1974).

According to this, gases can generally be classified into three different groups. Substances with high solubility have their main resistance on the air side. These air-side controlled gases comprise, for example, NH_3 and H_2O. Conversely, species with low solubility are primarily controlled on the water side. Some examples of these gases are CO_2, O_2, and N_2O. Furthermore, some gases fall into the transition zone in between, where the gas exchange is equally influenced by the air and the water side. Where exactly the transition zone is located depends on the Schmidt number and the surface conditions of the air-water interface. Typically, the solubility is plotted against the Schmidt number to classify the gases, as shown in Fig. 2.2. It is worth noting that heat and momentum transport can be classified in the same manner, both of which are clearly air-side controlled.

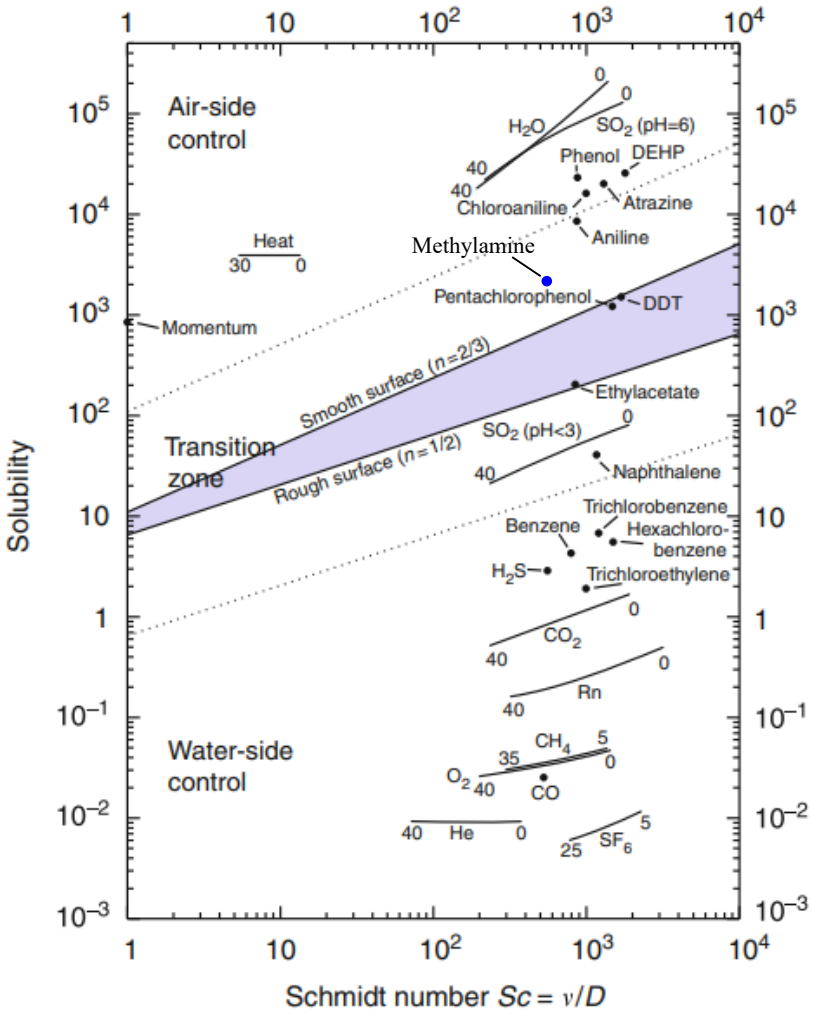

Figure 2.2: Schmidt number solubility diagram for selected trace gases and volatile species. It classifies the species according to their position above or below the purple area into air-side or water-side controlled substances respectively. The transition zone has two limits depending on the boundary conditions of a smooth or rough surface. Modified after Garbe et al. (2014).

Mass Boundary Layer Approach

As an alternative to the general quantification of gas exchange discussed prior, we can adopt a simplified approach relying on the concept of mass boundary layer. This idea assumes that the efficiency of gas exchange is closely related to the thickness of the mass boundary layer, as this is where the main resistance to transport resides. We define the mass boundary layer thickness z_* as the depth at which the surface concentration c_s has dropped to the bulk concentration c_b, assuming the concentration profile follows a linear gradient from the surface. Applying Eq. (2.32) we obtain

$$z_* = \frac{c_s - c_b}{\frac{\partial c}{\partial z}\big|_{z=0}} = D\frac{\Delta c}{j_c} = \frac{D}{k}. \tag{2.39}$$

This is equivalent to a slope triangle formed by the linear gradient of the surface concentration and the z-axis.

Finally, in addition to the characteristic velocity k and length z_*, it is also possible to quantify gas exchange by a characteristic time t_*. This transfer time represents the time required for a gas to cross the mass boundary layer, calculated by

$$t_* = \frac{z_*}{k} = \frac{D}{k^2}. \tag{2.40}$$

Hence, gas exchange is quantifiable by three different concepts, each yielding one of the three parameters k, z_*, and t_*. By means of the diffusion constant D and the Eqs. (2.39) and (2.40), these parameters can be converted into each other. As a result, gas exchange experiments can determine the transfer velocity not only through direct measurement but also indirectly by assessing the boundary layer thickness or the transfer time (Jähne & Haußecker, 1998).

Friction Velocity

So far, we have seen that the efficiency of gas exchange depends not only on invariable material properties such as diffusivity D, solubility α, and Schmidt number Sc, but above all on the turbulence state $K(z)$ within the boundary layers. The most important factor influencing this turbulence is the wind blowing on the air side, which induces a shear stress τ on the water surface due to friction. This frictional force transfers momentum and energy into the system leading to the development of turbulent flows on the water side. An essential quantity to measure the momentum transferred by the wind into the water is the friction velocity u_* defined as

$$u_* = \sqrt{\frac{\tau}{\rho}}. \tag{2.41}$$

Given the conservation of momentum, the momentum transport across the interface must be continuous, in accordance with $\tau_a = \tau_w$. So, when considering the friction velocity either from the air side or from the water side, the following relationship applies

$$u_{*,w} = \sqrt{\frac{\rho_a}{\rho_w}} u_{*,a}, \tag{2.42}$$

where ρ_a and ρ_w denote the densities of air and water respectively. In summary, an appropriate physical quantification of gas exchange should parameterize the transfer velocity or transfer resistance not only in terms of material-dependent constants but also as a function of the friction velocity (Jähne, 2019).

2.2.3 Models of Gas Exchange

A number of gas exchange models have been proposed in order to obtain a suitable parameterization of the transfer velocity. What all these approaches have in common is to find a simplified description of turbulence within the mass boundary layer. Due to the complex nature of turbulence, these models are rather conceptual or semi-empirical in their methodology. An illustrative overview of the most important models is given in Fig. 2.3.

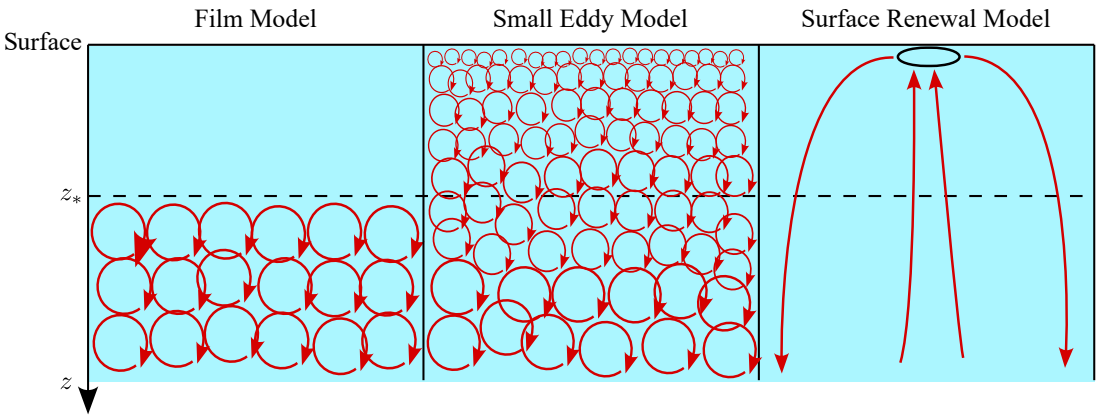

Figure 2.3: Overview of gas exchange models. The near-surface turbulence fields are drawn, with the size of the eddies scaling with the turbulence strength. The dashed line indicates the mass boundary layer thickness. Modified after Krall (2013).

Film Model

The simplest model we can imagine is the so-called film model, which goes back to Whitman (1923). It assumes that within the mass boundary layer only diffusive transport occurs and turbulent transport is completely excluded. Outside the boundary layer, the fluid is perfectly mixed by fully developed turbulence. This description conceptualizes the mass boundary layer as a stagnant film, which leads to its name. By assuming $K(z) = 0$ within the boundary layer and integrating Eq. (2.33) over the mass boundary layer thickness z_*, we achieve the already known parameterization for the transfer velocity

$$k = -\left(\int_0^{z_*} \frac{1}{D}\, dz\right)^{-1} = \frac{D}{z_*} = \frac{\nu}{z_*} Sc^{-1}, \tag{2.43}$$

whereby this is expressed in terms of the Schmidt number in the second step. The rationale for this transformation will become evident later. Obviously, the film model represents an oversimplification of the real dynamics, as the turbulence always extends into the mass boundary layer. Nevertheless, it is often used because it provides a lower limit for the transfer velocity.

Small Eddy Model

A more realistic and very intuitive description of turbulence in the mass boundary layer is given by the Small Eddy model. In this approach, turbulence is represented by a continuous depth profile $K(z)$ that vanishes at the air-water interface and increases with depth while still penetrating the mass boundary layer. This reflects the idea that turbulent eddies become progressively smaller as they near the surface, leading to a decrease in turbulent mixing. To parameterize the transfer velocity, the integral in Eq. (2.34) must be fully evaluated for the corresponding function $K(z)$.

An analytical expression for this turbulent diffusivity can be derived for two special cases. These calculations follow Coantic (1986), based on solving the averaged transport equation under certain boundary conditions. A more detailed derivation can also be found in Degreif (2006) and Friedl (2013). For a wavy water surface, we can assume that turbulence-induced velocity fluctuations at the

surface itself are allowed parallel to this interface, but are prohibited perpendicular to it

$$w' = 0|_{z=0}\,, \tag{2.44}$$

allowing the existence of convergence and divergence zones at the boundary. Under these conditions, the turbulent diffusivity follows a quadratic dependence on the distance from the water surface

$$K(z) \propto z^2. \tag{2.45}$$

In contrast, for a smooth water surface, even velocity fluctuations parallel to the interface are forbidden at the surface

$$u' = v' = w' = 0|_{z=0}\,, \tag{2.46}$$

implying there is neither convergence nor divergence at the surface. These conditions produce a cubic dependence of turbulent diffusivity on depth

$$K(z) \propto z^3. \tag{2.47}$$

In general, the turbulent diffusivity can be formulated as a power law

$$K(z) = a_m z^m, \tag{2.48}$$

where $m = 2$ holds for a free surface and $m = 3$ implies a rigid surface. By integrating this expression, we obtain a dependence of the transfer velocity on the Schmidt number as $k \propto Sc^{-\frac{1}{2}}$ for a wavy boundary and $k \propto u_* Sc^{-\frac{2}{3}}$ for a smooth boundary. The relationship can be summarized in the following form

$$k \propto Sc^{-\frac{m-1}{m}}. \tag{2.49}$$

An alternative approach to the model originates from Deacon (1977). The starting point for his theory is Reichardt's model (Reichardt, 1951), which provides an expression for the turbulence profile in the vicinity of a solid wall. This corresponds to a smooth water surface and again predicts a cubic dependence of turbulent diffusivity with depth close to the interface. Deacon's numerical integration yields the following parameterizations for the transfer resistance assuming the cubic turbulence profile persists across the mass boundary layer

$$R = \frac{15.2}{u_*} Sc^{0.61} \qquad \text{for } 0.6 < Sc < 10, \tag{2.50}$$

$$R = \frac{12.1}{u_*} Sc^{\frac{2}{3}} + 2.7 \log_{10}(Sc) + 2.9 \qquad \text{for } Sc > 10. \tag{2.51}$$

While the first equation holds for small Schmidt numbers, which primarily describes the air-side transport, the second equation is valid for larger Schmidt numbers, corresponding to water-side transport. For even larger Schmidt numbers, two of the terms can be neglected. After Jähne (1980),

the following approximation applies

$$R = \frac{12.1}{u_*} Sc^{\frac{2}{3}} \qquad \text{for } Sc > 60. \tag{2.52}$$

All these parameterizations are only suitable for low wind speeds or film-covered water surfaces, i.e. scenarios in which the water surface is smooth and rigid and Reichardt's law of the solid wall is applicable. However, this assumption no longer applies to a free and rough water surface at high wind speeds. Instead, similar theories also suggest a quadratic dependence of turbulent diffusivity on depth. Nevertheless, a generally valid theory to describe these boundary conditions is still lacking.

Surface Renewal Model

The surface renewal model introduced by Higbie (1935) and Danckwerts (1951) takes a fundamentally different approach to describing turbulence than the concept of turbulent diffusivity. Instead, the model assumes that transport through the mass boundary layer occurs by intermittent renewal of the surface alongside with molecular diffusion. According to this, liquid parcels remain at the water surface until they are carried to deeper layers by large-scale turbulent eddies, while fresh liquid parcels simultaneously rise from the bulk. This perspective shifts the focus from a description of turbulent diffusivity to the temporal and spatial characteristics of these renewal events. Their frequency and efficiency play a crucial role in determining the overall transport rate, describable by a renewal rate λ and generally parameterized in the following form

$$\lambda = \lambda_p z^p, \tag{2.53}$$

allowing for a potential dependence on depth by the parameter p (Jähne, 1985). Intuitively, the concentration change associated with surface renewal events should be understood to depend on both the renewal rate λ and the surface concentration c. So, to incorporate the surface renewal model into a transport equation, the turbulent transport term is replaced by the product of λ and c, introducing a sink term into the equation

$$\frac{\partial c}{\partial t} = D\Delta c - \lambda c. \tag{2.54}$$

This transport equation can be solved for a few specific cases. One such case is $p = 0$, dropping the depth dependence and assuming renewal rate to be constant with depth, as described in Danckwerts (1951) and Harriott (1962). Specifically, in this condition the renewal rate at the surface remains non-zero, which characterizes a free water surface. Solving the steady-state form of the transport equation yields an exponential concentration depth profile, with the transfer rate given by

$$k = \sqrt{\lambda D}. \tag{2.55}$$

Remarkably, this expression is identical to Eq. (2.40) with $\lambda = t_*^{-1}$, illustrating the direct correlation between surface renewal events and transfer time through the mass boundary layer. A dimensional analysis further reveals the following Schmidt number dependence of the transfer velocity for surface

renewals on a wavy water surface

$$k \propto u_* Sc^{-\frac{1}{2}}. \tag{2.56}$$

In contrast, for $p = 1$, the renewal rate increases linearly with depth, meaning that it approaches zero at the surface. This behavior gives a plausible model for the description of a smooth water surface. Following the calculations of Jähne et al. (1989), the transfer velocity is given by

$$k \propto u_* Sc^{-\frac{2}{3}}. \tag{2.57}$$

In more general terms, the transfer velocity follows the relationship

$$k \propto u_* Sc^{-\frac{p+1}{p+2}}, \tag{2.58}$$

where $p = 0$ corresponds to a free water surface and $p = 1$ to a rigid water surface.

General Formulation

Although the various gas exchange models adopt different approaches to describe turbulence, they ultimately converge to a general parameterization. Accordingly, the water-side gas transfer velocity k follows a function of the friction velocity u_*, a dimensionless parameter β and the Schmidt number Sc, scaled up to a certain exponent n, given by

$$k = \frac{u_*}{\beta} Sc^{-n}. \tag{2.59}$$

Both β and n depend strongly on the boundary conditions at the water surface. This underlines the rationale for reformulating the film model's parameterization in terms of the Schmidt number. While this model predicts a Schmidt number exponent of $n = 1$ and thus underestimates the gas exchange, other models suggest values of $n = \frac{2}{3}$ for a smooth water surface and $n = \frac{1}{2}$ for a wavy water surface. However, there are only reliable theoretical foundations for these specific boundary conditions. A comprehensive theory describing the transition of the Schmidt number exponent in the intermediate states between a perfectly rigid and a completely free water surface does not yet exist (Garbe et al., 2014). Based on the expression in Eq. (2.59), a crucial formula arises that plays an essential role in gas exchange experiments. Considering the relationship for two different gases and assuming identical surface conditions, the ratio of their transfer velocities ends up with

$$\frac{k_1}{k_2} = \left(\frac{Sc_1}{Sc_2}\right)^{-n}. \tag{2.60}$$

It is therefore possible to find the transfer velocity k_1 of one trace gas by knowing the Schmidt numbers Sc_1 and Sc_2 of both species and measuring the transfer velocity k_2 of the other trace gas, provided that the Schmidt number exponent n is known or can be reasonably measured. Conversely, simultaneous measurement of the transfer velocities of two different gases also allows to draw conclusions about the Schmidt number exponent n, which is a good measure of the turbulence state of the water surface. The formula in Eq. (2.60) offers a way of referencing and comparing transfer velocities of different gases.

Typically, transfer velocities are translated to CO_2 due to its relevance as greenhouse gas. This is advantageous because the gas exchange for a number of trace gases is easier to measure experimentally than the slow transfer of CO_2. The Schmidt number for CO_2 is usually reported in the literature as $Sc = 660$ for seawater and $Sc = 600$ for freshwater at 20 °C (Garbe et al., 2014).
Since it remains challenging to describe the turbulence state of the entire water surface by means of a single universal boundary condition, the facet model was developed from Jähne and Bock (2000) by extending Eq. (2.59). This model divides the water surface into smooth and wavy regions. In the smooth regions, the rigid boundary condition applies, while in the wavy regions, the free boundary condition is considered. As a result, the transfer velocity is parameterized as the sum of the contributions from each region, weighted by their respective fractional areas, leading to

$$k = a_s k_s + a_w k_w = (1 - a_w)\frac{u_*}{\beta_s} Sc^{-n_s} + a_w \frac{u_*}{\beta_w} Sc^{-n_w}, \tag{2.61}$$

where a_w gives the fraction of the total surface covered by waves. Furthermore, the Schmidt number exponents in this formulation correspond to the values $n_s = \frac{2}{3}$ for a smooth and $n_w = \frac{1}{2}$ for a wavy surface, while the dimensionless scaling parameter has been experimentally evaluated to be $\beta_s = 12.2$ for the rigid case and $\beta_w = 6.7$ for the free surface (Krall, 2013). By combining Eqs. (2.59) and (2.61) and differentiating with respect to the Schmidt number, a lengthy calculation yields the following analytical expression for the exponent

$$n(a_w) = \frac{\frac{2}{3}(1 - a_w)\frac{1}{\beta_s} Sc^{-n_s} + \frac{1}{2} a_w \frac{1}{\beta_w} Sc^{-n_w}}{(1 - a_w)\frac{1}{\beta_s} Sc^{-n_s} + a_w \frac{1}{\beta_w} Sc^{-n_w}}. \tag{2.62}$$

Along with the established constants, this exponent is clearly determined solely by the wavy surface fraction a_w. By further inserting Eq. (2.62) into Eq. (2.59), an equivalent parameterization can be obtained for the dimensionless scaling factor

$$\beta(a_w) = \frac{Sc^{-n}}{(1 - a_w)\frac{1}{\beta_s} Sc^{-n_s} + a_w \frac{1}{\beta_w} Sc^{-n_w}}, \tag{2.63}$$

being a function of a_w. This finally leads to an alternative formulation of the facet model as

$$k = \frac{u_*}{\beta(a_w)} Sc^{-n(a_w)}. \tag{2.64}$$

The description of the surface conditions remains equivalent whether expressed as a sum in Eq. (2.61) or as a single term in Eq. (2.64), taking the Schmidt number exponent $n(a_w)$ from Eq. (2.62), which varies between $n = \frac{2}{3}$ and $n = \frac{1}{2}$, and the parameterized dimensionless scaling factor $\beta(a_w)$ from Eq. (2.63), ranging from $\beta = 12.2$ to $\beta = 6.7$. Consequently, this equation captures the transition of the Schmidt number exponent and the dimensionless scaling factor from a completely smooth surface to a wavy surface as a function of a_w. It has been considered appropriate to define a_w as the area where surface renewal events takes place through what is known as microscale wave breaking (cf. Sec. 2.2.4). We expect that in these regions the boundary conditions will resemble those of a completely free water surface. Alternatively, the mean square slope of the wave field could also serve

as a parameter for a_w, as experimentally demonstrated in Jähne and Bock (2000) and Krall (2013).

2.2.4 Air-Sea Interaction Phenomena

Although gas exchange can be described in a simplified and generalized way using the presented models, the reality is far more complex. In fact, there are a variety of different fluid dynamic effects and phenomena happening close to the air-water interface, which mutually interact and affect both the boundary conditions and the turbulence state within the mass boundary layers. In essence, gas exchange is primarily driven by wind, which introduces energy into the system through both shear stress at the water surface and the generation of wind waves. This energy transfer induces turbulent flows in the water phase, enhancing gas exchange by increasing mixing and reducing the thickness of the mass boundary layer. As viscosity only gradually dissipates the introduced energy, the resulting turbulence remains effective over a longer period of time. At higher wind speeds, additional processes such as spray generation and bubble formation become significant, further accelerating the transfer of gases across the interface. However, the exact extent of their contribution is the subject of ongoing research. In the following we provide an overview of these key phenomena.

Shear Flow

When wind blows over the sea surface, it exerts a shear stress at the interface, driving the vertical momentum transport and causing near-surface shear flows. Directly at the interface, this flow is laminar as the turbulence is suppressed, creating a viscous sublayer in which viscous forces dominate. Within this layer, the velocity profile increases linearly with depth. Further down, the turbulent effects become more significant and the velocity profile transitions to a nonlinear form. In fully turbulent regions, the velocity profile approaches a logarithmic distribution with depth. This described stratification corresponds to the case of the so-called wall-bound shear flow, according to which the water surface can be regarded hydrodynamically as a solid boundary (Kundu & Cohen, 2008). It has been shown that shear currents are responsible for the formation of three-dimensional coherent turbulence structures, in particular small-scale vortices, that modulates gas exchange (Peirson, 1997; Tsai et al., 2005). The vertical distribution of these structures governs the shape of the velocity profile, especially in the nonlinear transition region between laminar and turbulent layers.

Wind Waves

Obviously the most prominent phenomenon that arises on the sea surface are wind waves. These arise from initial perturbations of the surface, which intensify when wind energy is transferred into the water. The partitioning of wind energy into shear-induced currents and wave growth is still not fully understood but is of central importance for air-sea gas and momentum transport.
A wave field's development depends to a large extent on the fetch, which describes the distance over which the wind blows unhindered. At very short fetch distances, waves behave linearly, whereas nonlinear wave behavior becomes rapidly dominant with increasing fetch distance. Roughly speaking, wind waves are divided into capillary and gravity waves based on the prevailing restoring force. Capillary waves with wavelengths below 1.7 cm and frequencies above 10 Hz are mainly determined

by surface tension. They exhibit small amplitudes, in the order of millimeters, and slow phase velocities usually less than $0.25\,\mathrm{m\,s^{-1}}$. In contrast, gravity waves are determined by gravitational forces that become dominant at wavelengths greater than 1.7 cm. Characteristic frequencies are below 10 Hz and phase velocities above $0.25\,\mathrm{m\,s^{-1}}$ (Lamb, 1975). Above a certain point, gravity waves start to break. This wave breaking occurs when the acceleration of the wave crest exceeds the gravitational acceleration (Phillips, 1958). When breaking, the wave crest tilts, often accompanied by air entrainment and the formation of foam and bubbles, which introduces turbulence into the surface boundary layer. In this context, the phenomenon of microscale wave breaking has attracted attention. MWB refers to small-scale wave breaking events without air entrainment, typically observed in short gravity waves. First identified by Banner and Phillips (1974), MWB events are characterized by parasitic capillary waves propagating along a wave crest and a trailing region of increased turbulent vorticity (Fig. 2.4). These events renew the water surface improving gas exchange, even in low and moderate wind conditions. Thermal imaging studies have shown that gas transfer velocities are locally increased in areas affected by MWB (Zappa et al., 2004).

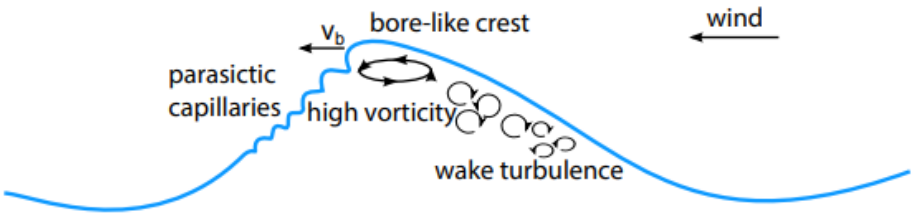

Figure 2.4: Microscale wave breaker. Characteristic profile with parasitic capillary waves in front of the wave and a highly turbulent area below the wave crest, which dissipates into wake turbulence behind it. Modified after Kräuter (2015).

Langmuir Circulation

Langmuir circulations are coherent flow structures that emerge at the sea surface due to wind forcing in the presence of gravity waves. First documented by Langmuir (1938), these circulations appear as an array of parallel, counter-rotating vortices aligned approximately with the wind direction. The associated flow pattern exhibits convergence zones, where surface water is pulled downward, and divergence zones, where water rises from below (Fig. 2.5). This enhances vertical mixing and tracer transport in the upper oceanic boundary layer.

The physical mechanism driving the formation of LCs relies on a nonlinear interaction between the wind-induced shear current and the wave-induced Stokes drift. It is described by the Craik-Leibovich (CL) theory (Craik & Leibovich, 1976; Leibovich, 1983), which introduces an additional body force, the CL vorticity force. This force is given by

$$\vec{f}_{\mathrm{CL}} = (\vec{u}_s \cdot \nabla)\,\vec{u} + (\nabla \times \vec{u}) \times \vec{u}_s, \tag{2.65}$$

where $\vec{u}_s$ refers to the Stokes drift velocity and $\vec{u}$ to the mean flow velocity. As a result, the standard Navier-Stokes equation modifies to

$$\frac{\partial \vec{u}}{\partial t} + (\vec{u} \cdot \nabla)\,\vec{u} = -\frac{1}{\rho}\nabla p + \nu \Delta \vec{u} + \vec{f}_{\mathrm{CL}}. \tag{2.66}$$

The effect of the CL vorticity is described by the Craik-Leibovich instability. According to this, the small-scale shear-induced vortices align and are amplified in the direction of the Stokes drift, creating a positive feedback mechanism that causes small perturbations to grow into large-scale, organized rolls. This instability breaks the isotropy of near-surface turbulence and leads to the formation of Langmuir cells that can penetrate several meters below the surface. Notably, the convergence and divergence zones associated with LCs create wind-aligned, streak-like signatures on the water surface and can be studied with imaging techniques (Marmorino et al., 2005). Studies indicate that LCs are a dominant driver of near-surface turbulence, particularly in low wind regimes, and thus play a key role in enhancing air-sea gas exchange (Veron & Melville, 2001).

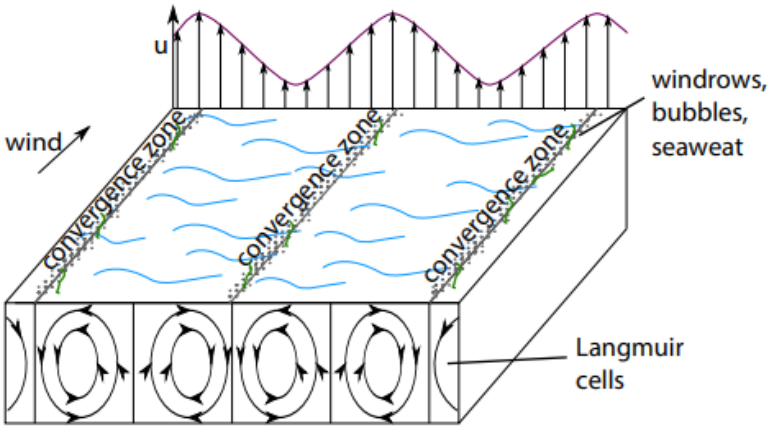

Figure 2.5: Langmuir circulations. The scale represents the surface velocity u. Accumulation of material is sketched in convergence zones. Divergence zones are not drawn. Modified after Thorpe (2004).

Small-Scale Turbulence

At the ocean surface, imaging techniques can also identify a variety of coherent small-scale turbulent structures that lie between the larger signatures of LC. The mechanisms underlying the formation of these fine-scale structures are not yet fully understood. Initial results from numerical simulations suggest that such structures can arise purely from turbulent shear-induced flows, without the involvement of surface waves (Schnieders et al., 2013; Tsai et al., 2005).

Among the most striking features are quasi-streamwise vortices (QSVs) and so-called “fish-scale” patterns. QSVs appear as elongated, tube-like structures that are roughly aligned with the surface current and create streak-like imprints on the surface (Tsai & Lu, 2023). In contrast, fish-scale patterns manifest as more intricate, net-like surface textures that resemble overlapping scales (Handler et al., 2001). Both types of structures reflect the organized nature of near-surface turbulence, but exhibit different anisotropic surface signatures. Similar forms of streak organization are also found in wall-

bound shear flows, suggesting that near-surface turbulence at the air-water interface shares important characteristics with turbulence at solid boundaries (Robinson, 1990; Smith & Paxson, 1983).

Surface Films

A significant fraction of the ocean surface is covered by surface films, which are recognized as critical modulators of gas exchange so that they have gained great importance in current research (Wurl et al., 2011). These films consist of organic substances released by biological activities as well as anthropogenic compounds. An important group of surface films are surface-active agents, known as surfactants. Surfactants are amphiphilic molecules consisting of a hydrophilic head and a hydrophobic tail. At an air-water interface, these molecules arrange themselves in a monomolecular layer, with their hydrophilic heads facing the water surface and their hydrophobic tails pointing towards the air. In higher concentrations, these molecules can also form micelles in the water body, with their hydrophobic parts trapped inside and the hydrophilic parts facing outwards (Hühnerfuss, 2006).
The presence of surfactants on an oceanic surface changes its interfacial dynamics considerably. In particular, the viscoelastic nature of surfactant films suppresses small-scale wave generation, including capillary and short gravity waves (Hühnerfuss et al., 1987). This wave damping effect, famously demonstrated by Franklin et al. (1774) with an oil droplet on a pond, inhibits the wave-induced surface renewal processes that are crucial for enhancing gas exchange. As a result, surface films indirectly reduce the efficiency of air-sea gas exchange by weakening turbulence-induced transport mechanisms. Although natural surface films are difficult to simulate, surfactants are also of particular importance in laboratory studies because they can be confined and maintained at the air-water interface under controlled conditions. The surfactant Triton X-100 has become established as a reference substance due to its chemical stability and similar behavior to natural surface films (Mesarchaki, 2014).

Spray and Bubbles

Sea spray and air bubbles are two phenomena that commonly emerge in highly turbulent sea states. While spray consists of tiny water droplets dispersed in the air, bubbles are small air pockets entrained in the water. So, both phenomena represent a mutual penetration of one phase into the other and challenge the established idea that air and water interact at only one interface. Additionally, these phenomena increase the near-surface turbulence. As the interactions in these highly turbulent regimes are therefore even more complex and it is expected that spray and bubbles make a decisive contribution to gas exchange, a separate branch of research has emerged to study these processes. In particular, bubble-mediated gas exchange is considered a key factor in accounting for the uncertainties observed at high wind speeds (Garbe et al., 2014).

2.3 Fluorescence

Fluorescence refers to the phenomenon of a medium emitting light after absorbing radiation. Along with phosphorescence, it belongs to the broader category of photoluminescence. The key distinction between these two phenomena lies in the time delay between absorption and emission. In fluorescence,

this delay is within the order of a few nanoseconds meaning emission ceases immediately once the excitation source is removed. In contrast, phosphorescence persists over much longer timescales, ranging from milliseconds to seconds, allowing the substance to continue glowing even after excitation has stopped. A detailed understanding of these processes is only possible through the principles of quantum mechanics (Lakowicz, 2006).

2.3.1 Quantum Mechanical Foundation

The quantum mechanical description of fluorescence is commonly represented in a Jablonski diagram (Fig. 2.6), which depicts the different atomic or molecular energy levels as horizontal lines. Fluorescence involves the ground state S_0 as well as the first and second excited states S_1 and S_2, all of which are singlet states meaning that the electron spins are paired. Each electronic state in turn contains multiple vibrational energy levels.

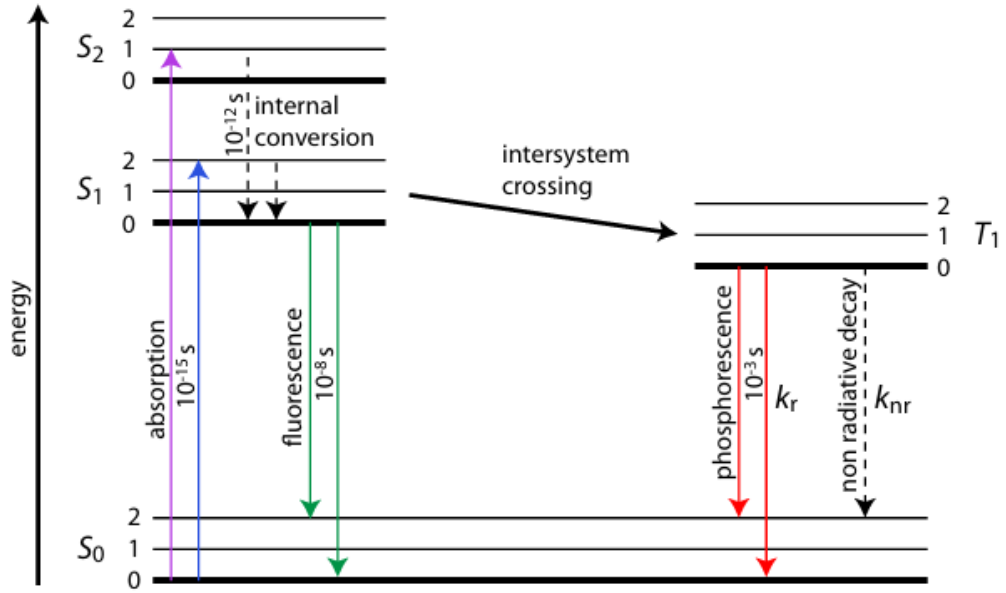

Figure 2.6: Jablonski diagram. The electronic singlet states are labeled with S_0, S_1, S_2 and the triplet state with T_1. All electronic states contain multiple vibrational sub-states indicated with $0, 1, 2$ (Friedl, 2013).

When a fluorophore absorbs radiation, its valence electron transitions to one of the excited states S_1 and S_2. Due to various interactions, e.g. atomic collisions, collectively referred to as internal conversion, the electron quickly relaxes to a lower excited state without emitting radiation. This relaxation occurs in the order of 10^{-12} seconds and typically ends at the lowest vibrational level of the S_1 state. The subsequent relaxation back to the ground state S_0 represents the actual fluorescence transition, occurring within 10^{-8} seconds and accompanied by light emission. As a result of the non-radiative energy losses associated with internal conversion, the energy of the emitted light is lower than that of the absorbed radiation, leading to a longer wavelength of emitted fluorescence compared to the excitation light. This difference in wavelength is known as Stokes shift and provides a natural means to spectrally separate excitation and emission light.

For the sake of completeness, phosphorescence should be mentioned briefly at this point. After excitation, electrons can alternatively undergo an intersystem crossing, transitioning from the singlet state

S_1 to the triplet state T_1. Since relaxations from the triplet state T_1 back to the singlet ground state S_0 are quantum mechanically forbidden, this triplet state tends to be metastable. Consequently, the decay to the ground state is slow, and light emission through this process, referred to as phosphorescence, can continue for 10^{-3} seconds to seconds after stopping the excitation (Lakowicz, 2006).

2.3.2 Absorption and Emission Laws

The intensity of fluorescent light emitted by a fluorophore depends first on the amount of absorbed light and second on how efficiently it is converted into fluorescence. To quantify the first aspect, the famous Lambert-Beer law is usually utilized. According to this principle, incoming radiation passing an absorbing medium undergoes a differential change in intensity dI on a differential length element dz. In liquid and gaseous phases, this change is directly proportional to the incident intensity I, the concentration c of the absorbing species, their molar absorption coefficient $\varepsilon(\lambda)$ and the path length dz, yielding

$$dI = -I\,\varepsilon(\lambda)\,c(z)\,dz. \tag{2.67}$$

As a material-specific and wavelength-dependent parameter, the absorption coefficient $\varepsilon(\lambda)$ characterizes the spectral absorption properties of the medium. The negative sign in the equation indicates that intensity decreases as the light propagates through the medium. By integrating Eq. (2.67) over a given path length L, we obtain the intensity attenuation law

$$I(L) = I_0 \cdot 10^{-\varepsilon(\lambda)\int_0^L c(z)\,dz} = I_0 \cdot 10^{-A(\lambda)}, \tag{2.68}$$

describing how the intensity declines over the propagation length. The exponent in this equation is usually combined into a quantity known as absorbance $A(\lambda)$ and defined as

$$A(\lambda) = \varepsilon(\lambda) \int_0^L c(z)\,dz. \tag{2.69}$$

Such a formulation represents the Lambert-Beer law in an alternative way. If multiple absorbing species are present in the solution, the Lambert-Beer law expands to

$$A(\lambda) = \sum_{n=0}^{N} \varepsilon_n(\lambda) \int_0^L c_n(z)\,dz, \tag{2.70}$$

with each species having its own absorption coefficient $\varepsilon_n(\lambda)$. Obviously, following Lambert-Beer's law, the transmitted intensity I_T decreases due to absorption, implying that any reduction in transmitted intensity is associated with an increase in absorbed intensity I_A. Hence, the opposite of Eq. (2.68) applies to the absorbed intensity, expressed by

$$I_A = I_0 - I_0 \cdot 10^{-A(\lambda)} = I_0 \left(1 - 10^{-A(\lambda)}\right). \tag{2.71}$$

However, this relationship only holds if reflecting and scattering aspects to the incident light are negligible. In this case, the sum of transmitted and absorbed intensity is equal to the input intensity, i.e. $I_A + I_T = I_0$, which is equivalent to conservation of energy (Valeur & Berberan-Santos, 2013).

The process of how the absorbed light is converted into fluorescence, has already been explained in Sec. 2.3.1 on the basis of quantum mechanics. In general, intensity of light is proportional to the number of photons, with each absorbed photon exciting an electronic state. The probability of this excited state decaying by fluorescence rather than by non-radiative relaxation is given by the quantum yield Φ of the fluorophore. It indicates the percentage of absorbed photons N_a producing fluorescence photons N_e, as given by

$$\Phi = \frac{N_e}{N_a}, \tag{2.72}$$

that describes the efficiency of the conversion (Wong et al., 2020). In summary, the fluorescence intensity is proportional to both the absorbed intensity and the quantum yield, which results in the following expression

$$I_F(L) \propto \Phi \cdot I_0 \left(1 - 10^{-A(\lambda)}\right). \tag{2.73}$$

By means of the absorption coefficients and the concentration profiles of each absorbing species, it is possible to calculate the intensity profile of the emitted fluorescent light in the solution. An integration over the entire extent of the medium gives the total emitted fluorescence intensity

$$I_{F,\text{tot}} = I_F(L) = \int_0^L I_F(z)\, dz. \tag{2.74}$$

A more detailed version of these calculations can be found in Papst (2019).

2.4 Concepts of Image Processing

This section presents an overview of key image processing concepts which are applied to analyze the image sequences recorded in the experiments.

2.4.1 Structure Tensor

The structure tensor or second-moment matrix is a powerful tool in image processing and computer vision for analyzing the local image structure. It provides a quantitative measure of how pixel intensity varies in different directions within a local neighborhood and captures information about edges, orientations and other spatial features. Hence, its computation relies on the image gradients I_x and I_y, which indicate the partial derivatives of pixel intensity I with respect to the horizontal and vertical image directions. More precisely, the structure tensor J is defined as the outer product of the gradient vector $(I_x, I_y)^T$ at each pixel, convolved with a Gaussian filter G_σ. In the two-dimensional case, this is represented by a symmetric and positive semi-definite matrix in the form

$$J = \begin{bmatrix} G_\sigma * I_x^2 & G_\sigma * (I_x I_y) \\ G_\sigma * (I_x I_y) & G_\sigma * I_y^2 \end{bmatrix}. \tag{2.75}$$

The choice of the window size for the Gaussian filter is one of the most crucial parameters in the calculation as it affects both smoothing and structural accuracy of the local neighborhood. On the one hand, a larger window ensures robustness against noise and captures wider structures, on the other

hand, a smaller window focuses on finer details but can be more sensitive to noise. Once the structure tensor has been calculated, the information about the local structure and orientation is encoded in its eigenvalues and eigenvectors. As a symmetric matrix, the structure tensor naturally yields real eigenvalues and orthogonal eigenvectors, which can be obtained by a principal axis transformation. This procedure solves the eigenvalue problem by rotating the coordinate system, thereby transforming the tensor into a diagonal form with the eigenvalues on the main diagonal. While the eigenvectors indicate the directions of the strongest or weakest intensity changes in the image, the eigenvalues give the corresponding magnitudes. By means of the two eigenvalues λ_1 and λ_2 for each pixel in a two-dimensional image, three different cases can be distinguished:

- If $\lambda_1 \gg \lambda_2$, there is a dominant image gradient in one direction that characterizes an oriented edge in the local neighborhood.
- If $\lambda_1 \approx \lambda_2 > 0$, significant image gradients exist in all directions, which is typical for corners or textured regions with uniform directional response.
- If $\lambda_1 \approx \lambda_2 \approx 0$, no intensity change is observed in any direction, corresponding to a constant and isotropically flat region without structural information.

Importantly, in any case, the eigenvector associated with the largest eigenvalue of the structure tensor at each pixel reveals the dominant orientation in the local region. Rather than explicitly solving the eigenvalue problem, Jähne (2012) shows that the local orientation can be computed simply from the tensor elements in two dimensions by rotating the coordinate system. It follows for the preferred orientation θ of the local structure the relationship

$$\tan(2\theta) = \frac{2J_{12}}{J_{11} - J_{22}}, \tag{2.76}$$

with J_{11} and J_{22} being the diagonal elements and J_{12} the off-diagonal element of the tensor. Since the orientation alone is not sufficient to distinguish between isotropic neighborhoods and distributed orientations, where no distinct orientation can be identified in either case, an additional parameter has to be considered to characterize the local structure. To differentiate between these cases, it is useful to consider the sum of the two eigenvalues, referred to the trace of the structure tensor. Thus, coherence has proven to be a complementary metric for identifying local structures which explicitly incorporates the trace in its calculation. This coherence c_c is defined as

$$c_c = \frac{\sqrt{(J_{11} - J_{22})^2 + 4J_{12}^2}}{J_{11} + J_{22}} = \frac{\lambda_1 - \lambda_2}{\lambda_1 + \lambda_2}, \tag{2.77}$$

with values ranging between 0 and 1. While a coherence of 1 corresponds to a perfectly oriented local structure, a value of 0 indicates a completely isotropic region with no intensity variations in the local neighborhood.

In conclusion, the structural features of an image can be effectively characterized by specifying orientation and coherence that form the basis for structural image analysis. Beyond this, the structure tensor serves as a foundation for a wide range of other image processing applications, such as feature

detection, optical flow estimation and image segmentation. The versatility of these applications is well documented in the literature (Brox et al., 2006; Jähne, 2012; Szeliski, 2011), providing a solid guide for further exploration.

2.4.2 Optical Flow

Optical flow is the fundamental element of motion analysis in image processing. It represents the visual flow of pixel intensities in an image sequence caused by the movement of the image objects or the camera. Conceptually, optical flow can be depicted as a displacement vector field that describes the shift of pixels between sequential frames. The estimation of this vector field relies on the assumption of brightness constancy, which supposes that the temporal change in intensity is solely due to the movement of objects within the scene across the image plane. In common with all conserved quantities, this can be expressed in a continuity equation

$$\frac{dI}{dt} = \frac{\partial I}{\partial t} + \frac{\partial I}{\partial x}\frac{\partial x}{\partial t} + \frac{\partial I}{\partial y}\frac{\partial y}{\partial t} = \frac{\partial I}{\partial t} + v\nabla I = 0, \tag{2.78}$$

with I denoting the pixel intensity and v the vector field of the optical flow. If this equation is fulfilled, the optical flow is identical to the motion field. Nevertheless, the brightness constancy assumption leads to the problem that the pixel intensity remains conserved during movement. Of course, this is violated if the illumination varies between consecutive frames or if additional dynamic processes are at work causing intensity changes. In this case, the optical flow is no longer equivalent to the motion field. Analogously to the general extension of a continuity equation, this can be handled by introducing a source term. So, Eq. (2.78) is modified to

$$\frac{dI}{dt} = \frac{\partial I}{\partial t} + v\nabla I = s, \tag{2.79}$$

where s comprises all effects that induce intensity changes apart from motion. There are several approaches to expressing this source term, which are summarized in Jähne (2007).

When estimating the optical flow, a distinction is made between differential methods, tensor methods, and correlation methods. While differential methods are based on solving the flow equation (2.78), tensor methods assess the optical flow by extending the structure tensor from Sec. 2.4.1 to the time dimension. In preparation for the evaluation we will focus on the correlation method and explain it in more detail below.

The correlation method estimates optical flow by comparing local image patches to identify the shift with the best correspondence between consecutive images. A common metric is cross-correlation, which generally quantifies the similarity between two signals $f(t)$ and $g(t)$. It involves shifting one of two functions above the other and measuring the product of their overlap, expressed mathematically as the integral

$$R_{xy}(\tau) = \int_{-\infty}^{\infty} f^*(t)g(t+\tau)\,dt. \tag{2.80}$$

Thus, cross-correlation describes the correlation of the two functions depending on the displacement τ, where a value of 1 indicates perfectly matched signals and 0 signifies completely uncorrelated

signals. For discrete, two-dimensional signals such as images, the integral is replaced by a sum and extended by one spatial dimension resulting in

$$R_{xy}(u, v) = \sum_{x,y=-\infty}^{\infty} f^*(x, y) \cdot g(x + u, y + v). \tag{2.81}$$

By calculating the cross-correlation for various displacements, the maximum value yields the optimal displacement, giving an estimate of the optical flow. To further improve the robustness of the calculations, a normalized cross-correlation is often applied, that normalizes the correlation values to the intensities of the compared image patches. This normalization addresses the problem stated in Eq. (2.79) that intensities may change between two frames and affect the accuracy of the motion estimation. For the image regions I and T in two consecutive images of an image sequence, the normalized cross-correlation is given by

$$R(x, y) = \frac{\sum_{x',y'} \left(\left(I(x + x', y + y') - \overline{I} \right) \cdot \left(T(x', y') - \overline{T} \right) \right)}{\sqrt{\sum_{x',y'} \left(I(x + x', y + y') - \overline{I} \right)^2 \cdot \sum_{x',y'} \left(T(x', y') - \overline{T} \right)^2}}, \tag{2.82}$$

with $\overline{I}$ and $\overline{T}$ denoting the mean images over the corresponding patches, respectively. Despite the high computational cost, this method is particularly effective for tracking highly dynamic objects in image sequences. Nevertheless, the limited spatial resolution due to dividing the image into patches can reduce the accuracy, especially when capturing fine motion details (Jähne, 2012; Szeliski, 2011).

3 Methods

This thesis employs a Fluorescence Imaging method for gas exchange studies. It refers to an imaging technique that allows to make horizontal concentration fields in the water-side mass boundary layer visible and provide insights into its dynamics. The fundamental idea involves applying a fluorescent dye which either acts as an indicator to the changing pH environment in the presence of a dissolved gas or reacts directly with this gas in an acid-base reaction. Regardless of the method, in both methods the gas exchange is made visible by fluorescence. This chapter begins with a brief overview of how the technique was developed and then explains in detail the current state of the method as used in the following experiments. Throughout the following, the term Fluorescence Imaging refers specifically to the method used in this work. Furthermore, the chemicals involved in the method are specified and three numerical simulations are introduced that validate the methodology. Finally, a brief description of the concept of mass balance is given. The findings of the simulations and mass balance calculations also serve in particular as a preparation for the subsequent data analysis.

3.1 Previous Work

Originally, the concept of Fluorescence Imaging stems from Hiby et al. (1967), who developed a technique to use fluorescence for investigating gas absorption in a falling film. This was the first instance where a fluorescent pH indicator was applied to image the concentration profile of an acidic or alkaline gas during mass transfer. Building on this idea, Jähne (1985) proposed an advanced method for directly making gas exchange visible in the laboratory. The appeal of using a Fluorescence Imaging method to study gas exchange lies in two key aspects. First, it represents a contactless measurement technique. These are suitable for examining the microscopic dynamics in the mass boundary layer, without disrupting the processes in return by the presence of a measuring device. Second, fluorescence is a highly sensitive property that is easily detectable even on the small scales of the mass boundary layer. Indeed, on these scales it would not be possible to measure concentrations based on absorption characteristics. Although the proposed Fluorescence Imaging held great potential for gas exchange measurements in the laboratory, it could not be realized for years due to the inadequate development of powerful light sources and precise high-resolution cameras for the excitation and detection of fluorescence.

The first laboratory techniques for investigating gas exchange using fluorescence were based on laser-induced fluorescence approaches. In these methods, a fluorescent dye is excited by a laser sheet to visualize vertical concentration gradients within the water-side mass boundary layer (Asher & Pankow, 1986; Herzog, 2010; Wolff & Hanratty, 1994). Variants of this approach include direct excitation of the gas itself (Friman & Jähne, 2019) or the use of fluorescence quenching, where the presence of a

trace gas reduces the fluorescence intensity of the dye (Friedl, 2013). LIF techniques are well suited to detect the vertical profile of gas concentrations near the water surface, but are subject to significant limitations. First, they require high vertical spatial resolution to resolve the thin mass boundary layer, which limits their use to low wind speeds where turbulence near the surface is minimal and the mass boundary layer is sufficiently thick. Second, large waves and high surface roughness lead to distortion of the laser sheet and make reliable detection of the concentration profile difficult. These techniques are therefore primarily suitable for use in small wind-wave facilities with low surface amplitudes. Last, these methods inherently provide horizontally averaged concentration profiles and thus neglect the horizontal variability of gas exchange dynamics.

To overcome the limitations of LIF, alternative techniques have been developed that allow two-dimensional horizontal imaging of gas concentration fields on a water surface. A first successful implementation of such a horizontal Fluorescence Imaging for studying gas exchange was realized in Kräuter (2015). This method achieved a two-dimensional horizontal imaging of gas exchange at the Heidelberg Aeolotron Wind-Wave Facility. It represents the method known as Boundary Layer Imaging (BLI), since here the fluorescence intensity serves as a direct measure for the thickness of the mass boundary layer. The measurement technique was subsequently applied in the work of Trofimova (2015) and Klein (2019). However, it was found that this method has its technical limitations at high wind speeds. At these conditions, gas exchange rates increase and the mass boundary layer becomes very small, making fluorescence inadequately detectable. In response to this problem, BLI was finally modified and validated in Papst (2019) to a new technique. Simply put, this approach utilizes a higher dye concentration, causing the fluorescence intensity to reflect the gas concentration rather than the boundary layer thickness. This improved method is the actual Fluorescence Imaging technique used as a starting point for the current study.

3.2 Principle

As previously stated, the underlying principle of Fluorescence Imaging is to replace an invisible trace gas with a fluorescent species at the air-water interface during gas exchange. This is achieved by coupling the trace gas with a fluorescent pH indicator via an acid-base reaction when the gas dissolves in water, thus making this technique particularly suited for invasion experiments.

In general, the method proceeds in three main steps. First, a fluorescent pH indicator is dissolved in acidified water and an alkaline trace gas is introduced into the air space above. In this initial state, the indicator remains almost entirely in its acidic form. Next, the alkaline gas dissolves in the water and in doing so reacts with the indicator, shifting it to its alkaline form through an acid-base reaction. Finally, the alkaline form of the pH indicator is selectively excited by light, typically from a laser or a specialized light source, to induce fluorescence. The emitted fluorescence signal is then detected by cameras. Thus, the recorded fluorescence intensity serves as a direct measure of the local gas concentration, which is responsible for forming the fluorescent species. The exact relationship between fluorescence intensity and gas concentration is rather complex and depends on the pH value and the concentration of the individual species. In addition to the fluorescent pH indicator, both methods use a further absorbing dye, which limits the penetration depth of the excitation light to

the uppermost water layers and suppresses the background fluorescence from the water bulk. This enhances the image contrast and ensures that the fluorescence signal originates primarily from the near-surface concentration fields, where the key dynamics of gas exchange take place. In the following, the two main variants of the method are examined in more detail. An illustrative comparison of the two methods is shown in Fig. 3.1.

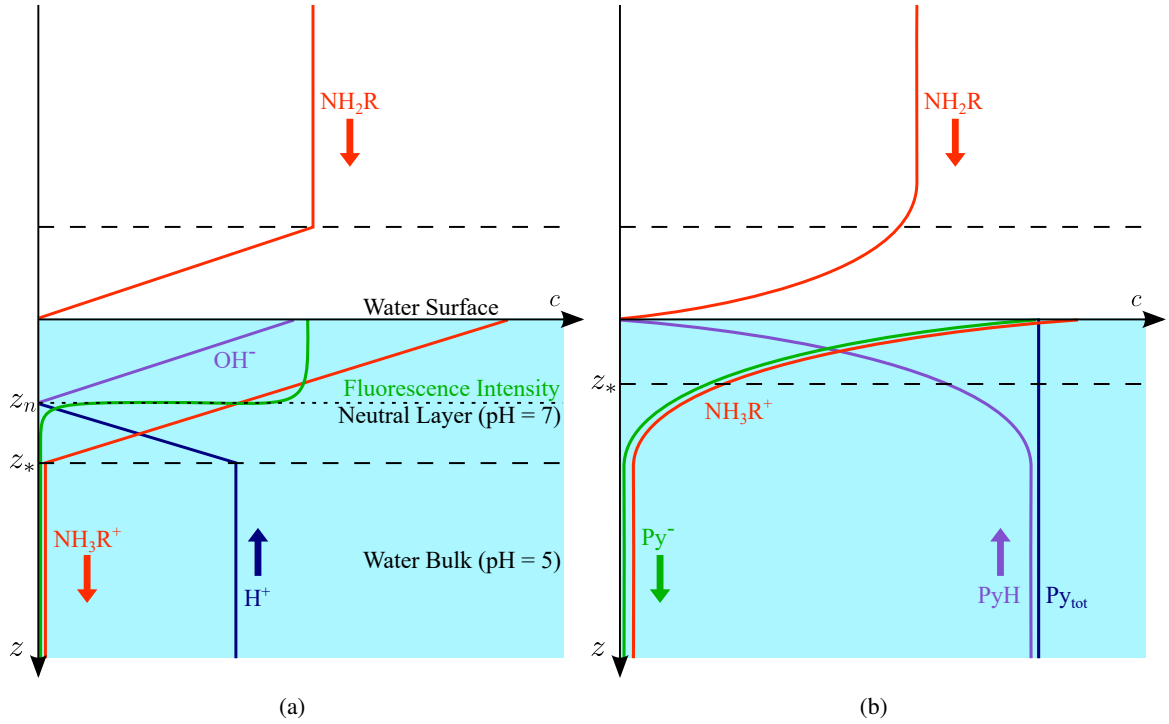

Figure 3.1: Comparison of the two Fluorescence Imaging techniques used in (a) Kräuter (2015) and (b) Papst (2019). The concentration profiles of the involved species are shown in the mass boundary layer. While BLI produces a step-like fluorescence profile up to the neutral layer, in Fluorescence Imaging the fluorescence profile is proportional to the gas concentration. For better recognizability, the abbreviation Py is used here instead of I for pyranine. Left sketch modified after Kräuter et al. (2014).

3.2.1 Boundary Layer Imaging

The Boundary Layer Imaging method outlined by Kräuter (2015) utilizes the pH indicator in low concentrations of $[\mathrm{I}]_{\mathrm{tot}} \approx 10^{-6}\,\mathrm{mol\,L^{-1}}$ in water. When an alkaline trace gas NH_2R dissolves in acidified water, the gas reacts with the H_3O^+ ions in an acid-base reaction,

$$\mathrm{NH_2R} + \mathrm{H_3O^+} \longrightarrow \mathrm{NH_3R^+} + \mathrm{H_2O}. \tag{3.1}$$

As more gas dissolves in the water during the invasion process, H_3O^+ ions are increasingly eliminated from the surface water. The H_3O^+ ions lost at the surface are replenished by the deeper layers of the bulk water. Since the acid-base reaction proceeds faster than the transport of H_3O^+ ions from the bulk through the mass boundary layer, it eventually reaches a point at which the mass boundary layer becomes nearly devoid of H_3O^+ ions. At this stage, the invasive gas reacts primarily with water

molecules, leading to the formation of OH^- ions

$$NH_2R + H_2O \longrightarrow NH_3R^+ + OH^-. \tag{3.2}$$

Consequently, the surface layer becomes alkaline, establishing a pH gradient. In this alkaline surface layer, the pH indicator reacts in its acidic form IH with the OH^- ions as in the following reaction

$$IH + OH^- \longrightarrow I^- + H_2O. \tag{3.3}$$

Accordingly, the concentration of the indicator's alkaline form I^- is significantly higher in the mass boundary layer than in the bulk water. By selectively exciting the alkaline form to fluoresce, the mass boundary layer can be made visible using this method. The measured fluorescence intensity thus correlates directly with the thickness of the alkaline mass boundary layer.

3.2.2 Fluorescence Imaging

The Fluorescence Imaging method, as developed by Papst (2019), relies on using a higher indicator concentration of $[I]_{tot} \approx 10^{-4}\,\mathrm{mol\,L^{-1}}$ in water. This increases the indicator concentration beyond that of the water ions, i.e. $[I]_{tot} \gg [H_3O^+]$, making the indicator the primary reactant for the gas. When the alkaline gas NH_2R dissolves in the water, it reacts directly with the pH indicator IH in an acid-base as

$$NH_2R + IH \longrightarrow NH_3R^+ + I^-. \tag{3.4}$$

It represents basically a direct combination of the reactions in Eqs. (3.2) and (3.3). This approach works most effectively when two major conditions are met. First, the concentrations $[H_3O^+]$ and $[OH^-]$ should be much lower than the indicator concentration $[I]_{tot}$ to ensure that the gas reacts primarily with the pH indicator rather than with the water ions, as in the BLI method. Second, the pH value should be considerably lower than the pK_a value of the trace gas. This guarantees that each gas molecule is reliably protonated when it enters the water, i.e. $[NH_2R]_{w,tot} \simeq [NH_3R^+]$. As a result, the gas invasion will not stop at any point, keeping the process controlled on the air side. If both conditions are satisfied, virtually every gas molecule NH_2R produces an alkaline indicator molecule I^- in the water, establishing a direct proportionality between the alkaline form of the indicator and the gas concentration

$$[I^-] \propto [NH_2R]_{w,tot}. \tag{3.5}$$

Due to the chemical reaction in Eq. (3.4), the concentration of the indicator's acidic form IH decreases in the mass boundary layer, while the concentration of the alkaline form I^- increases. This leads to opposing fluxes of I^- from the mass boundary layer to the bulk and of IH from the bulk to towards the surface, related by

$$j_{NH_2R} \simeq j_{NH_3R^+} \propto j_{I^-} = -j_{IH}. \tag{3.6}$$

Whether the reaction in Eq. (3.4) proceeds continuously or reaches saturation depends on the balance between the gas influx j_{NH_2R} and the resupply j_{IH} from the depths. Only if the upward transport of IH keeps pace with the gas flux from the air the formation of I^- remains proportional to the gas

concentration as in Eq. (3.5). Otherwise, the IH is depleted at the surface, leading to an accumulation of I^- and a breakdown of the direct coupling between gas concentration and fluorescence signal.
In summary, the method works best within a pH range of 6 to 8 (Papst, 2019), where the indicator concentration is significantly higher than the concentration of water ions. This ensures that reaction in Eq. (3.4) takes precedence over reaction in Eq. (3.1). In addition, the pK_a value of the trace gas should be greater than 9 to ensure that all gas molecules constantly remain protonated. Under these conditions, the measured fluorescence intensity is proportional to the local dissolving gas concentration (Hofmann & Jähne, 2023).

3.2.3 Generalization of Fluorescence Imaging

The methodology adopted in this study for measuring gas exchange is essentially based on Fluorescence Imaging as described in Sec. 3.2.2. However, several experimental challenges have necessitated adaptations to the original approach.
A primary challenge involves obtaining high-contrast images of concentration fields within the mass boundary layer. Optimal contrast is achieved by minimizing the background fluorescence signal, which is directly influenced by the pH of the water. Specifically, lower pH values reduce the concentration of the indicator's alkaline form in the bulk water, enhancing the image contrast. Experimental observations suggest that the pH value should not exceed 7, ensuring that only around 10 % of the indicator is present in its alkaline form given a typical pK_a value around 8 for the pH indicator.
A further consideration arises due to the fact that in sequentially performed invasion experiments, the cumulative input of the alkaline trace gas leads to a gradual increase of the pH value. So that as many measurements as possible can be carried out without the need for re-acidification between runs, it is advantageous to begin at a low initial pH value. This ensures that the pH value remains below 7 even after several experiments.
Overall, these considerations suggest that operating within a pH range of 5 to 7 is most appropriate from an experimental point of view. However, this range deviates from the originally intended pH range of 6 to 8, which is commonly used in Fluorescence Imaging and predicts a linear relationship between the fluorescence signal and the gas concentration. Thus, this simplified linear correlation is no longer valid in our case. Instead, a more general approach is required that takes into account the nonlinear response of the indicator outside the ideal linear range. This requires numerical simulations of the chemical reactions, which will be presented in Sec. 3.4.

3.3 Chemical Species

The basic chemical framework of Fluorescence Imaging requires a fluorescent dye, an additional absorbing dye as well as an alkaline gas. This section motivates the selection of these three species and gives a more detailed characterization of their properties.

3.3.1 Pyranine

As a pH-sensitive fluorophore, the substance pyranine has previously proven to be a suitable dye for the Fluorescence Imaging method. It is a water-soluble colorant molecule with the systematic name 8-Hydroxypyrene-1,3,6-trisulfonic acid (HPTS) and the molecular formula $C_{16}H_7Na_3O_{10}S_3$ belonging to the group of arylsulfonates. Its molar mass is 524.37 g mol^{-1}. The ability of the pyranine compound to act as a pH indicator is due to the hydroxyl group attached to the pyrene backbone. Thus, the molecule can switch between an acidic and an alkaline form by donating or accepting a proton.
A detailed fluorimetric analysis of these two components is provided in Wolfbeis et al. (1983). In particular, there are different absorption spectra (Fig. 3.2), but identical emission spectra for the acidic and alkaline components of the fluorescent dye in the visible spectral range. While the acidic form has its absorption maximum at 406 nm, the maximum of the alkaline form peaks at 455 nm. Spectrally, the components are separated by the isosbestic point at 413 nm, with the absorption of the acidic form dominating below and that of the alkaline form above this wavelength. Immediately at the isosbestic point, the absorbance is independent of the pH value. When exciting one of the two components, the absorbed light leads to the emission of fluorescence. With a quantum yield of 0.98 and a decay time of 5.3 ns, virtually the entire absorbed light is immediately converted into fluorescence. The emission spectrum has its maximum intensity at 511 nm, producing the characteristic green color of the dissolved dye.
Another advantageous property of pyranine concerns the proximity of its equivalence point to the neutral point. According to measurements by Wolfbeis et al. (1983), the pK_a value of the dye's aqueous solutions varies between 8.03 in pure water and 7.29 depending on which additional ions are present in the solution. With increasing ion concentration in the solution, the pK_a value decreases. Since we use a pyranine preparation that contains some ionic derivatives and has a specified purity of 78 %, we have verified the pK_a value of this specific mixture to be pK_a(I) = 7.9547 ± 0.0027 before performing the gas exchange experiments. This determination of the pK_a value involves measuring absorption spectra (Fig. 3.2) at different pH values using a UV-VIS spectrometer to monitor the transition between the acidic and alkaline forms of pyranine (cf. Sec. 5.3.1).

3.3.2 Tartrazine

In addition to the fluorescent pyranine, the absorbing dye tartrazine is used to suppress the bulk fluorescence. This is a synthetic azo dye molecule which is mainly used in the food industry under the name Food Yellow 4. Its systematic name is trisodium 5-hydroxy-1-(4-sulfonatophenyl)-4-[(4-sulfonatophenyl)diazen-1-yl]-1H-pyrazole-3-carboxylate and has the molecular sum formula $C_{16}H_9N_4Na_3O_9S_2$ with a molar mass of 534.36 g mol^{-1}. This dye molecule is also soluble in water and can switch between acidic and alkaline forms by releasing or absorbing a proton.
In contrast to pyranine, the absorption spectra (Fig. 3.3) of the acidic and alkaline components of tartrazine are not spectrally separated from each other. Both absorption spectra also overlap significantly with those of pyranine and the excitation wavelength of 455 nm. The absorption of the acidic form is slightly stronger in this range than that of the alkaline form, with the absorption maximum of the acidic form occurring at 426 nm. This means that tartrazine absorbs a large proportion of the

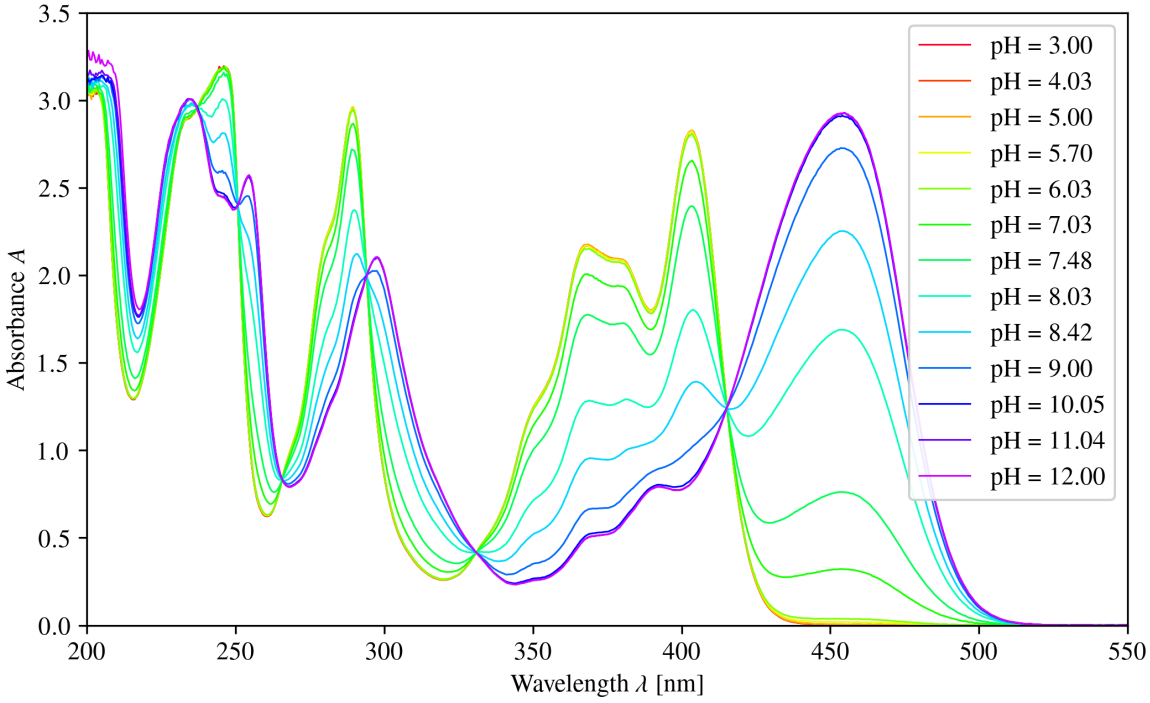

Figure 3.2: Reference absorption spectra for pyranine. The spectra are recorded with a reference concentration of $1.29 \cdot 10^{-4}\,\mathrm{mol\,L^{-1}}$ for different pH values within a cuvette of 1 cm optical path length. The absorbance spectrum at pH $\approx$ 3 corresponds to the pure absorbance of the acidic component and at pH $\approx$ 12 to the pure absorbance of the alkaline component.

excitation light regardless of the pH value.

The pK_a value of tartrazine in aqueous solution also varies strongly with the ion concentration ranging from 10.0 in pure water to 9.4 in the presence of additional ions (Syms, 2017). In any case, this is considerably higher than the pK_a value of pyranine. As a result, tartrazine is almost exclusively present in its acidic form within our considered pH range. Again, the dissociation constant of the compound used for this dye molecule is verified to be pK_a(T) = 9.9856 ± 0.0253 by our own measurements (Fig. 3.3), following the same procedure as described for pyranine.

The absorption properties of tartrazine are advantageous for limiting the penetration of excitation light into the water column. Due to its strong absorption, only about the top centimeter of the water body is excited. This ensures that the fluorescence excitation in the bulk water is effectively suppressed, thus increasing the contrast and making the gas exchange processes near the surface more prominent. Consequently, the fluorescence signal reflects solely the processes and dynamics in the vicinity of the water surface, which are crucial for gas exchange.

3.3.3 Methylamine

In previous applications of Fluorescence Imaging, ammonia was typically used as alkaline gas in the measurements. However, in the current experiments we have chosen to replace it with methylamine, a derivative of ammonia. Methylamine is a colorless, pungent smelling gas with the molecular formula NH_2CH_3, so one hydrogen atom of ammonia is substituted by a methyl group. It is easily soluble in water and reacts strongly alkaline in aqueous solution. A significant advantage of methylamine is

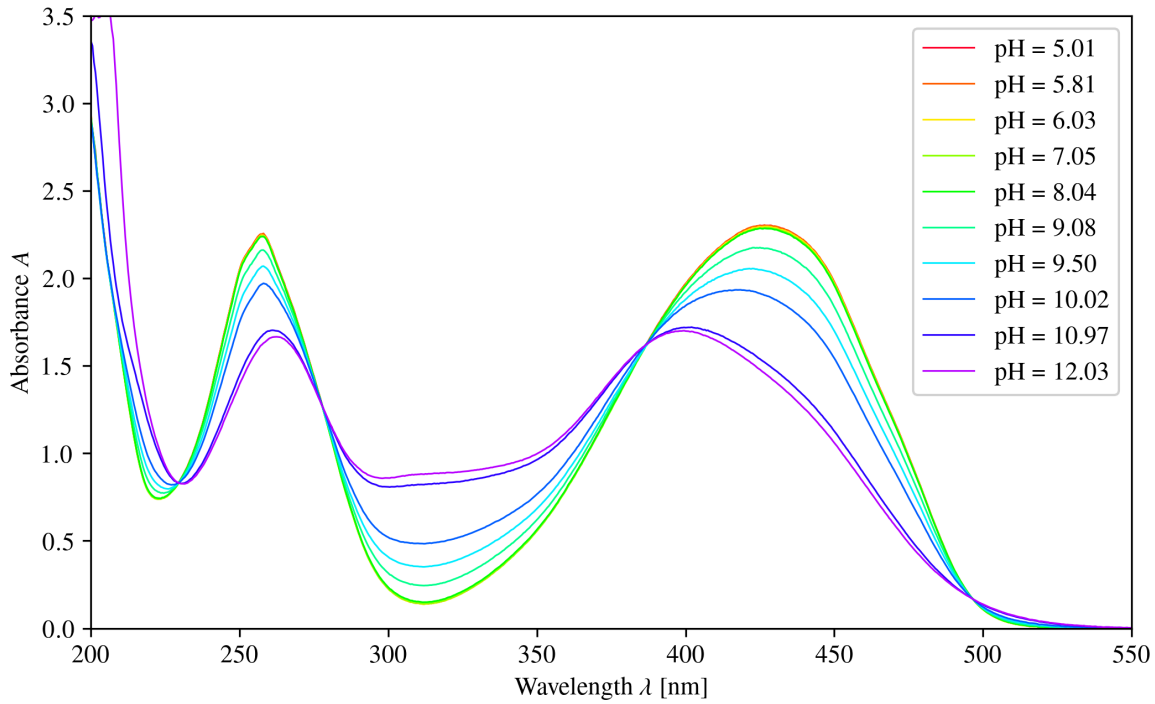

Figure 3.3: Reference absorption spectra for tartrazine. The reference concentration is $1 \cdot 10^{-4}\,\mathrm{mol\,L^{-1}}$ and the optical path length is 1 cm. The absorption spectrum at pH $\approx$ 5 corresponds to the acidic component and at pH $\approx$ 12 to the alkaline component.

its higher pK_a value of 10.63 compared to ammonia's pK_a value of 9.24 (Jones & Fleming, 2014). This higher pK_a value makes methylamine a more suitable choice for the experiments, as it results in a stronger basicity in solution. A drawback is the increased toxicity of methylamine compared to ammonia, something that should not be ignored during the experiments. When dissolved in water, methylamine reacts in an acid-base reaction by taking up a proton through the amino group. In the BLI method, reaction in Eq. (3.1) predominates

$$\mathrm{NH_2R + H_3O^+ \longrightarrow NH_3R^+ + H_2O}, \tag{3.7}$$

whereas in Fluorescence Imaging, the direct reaction in Eq. (3.4) becomes the primary mechanism

$$\mathrm{NH_2R + IH \longrightarrow NH_3R^+ + I^-}. \tag{3.8}$$

As a result of these chemical reactions, methylamine is not only physically dissolved, but also exists in solution as methylammonium ions $\mathrm{NH_3CH_3^+}$. This enhances the solubility of methylamine as the chemical reaction allows a greater overall uptake of the gas, a phenomenon described by the effective solubility

$$\alpha_{\mathrm{eff}}(\mathrm{NH_2CH_3}) = \frac{[\mathrm{NH_2CH_3}]_w + [\mathrm{NH_3CH_3^+}]_w}{[\mathrm{NH_2CH_3}]_a} = \alpha(\mathrm{NH_2CH_3})\left(1 + 10^{-\mathrm{pH}+\mathrm{p}K_a(\mathrm{NH_2CH_3})}\right). \tag{3.9}$$

Thus, the effective solubility α_{eff} is always higher than the physical solubility α and is primarily influenced by the difference between the pK_a and the pH value of the solution. In the literature, the

values for pure physical solubility of methylamine vary widely between 868 and 2975 (Sander, 2023). We will use the frequently referenced value of $\alpha = 2206$ at 25 °C from Burkholder et al. (2015). In addition, the diffusion constant of methylamine in water is reported to be $D_{NH_2CH_3} = 1.61 \cdot 10^{-5}$ cm^2 s^{-1} at 25 °C (Yaws, 1995), yielding a Schmidt number of $Sc_{NH_2CH_3} = 555$. According to Fig. 2.2, methylamine is therefore clearly classified as an air-side controlled gas.

3.4 Simulations

This simulation section attempts to numerically simulate both the chemical system used in Fluorescence Imaging and the resulting fluorescence intensity profiles in water. The primary objective is to establish a quantitative relationship between the input gas concentration and the observed fluorescence signal. It is necessary to be able to draw conclusions about the gas concentration and the transport processes from the fluorescence detected in the experiments. Initially, the simulations of the chemical system and the fluorescence profiles are discussed separately, as already implemented in Papst (2019). In the next step, these simulations are combined and extended to include transport processes. This gives a more comprehensive description, which is also essential for the subsequent data analysis.

3.4.1 Chemical System

The chemical system builds the foundation of the Fluorescence Imaging technique and relies on coupled acid-base reactions. A mathematical representation of these equilibrium reactions allows to deterministically calculate the species concentrations by solving a system of equations.

Simulation Scheme

All chemical reactions involved can be expressed in the following general form

$$\nu_\mathrm{A}\mathrm{A} + \nu_\mathrm{B}\mathrm{B} \rightleftharpoons \nu_\mathrm{C}\mathrm{C} + \nu_\mathrm{D}\mathrm{D}, \tag{3.10}$$

with the reactants A and B, the products C and D, and the stoichiometric factors ν_A, ν_B, ν_C, and ν_D. The equilibrium concentrations of such a reaction are governed by the law of mass action

$$K = \frac{k_f}{k_b} = \frac{[C]^{\nu_C}[D]^{\nu_D}}{[A]^{\nu_A}[B]^{\nu_B}}, \tag{3.11}$$

where K denotes the equilibrium constant. This quantity reflects the ratio of forward and backward reaction rates k_f and k_b, and can be determined experimentally. Specifically applicable to acid-base reactions is the following definition between the equilibrium constant K_a and the pK_a value

$$\mathrm{p}K_a = -\log(K_a), \tag{3.12}$$

indicating the strength of an acid or base (Riedel & Janiak, 2011).
We now consider an aqueous solution containing the two dyes pyranine and tartrazine as well as the alkaline gas methylamine. Based on the conservation of mass for these three species and the

potentially occurring acid-base reactions in Eqs. (3.1) and (3.3), we arrive using Eq. (3.11) at the following system of equations,

$$[H_3O^+] \cdot [OH^-] = 10^{-pK_w}, \tag{3.13a}$$

$$[NH_2R]_w + [NH_3R^+]_w = [NH_2R]_{w,\mathrm{tot}}, \tag{3.13b}$$

$$\frac{[H_3O^+] \cdot [NH_2R]}{[NH_3R^+]} = 10^{-pK_a(NH_2R)}, \tag{3.13c}$$

$$[IH] + [I^-] = [I]_{\mathrm{tot}}, \tag{3.13d}$$

$$\frac{[H_3O^+] \cdot [I^-]}{[IH]} = 10^{-pK_a(I)}, \tag{3.13e}$$

$$[TH] + [T^-] = [T]_{\mathrm{tot}}, \tag{3.13f}$$

$$\frac{[H_3O^+] \cdot [T^-]}{[TH]} = 10^{-pK_a(T)}. \tag{3.13g}$$

Here, the autoprotolysis of water is also taken into account, which describes the self-ionization process of two water molecules reacting to form H_3O^+ and OH^- ions. This equilibrium is characterized by a dissociation constant of $K_w = 10^{-14}$ at 25 °C, corresponding to a pK_w of 14, which forms the basis of the pH scale. The remaining acid dissociation constants $pK_a(I) = 7.95$, $pK_a(T) = 9.99$, and $pK_a(NH_2R) = 10.63$ for pyranine, tartrazine, and methylamine have already been introduced in the previous section. All chemical reactions occurring among these chemical species in an aqueous solution are included in these equilibria.

A crucial extension of the chemical system is to incorporate the carbonate buffer that naturally occurs in aqueous solutions. It originates from the fact that atmospheric CO_2 dissolves in water until reaching an equilibrium state. In water, CO_2 exists both physically dissolved and in hydrated form as carbonic acid H_2CO_3. Since carbonic acid also has the ability to undergo an acid-base reaction, CO_2 forms a natural buffer system in the water. This consists of the following two reactions, whereby a two-step proton release can lead to the formation of hydrogen carbonate and bicarbonate

$$CO_2 + 2\,H_2O \rightleftharpoons HCO_3^- + H_3O^+, \tag{3.14}$$

$$HCO_3^- + H_2O \rightleftharpoons CO_3^{2-} + H_3O^+. \tag{3.15}$$

Consequently, the alkaline gas not only reacts with water or the indicator, but also with the carbonate system. Based on reaction in Eqs. (3.14) and (3.15), the system of equations is expanded by the following three additional equations,

$$[CO_2]_w + [HCO_3^-] + [CO_3^{2-}] = [CO_2]_{w,\mathrm{tot}}, \tag{3.16a}$$

$$\frac{[H_3O^+] \cdot [HCO_3^-]}{[CO_2]_w} = 10^{-pK_a(CO_2)}, \tag{3.16b}$$

$$\frac{[H_3O^+] \cdot [CO_3^{2-}]}{[HCO_3^-]} = 10^{-pK_a(HCO_3^-)}. \tag{3.16c}$$

The relevant pK_a values of the carbonate buffer system are given in the literature as $pK_a(CO_2) = 6.4$ (Harned & Davis, 1943) and $pK_a(HCO_3^-) = 10.3$ (Harned & Scholes, 1941).

As the system of equations is so far underdetermined, one condition is missing to make it computable. It is given by the conservation of charge, which balances the positive and negative ions of the species involved and ensures that the solution remains neutral overall

$$[H_3O^+] + [NH_3R^+] = [OH^-] + [I^-] + [T^-] + [HCO_3^-] + 2 \cdot [CO_3^{2-}] + [Cl^-]. \tag{3.17}$$

We also assume that the solution contains chloride ions. These are present as a result of the initial acidification of the system with hydrochloric acid to adjust the pH value. Since hydrochloric acid is a strong acid, it dissociates completely in water, so the concentration of chloride ions corresponds exactly to the amount of added hydrochloric acid, i.e. $[HCl] = [Cl^-]$.
Overall, the system of equations will be defined by the input concentrations $[I]_{tot}$, $[T]_{tot}$, $[NH_2R]_{w,tot}$, $[CO_2]_{w,tot}$, and $[Cl^-]$. Hence there are the 11 equations (3.13a) to (3.13g), (3.16a) to (3.16c), and (3.17) with the 11 variables $[H_3O^+]$, $[OH^-]$, $[NH_2R]_w$, $[NH_3R^+]_w$, $[IH]$, $[I^-]$, $[TH]$, $[T^-]$, $[CO_2]_w$, $[HCO_3^-]$, and $[CO_3^{2-}]$ which therefore has a unique solution. Typically, fixed values are set for the total concentrations of the two dyes $[I]_{tot}$ and $[T]_{tot}$ in the simulation and the system's response is analyzed by adding NH_2R, CO_2, or HCl. In each case, two of the species $[NH_2R]_{w,tot}$, $[CO_2]_{w,tot}$, and $[Cl^-]$ are kept constant while increasing the concentration of the third species gradually and solving the system of equations in each step. This approach allows to simulate the equilibrium behavior of the chemical system when adding one of the species NH_2R, CO_2, or HCl up to a target concentration, thereby modeling a gas invasion of methylamine or carbon dioxide as well as the acidification of the system.

Simulation Results

In order to demonstrate the simulation approach and validate the chemical system, we carry out a representative scenario. A pyranine concentration of $[I]_{tot} = 5 \cdot 10^{-5}\,\mathrm{mol\,L^{-1}}$ and a tartrazine concentration of $[T]_{tot} = 2 \cdot 10^{-5}\,\mathrm{mol\,L^{-1}}$ are set, as these values have proven suitable in preliminary experiments. The concentration of dissolved CO_2 is assumed to be in equilibrium with the atmosphere and is therefore kept constant throughout the simulation. Assuming a typical air CO_2 concentration in well-ventilated indoor environments of concentration of $[CO_2]_{a,tot} = 600\,\mathrm{ppm}$ (Satish et al., 2012) and a solubility coefficient of $\alpha_{CO_2} = 0.8$ (Sander, 2023), this gives a resulting equilibrium CO_2 concentration in water of $[CO_2]_{w,tot} = 2 \cdot 10^{-5}\,\mathrm{mol\,L^{-1}}$. In this initial state, before adding methylamine or hydrochloric acid, the system is in equilibrium and solving the system of equations yields an initial pH of 5.6.
Before performing any gas exchange experiments, the pH value is first lowered to 5.0, which optimizes the contrast between the fluorescence signal of the mass boundary layer and the background. In this first simulation procedure, this acidification is modeled by incrementally increasing $[Cl^-]$, while keeping the methylamine concentration at zero, i.e. $[NH_2R]_{w,tot} = 0$. This represents an addition of hydrochloric acid. The iteration continues until the desired pH of 5.0 is reached. In Fig. 3.4, the simulation results of the acidification step are shown, indicating that a hydrochloric acid concentration of $[Cl^-] \approx 9 \cdot 10^{-6}\,\mathrm{mol\,L^{-1}}$ is required to adjust the target pH.
In the second procedure, the actual gas exchange process of the trace gas is simulated. Contrary to the

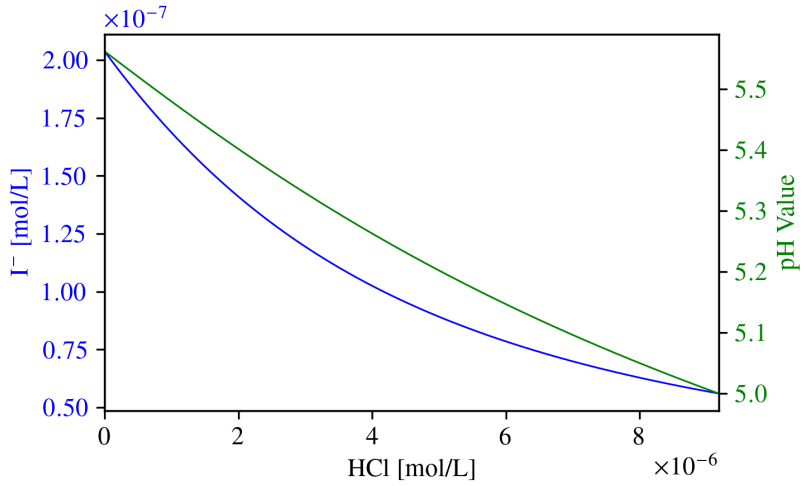

Figure 3.4: Simulation results of acidification. The diagrams show the decrease in I^- concentration and pH value with the addition of acid.

previous step, this is done by gradually increasing the concentration of the dissolving methylamine $[NH_2R]_{w,\text{tot}}$ whereas the previously determined hydrochloric acid concentration $[Cl^-]$ is kept constant. This simulation is continued until a final pH value of 9.0 is reached, allowing to evaluate the complete response of the system to the gas input over the entire relevant pH range. Fig. 3.5 shows these simulation results with particular emphasis on the concentration of pyranine's alkaline form as a function of the methylamine concentration. Three distinct ranges can be identified in this resulting profile:

- pH $\approx$ 5 – 7: The relationship between the methylamine concentration $[NH_2R]_{w,\text{tot}}$ and the alkaline form of the indicator $[I^-]$ is nonlinear in this range. This is due to the higher H_3O^+ concentration and the proximity to the first equivalence point of the carbonate buffer. Consequently, NH_2R reacts not only with the indicator, but also with H_3O^+ and components of the carbonate buffer system as H_2CO_3.

- pH $\approx$ 7 – 8.5: A predominantly linear relationship is observed as IH becomes the primary reactant for NH_2R. In this range, buffer effects and proton competition are minimized and the fluorescence intensity is directly proportional to the local gas concentration. It is therefore particularly suitable for quantitative analysis.

- pH $\approx$ 8.5 – 9: The system shows a saturation behavior, as most of the indicator is already present in its alkaline form I^-. This limits the availability of suitable reactants for NH_2R. In addition, the system approaches the equivalence point for methylamine, which results in some of the added methylamine remaining in its deprotonated form NH_2R. So, this range shows a strong nonlinear effect.

The simulations of acidification and gas invasion can be repeated as often as required. As the experimental procedure involves several consecutive measurements, the simulation can reproduce this behavior by iteratively alternating between acidification with resetting to pH of 5.0 and gas invasion with increasing methylamine concentrations. This allows for a stepwise analysis of the relation

between the total methylamine input and the indicator concentration for each individual measurement, directly corresponding to the experimental workflow.

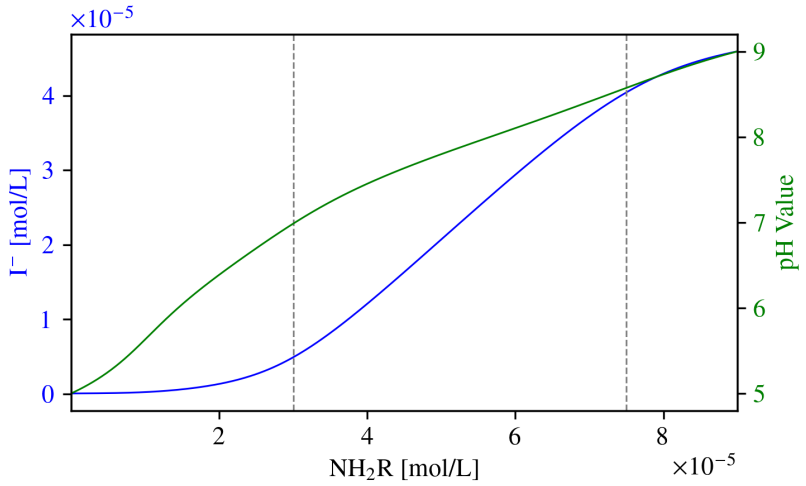

Figure 3.5: Simulation results of a gas invasion. The increase in I^- concentration and pH value with gas input is shown. The relationship between I^- concentration and NH_2R input shows three distinct regimes.

Finally, to assess the specific impact of the carbonate buffer system on the chemical behavior, the simulation is repeated as before, while excluding the three equations (3.16a) to (3.16c) describing the carbonate equilibria. As this simplification removes three variables and three equations, the system of equations remains solvable, making a direct comparison between the complete and the reduced model possible. The simulation results (Fig. 3.6) reveal two significant differences. First, the linear range of the reaction curve between NH_2R and I^- shifts to lower pH values. This displacement can be attributed to the absence of carbonate species, which otherwise act as potential proton donors in reactions with methylamine. Without these buffer components, the system reaches a certain pH with a lower methylamine concentration, pushing the linear range into a more acidic region. Second, the nonlinear transitions in the low pH range become more abrupt in the absence of the carbonate buffer. The complete model, which includes the coupled equilibria of the carbonate system, exhibits an increased nonlinearity due to the additional reaction pathways that affect proton availability. When these reactions are removed, the response of the system becomes more rapid, with sharper transitions between different pH ranges and more sensitive to changes in methylamine concentration near the lower pH limit.

These observations underline the chemical relevance of the carbonate buffer system in shaping the pH response. Including carbonate equilibria not only extends the linear range and enhances the nonlinearity near the pH limits, but also reflects the influence of dissolved atmospheric CO_2. This factor is likely to play a role under experimental conditions. In Sec. 5.3.4, we will see that the experimentally observed relationship between total methylamine input and the resulting pH is more accurately reproduced by simulations that include the carbonate buffer. As a consequence, the inclusion of the carbonate buffer system in the simulation of the chemical system is essential.

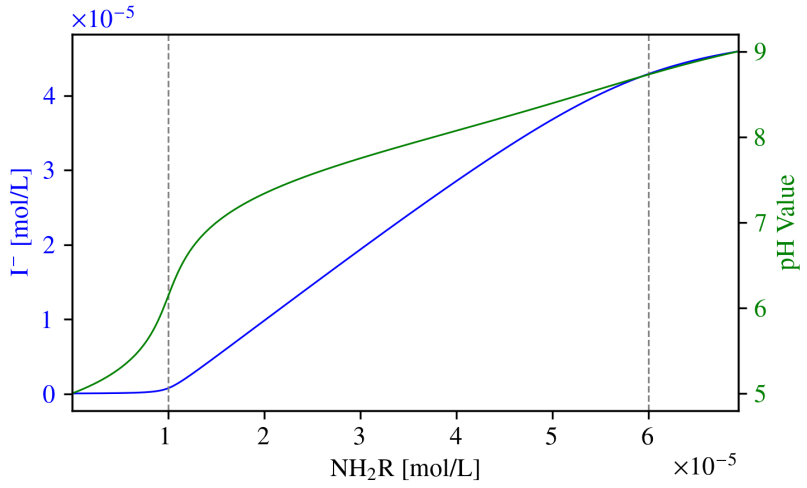

Figure 3.6: Simulation results of a gas invasion without carbonate buffer. Analog representation as in Fig. 3.5.

3.4.2 Fluorescence Profile

The fluorescence signal generated within the mass boundary layer depends essentially on the concentration profiles of the two dyes and obeys the fundamental relationships in Eqs. (2.70) and (2.73). Since an analytical solution for the total fluorescence from multiple interacting species is not feasible, the problem is approached numerically. This simulation relies on the iterative calculation of absorption and emission processes along differential path elements within a discretized one-dimensional water column using the Lambert-Beer law as described in Eq. (2.67). It is important to note that the Fluorescence Imaging technique is specifically designed such that the excitation light comes straight from above the water surface, while the emitted fluorescence is recorded from below the water column. Thus, in order to simulate the detected fluorescence signal, integrating the emitted fluorescence over the entire water depth is required. Generally, this model assumes a flat water surface and neglects refraction as well as scattering within the water.

Simulation Scheme

We simulate the fluorescence response in an aqueous solution containing the two pH-sensitive dyes pyranine and tartrazine. All other chemical species are assumed to contribute negligibly to the absorption and fluorescence processes and are therefore excluded from the model. Hence, the following applies to the differential absorption dI_A within a differential length element dz,

$$dI_A(\lambda, z) = -I(\lambda, z) \sum_{i=1}^{4} \ln(10)\varepsilon_i(\lambda)c_i(z)\, dz, \tag{3.18}$$

where the indices $i = 1, 2$ refer to the acidic and alkaline components of pyranine, respectively, and $i = 3, 4$ represent the acidic and alkaline forms of tartrazine.
The simulation is performed on a grid with discretized depth elements Δz (Fig. 3.7) and wavelength intervals $\Delta\lambda$. Specifically, the vertical water column is divided into $N = 200$ adaptive depth cells as follows:

- The upper 100 cells, starting at the air-water interface, have a uniform thickness of 20 µm covering the upper millimeter of the water column where the steepest concentration gradients are expected.
- The remaining lower 100 cells are progressively enlarged in thickness according to a geometric sequence and extend from 2 mm to 1 m water depth. This decreasing resolution with depth is justified because the excitation light only penetrates about the uppermost centimeter of the water column, so that deeper layers are irrelevant for the fluorescence signal.

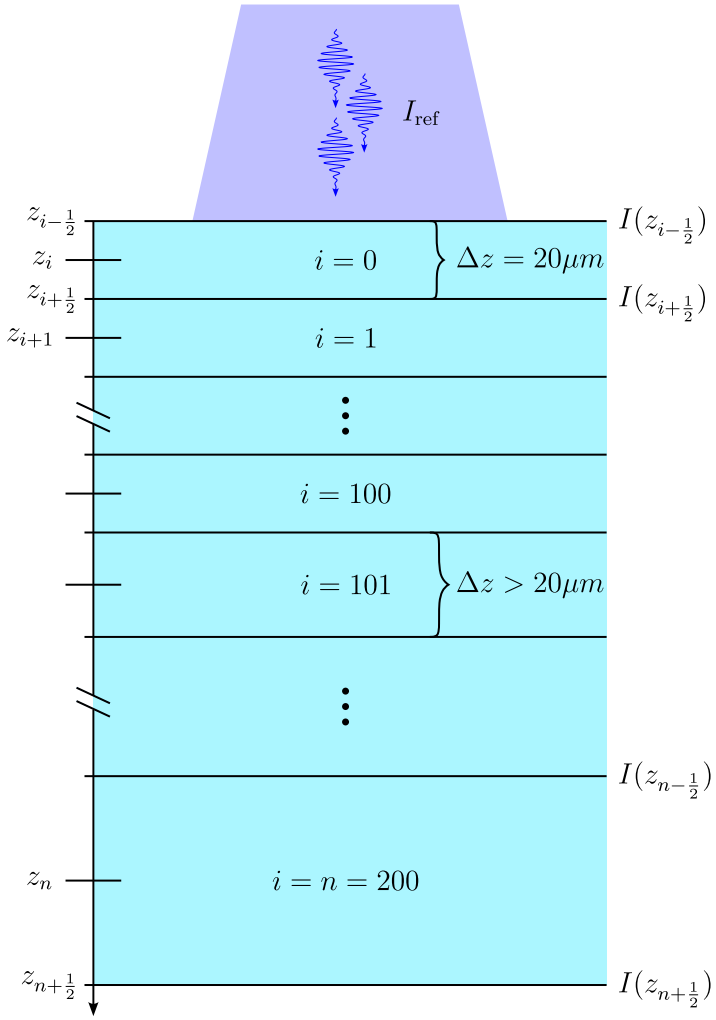

Figure 3.7: Grid for simulating the fluorescence intensity. Adaptive grid consisting of 200 depth cells, in which the first 100 cells have a fixed size of 20 µm and the remaining 100 cells have a geometrically increasing size. Note that the z-positions are defined at the cell centers and the intensities at the cell boundaries. Positions of the cell boundaries have half-integer indices.

This adaptive mesh structure provides an optimal balance between computational efficiency and high spatial resolution near the surface, especially important for accurately capturing the dynamics within the mass boundary layer. Within each depth cell, the concentrations of the dye components are considered spatially constant. Consequently, the absorption properties within each depth element are also assumed to be spatially uniform, but may vary with depth depending on the local concentrations. The absorption coefficients for the acidic and alkaline forms of the two dyes are taken from the

experimentally measured reference spectra in Figs. 3.2 and 3.3. Note that these reference spectra were obtained at a certain reference concentration and an optical path length of 1 cm. So, it is necessary to scale the absorption coefficients according to the local dye concentrations and the thickness of the individual cells when applying them to the simulation grid. The spectral resolution of these absorption spectra also dictates the discretization of the wavelength intervals, which is set to $\Delta\lambda = 0.5$ nm. Finally, the concentration profiles of the dye components must be defined as input parameters. These profiles can be obtained either from numerical simulations of the chemical system or from experimental measurements.

We start the simulation by setting the emission spectrum of the excitation light source (Fig. 4.4) as the initial condition at the water surface z_0. This excitation spectrum $I_0(\lambda_k, z_0)$ indicates the light intensity I_0 at each wavelength λ_k and was measured experimentally for our setup. An integration over the spectral range with the resolution $\Delta\lambda = 0.5$ nm gives the total excitation intensity I_{ref} at the water surface according to

$$I_{\text{ref}}(z_0) = \sum_k I_0(\lambda_k, z_0)\,\Delta\lambda. \tag{3.19}$$

All following calculated intensities are normalized to this value, i.e. they represent a fraction of the total intensity of the excitation light at the water surface. Naturally, the fluorescence intensity at the water surface is zero, i.e. $I_F(z_0) = 0$. As the simulation progresses into the depth of the water column, the excitation light is attenuated layer by layer due to absorption by the dye molecules. The transmitted excitation intensity I_T at the next cell interface z_{n+1} is updated iteratively based on the Lambert-Beer law,

$$\Delta I_T(\lambda_k, z_{n+1}) = -I_T(\lambda_k, z_n) \sum_{i=1}^{4} \ln(10)\varepsilon_i(\lambda_k)c_i(z_{n+1})\,\Delta z, \tag{3.20}$$

$$I_T(\lambda_k, z_{n+1}) = I_T(\lambda_k, z_n) + \Delta I_T(\lambda_k, z_{n+1}). \tag{3.21}$$

The total transmitted excitation intensity at depth z_{n+1} is then given by

$$I_T(z_{n+1}) = \sum_k I_T(\lambda_k, z_{n+1})\,\Delta\lambda. \tag{3.22}$$

Simultaneously, a part of the absorbed excitation light is converted into fluorescence. Only the fluorescence-active components of pyranine contribute to this process. The fluorescence generated in each depth cell is calculated as

$$\Delta I_F(\lambda_k, z_{n+1}) = I_T(\lambda_k, z_n) \sum_{i=1}^{2} \ln(10)\varepsilon_i(\lambda_k)c_i(z_{n+1})\,\Delta z. \tag{3.23}$$

The total fluorescence intensity generated at depth z_{n+1} is obtained by summing the contributions from all excitation wavelengths and weighting by the fluorescence quantum yield Φ_F,

$$I_F(z_{n+1}) = \Phi_F \sum_k \Delta I_F(\lambda_k, z_{n+1})\,\Delta\lambda. \tag{3.24}$$

Since the fluorescence is detected from below, the total detectable signal is finally computed by summing the fluorescence intensities of all depth layers,

$$I_{F,\text{tot}} = \sum_{n=0}^{N} I_F(z_n)\,\Delta z. \tag{3.25}$$

It is important to note that the intensity profiles I_T and I_F are defined at the cell interfaces, i.e. the boundaries between adjacent depth layers. In contrast, the concentrations $c_i(z_{n+1})$ and absorption coefficients $\varepsilon_i(\lambda_k)$ are defined within each depth cell. This staggered grid approach corresponds to a physically meaningful modeling of light attenuation and fluorescence generation.
Overall, the simulation requires the concentration profiles of pyranine and tartrazine as the only input parameters to be specified. These can either be measured experimentally or modeled based on the expected diffusion and reaction dynamics. It then provides spatially resolved intensity profiles of both the excited and emitted fluorescence light $I_T(z_n)$ and $I_F(z_n)$ as well as the total fluorescence signal $I_{F,\text{tot}}$ that is measurable at the bottom of the water column.

Simulation Results

As a validation for the behavior of the fluorescence signal during a gas exchange experiment, we simulate the fluorescence response for varying concentration ratios of the two pyranine forms. For simplicity, the concentration profiles of all dye species IH, I^-, TH, and T^- are assumed to be constant in depth, which is equivalent to a static equilibrium where all species have been homogeneously distributed. Based on the previously calculated chemical equilibrium states in Fig. 3.5, the corresponding component concentrations for each simulation point are used as input parameters for the fluorescence simulation model. This yields a complete profile of the expected fluorescence signal across the entire experimentally relevant pH range from 5 to 9.
The results of this simulation are presented in Fig. 3.8. As expected, the fluorescence intensity increases with rising concentrations of the alkaline form of pyranine (Fig. 3.8(b)). This trend forms the basis for calibrating the fluorescence intensity in the image analysis.
In addition, the simulated excitation intensity profiles allow to estimate its penetration depth into the water. Regardless of the dye composition, the excitation light penetrates approximately 1.5 cm below the surface (Fig. 3.8(a)). This depth is largely unaffected by the increasing pH value, as the primary absorber in the excitation wavelength range is tartrazine. Given its high pK_a value, the concentration ratio of tartrazine's two protonation states remains relatively stable within the investigated pH range. Moreover, the spectral absorption characteristics of both tartrazine species are sufficiently similar in the excitation range, which further supports the observed invariance in light penetration depth.

3.4.3 Mass Transport

The simulation of mass transport integrates the previous calculations of the chemical system and the fluorescence profile with an additional numerical treatment to solve the transport equation. It aims to simulate the transport dynamics and chemical reactions of methylamine entering the water and to extract the resulting fluorescence signal. Based on this implementation, an approach for calculating

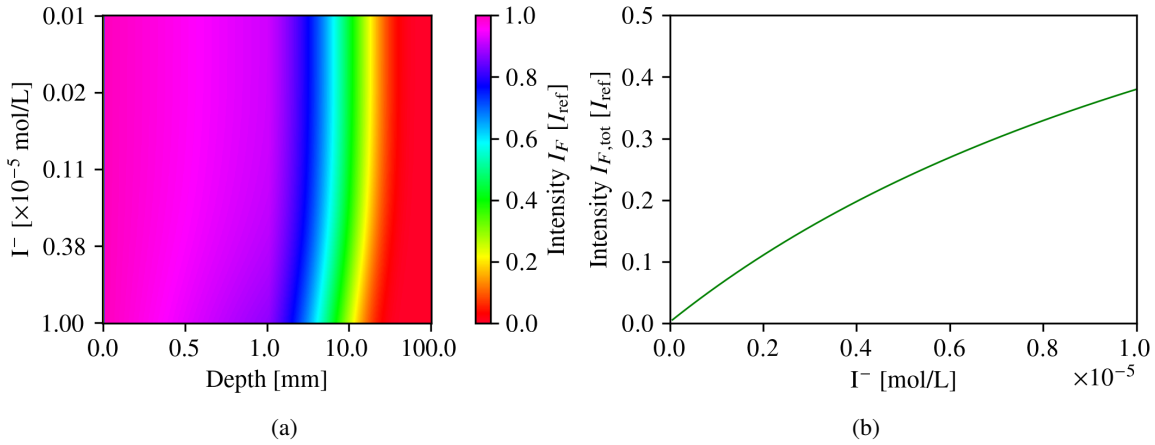

(a) (b)

Figure 3.8: Simulation results of fluorescence intensity. (a) Depth profiles of fluorescence intensity and (b) integrated fluorescence intensity over the water column at varying I^- concentrations. For better visualization, each fluorescence depth profile in (a) is normalized to its highest value at the surface. Actually, the fluorescence increases at each depth with increasing I^- concentration, as depicted in (b). The curve of integrated fluorescence intensities in (b) is later used for brightness calibration.

the gas transfer velocity will follow in the analysis. This simulation approach is similar to that in Haußecker (1996), where it was implemented for heat transport.

Simulation Scheme

Since mass transport includes diffusion, turbulence, and chemical reactions in our case, we base the numerical simulation on the general transport equation (2.26)

$$\frac{\partial C}{\partial t} = \nabla \cdot ((D + K(z))\nabla C) + R(C). \tag{3.26}$$

In one-dimensional form, considering only vertical transport, this equation simplifies to

$$\frac{\partial C}{\partial t} = \frac{\partial}{\partial z}\left(D_{\text{eff}}(z)\frac{\partial C}{\partial z}\right) + R(C), \tag{3.27}$$

where $D_{\text{eff}}(z) = D + K(z)$ represents the effective diffusivity, accounting for both molecular diffusion and additional turbulence. The depth profile of $D_{\text{eff}}(z)$ is assumed to be known and defined throughout the following implementation.

A finite difference method is applied to discretize the continuous transport equation by replacing derivatives with difference quotients. This approach allows the differential equation to be solved on a spatially and temporally discretized grid. As for the spatial simulation grid, the adaptive one-dimensional depth grid introduced for the fluorescence simulation is adopted. In this context, spatial cell centers are consistently labeled with the index i, cell boundaries with a half-integer index $i + \frac{1}{2}$ and temporal steps with the index n. We use an implicit scheme to ensure numerical stability.

Initially, the temporal derivative on the left-hand side of the transport equation is approximated using a backward Euler scheme

$$\frac{\partial C}{\partial t} \approx \frac{C_i^{n+1} - C_i^n}{\Delta t}, \tag{3.28}$$

with Δt denoting the time step between the two computational iterations n and $n+1$. Additionally, the second spatial derivative of the diffusion term is approached using a modified central difference scheme

$$\frac{\partial}{\partial z}\left(D_{\text{eff}}(z)\frac{\partial C}{\partial z}\right) \approx \frac{1}{\Delta z_i}\left[D_{\text{eff},i+\frac{1}{2}}\frac{C_{i+1}-C_i}{\Delta z_{i+\frac{1}{2}}} - D_{\text{eff},i-\frac{1}{2}}\frac{C_i - C_{i-1}}{\Delta z_{i-\frac{1}{2}}}\right]. \tag{3.29}$$

This differs from the standard central difference approach, as the inner derivative only operates on concentrations, while the outer derivative acts on the product of the inner derivative with the diffusivities. Notably, the concentrations are specified at the cell centers $i+1$, i, and $i-1$, while the turbulent diffusivity is defined at the cell boundaries $i+\frac{1}{2}$ and $i-\frac{1}{2}$. Consequently, the inner difference is calculated between two cell centers, but the outer difference between two cell boundaries. In an adaptive grid, these distances may vary slightly. By merging Eqs. (3.28) and (3.29) in an implicit Euler scheme, the transport equation ends up in a discretized solvable form,

$$\frac{C_i^{n+1}-C_i^n}{\Delta t} = \frac{1}{\Delta z_i}\left[D_{\text{eff},i+\frac{1}{2}}\frac{C_{i+1}^{n+1}-C_i^{n+1}}{\Delta z_{i+\frac{1}{2}}} - D_{\text{eff},i-\frac{1}{2}}\frac{C_i^{n+1}-C_{i-1}^{n+1}}{\Delta z_{i-\frac{1}{2}}}\right], \tag{3.30}$$

$$C_i^{n+1} + \frac{\Delta t}{\Delta z_i}\left[\frac{D_{\text{eff},i+\frac{1}{2}}}{\Delta z_{i+\frac{1}{2}}} + \frac{D_{\text{eff},i-\frac{1}{2}}}{\Delta z_{i-\frac{1}{2}}}\right]C_i^{n+1} - \frac{\Delta t}{\Delta z_i}\frac{D_{\text{eff},i+\frac{1}{2}}}{\Delta z_{i+\frac{1}{2}}}C_{i+1}^{n+1} - \frac{\Delta t}{\Delta z_i}\frac{D_{\text{eff},i-\frac{1}{2}}}{\Delta z_{i-\frac{1}{2}}}C_{i-1}^{n+1} = C_i^n. \tag{3.31}$$

To solve this equation implicitly, it is further reformulated into a matrix system

$$AC^{n+1} = B, \tag{3.32}$$

where the matrix A comprises the transport coefficients, the vector $B = C^n$ represents the current concentration values at each depth cell and the vector C^{n+1} gives the concentration values for the next time step. The inner elements of the matrix are defined as

$$A_{i,i-1} = -\frac{\Delta t}{\Delta z_i}\frac{D_{\text{eff},i-\frac{1}{2}}}{\Delta z_{i-\frac{1}{2}}}, \tag{3.33}$$

$$A_{i,i} = 1 + \frac{\Delta t}{\Delta z_i}\left(\frac{D_{\text{eff},i+\frac{1}{2}}}{\Delta z_{i+\frac{1}{2}}} + \frac{D_{\text{eff},i-\frac{1}{2}}}{\Delta z_{i-\frac{1}{2}}}\right), \tag{3.34}$$

$$A_{i,i+1} = -\frac{\Delta t}{\Delta z_i}\frac{D_{\text{eff},i+\frac{1}{2}}}{\Delta z_{i+\frac{1}{2}}}, \tag{3.35}$$

while the boundary elements differ slightly to account for the boundary conditions. We assume that all species remain within the water reservoir preventing any transport beyond the computational grid. This assumption is justified, on the one hand, by the solid bottom boundary and, on the other hand, by the high solubility of the species, which makes an escape at the water surface thermodynamically unfavorable. Mathematically, this corresponds to closed boundary conditions, which can be implemented conveniently by assuming zero diffusivity at the boundaries, i.e. $D_{\text{eff},-\frac{1}{2}} = D_{\text{eff},N+\frac{1}{2}} = 0$.

Consequently, the boundary elements of the matrix are given by

$$A_{0,0} = 1 + \frac{\Delta t}{\Delta z_0} \frac{D_{\text{eff},\frac{1}{2}}}{\Delta z_{\frac{1}{2}}}, \tag{3.36}$$

$$A_{0,1} = -\frac{\Delta t}{\Delta z_0} \frac{D_{\text{eff},\frac{1}{2}}}{\Delta z_{\frac{1}{2}}}, \tag{3.37}$$

$$A_{N,N} = 1 + \frac{\Delta t}{\Delta z_N} \frac{D_{\text{eff},N-\frac{1}{2}}}{\Delta z_{N-\frac{1}{2}}}, \tag{3.38}$$

$$A_{N,N-1} = -\frac{\Delta t}{\Delta z_N} \frac{D_{\text{eff},N-\frac{1}{2}}}{\Delta z_{N-\frac{1}{2}}}. \tag{3.39}$$

With this fully occupied matrix A and the concentration vector C^n of the current time step n, the matrix equation (3.32) becomes uniquely solvable and enables the calculation of the concentration values C^{n+1} in each depth cell for the next time iteration $n+1$. In this way, the transport equation can be solved numerically.

Next, we have to address the chemical reaction term $R(C)$. Commonly, chemical reactions are incorporated into transport simulations via reaction rate expressions. In the present system, however, many of the chemical reactions are coupled as well as their individual reaction rates are not known. So, an explicit inclusion would imply a large and complicated system of coupled differential equations with significant uncertainties and computational costs. Avoiding this, we adopt an alternative approach based on the assumption that the system is transport-limited rather than kinetically controlled. This is justified because all reactions involved are acid-base reactions, which are known to proceed extremely fast compared to diffusion-controlled mass transport close to the surface. Consequently, it can be assumed that the chemical system reaches a local equilibrium in each grid cell at each time step. This allows for a modular simulation strategy in which chemical reactions and transport are treated separately. At each time step, the chemical system is first solved independently in each depth cell by determining the local equilibrium concentrations between species S via the system of algebraic equations as implemented in Sec. 3.4.1. In very simplified terms, this corresponds to the solution of

$$f(C^n_{i,S}) = 0. \tag{3.40}$$

These concentrations then serve as input to the subsequent transport step, in which the discretized transport equation is solved independently for each species S.

Finally, the simulation must be linked to the invasion of methylamine and the resulting fluorescence signal, which serve as input and output of the model. To account for the invasion of methylamine from the gas phase, we impose a given flux of methylamine $J_{\text{NH}_2\text{R}}$ into the surface layer $i = 0$ at the beginning of each time step. This results in an increase of the methylamine concentration in the uppermost grid cell by

$$C^n_{0,\text{NH}_2\text{R}} = C^n_{0,\text{NH}_2\text{R}} + J_{\text{NH}_2\text{R}} \frac{\Delta t}{\Delta z_0}. \tag{3.41}$$

After running the reaction and transport simulation steps, new concentration profiles of pyranine and tartrazine results from the added methylamine. The fluorescence signal is then obtained by entering the

concentration profiles of the acidic and alkaline forms of pyranine and tartrazine into the fluorescence simulation described in Sec. 3.4.2.
In summary, the numerical simulation of mass transport proceeds in four steps per time iteration:

1. Increasing the methylamine concentration in the top grid cell according to the invasion flux J_{NH_2R}.
2. Solving the chemical equilibrium independently for each grid cell.
3. Solving the transport equation for each chemical species.
4. Determining the fluorescence signal by applying the concentration profiles of both dyes to the fluorescence simulation.

By iterating this procedure over time, the simulation yields a time-resolved fluorescence signal in response to a temporal methylamine input.

Simulation Results

The simulation is now carried out for various depth profiles of the turbulent diffusivity $K(z)$ to examine the impact of different degrees of turbulence on the fluorescence intensity. In all simulations, the input gas flux is maintained constant over time to isolate the effects of turbulence.
We begin by considering the situation of a wavy water surface, modeled using a quadratic, depth-dependent turbulence profile, as introduced in Sec. 2.2.3. The simulation is performed for a wide range of the free parameter a, spanning several orders of magnitude from $a = 10^{-2}$ to $a = 10^{1}$, with values logarithmically distributed. With the diffusion constants of the species involved, an effective diffusivity depth profile is defined for each substance. The corresponding diffusion coefficients are summarized in Tab. A.1 (see Appendix A.1). The methylamine flux into the system is set to a constant value of $J_{NH_2R} = 1 \cdot 10^{-5}\,\mathrm{mol\,m^{-2}\,s^{-1}}$, matching the typical magnitude observed in gas invasion experiments. In addition, the temporal discretization follows an equidistant sampling period of $\Delta t = 0.1\,\mathrm{s}$ with a total of 5000 iteration time steps, resulting in a total simulation time of $T = 500\,\mathrm{s}$.
An exemplary result of such a mass transport simulation at three selected time points is presented in Fig. 3.9. The figure shows the concentration profiles of the various involved species along the water column, as well as the corresponding pH depth profile. Videos showing the full temporal evolution of the simulation for two different gas fluxes are available in Hofmann (2025a) and Hofmann (2025b) providing an animated view of the evolving concentration and pH profiles. It becomes immediately evident that the concentration of I^- approaches saturation at the water surface under the typical invasion flux used in gas exchange experiments. This means there is no continuously decreasing concentration gradient within the mass boundary layer, in contrast to what would be expected under purely diffusive conditions (cf. Fig. 2.1). Later analysis will show that a continuously decreasing I^- concentration profile within the mass boundary layer cannot explain the fluorescence intensities measured in the experiments either.
Applying the simulated concentration profiles IH, I^-, TH, and T^- as input for the simulation of fluorescence profile over each time point, results in the temporal evolution of the fluorescence signal.

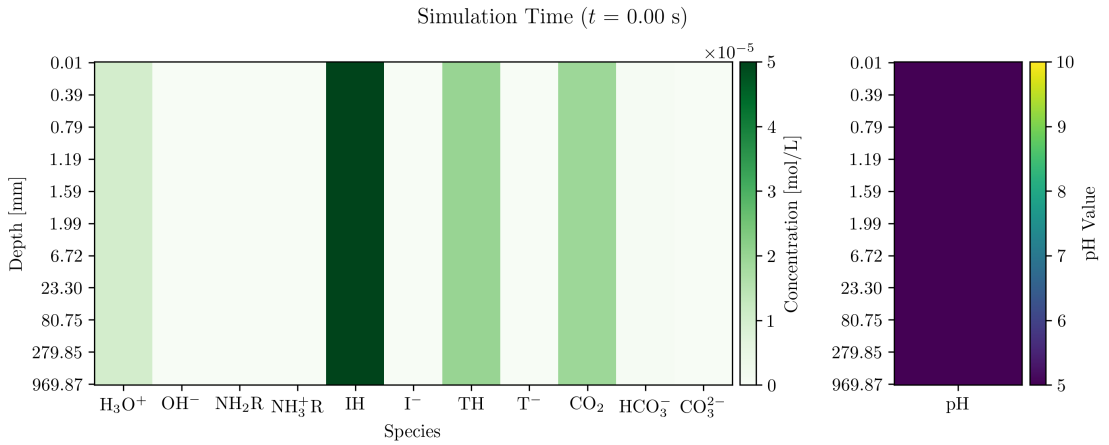

(a)

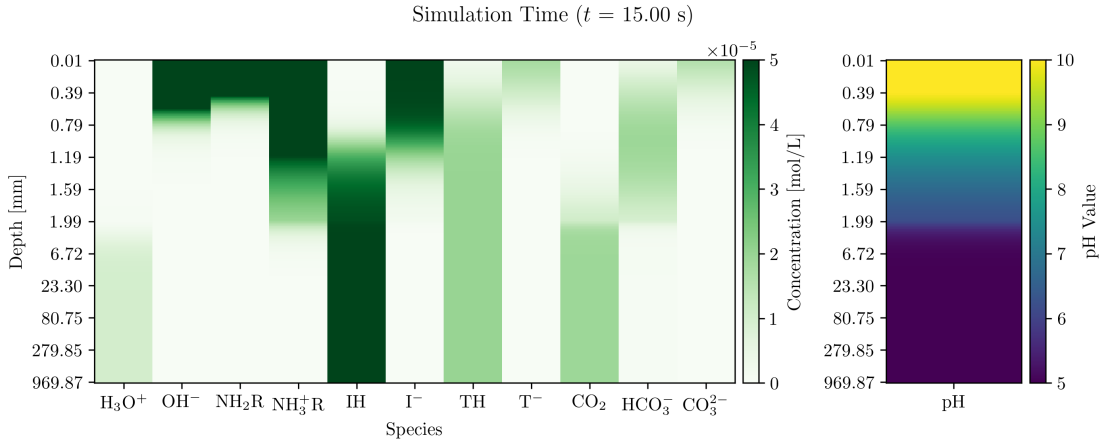

(b)

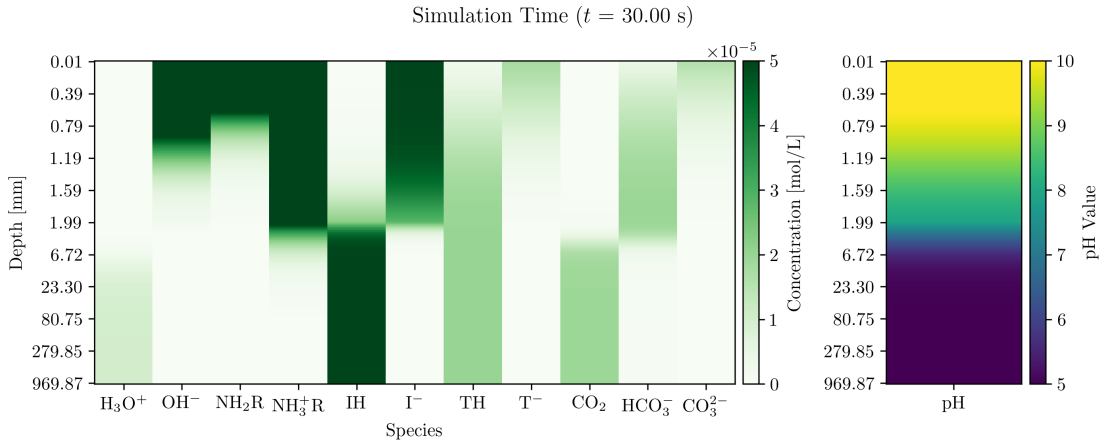

(c)

Figure 3.9: Temporal snapshots of the mass transport simulation. The time points are (a) 0 s, (b) 15 s, and (c) 30 s. On the left side the concentration depth profiles of the species involved in the chemical system are shown and on the right side the depth profile of the pH value. Note the adaptive depth grid introduced in Sec. 3.4.2. The concentration color scale is normalized to the pyranine concentration. Therefore, concentrations of other species higher than $5 \cdot 10^{-5}$ mol L^{-1} become color saturated.

These resulting temporal fluorescence curves for different values of the parameter a are shown in Fig. 3.10. In each case, the fluorescence increases with time and eventually reaches a steady-state plateau, reflecting saturation of the fluorescence signal. Here, a clear trend is observed as the parameter a decreases, corresponding to weaker turbulence, and the steady-state fluorescence intensity increases. This behavior arises from the interplay of turbulent mixing and light absorption. In highly turbulent systems, the fluorescent species pyranine I^- produced at the surface is rapidly mixed into deeper layers, flattening its vertical concentration profile. However, the excitation light is significantly attenuated with increasing depth due to absorption by tartrazine. As a result, I^- contributes less to the overall fluorescence signal at depth, leading to a lower intensity. Conversely, under low turbulence conditions, the influence of diffusion as the dominant transport mechanism increases and vertical transport becomes slower overall. This causes a pronounced accumulation of I^- near the surface, where excitation is most efficient. Consequently, the fluorescence intensity is enhanced. A second aspect to consider is the time required to reach a steady state varies with the strength of the turbulence. With stronger turbulence transport, equilibrium is reached faster due to efficient mixing via the vertical expansion of the water column. However, with weaker turbulence, the system relies primarily on slower diffusive transport, to disperse the species, delaying the onset of saturation.

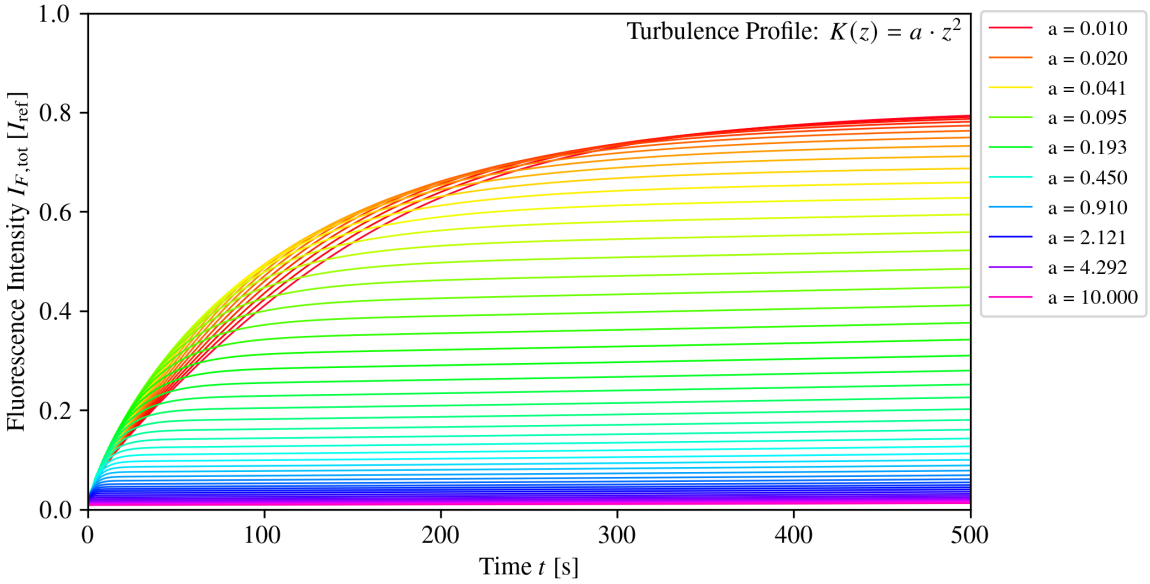

Figure 3.10: Simulation of mass transport with a quadratic depth profile of turbulent diffusivity. The simulation is carried out with different parameter values a, with only 10 values listed in the legend for orientation purposes of the color scale. A constant mass flux of $J_{\mathrm{NH_2R}} = 1 \cdot 10^{-5}\,\mathrm{mol\,m^{-2}\,s^{-1}}$ of methylamine is assumed. The fluorescence values are given in units of the reference intensity I_{ref} of the excitation light at the water surface.

Subsequently, the simulation is repeated for a smooth water surface. Here, the turbulent diffusivity is assumed to follow a cubic depth profile, again with identical values for a, and all other parameters kept constant. As shown in Fig. 3.11, the overall fluorescence dynamics exhibit the same qualitative trends as in the wavy surface case. Nevertheless, the curves are generally less steep and saturation occurs later. This difference can be attributed to the nature of the cubic profile, which increases more gradually with depth than its square counterpart in the orders of magnitude considered. As a result, the turbulence remains weak over a larger part of the water column, especially in the mass boundary

layer. The diffusive transport dominates over larger depths, leading to extended mass boundary layers. This slows both the vertical mixing of species and the evolution of the system towards a steady state.

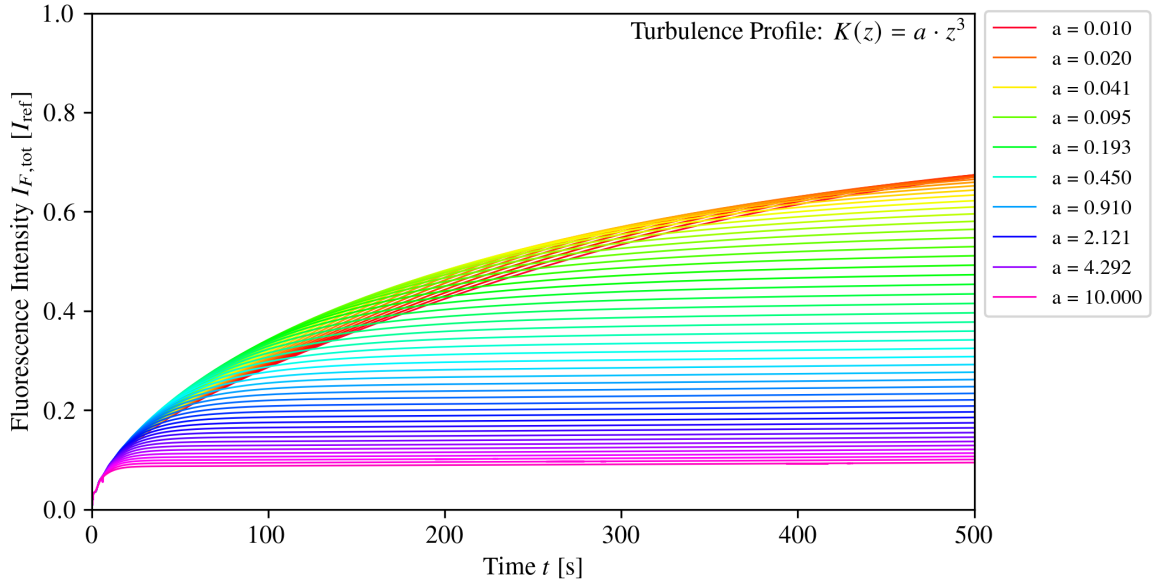

Figure 3.11: Simulation of mass transport with a cubic depth profile of turbulent diffusivity. Analogous settings as in Fig. 3.10.

Collectively, these results illustrate how different turbulence profiles lead to distinct dynamic fluorescence responses. Most importantly, this insight gives rise to the idea of the following powerful analytical approach. Given a known methylamine flux and an experimentally measured fluorescence signal, we can reverse-engineer the underlying turbulent diffusivity profile that best represents the observed data. This concept forms the basis for the subsequent analysis, where the simulation framework is used to determine the turbulence profiles yielding the closest fit to the experimental fluorescence intensities.

3.5 Mass Balance

The mass balance approach is a classical method for measuring gas exchange by deriving mass fluxes from the temporal development of gas concentrations on the air and water side. Its underlying principle is the conservation of mass. Typically, gas exchange is modeled using a two-box model consisting of an air and a water compartment as illustrated in Fig. 3.12. Both compartments are assumed to be well-mixed and closed reservoirs.

Based on this, we consider a gas with concentration c_a in the air volume V_a and concentration c_w in the water volume V_w. The gas is capable of exchanging at the interface A between the two phases. Assuming a gas input flux into the air compartment with a volumetric input rate $\dot{V}_i$, an input concentration c_i, and a leakage loss at a rate $\dot{V}_{\mathrm{leak}}$, the following system of coupled differential

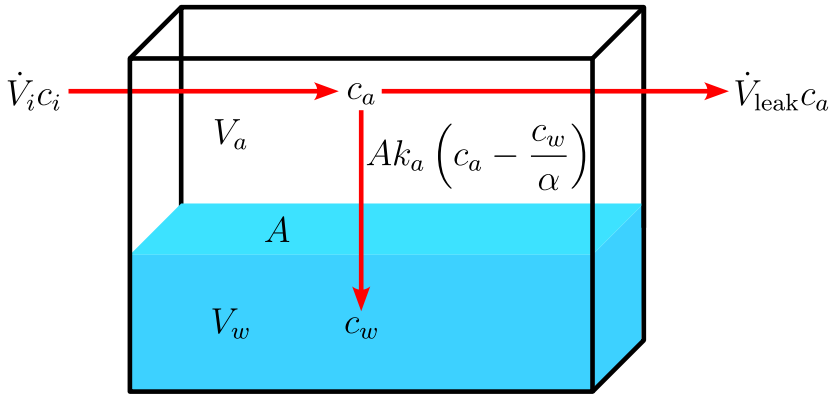

Figure 3.12: Box model of an invasion experiment with a highly soluble gas. The gas is injected into the air space and dissolves in the water. Losses due to leaks are only assumed on the air side. Modified after Papst (2019).

equations is obtained from mass conservation

$$V_a \dot{c}_a = -Ak_a \cdot \left(c_a - \frac{c_w}{\alpha}\right) + \dot{V}_i c_i - \dot{V}_{\text{leak}} c_a, \tag{3.42}$$

$$V_w \dot{c}_w = Ak_a \cdot \left(c_a - \frac{c_w}{\alpha}\right). \tag{3.43}$$

These equations describe the gas exchange dynamics from the perspective of the air compartment. Here, k_a refers to the air-side transfer velocity, representing the velocity at which the gas dissolves from the air phase in the water body. This system of equations corresponds to an invasion experiment in which the water-side gas input and leakages are neglected. It allows to describe gas exchange on a macroscopic scale and provides the dynamic concentration profiles in the air and water components by solving the equations.

The experiments on methylamine invasion presented above represent the case of a highly soluble gas. According to $c_a \gg \frac{c_w}{\alpha}$ for highly soluble gases, the system decouples and reduces to

$$0 = \dot{c}_a + \left(\frac{Ak_a}{V_a} + \frac{\dot{V}_{\text{leak}}}{V_a}\right) c_a - \frac{\dot{V}_i}{V_a} c_i. \tag{3.44}$$

We now examine the case where an initial amount of gas c_0 is introduced into the air space, which then dissolves in the water. In this scenario, $c_i \approx 0$, and solving the differential equation leads to an exponential decrease in the air concentration over time

$$c_a(t) = c_0 \exp(-\lambda_a t). \tag{3.45}$$

Here, λ_a indicates the decay rate, defined as

$$\lambda_a = \frac{Ak_a}{V_a} + \frac{\dot{V}_{\text{leak}}}{V_a}. \tag{3.46}$$

The first term takes into account the decrease in air concentration due to gas transfer into the water, while the second term represents the loss due to leakage. Finally, it is possible using the effective height of the air space $h_a = \frac{V_a}{A}$ and the leakage rate $\lambda_{\text{leak}} = \frac{\dot{V}_{\text{leak}}}{V_a}$ to deduce the air-side gas transfer

velocity

$$k_a = h_a \left(\lambda_a - \lambda_{\text{leak}}\right) . \tag{3.47}$$

It follows that, under the given assumptions with no additional gas being introduced into the system, the air-side gas transfer velocity k_a can be derived from the decay of the air-side concentration over time. Similarly, the leakage rate λ_{leak} can be found by analyzing the decay of the air-side concentration of a non-soluble gas for which $k_a \approx 0$ applies.
The mass balance calculations presented here will be particularly important for determining the invasive gas flux required for the simulation of mass transport.

4 Experiments

This chapter presents the experimental implementation of the proposed Fluorescence Imaging method in a large-scale wind-wave channel. It includes a comprehensive description of the setup developed to image gas concentration fields near the air-water interface as well as an overview of the realized measurement campaign. All experiments have been carried out at the Heidelberg Aeolotron Wind-Wave Facility. Over the past 25 years, numerous studies have been performed at this facility to investigate air-sea interactions involving the exchange of masses, heat, and momentum. However, the measurement campaign presented in this thesis marks the final series of experiments at the Aeolotron.

4.1 Setup

In order to accurately reconstruct the dynamics of gas transfer at the air-water interface, a high spatial and temporal resolution imaging of concentration fields in the mass boundary layer is required. A precise recording setup was designed for this purpose, consisting of multiple laser light sources and a high-resolution multi-camera array. This section gives a detailed description of the experimental setup, with particular emphasis on the implementation of the illumination and recording units. Furthermore, the instrumentation of the wind-wave channel for measuring substance concentrations in air and water as well as other environmental parameters is outlined.

4.1.1 Aeolotron

The Heidelberg Aeolotron is an annular wind-wave facility with a diameter of approximately 10 m. It consists of a water channel with an enclosed air space where wind can be generated to create waves. Cross-sectional, the channel measures 61.5 cm in width and 240.3 cm in height. At a maximum water level of 100 cm, the Aeolotron contains approximately 18 000 L of water over an area of about 18 m^2, with an air volume of 25 400 L above it. In Fig. 4.1 a schematic sketch of the facility is shown, visualizing its dimensions. The facility is partitioned into a total of 16 equally sized segments, with numbering running clockwise. There are four axial fans with 90° of separation between two fans in segments 4, 8, 12, and 16, with an output power of 2.2 kW each, which generate the wind. It can reach wind speeds of up to 22.5 m s^{-1} and blows counterclockwise (Krall & Jähne, 2025).
In general, the facility is operated with fully deionized water, measurement campaigns with seawater and artificial seawater also been carried out. So, it is possible to use chemically sensitive measurement methods such as Fluorescence Imaging, which would not be suitable for field experiments. Additionally, the channel is thermally insulated with Styrodur® to enable measurements of heat exchange between air and water. This is accomplished using thermographic measurement methods (Kunz, 2017; Nagel, 2014). Another feature is that the Aeolotron's inner walls are coated with Teflon® foil

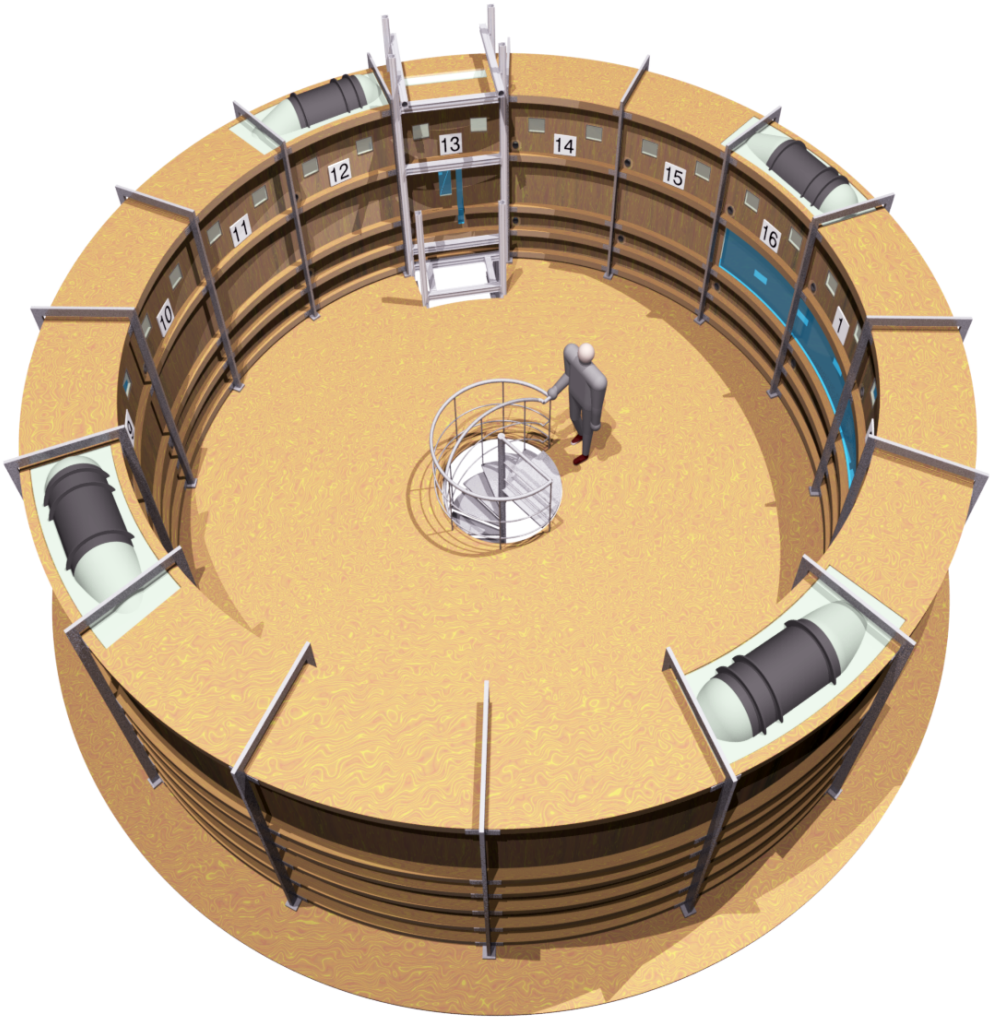

Figure 4.1: Heidelberg Aeolotron Wind-Wave Facility. Sketch modified after Krall (2013).

to prevent the adhesion of water-insoluble substances. This also allows measurements with chemical or biological surface films. Within the research on gas exchange, the Aeolotron is the largest annular wind-wave facility of its kind worldwide. On the one hand, its annular shape enables a theoretically infinite fetch of the wind over the water compared to linear wind-wave tunnels. As a result, the flow and wave fields are expected to be the same anywhere along the facility. On the other hand, wall effects of the curved channel cause secondary flows in wind and water, so that their flows deviate from realistically occurring flow profiles. In particular, there is no logarithmic wind profile in this system (Bopp, 2014).

As already noted, the Fluorescence Imaging technique is perfectly tailored for experiments in the Aeolotron. First, it is essential to utilize fully deionized water due to the sensitive chemical balance that the technique relies on. Second, the annular shape of the channel ensures that the measurement results are independent of the specific location along the circumference. The measuring section of this technique is located in segment 13, which is equipped with windows on roof, floor, and inner wall of the channel through which the fluorescence on the water surface can be excited or detected. More specifically, an illumination unit is installed on the roof of the Aeolotron that excites the fluorescence

in the mass boundary layer through the roof window and a multi-camera unit constructed below the channel to record the fluorescence signals through the floor window. An additional camera installed on the inner wall of the channel detects the fluorescence from the side through a third window. The complete overview of the installation of all used instruments in the Aeolotron is presented in Fig. 4.2. In addition, Fig. 4.3 shows a more detailed view on the measuring segment, especially regarding the setup of the illumination and recording system. A precise description of those main measuring devices is given in the following sections.

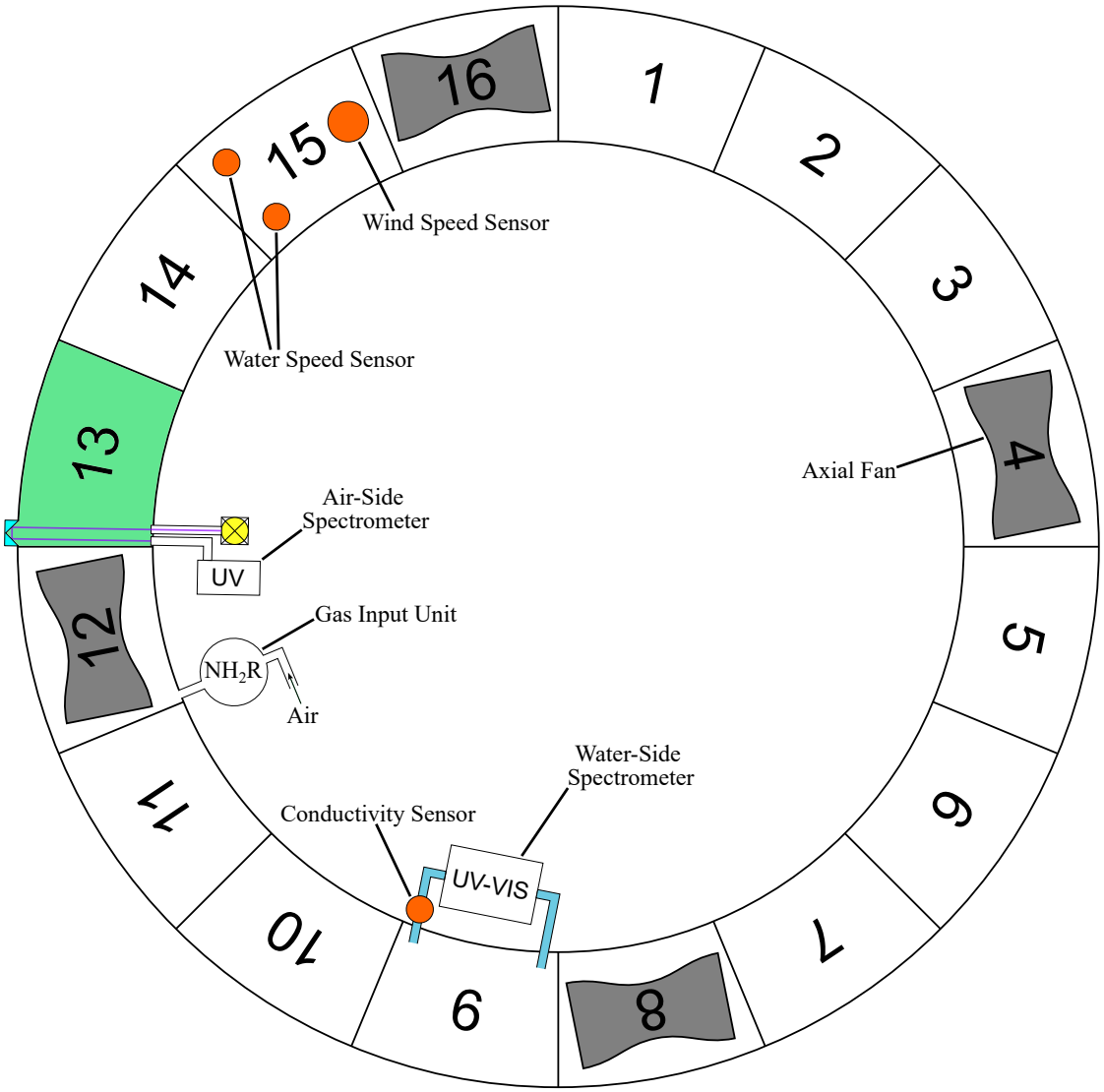

Figure 4.2: Instrumentation of the Aeolotron. The green marked segment 13 represents the measuring section, which contains the illumination and camera setup. For the sake of clarity, these are not depicted here.

4.1.2 Illumination Setup

As the fluorescence signal is generated only within a thin layer beneath the water surface, it requires high excitation intensities to obtain a significant fluorescence response. To achieve this, a high-performance illumination system was designed.

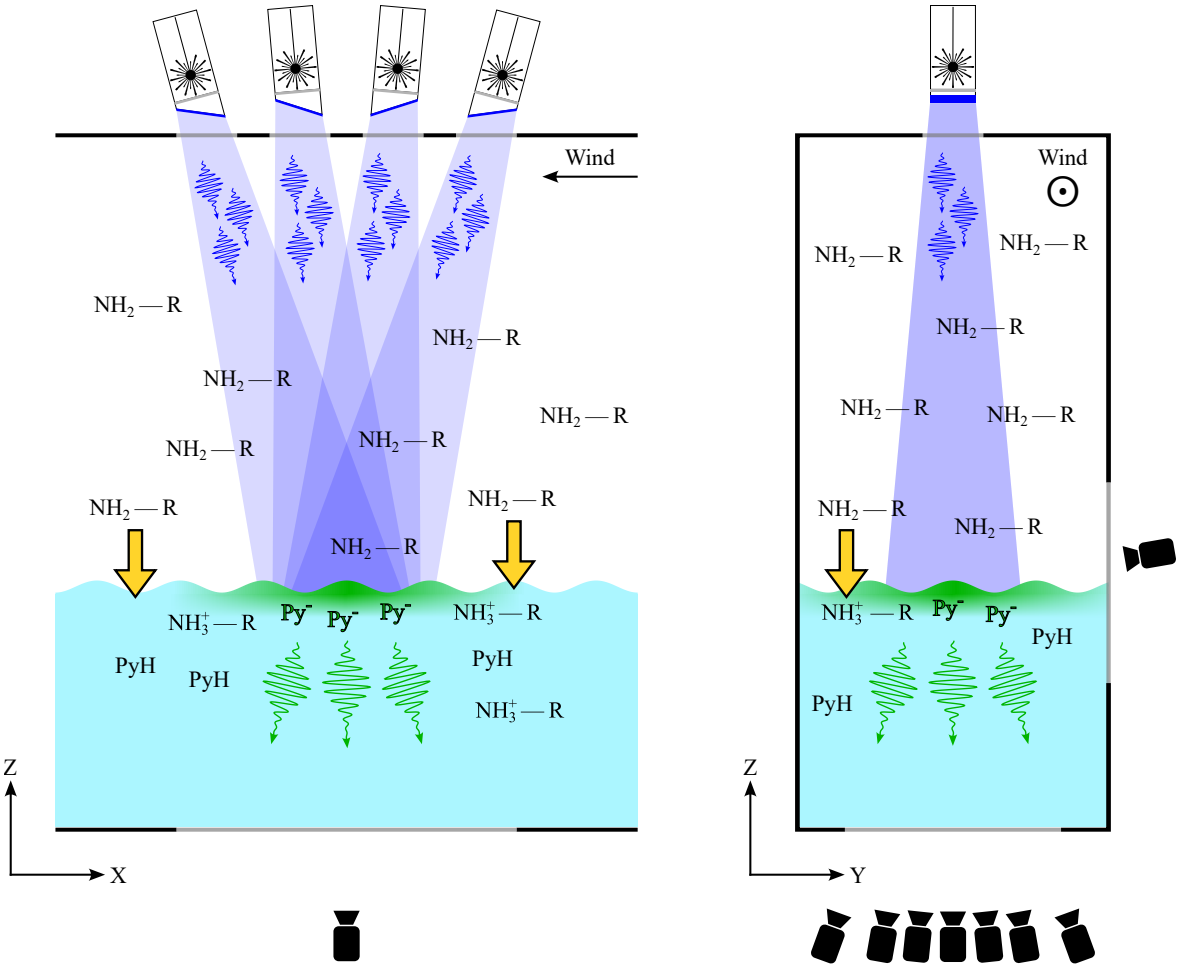

Figure 4.3: Laser array illumination and camera setups in longitudinal and transverse view of measuring segment 13. For better clarity, the laser line unit, positioned parallel to the laser array on the roof, as well as the height control stages of the cameras are not shown. In addition, the invasion of methylamine and the formation of pyranine's alkaline form are shown to demonstrate the method. The concentration ratios are obviously not correct. For better recognizability, the abbreviation Py is used here instead of I for pyranine.

Laser Array Illumination

This illumination setup consists of four laser light sources mounted on top of the facility. Each light source is equipped with two Nichia Blue Laser Diode Banks of type NUBM08, containing eight laser diodes with collimator lenses per bank. With 4 W output power per diode, the 16 laser diodes generate an overall power of 64 W per light source. To manage the generated heat, we use two Peltier elements and a CPU cooler for each laser array unit, whereby a temperature sensor regulates the system to prevent the temperature at the laser diodes from exceeding the ambient temperature by more than 5 °C. The laser light emitted from the diodes passes through two sequentially arranged holographic diffusers (Edmund Optics), made of polycarbonate. Both diffusers have a transmission efficiency of over 85 % and a scattering angle of 5°. This converts the initially coherent laser light into a broader, homogeneous LED-like illumination profile, while effectively suppressing the formation of speckles. At the end of the optical path, a DT Blue D50 mm short-pass filter is fitted, which

suppresses long-wavelength light above 458 nm that would otherwise interfere with the fluorescence signal. As a result, the spectral bandwidth of the laser light is limited to a range between 448 nm and 458 nm (Fig. 4.4), that coincides exactly with the absorption maximum of the alkaline component of pyranine (cf. Fig. 3.2). The DT Blue filter is positioned at an angle to avoid unwanted reflections in the fluorescence signals. If the filter would be positioned perpendicular to the optical axis, the fluorescent light emitted at the water surface could be reflected back onto the water surface by the filter, resulting in visible artifacts in the images. Its inclined orientation directs fluorescent light emitted to the channel's ceiling off the detection path. All four laser array units are collectively arranged with their individual light cones converging at the maximum water level of 1 m to form a single, focused illumination area. The cumulative optical power of all units amounts here to 256 W on a circular area of approximately 0.2 m^2, which is comparable to the optical power of the sunlight on the earth's surface.

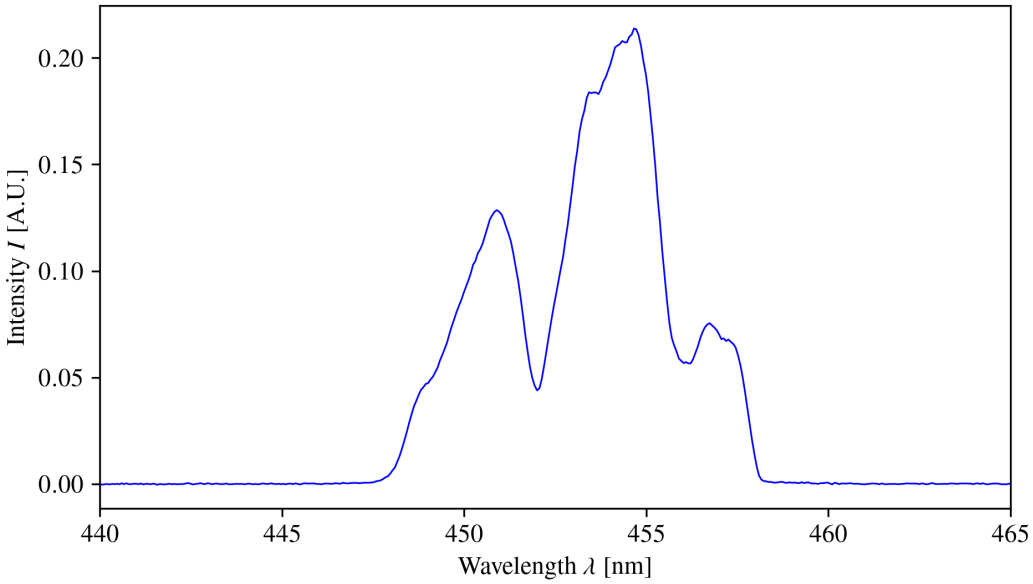

Figure 4.4: Emission spectrum of the laser array illumination system. Its spectral range extends between 448 nm to 458 nm with the maximum intensity at around $\lambda_{max} = 455$ nm.

Laser Line

Along with the primary laser array illumination system, a separate laser unit is installed on the facility's roof. This setup comprises a series of four additional laser diodes, each equipped with a cylindrical lens (Edmund Optics 47891 PCX 20 mm × 100 mm VIS, Edmund Optics 34659 CYL 12.7 mm × −25 mm VIS) to expand the point-shaped laser beam into a focused laser line. The four modules are aligned so that their laser lines merge into a single, seamless line on the water surface. The emission wavelength of the lasers ranges between 406 nm to 413 nm, which is close to the isosbestic point of pyranine, but clearly within the absorption range of its acidic component. Since this component is always present in sufficient concentration over the pH range of the measurements, the laser line remains visible in all image sequences. Thus, the laser line can serve for continuous detection of the water surface profile and as a reference for the fluorescence intensity.

4.1.3 Camera Setup

The camera setup was designed to record the dynamics of gas exchange with high spatial and temporal resolution. This combines a high-speed imaging array with a precise height measuring camera.

Camera Specifications

A total of eight industrial high-speed cameras are employed in the setup to capture the fluorescence signal generated at the water surface. We utilize the camera model ATX051S-MC from the manufacturer Lucid Vision, with a native resolution of 2448 px × 2048 px. However, in order to achieve the desired frame rate of 500 Hz, the effective sensor resolution is reduced to 1224 px × 960 px by applying 2 px × 2 px binning and cropping the image area. These settings increase the temporal resolution at the expense of spatial resolution while ensuring that the captured images can be processed and written to the hard disk in real time. The resulting effective pixel size of the sensor equals 5.48 µm × 5.48 µm, ensuring an optimal balance between spatial resolution and light collection efficiency. All cameras operate in Mono8 pixel format, storing grayscale images with a depth of 8 bits per pixel. This setting optimizes data storage while maintaining a sufficient dynamic range for the fluorescence signal. To further improve image quality and storage efficiency, gamma correction is applied to the sensor data. Normally, the relationship between the incident light intensity and the measured image brightness is linear. However, gamma correction introduces a nonlinear transformation, modifying this relationship as

$$I_{\text{out}} = I_{\text{in}}^{\gamma}, \tag{4.1}$$

where I_{in} and I_{out} are the normalized input and output intensities, respectively, which range in the interval between 0 and 1. We select the commonly used gamma correction factor of $\gamma = 0.5$, corresponding to a square root dependency. The key motivation for this correction relies on how the signal-to-noise ratio (SNR) changes with light intensity. Without correction, the acquired image signal is obviously proportional to the number of incident photons N. Concurrently, the photon noise follows a Poisson distribution where the standard deviation of the noise scales with the square root of the number of photons (Jähne, 2013). As a result, the SNR grows with increasing light intensity according to

$$SNR \propto \frac{N}{\sqrt{N}} = \sqrt{N}. \tag{4.2}$$

This implies that darker image regions inherently exhibit a lower SNR than brighter regions. To mitigate this, gamma correction scales the recorded intensities nonlinearly, expanding the range of grayscale values in dark areas and mapping them to higher brightness levels. This improves the perceptibility of details with low intensity and increases the overall image quality without having to extend the bit depth, as this would otherwise lead to significantly higher storage requirements. However, as this transformation changes the relationship between the recorded pixel values and the actual light intensities, an inverse gamma correction must be applied during further processing of the image data in order to restore the physically correct intensity distribution.

Optical Alignment

Seven cameras are installed in a linear array beneath the channel, observing the water surface through a window. This positioning below the facility was specifically chosen to minimize the reflections of the excitation laser light on the distorting water surface in the images. Each camera is equipped with a 25 mm Tamron lens of type 23FM25SP and an Edmund Optics band-pass filter BP525 × 92 nm-M30.5, which only transmits wavelengths approximately between 480 nm to 580 nm and thus partially suppresses the excitation light. The remaining laser light is further absorbed by tartrazine in the water bulk so that the cameras exclusively detect the fluorescence emissions. The focal lengths of the lenses are adjusted manually to an object distance between the scale values 1 m and infinity, with focusing on the water surface. In addition, the aperture is set to a value close to $f/5.6$ at which an approximately consistent brightness is achieved across all cameras. However, the manual setting of the lenses is inherently imprecise. To allow an exact determination of the intensity variations between the cameras, it is necessary to carry out a brightness calibration. The seven cameras are precisely tilted at angles of +6.6°, +3.2°, +1.6°, 0°, −1.7°, −3.6°, and −7.2° relative to the vertical optical axis to ensure that all of them capture the same field of view of the water surface. This configuration builds an optical setup similar to a light field array, which extends the depth of field and enables a 3D reconstruction of the recorded scene.
Additionally to the multi-camera array, an eighth camera is located at the inner wall of the Aeolotron, viewing the water surface from above through a side window. This camera is dedicated to tracking the laser line on the water surface and provides information about the wave field. It is mounted horizontally and uses a Canon 17 mm f4 FDn lens with a Fotodiox Shift Lens Mount Adapter to capture an oblique view on the water surface and give a clear and undistorted image of the laser line. The shift adapter is modified from a Sony mount to a C-mount to ensure compatibility with the camera system. The focal length of the lens is fixed to an object distance of 0.6 m, bringing the laser line into precise focus, while the aperture is set to $f/4$, which achieves sufficient exposure.

Height Control

Both the multi-camera array and the height camera are mounted on a motorized translation stage, enabling them to dynamically follow the waves. This tracking mechanism is particularly important at medium and high wind speeds, where significant vertical displacements of the water surface occur. On the one hand, this ensures that the water surface remains within the field of view of the height camera and, on the other hand, that the camera array keeps its focus on the water surface. The tracking system operates on the basis of the real-time position of the laser line, which is extracted from the images captured by the height camera. First, the center of mass of this segmented laser line is determined in the current image. Any deviation between the observed laser position and the reference position in the image center in vertical direction is then used to calculate a displacement correction. It was found for this correction that a shift of 10 px corresponds to approximately 1 mm. To account for the inertia of the system, the correction factor is set slightly higher than the actual absolute deviation. Furthermore, if the deviation exceeds 400 px, an even stronger correction factor is applied to prevent the laser line from moving out of the field of view. Finally, the calculated displacement correction

factor is transmitted simultaneously to the two translation stages via CAN communication ensuring synchronized movement of both camera systems. The available range of movement extends from 20 cm above to 15 cm below a reference height to which the stages are positioned at a water level of 1 m. Throughout the tracking, the linear stages continuously report their current positions, allowing for precise synchronization and logging of the camera system's movement.

4.1.4 Trigger and Control Unit

The trigger or control unit is responsible for synchronizing the illumination system with the camera acquisition. Its core is a circuit board equipped with a Teensy microcontroller. An external computer commands this microcontroller to initiate a predefined trigger routine which controls that both illumination and image capture run simultaneously.

System Architecture

In general, the control unit comprises the actual trigger box, which generates the synchronization signals, along with two additional boxes that manage the power supply for the illumination system. Both power supply boxes also use a Teensy microcontroller. The entire illumination system operates with a supply voltage of 37.5 V, with the power being divided over a total of nine channels, two channels for each of the four laser array units and one channel for the laser line. These channels are accurately regulated by a digital-to-analog converter (DAC) via an SPI interface, allowing fine tuning of the brightness or current in each channel. All laser array channels are always set to their maximum permissible values (4095/4095) in order to generate sufficient fluorescence intensity. Under this full load, the laser array draws a total current of 2 A. In contrast, the laser channel is current capped at 800/4095, as this produces sufficient intensity for the laser line's visibility.

Trigger Routine

In response to a command received from the computer, the microcontroller releases a trigger routine to activate the illumination and camera systems. This trigger routine is depicted in Fig. 4.5. In principle, the cameras are configured to start recording images 20 µs before the onset of the illumination pulse and to continue for 20 µs after its termination. This strategy guarantees that the entire period of light emission is recorded. As a rule, all pulses are kept short enough to accumulate sufficient light while minimizing the risk of motion blur. Specifically, the multi-camera array is set with an exposure time of 290 µs and the height camera with 90 µs. The trigger sequence is divided into two phases:

1. Multi-Camera Array: Simultaneous pulses activate the laser array illumination for 250 µs and the laser line for 20 µs. In this phase, the multi-camera array records the fluorescence signal while the laser line also appears in the image sequences.

2. Height Camera: After a short delay, a second pulse triggers the laser line again for 50 µs and the height camera records the corresponding signal from the water surface.

The temporal separation of the two phases ensures that the fluorescence signal from the laser array excitation does not interfere with the laser line signal used for the height measurement. In order to

verify the correct operation of the system with regard to complete image acquisition, the laser line pulse is deliberately omitted every 100th trigger cycle. The resulting images with missing laser lines serve as a sequence check and facilitate the subsequent assignment of image sequences in case of missing images.

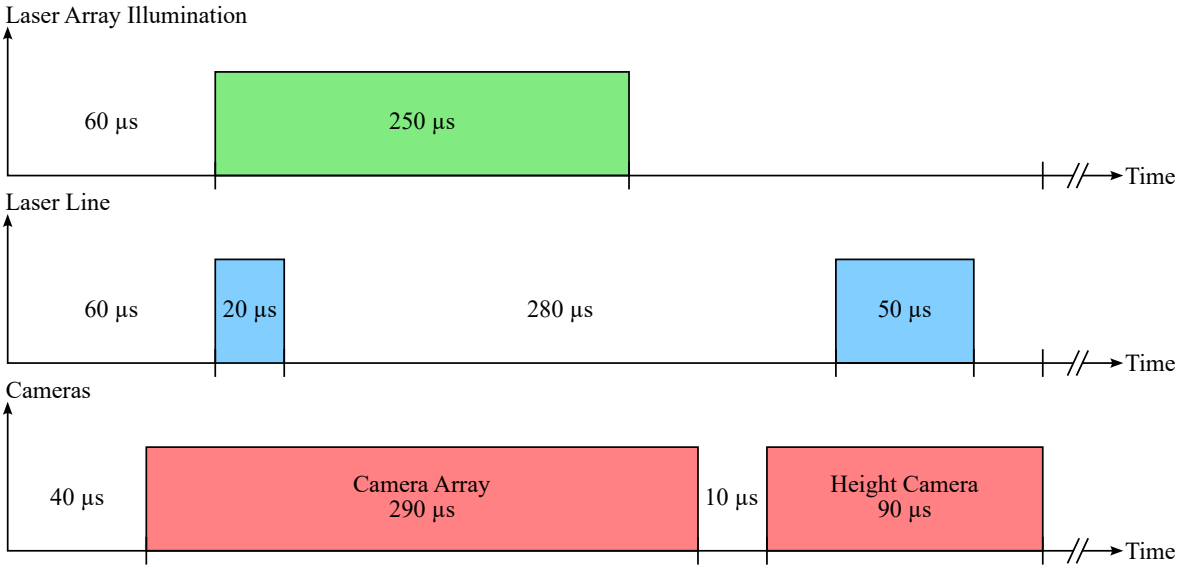

Figure 4.5: Trigger routine for laser array illumination, laser line, and camera setups. The width of the pulses is not to scale, only the synchronicity is indicated. The trigger scheme runs at a frequency of 500 Hz.

4.1.5 Gas Input Unit

The injection of methylamine into the air space of the Aeolotron happens through a gas washing bottle and a mass flow controller, both connected in series via tubes. First, the gas washing bottle is partially filled with sand that is wetted with a 40 % aqueous solution of methylamine and thus contains the actual gas. Second, the mass flow controller, positioned upstream, regulates the inflow of dry air into the bottle. When the air flows through the sand bed, the methylamine transitions from the aqueous phase into the gas phase and is then transported into the channel via an outlet tube. This gas input unit is located in segment 12, directly downwind of the axial fan. As a result, the methylamine-loaded air travels through an almost complete cycle before it reaches the measuring section, ensuring the highest possible mixing and homogeneous distribution of the trace gas.

4.1.6 Air-Side UV Spectrometer

A UV absorption path is installed on the air side to monitor the concentration of methylamine in the channel's atmosphere. It consists of a Hamamatsu 2W xenon flash lamp with UV window operating at a frequency of 10 Hz, a Maya2000Pro spectrometer, and a retroreflector (Fig. 4.6). Both the xenon lamp and the spectrometer are mounted on the inner wall of the measuring segment 13, while the retroreflector is positioned opposite on the outer wall. The xenon flash lamp emits UV light in the spectral range of 189 nm to 294 nm, passing through a set of lenses into the Aeolotron and reflected back by the retroreflector. An optical fiber captures the returning light and guides

it into the Maya spectrometer, where the light is projected onto an image sensor and produces a transmission spectrum of the excitation light. The spectrometer acquires spectra with an exposure time of 20 ms. Two consecutive spectra are always averaged to reduce noise, resulting in a single average spectrum. Operating at a sampling rate of 10 Hz, the spectrometer provides 10 of these averaged transmission spectra per second, allowing a high-resolution concentration monitoring. Depending on the corresponding gas content within the beam path, a change in the transmission spectra occurs (cf. Sec. 2.3). By comparing the pure lamp spectrum with the transmission spectra recorded in the presence of methylamine, the absorption spectrum of the trace gas can be determined, which enables a calculation of the gas concentration. As the light traverses the channel width twice, the effective absorption path length in this setup is 123.0 cm. There are two interchangeable probe holders at different heights available for the UV absorption path. These are located approximately 45 cm and 90 cm above the water surface and allow flexible vertical positioning of measurements to different wave heights.

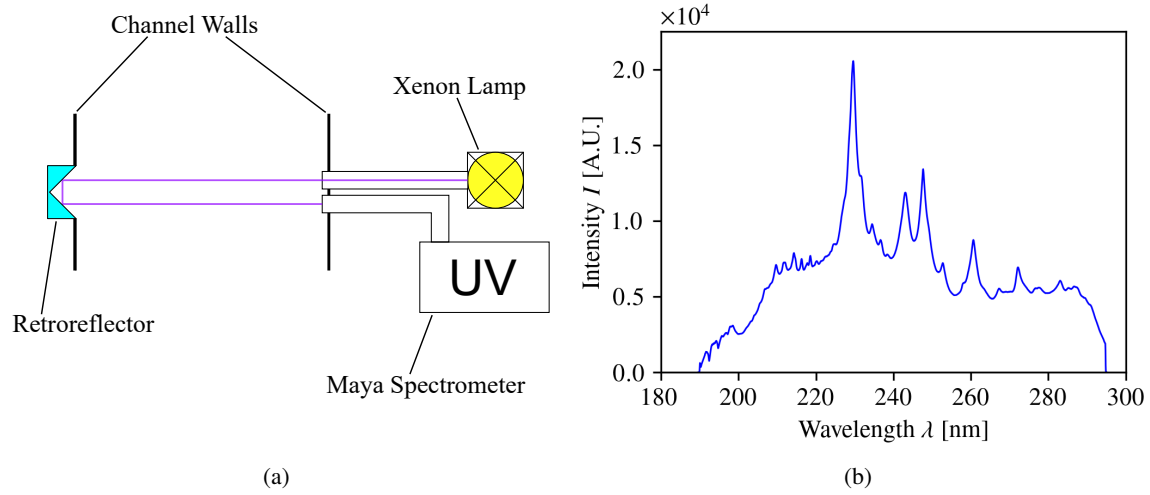

Figure 4.6: Air-side UV absorption setup. (a) UV absorption path in cross-section for measuring the gas concentration in the air space of the Aeolotron. (b) UV lamp spectrum of the xenon flash lamp.

4.1.7 Water-Side UV-VIS Spectrometer

A second spectrometer setup measures the UV-VIS absorption of the two dyes in the water phase. This unit comprises a Shimadzu UV-2700 dual-beam spectrometer integrated into a secondary water circuit branching off from the bottom of the Aeolotron in segment 9. Its primary purpose is to determine the proportions of the acidic and alkaline forms of the dye based on their absorption spectra, providing information on the pH value. The spectrometer records spectra of the tank water in a spectral range from 200 nm to 550 nm with a resolution of 0.5 nm. Its internal grating slit width is set to 1 nm. Water sampling is carried out either via a sipper unit or a flow cell. The sipper unit draws discrete water samples from the bypass circuit for spectral measurement under precisely defined and stable concentration conditions. In contrast, the flow cell operates under constant water flow and enables continuous, time-resolved spectral monitoring of the absorbance. Both systems use a cuvette with a

path length of 1 cm. Additionally, the bypass circuit contains a conductivity probe for measuring the electrical conductivity of the sampled water.

4.1.8 Instrumentation of Environmental Variables

In addition to the central measuring systems described up to this point, there are a number of other sensors in the Aeolotron that measure environmental variables such as wind and water speed, temperature, pressure, or humidity. Among the most important units are the sensors for measuring the wind speed. On the one hand, there is a Pitot tube located on the inner wall of segment 14, and on the other hand, an ATMOS 22 ultrasonic anemometer is attached to the ceiling of segment 15. Both devices measure the wind speed in different ways. While the Pitot tube detects the difference between the static atmospheric pressure and the wind-induced dynamic pressure, the ultrasonic probe determines the sound propagation time in different directions. It is important to note that the two measuring devices do not produce comparable wind speed data, as the measurements are taken at different positions while there is no homogeneous wind field in the channel (Bopp, 2014). Furthermore, the wind speeds cannot be converted to reference speeds from other wind tunnels, as the Aeolotron does not have a logarithmic wind profile due to secondary currents, unlike it exists in linear wind-wave channels or in field studies. Therefore, these wind speeds can only be considered as a reference for the Aeolotron. Instead, the wind speeds in the Aeolotron are usually given in the more reproducible form of the wind control frequency of the axial fans. Another important sensor system are two Höntzsch vane anemometers located at the bottom of segment 15 to measure the water speed. Normally, the wind-induced water flow is minimal at the channel's floor. Therefore, the measured water speed represents a lower limit. A variety of other sensors are located in segment 15 and include two Pt1000 temperature probes on both the air and water sides, a Bosch BMP 390 pressure sensor on the air side, and a HYT939 humidity sensor as well as a Presens Oxybase oxygen sensor to monitor the relative humidity and oxygen content in the air.

4.2 Measurements

Within the Fluorescence Imaging measurement campaign, systematic experiments were carried out at the Aeolotron over a total of 6 weeks between November 2023 and September 2024. These measurements cover the entire realizable wind speed regime of the facility, classified into low, moderate, and high wind speeds (Tab. 4.1). The experiments at low wind speeds in the first three measurement weeks also include measurements of gas exchange under the influence of surface films. Both insoluble films of hexadecanol and olive oil as well as soluble films of Triton X-100 are used. Additionally, two measurements are carried out with reduced surface tension achieved by adding hexanol and one measurement with a heavy atmosphere by replacing the air with argon. The experiments at high wind speeds are supplemented by measurements with a seawater model in addition to the standard measurements. Here, the bubble-induced gas exchange is the primary subject of investigation. A complete overview of all measurement series carried out with the corresponding conditions is listed in Tab. A.2 (see Appendix A.2). The following sections provide a more detailed explanation of the exact procedure and measuring conditions of the experiments.

Table 4.1: Classification of the wind control settings

Wind Control Frequency [Hz]		
Low Regime	Moderate Regime	High Regime
5.0	17.8	31.7
5.6	20.0	35.6
6.3	22.4	40.0
7.1	25.2	44.9
7.9	28.3	50.0
8.9		
10.0		
11.2		
12.6		
14.1		
15.9		

4.2.1 Preparatory and Post-Experimental Procedures

At the beginning of each measurement week, we prepare a new tank load of deionized water for the Aeolotron. Initially, the corresponding amounts of pyranine and tartrazine are dissolved in the water. In weeks 1 to 4 the pyranine concentration is adjusted to about $5 \cdot 10^{-5}\,\mathrm{mol\,L^{-1}}$, in weeks 5 and 6 it is raised to $7.5 \cdot 10^{-5}\,\mathrm{mol\,L^{-1}}$. Whereas the tartrazine concentration remains constant at about $2 \cdot 10^{-5}\,\mathrm{mol\,L^{-1}}$ for all measurements. The exact dye concentrations will be determined using the water-side UV-VIS spectroscopy setup. In the second step, the water is acidified by adding hydrochloric acid. Approximately 250 mL of 1 M HCl are required to reduce the pH value of the tank water to around 5. The preparatory work for each measurement day begins with recording dark and zero sequences for each camera. A dark sequence is taken by covering the camera lenses in order to determine the devices' background current. The zero sequence is recorded with the covers removed, capturing a sequence of the completely flat water surface, preferably at an exact water level of 1 m. On the one hand, this serves to detect the brightness of the background fluorescence in the acidic range as well as to identify the exact position of the laser line in the image. Additionally, a dark and a lamp spectrum are acquired with the air-side UV absorption path. Since the xenon lamp exhibits thermal instability, it must be preheated for at least two hours to ensure a stable lamp spectrum. The lamp spectrum is regularly updated throughout the measurement day to minimize intensity variations. Subsequently, background and zero spectra are measured with the water-side UV-VIS spectrometer. A background spectrum is acquired with a sample of fully deionized water to obtain a baseline for the absorbance. The zero spectrum is then recorded by measuring the tank water. This provides information on the initial dye concentration in the acidic pH range. In addition, the pH value of the tank water is checked manually with a pH electrode to ensure consistency. Before starting the actual measurements, the water surface is cleaned with a skimmer for about 30 min to remove any surface films. All gas exchange measurements are carried out with the channel closed.

The experiments are run sequentially, with the pH value of the tank water gradually increasing due to the successive gas input. In measurement series with high wind speeds, involving larger gas fluxes,

the tank water must be re-acidified between individual recordings by adding hydrochloric acid. This is necessary to restore sufficient contrast in the fluorescence patterns, which would otherwise degrade as the pH value increases. An exact procedure of the Fluorescence Imaging experiments is given in the following section. Along with the primary gas invasion experiments, the measurement series are occasionally supplemented by brightness or calibration measurements at the end of a measurement day. In brightness measurements, a sequence of the flat water surface is acquired analogous to the zero sequence for determining the overall background image brightness. In parallel, a UV-VIS spectrum of the tank water is recorded. These data allow a later correlation of the image brightness with the concentration of the alkaline form of pyranine. When performing calibration measurements, a reference target with a known geometric pattern is placed on the flat water surface and imaged while the exact water level is documented. These calibration data are used for a subsequent geometric mapping of the image data. Details on the use of brightness and calibration measurements are provided in Secs. 5.4.2 and 5.4.3.
At the end of each gas exchange measurement series, a final UV-VIS spectrum of the tank water is recorded and the pH value is measured again with a pH electrode. In the last step of each measurement day, the tank water is acidified again by adding hydrochloric acid to reduce the pH value to approximately 5, thus preparing the system for the next day's measurements.

4.2.2 Measurement Procedure

An actual gas exchange measurement is performed by running a predefined wind scheme while injecting a controlled amount of methylamine into the channel's air space. The ongoing gas exchange is recorded with the Fluorescence Imaging setup, and spectra are simultaneously acquired with the air-side UV absorption setup and the water-side UV-VIS spectrometer. In principle, acquisition of the air-side UV spectra starts immediately with the onset of methylamine injection and continues throughout the experiment. The water-side UV-VIS spectral measurements depend on the used sampling system. When utilizing the sipper unit, a single water sample is collected at the end of the experiment, from which a total of three spectra are acquired. In contrast, with the flow cell, spectra acquisition is initiated approximately 30 s after the start of the gas exchange experiment with ten consecutive spectra recorded over the course of the measurement.
The wind program follows one of two selected schedules, which are explained in more detail here:

Equilibrium Mode The Equilibrium mode refers to measurements in which the wave field has reached equilibrium with the wind when the measurement is started. This requires the wind to be switched on at least 20 min before starting the measuring process. Usually, measurements are taken under equilibrium conditions for about 5 min to 10 min after which the wind is switched off for a short time and then switched on again. Additional switching off and on is applied in order to also capture the dynamics of the decaying and subsequently redeveloping wave field.

Fetch Mode The Fetch mode means measuring the fetch dependency by applying the wind just at the start of the measurement. In this case, the waves are first brought into equilibrium with the wind and switched off about 15 min prior to starting the measurement. After these 15 min, the waves have

dissipated while the water bulk is still in motion. When measuring has started, the wind is switched on to measure the wave field as it builds up for about 5 min to 10 min, followed by switching the wind off for a few minutes and back on again for the purposes mentioned above.

For gas injection, a certain volume of a 40 % aqueous methylamine solution is added to the gas washing bottle prior to each measurement so that the sand packing is just completely wetted with liquid. The gas input flow is regulated by means of the mass flow controller applying two different methods:

1. Constant Mass Flow Method (Week 1): A constant mass flow rate is applied over a time interval of approximately 30 s to 50 s. After this, the mass input is stopped.

2. Regulated Mass Flow Method (Week 2–6): A target UV spectrum from a previous measurement is chosen as a reference. While the experiment is running, the difference between the measured UV spectrum and the reference spectrum yields a correction factor for the mass flow controller, which dynamically adjusts the gas input. This approach aims to maintain a relatively stable methylamine concentration in the air and thus ensure a constant concentration difference between air and water. The correlation between the deviation from the target spectrum and the correction factor for the mass flow controller is based on empirical data from preliminary tests. In the majority of measurements, we stop the gas input shortly before switching off the wind to monitor the decrease of the air-side gas concentration while equilibrium conditions still prevail. This procedure guarantees getting reliable data on the dynamics of the air-side gas exchange, as it allows the assessment of the gas concentration decrease without additional external inputs.

After each measurement, the total amount of injected methylamine is determined by weighing the gas washing bottle. Generally, it is crucial to only inject gas during active wind, because this guarantees sufficient mixing and prevents the formation of local accumulations in the input segment. Fig. 4.7 summarizes the exact time schedule with regard to wind control and gas input for the two measuring modes.

4.2.3 Measurement Conditions

Apart from the standard measurements with clean deionized water at various wind speeds, additional measurement conditions were considered in the campaign. These are explained in more detail below.

Surface Film The surface film studies encompass gas exchange experiments with three different surfactants: the two water-insoluble agents hexadecanol and olive oil, as well as the frequently used water-soluble substance Triton X-100. To apply the insoluble films on the surface, these substances have to be dissolved in ethanol beforehand. We prepared solutions of 1.02 g hexadecanol to 200 mL ethanol and 1.00 g olive oil to 200 mL ethanol. Using a syringe, 8.0 mL of one of these solutions was evenly dosed onto the previously skimmed water surface of the channel. Complete suppression of the waves was observed with the hexadecanol film at 6.5 mL and with olive oil at 5.0 mL. The advantage of these insoluble films is that they could be easily removed by skimming off the water surface after a

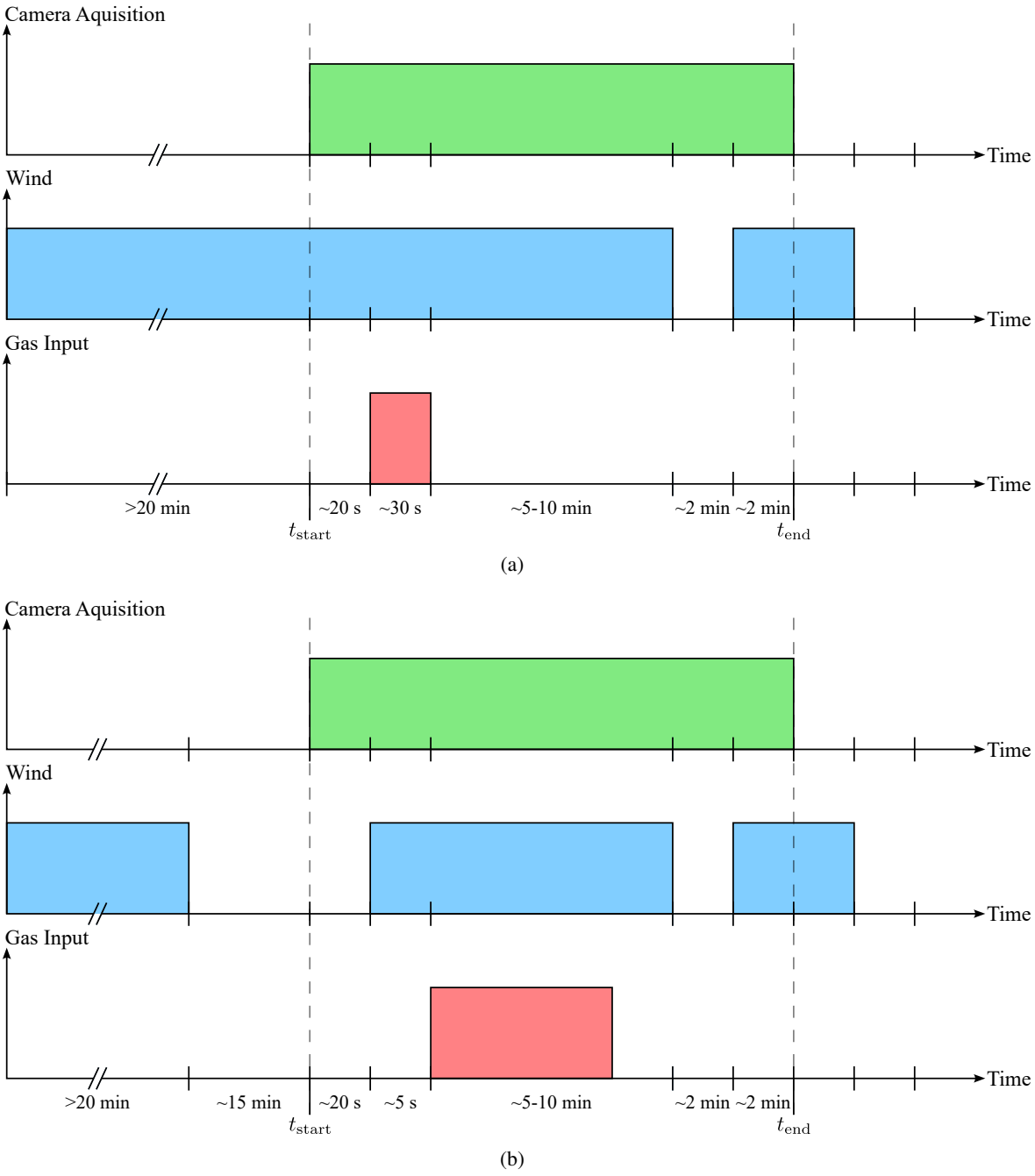

Figure 4.7: Measurement schedule for (a) equilibrium mode and (b) fetch mode. The time specifications are approximate. Note that in equilibrium mode the gas input may take longer than 30 s, depending on whether measurements are taken with constant mass input or controlled mass input. In fetch mode, the gas input is always controlled.

measurement day. In contrast, the soluble film was applied simply by mixing Triton X-100 in the tank water. For this purpose, 101.4 g Triton X-100 was premixed in 2 L water and added to the channel. As the substance dissolves completely in the water, the tank load was disposed of after the measurement day.

Surface Tension In these experiments, we examined the effect of surface tension on gas exchange. Here, a larger amount of hexanol was added to the tank water, which reduces the water's surface tension. It was measured with the two different hexanol concentrations $1 \cdot 10^{-2}\,\mathrm{mol\,L^{-1}}$ and $2 \cdot 10^{-2}\,\mathrm{mol\,L^{-1}}$. The associated surface tension was determined on a water sample by means of a bubble pressure tensiometer (Krüss BPT Mobile). We found a decrease in surface tension from $72\,\mathrm{mN\,m^{-1}}$ to $52\,\mathrm{mN\,m^{-1}}$ at the low concentration and from $72\,\mathrm{mN\,m^{-1}}$ to $45\,\mathrm{mN\,m^{-1}}$ at the higher concentration.

Atmosphere This study investigates the impact of a heavy atmosphere on gas exchange by injecting the noble gas argon into the channel's air space as a partial substitute for air. The proportion of argon in the channel's atmosphere was monitored by measuring the oxygen concentration in the air. Two different atmospheric compositions were tested, one with atmospheric oxygen reduced to 11.0 % and one with the oxygen reduced to 7.5 %.

Sea Water The seawater experiments examined gas exchange with seawater model. To simulate the bubble characteristics of seawater, butanol was added to the tank water. Previous experiments have shown that a butanol-water mixture exhibits a bubble spectrum comparable to that of seawater (Krall, 2013). A quantity of approximately 1 L butanol was dissolved in the tank water to achieve the desired bubble effect. The surface tension was measured with a bubble tensiometer to ensure that the added butanol does not significantly change this property.

4.2.4 Setup Modifications

Throughout the measurement campaign, several modifications to the experimental setups were necessary. These changes were made either to adapt the system to varying measurement conditions or to address technical issues that arose with certain measurement units. Specifically, the adaptations concern the illumination system, the air-side UV absorption setup, and the water-side UV-VIS absorption spectrometer. The following section presents an overview of these essential changes assigned to the different measurement weeks in Tab. 4.2 as well as a detailed explanation of the modifications. It is important to consider these modifications when analyzing the collected data, as they may influence the way we process the data, as well as the comparability of the results across different phases of the measurement campaign.

Table 4.2: Modifications of the setups

Measurement Week	Illumination Setup	Air-Side UV Absorption Setup	Water-Side UV-VIS Absorption Setup
1 2	4 Laser Units	Lower Path Position	Sipper Unit
3 4	2 Laser Units	Upper Path Position	Flow Cell Unit
5 6	4 Laser Units	Upper Path Position	Flow Cell Unit

Illumination Setup In measurement weeks 3 and 4, due to a malfunction in the power supply of the control unit, the outer laser array modules had to be deactivated. Consequently, only two of the four laser array modules were operational during this period, resulting in reduced overall illumination intensity.

Air-Side UV Absorption Setup At low wind speed, the lower probe position is used. However, at higher wind speeds, the beam path must be elevated to the upper position to avoid interference from wave formation and water spray, which could distort the optical path.

Water-Side UV-VIS Absorption Setup In the first two measurement weeks, a sipper unit was used as no significant concentration changes of the dyes in the water were expected. From week 3 to 6, a flow cell was implemented to capture rapid concentration changes at higher wind speeds and gas injection, allowing continuous measurement and dynamic tracking of concentrations during the experiment.

4.2.5 Measurements of Friction Velocities

Since the wind speeds adjustable in the Aeolotron (cf. Tab. 4.1) are specified in terms of wind control frequencies, a system-specific parameter, comparisons of measurement results with data from other wind-wave facilities or field studies are limited when using this parameterization. It is therefore essential to additionally determine the friction velocity for all measurements in order to enable a more general and transferable parameterization of the results.
This quantity is measured using a thermographic measurement technique applied in parallel to the Fluorescence Imaging experiments. In this method, a narrow line is heated on the water surface perpendicular to the wind direction using a near-infrared laser. The downstream transport of the thermal pattern by the surface shear current is then recorded with an infrared camera. Based on these data, the friction velocity is determined using an image processing algorithm based on a modified version of the approach in Voigt (2021). The corresponding friction velocity values for the different experiments are provided by B. Jähne and are listed in Tab. A.3 (see Appendix A.3). Due to the increased complexity of image processing at higher wind speeds, only values for the experiments of measurement week 1 are currently available.

5 Data Processing

In the Fluorescence Imaging studies, we collect three different types of data sets: air-side UV spectroscopic data, water-side UV-VIS spectroscopic data, and the key image data. Obviously, the high-speed image sequences make up almost the entire amount of data, while the spectroscopic data sets are comparatively small. However, each data set plays a crucial role in the overall analysis of gas exchange. This chapter outlines the data processing workflow, detailing the extraction of gas concentrations from UV spectra, the determination of dye concentrations from UV-VIS spectra, and the preprocessing and calibration steps of image sequences to convert raw data into physically meaningful fluorescence values. Supplementary to this, the first subsection describes reference measurements, which are required for many of these evaluations.

5.1 Reference Measurements

Beyond the primary gas exchange experiments, we conduct a series of reference measurements to obtain comparative data for calibration. These include reference spectra for both UV and UV-VIS spectroscopy as well as conductivity measurements to determine the diffusion constant of pyranine.

5.1.1 UV Reference Spectra

In order to calibrate the UV absorption system, it is necessary to record a reference spectrum for a known gas concentration of methylamine. Based on this spectrum, the gas concentrations can be conversely derived from the measured UV spectra of the experiments. The reference measurement is carried out in the closed Aeolotron without water to ensure a controlled, constant gas concentration in the air space by minimizing gas losses due to dissolution in the water. Additionally, the wind is set at 10 Hz to guarantee adequate mixing of the air volume.
Initially, we record dark and lamp spectra. Methylamine is then introduced into the channel via the gas injection unit, consisting of gas washing bottle and mass flow controller. The air flow into the gas washing bottle is set to a constant rate of $5\,\mathrm{L\,min^{-1}}$ to inject methylamine into the channel over a defined injection period of 60 s, while time-resolved spectra are recorded via the UV absorption path. Spectral acquisition continues for a total duration of 5 min. By means of dark and lamp spectra, the time-resolved intensity spectra are converted into absorption spectra. The detailed procedure for extracting these spectra is explained in Sec. 5.2.1.
In order to determine a representative reference spectrum from the time-resolved UV absorption data, we first identify the spectrum exhibiting the maximum mean absorption. It is assumed that this point corresponds to the time at which the entire injected amount of methylamine has reached the air volume, meaning any retardation effects from the injection phase are minimized. To further

mitigate the influence of spatial and temporal inhomogeneities, all spectra within a symmetrical time window comprising 20 time points before and after the maximum are averaged. Each time point contains the average of 10 consecutive spectra, resulting in a total of 400 spectra contributing to the final reference spectrum. The choice of this averaging window ensures that the gas distribution has stabilized over time, while losses from possible leakages are negligible temporally. In addition, the window is sufficiently long to compensate for short-term fluctuations in lamp intensity (Kühn, 2022) and gas concentration. This yields a solid and representative absorption spectrum for methylamine (Fig. 5.1).

The corresponding reference gas concentration in the channel is determined by weighing the mass loss m_{gas} of methylamine in the gas washing bottle. Using the molar mass of methylamine M_{gas} and the total volume V_{tot} of the Aeolotron without water, we obtain the following reference concentration

$$c_{\text{ref}} = \frac{m_{\text{gas}}}{V_{\text{tot}} M_{\text{gas}}} = \frac{1.55\,\text{g}}{(43400\,\text{L}) \cdot (31.06\,\text{g} \cdot \text{mol}^{-1})} = 1.15 \cdot 10^{-6}\,\text{mol} \cdot \text{L}^{-1}. \tag{5.1}$$

In order to account for uncertainties in the channel volume and the mass input, a relatively high uncertainty of $\Delta m_{\text{gas}} = 0.2\,\text{g}$ is assumed, corresponding to $\Delta c_{\text{ref}} = 1.48 \cdot 10^{-7}\,\text{mol}\,\text{L}^{-1}$. The reference spectrum in combination with the specified gas concentration c_{ref} serves as calibration basis for the quantitative analysis of methylamine concentrations in all subsequent measurement data.

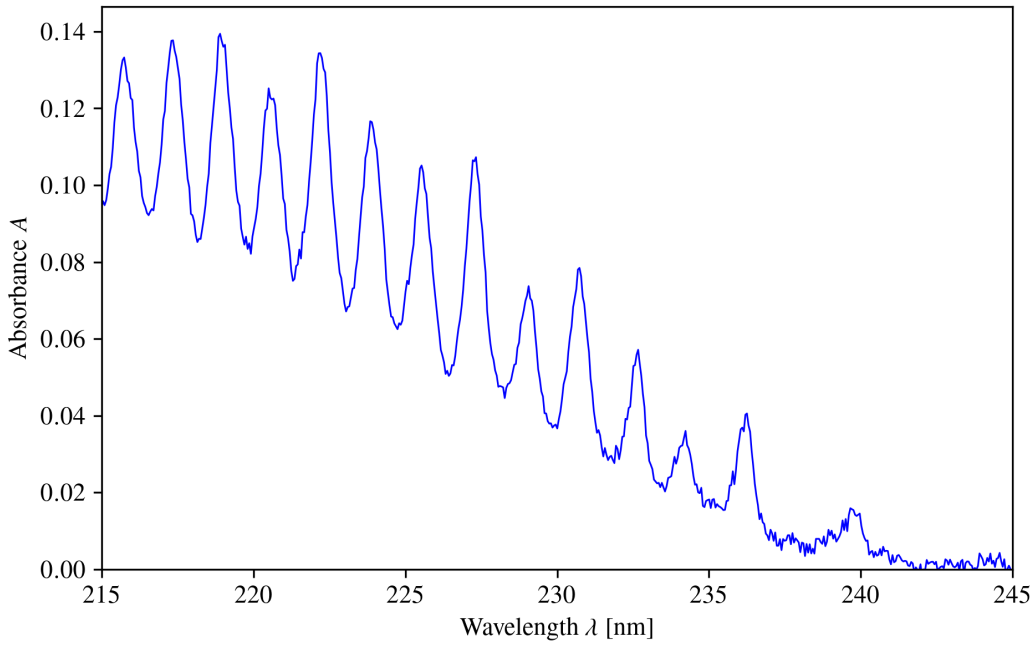

Figure 5.1: Reference absorption spectrum for methylamine. The reference gas concentration in the air is $1.15 \cdot 10^{-6}\,\text{mol}\,\text{L}^{-1}$ and the optical path length measures 123.0 cm.

5.1.2 UV-VIS Reference Spectra

Calibrating the UV-VIS spectroscopy setup involves measuring reference spectra for the dyes pyranine and tartrazine in aqueous solutions with known concentrations. An initial stock solution of pyranine

is prepared for this by dissolving 674 mg of the dye with purity of 78 % (Lanxess Pyranin 120 %) in 1 L of deionized water. By further diluting 100 mL of this solution to 1 L with deionized water, a stock solution with a concentration of $1.29 \cdot 10^{-4}\,\mathrm{mol\,L^{-1}}$ is adjusted. From this solution, subsamples are adjusted to different integer pH values between 3 and 12 by adding 1 M HCl or 1 M NaOH.
First, a blank measurement with deionized water is taken with the UV-VIS spectrometer setting its absorbance to zero. Then, the individual pyranine samples are measured under the same conditions. The resulting spectra, shown in Fig. 3.2, correspond directly to the absorption spectra of pyranine. It is assumed that pyranine exists exclusively in its protonated form at pH < 4 and in its deprotonated form at pH > 11. Consequently, the spectra at pH ≈ 3 and pH ≈ 12 are selected as reference spectra for the acidic and alkaline forms, respectively. All other spectra represent combinations of the absorption spectra of these two species, weighted according to their respective concentrations. Applying Eq. (2.70), the absorption spectrum $A_{\mathrm{I}}(\lambda)$ at a given pH value can be expressed as

$$A_{\mathrm{I}}(\lambda) = c_{\mathrm{IH}} A_{\mathrm{IH}}(\lambda) + c_{\mathrm{I^-}} A_{\mathrm{I^-}}(\lambda), \tag{5.2}$$

where $A_{\mathrm{IH}}(\lambda)$ and $A_{\mathrm{I^-}}(\lambda)$ are the reference spectra of the protonated and deprotonated forms, while c_{IH} and $c_{\mathrm{I^-}}$ are the relative concentrations of each species. This equation serves as a fit function to extract the relative concentrations of two components from any measured spectrum.
A further analysis allows to validate the pK_a value of pyranine. This is done by fitting the collected spectra according to Eq. (5.2) to calculate the concentrations of acidic and alkaline species at each pH value. The fit interval is chosen between 330 nm to 510 nm. Assuming the total concentration remains constant, the following relations, obtained from the rearranged Henderson–Hasselbalch equation, hold

$$[\mathrm{I}]_{\mathrm{tot}} = [\mathrm{IH}] + [\mathrm{I^-}], \tag{5.3}$$

$$[\mathrm{IH}] = \frac{[\mathrm{I}]_{\mathrm{tot}}}{10^{-\mathrm{p}K_a(I)+\mathrm{pH}} + 1}, \tag{5.4}$$

$$[\mathrm{I^-}] = \frac{[\mathrm{I}]_{\mathrm{tot}}}{10^{-\mathrm{pH}+\mathrm{p}K_a(I)} + 1}. \tag{5.5}$$

By plotting the concentrations of the two species against the pH values and fitting the above Eqs. (5.4) and (5.5) to the data, we obtain the pK_a value of pyranine. The results of this analysis are summarized in Fig. 5.2, which yields a value of $\mathrm{p}K_a(\mathrm{I}) = 7.9547 \pm 0.0027$, corresponding to the average value obtained from independent fittings for both species.
Analogous measurements are performed for tartrazine. This is done using a stock solution with concentration of $1.00 \cdot 10^{-4}\,\mathrm{mol\,L^{-1}}$ prepared with 534 mg of tartrazine dissolved in 1 L of deionized water, followed by dilution of 100 mL to 1 L. The spectroscopic measurements follow the same procedure as for pyranine, except that pH values between 5 and 12 are adjusted for the sample solutions due to the higher pK_a value. The resulting spectra, as shown in Fig. 5.3, reveal that the spectra at pH ≈ 5 and pH ≈ 12 serve as suitable reference spectra for the acidic and alkaline forms. Subsequent analysis of the spectral data lead to a pK_a value of $\mathrm{p}K_a(\mathrm{T}) = 9.9856 \pm 0.0253$ for tartrazine.

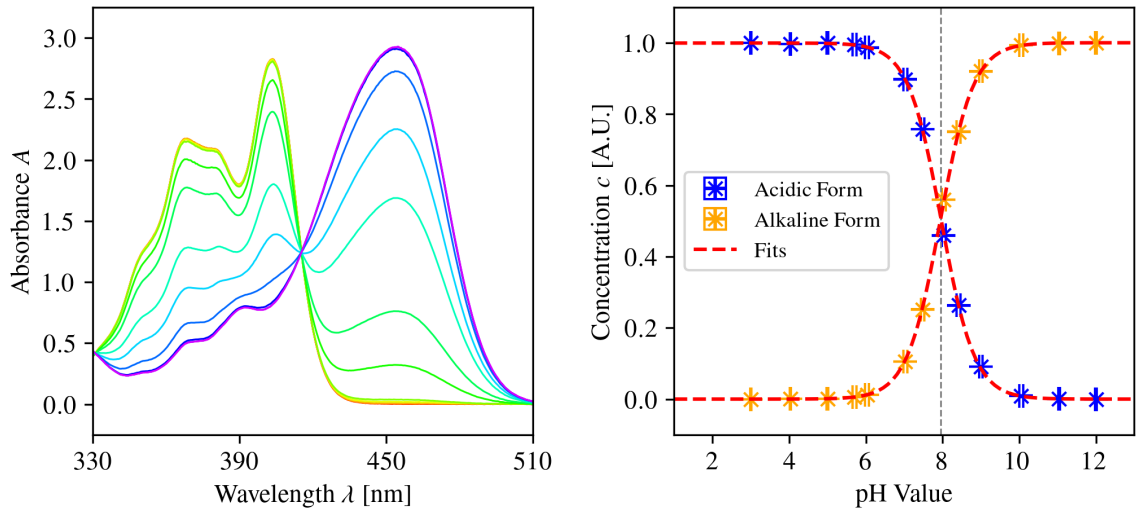

(a) (b)

Figure 5.2: Results of the pK_a calculation from the reference measurement of pyranine. (a) Reference spectra at different pH values in the considered fit interval. Spectra correspond to the data from Fig. 3.2 (b) Calculated concentrations of IH and I^- as a function of pH from the fits of the curves in (a). Fitting the concentration ratios yields the pK_a value (gray line).

5.1.3 Conductivity Measurement of Pyranine

An additional reference measurement involves the conductivity analysis of a pyranine solution. This serves to verify the diffusion constant of the pyranine compound used in the study, since the literature reports significantly varying values. For this purpose, a stock solution is initially prepared by dissolving 541 mg of pyranine in 1 L of deionized water, giving a concentration of $1.03 \cdot 10^{-3}\,\mathrm{mol\,L^{-1}}$. Then, a dilution series is performed by iteratively diluting the stock solution with water to prepare solutions with concentrations of $0.2\,\mathrm{mmol\,L^{-1}}$, $0.1\,\mathrm{mmol\,L^{-1}}$, $0.05\,\mathrm{mmol\,L^{-1}}$, $0.02\,\mathrm{mmol\,L^{-1}}$, $0.01\,\mathrm{mmol\,L^{-1}}$, and $0.005\,\mathrm{mmol\,L^{-1}}$. A volume uncertainty of 1 mL is assumed, which naturally accumulates with each dilution step. We measure the specific conductivity κ at each dilution step using a conductivity probe with $\Delta\kappa = 0.1\,\mu\mathrm{S\,cm^{-1}}$. The resulting conductivity values are plotted against the corresponding pyranine concentrations in Fig. 5.4.

The first step in calculating the diffusion constant from these conductivity measurements is to identify the limiting conductivity Λ^0. This quantity represents the molar conductivity of an ion in the hypothetical limiting case of an infinite dilution. To obtain this parameter, the molar conductivities Λ are calculated from the measured electrical conductivities κ by means of

$$\Lambda = \frac{\kappa}{c}, \tag{5.6}$$

and plotted as a function of concentrations while extrapolating the conductivity at $c = 0$. Several empirical theories exist that aim to explain the dependence of molar conductivity on concentration, but a rigorous theoretical framework for the limiting conductivity is still lacking. The most widely

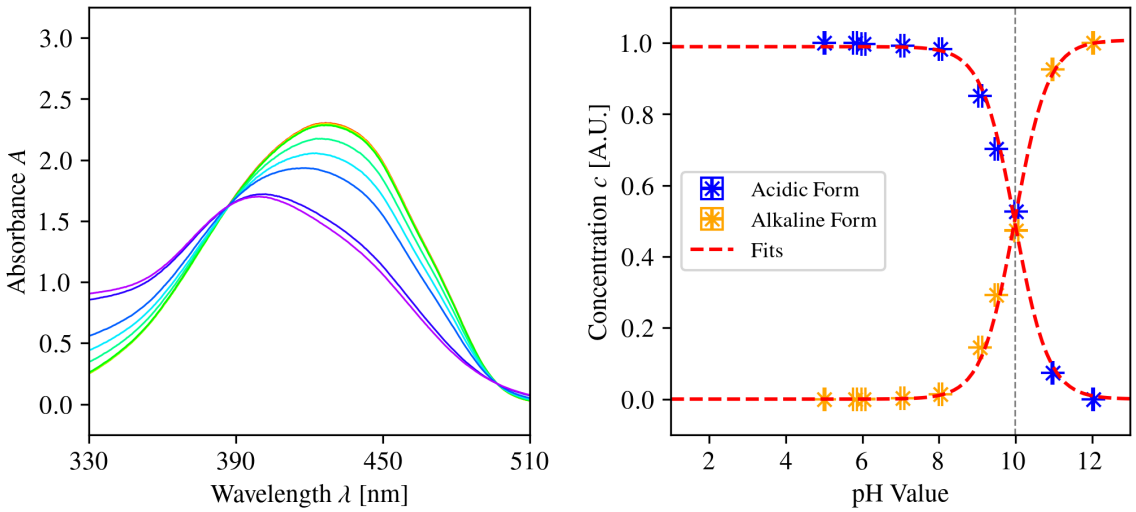

(a) (b)

Figure 5.3: Results of the pK_a calculation from the reference measurement of tartrazine. Analogous to Fig. 5.2.

accepted empirical model is Kohlrausch's law, expressed by

$$\Lambda(c) = \Lambda^0 - K \cdot \sqrt{c}, \tag{5.7}$$

where K represents an empirical constant (Cussler, 2009). By fitting this function to the experimental data, we obtain the y-intercept of Kohlrausch's law as the limiting conductivity at infinite dilution, referred to as $\Lambda^0 = (345.19 \pm 5.20)\,\mathrm{mS\,cm^2\,mol^{-1}}$. Finally, the Nernst-Einstein equation, given by

$$D = \frac{RT\Lambda^0}{F^2 z^2}, \tag{5.8}$$

relates the limiting conductivity Λ^0 to the diffusion constant D. As a result of the determined fit parameters, the diffusion constant for pyranine is determined with $D = (5.71 \pm 0.15) \cdot 10^{-6}\,\mathrm{cm^2\,s^{-1}}$.

5.2 Air-Side UV Spectroscopic Data

The processing of the air-side UV spectroscopic data aims to quantify the methylamine concentration in the channel's air space. This overall analysis comprises three steps: extraction of the gas phase concentrations by means of UV data, derivation of the air-side gas transfer velocities from the concentration time series and calculation of the gas flux into the aqueous phase.

5.2.1 Determination of Gas Concentration

Each measurement series contains a time-resolved series of UV spectra acquired at a frequency of 10 spectra per second, complemented by a lamp spectrum and a dark spectrum. The lamp and dark spectra are the average spectra of 100 individual acquisitions, representing the raw emission spectrum of the light source and the spectrometer's intrinsic background signal, respectively. All spectra are

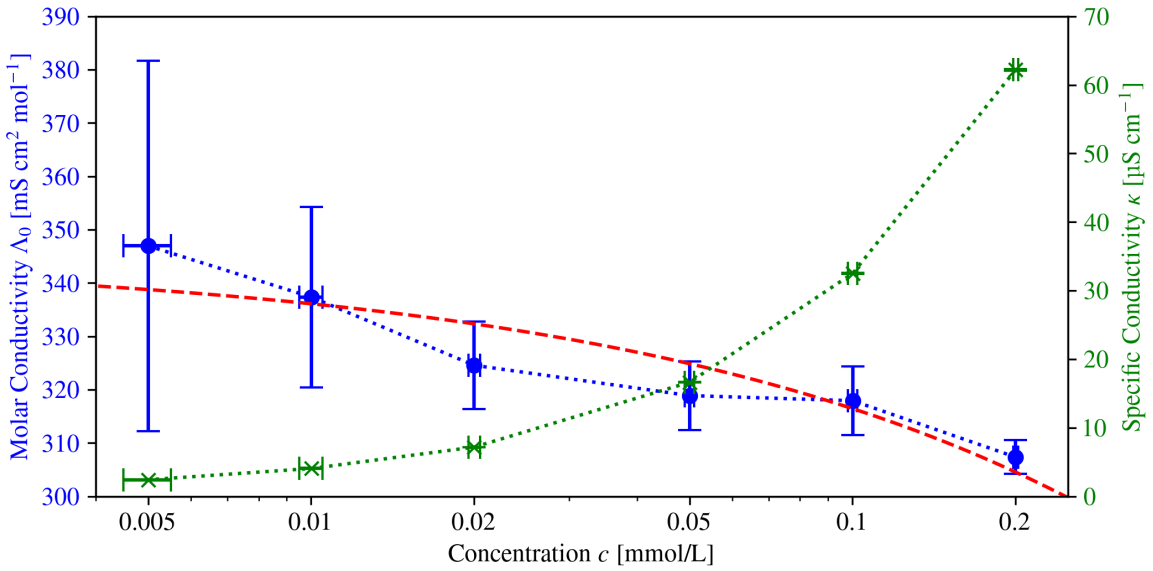

Figure 5.4: Conductivity measurement for determining the diffusion constant of pyranine. The molar conductivity values Λ^0 are calculated from the measured specific conductivity values κ from a dilution series. The fit of the molar conductivity values follows the Kohlrausch's square root law (red). The Kohlrausch's fit curve refers to the left y-axis. Notice the x-axis is logarithmic but the y-axes are linear, so the y-intercept is outside the diagram range.

captured as raw intensity spectra but have to be converted into absorption spectra $A(\lambda)$ according to the Lambert-Beer law

$$A(\lambda) = -\log_{10}\left(\frac{I(\lambda)}{I_0(\lambda)}\right). \tag{5.9}$$

In this formulation, $I(\lambda)$ denotes the measured light intensity after passing through the gas sample while $I_0(\lambda)$ refers to the reference intensity in the absence of absorption. So, $I_0(\lambda)$ corresponds to the lamp spectrum, which characterizes the unattenuated spectral output of the light source under identical optical conditions. Exemplary UV intensity spectra of the lamp, showing both the reference intensity $I_0(\lambda)$ without absorption and the attenuated intensity $I(\lambda)$ after transmission through methylamine, is given in Fig. 5.5(a).

The transformation to absorbance spectra begins by subtracting the dark spectrum from each time-series spectrum and from the lamp spectrum, effectively eliminating the contributions of background signal. According to Eq. (5.9), the background-corrected spectra are normalized by the lamp spectrum to obtain the absorption spectra. All these calculations are performed only within the spectral range between 215 nm to 245 nm, as this band has been found to contain the most important absorption features of methylamine. In addition, this narrow spectral range effectively excludes intensity fluctuations of the UV lamp in the lower UV range, which guarantees a more accurate absorbance spectrum (Kühn, 2022). A representative single absorption spectrum and the corresponding time series of spectra are shown in Figs. 5.5(b) and 5.5(c), respectively.

To determine the methylamine concentration, the absorption spectra are compared to the reference spectrum from Sec. 5.1.1. Since all measurements, including the reference, are carried out at constant optical path length and assuming lateral homogeneity of the gas in the channel, the path length integral in the Lambert-Beer law in Eq. (2.69) can be dropped. This establishes a simplification of the

relationship between the measured and the reference absorbance according to

$$A_{\text{meas}}(\lambda) = \frac{c_{\text{meas}}}{c_{\text{ref}}} A_{\text{ref}}(\lambda) + B. \tag{5.10}$$

It corresponds to a linear regression between the measured absorbance $A_{\text{meas}}(\lambda)$ and the reference absorbance spectrum $A_{\text{ref}}(\lambda)$, where the slope of the fit gives the relative gas concentration with respect to the reference. By multiplying this value by the known reference gas concentration c_{ref}, the absolute methylamine concentration c_{meas} is determined. Additionally, a constant offset term B is included in the fit to account for minor baseline fluctuations over time without affecting the accuracy of the concentration estimate. Finally, the reference spectrum is fitted to each absorption spectrum of the time series using Eq. (5.10), which gives a concentration value of methylamine for each time point, which is shown in Fig. 5.5(d). The uncertainties of corresponding gas concentrations are determined by Gaussian error propagation from the fit uncertainties of Eq. (5.10) and the uncertainty of the measured reference gas concentration c_{ref}. In summary, the processing of the UV data results in a reconstruction of the temporal gas concentration curve within the air space.

5.2.2 Determination of Air-Side Gas Transfer Velocities

Air-side gas transfer velocities are derived from the temporal evolution of gas concentration using a mass balance approach as discussed in Sec. 3.5. This analysis only works on the assumption that the system is in dynamic equilibrium, meaning that wind and wave fields are balanced and the gas exchange rate is temporally constant. Under such steady-state conditions, we expect an exponential decrease of the gas concentration in the air phase over time once the gas input has ceased as in

$$c_a(t) = c_0 \exp(-\lambda_a t). \tag{5.11}$$

This exponential fit is applied exclusively to certain time intervals where wind and waves are already in momentum equilibrium and no additional gas input occurs during the period. Such intervals should feature a clear exponential decrease in the gas concentration as shown in Fig. 5.5(d) with an exemplary fit.

Only measurement series that contain these valid intervals are taken into account in the analysis. The decay constant λ_a is extracted by fitting the gas concentration data from Sec. 5.2.1 within the selected interval to the exponential model in Eq. (5.11). The air-side gas transfer velocity k_a is then calculated as follows

$$k_a = \frac{V_a}{A}(\lambda_a - \lambda_{\text{leak}}), \tag{5.12}$$

where V_a denotes the volume of the channel's air space, A is the total interfacial area between air and water, and λ_{leak} represents the leakage rate of the wind-wave channel. The leakage rates have been measured independently in calibration experiments by K. Krall and are known to vary with wind speed in the different measurement series (see Appendix A.4).

It is important to emphasize that this analysis step is only applicable to data sets that exhibit equilibrium between wind and waves and an exponential decay behavior. Otherwise, the assumption of a constant transfer rate is violated, which invalidates the evaluation.

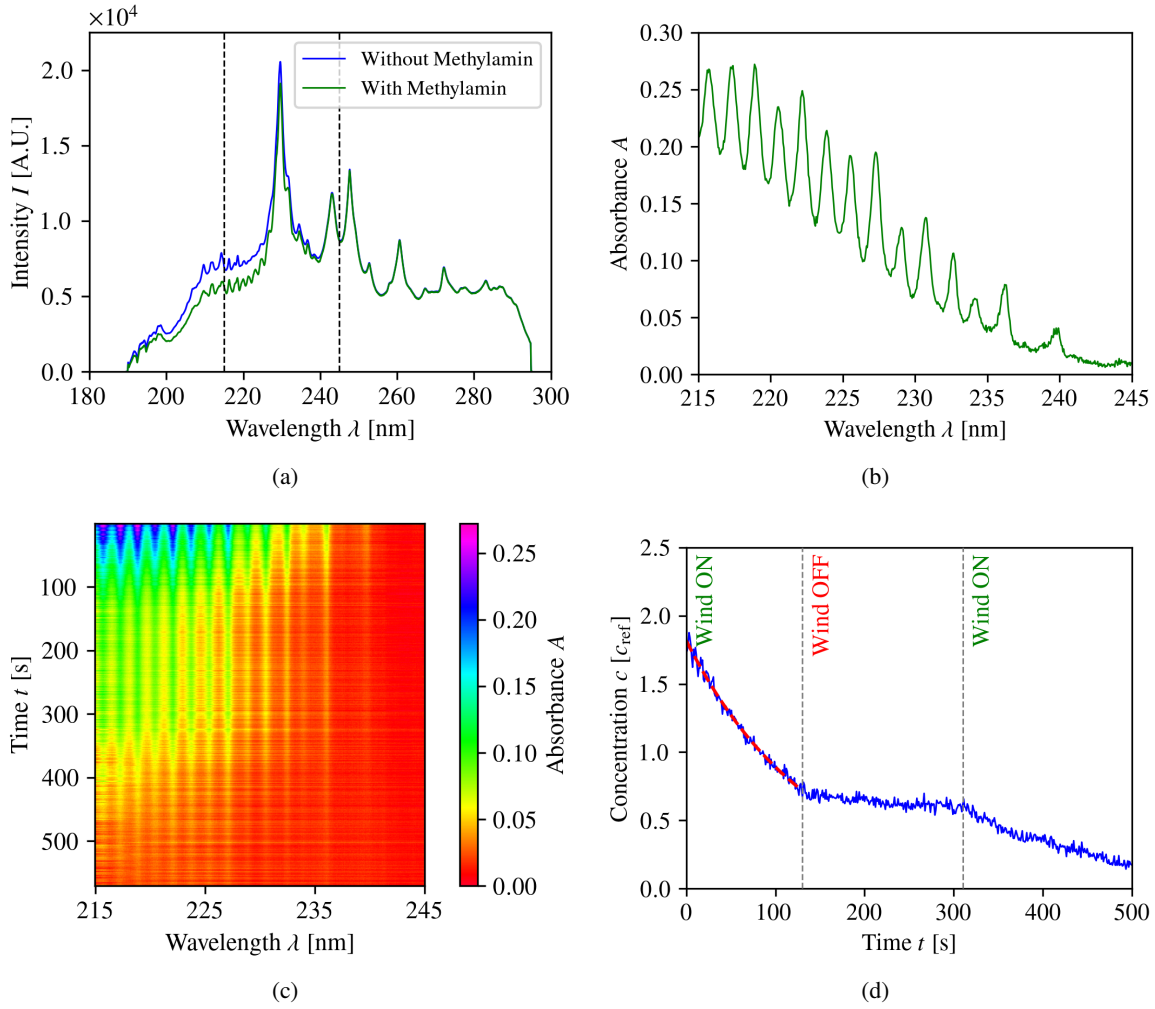

Figure 5.5: Processing of the air-side UV spectroscopic data. (a) Intensity spectra with and without methylamine in the air space. The gray lines show the spectral range selected for further analysis. (b) Extracted absorption spectrum of methylamine in the selected spectral range. (c) Time series of absorption spectra extracted from time series of intensity spectra. Time axis runs from top to bottom with approximately one spectrum per second. (d) Time series of the gas concentration extracted from the fits of the reference spectrum to the time series of absorption spectra. During the time series, the wind is switched off at 130 s and on at 310 s. The exponential decay fit (red) in the first wind regime is used to calculate the air-side gas transfer velocity.

5.2.3 Determination of Gas Flux

Finally, combining the determined air-side gas concentrations with the corresponding transfer velocities enables the calculation of gas flux into the water. Here, the flux j_a from the air into the water is given by

$$j_a = k_a \left([\mathrm{NH_2R}]_{a,b} - [\mathrm{NH_2R}]_{a,s} \right), \tag{5.13}$$

where $[\mathrm{NH_2R}]_{a,b}$ represents the bulk gas concentration in the air phase and $[\mathrm{NH_2R}]_{a,s}$ the air-side gas concentration at the air-water interface. While the bulk gas concentrations have already been determined from UV data (Sec. 5.2.1), the surface concentrations remain unknown. Nonetheless, given that methylamine is classified as an air-side controlled gas, it is assumed to dissolve immediately

upon contact with the water surface. This justifies the approximation

$$[NH_2R]_{a,b} \gg [NH_2R]_{a,s}, \tag{5.14}$$

which simplifies the flux equation (5.13) to

$$j_a = k_a [NH_2R]_{a,b}. \tag{5.15}$$

This allows for the direct calculation of the gas flux into the aqueous phase by multiplying the obtained gas transfer velocity with the extracted gas concentration curve. The uncertainty of gas flux results from the uncertainties of the gas concentrations and the uncertainty of gas transfer velocity from the exponential fit using Gaussian error propagation. In analogy to the determination of air-side transfer velocities, a reliable flux estimate requires the system to be in dynamic equilibrium. Consequently, the flux analysis is limited to the measurement series with those intervals in which both the transfer velocity and the gas concentration are defined under steady-state conditions.

5.3 Water-Side UV-VIS Spectroscopic Data

The objective of the water-side UV-VIS spectroscopic analysis is to determine the concentrations of the acidic and alkaline forms of pyranine and tartrazine in the tank water. Based on the ratio of these protonation states, the pH value of the water can be estimated. The data from measurement weeks 1 and 2 comprise three spectra from each measurement series recorded at the end of each measured wind condition. Since these originate from the same water sample, they are averaged to obtain a representative spectrum per measurement series. In contrast, the data from measurement weeks 3 to 6 include ten time-resolved spectra per series, which were acquired continuously during a gas exchange experiment. Supplementing the data is an average spectrum from 3 individual spectra recorded at the beginning and end of each measurement day. All spectra are recorded as absorption spectra with baseline correction already applied and thus do not require any further preprocessing.

5.3.1 Determination of Dye Concentration

Determining the dye concentrations from the UV-VIS spectra relies on the reference spectra of pyranine and tartrazine. Analogous to Eq. (5.2), we assume that a measured absorption spectrum is a linear combination of the absorbances of all absorbing species present in the water. This gives

$$A_{\text{meas}}(\lambda) = c_{\text{IH}} A_{\text{IH}}(\lambda) + c_{\text{I}^-} A_{\text{I}^-}(\lambda) + c_{\text{TH}} A_{\text{TH}}(\lambda) + c_{\text{T}^-} A_{\text{T}^-}(\lambda) + B, \tag{5.16}$$

where $A_{\text{IH}}(\lambda)$ and $A_{\text{I}^-}(\lambda)$ denote the absorption spectra of the protonated and deprotonated forms of pyranine, respectively, while $A_{\text{TH}}(\lambda)$ and $A_{\text{T}^-}(\lambda)$ represent the spectra for tartrazine's components. The coefficients c_{IH}, c_{I^-}, c_{TH}, and c_{T^-} correspond to the relative concentrations of each species with respect to the reference concentrations used to determine the pure component spectra. A constant offset term B is also included to account for minor fluctuations or shifts in the baseline over the course of measurements.

All recorded UV-VIS spectra are fitted to this linear model to extract the concentrations of all dye components. It is found that reliable results can be obtained by restricting the fitting interval to the spectral region surrounding the peak of I^-, between 415 nm to 495 nm. This interval includes the entire peak of I^- as well as the falling edge of the IH peak. In contrast, attempts to extend the fitting interval to include the maximum of the IH peak lead to unrealistic concentration estimates. The main reason is that this approach systematically fails to capture the shape of the IH peak accurately, resulting in underestimated IH concentrations. These residuals arise likely due to nonlinearities in the spectral response. To overcome these problems, the chosen fitting interval deliberately excludes the IH maximum and only includes its declining edge as well as the entire I^- peak. Nevertheless, this still produces reliable concentration estimates, as within the relevant experimental pH range the deprotonated form I^- is present in much lower concentrations than the protonated form IH. Thus, the system responds more sensitively to changes in the I^- concentration. However, this also implies that the fits become less robust at low pH values where the I^- concentrations are close to the detection limit. Furthermore, it is found that for all fits the concentration of deprotonated tartrazine T^- can be consistently set to zero, i.e. $[T^-] \approx 0$, as the experimentally observed pH values do not exceed pH 7. Under these conditions, the fraction of T^- is below 1 % and thus contributes only negligibly to the total absorbance.

5.3.2 Determination of pH Value

Based on the determined concentrations of the dye components, it is possible to calculate the pH value of the water. Only the concentrations of the pyranine species are used for this purpose, as the equivalence point of tartrazine is far outside the experimental pH range. Hence, the ratio of its protonated and deprotonated forms is too small to yield reliable pH estimates. The pH value for each spectrum is calculated using the following expression derived from the Henderson-Hasselbalch equation

$$\mathrm{pH} = \mathrm{p}K_a - \log\left(\frac{[\mathrm{I}]_{\mathrm{tot}}}{[\mathrm{I}^-]} - 1\right). \tag{5.17}$$

The uncertainties of pH calculation result from the Gaussian error propagation of Eq. (5.17) with the fit errors of the concentrations as well as the uncertainty of the measured $\mathrm{p}K_a$ value. The fit results of a representative data series of spectra over one measurement day as well as its extracted concentrations and pH values are shown in Fig. 5.6. Calculating the pH value has proven to be particularly useful from an experimental perspective to monitor the progression of I^- production over the course of a measurement day. It gives a valuable insight into the ongoing chemical equilibrium of the system and allows us to determine, for instance, when re-acidification of the water is required. In addition, the pH value serves as a reliable criterion for assessing the quality of spectral fits, as will be explained in the following.

5.3.3 Validation of Fit Results

To validate the quality of fits performed on the UV-VIS spectra, we rely primarily on the comparison between the resulting pH values derived from the fit data and the values measured with a pH electrode at the beginning and end of each measurement day. Ideally, the spectroscopically determined pH values

obtained from consecutive spectra of a measurement day should lie between these two reference points. In practice, however, this ideal scenario is not always achieved, especially at lower pH values where the concentration of I^- becomes very low. In this range, the fitting procedure is more sensitive to small deviations, making accurate quantification difficult. Importantly, an exact matching between the spectroscopic and electrode-derived pH values is not necessary, as the electrode measurements themselves are subject to considerable uncertainties, especially in the higher pH range.
Nevertheless, the chosen fitting procedure consistently provides pH estimates that are in best agreement with the measured reference values. Fortunately, the two measures complement each other well, as pH values around 5 can still be reliably measured with the electrode, while the spectroscopic method provides accurate results for pH values above 6. So, a good estimate is possible for the entire pH range.

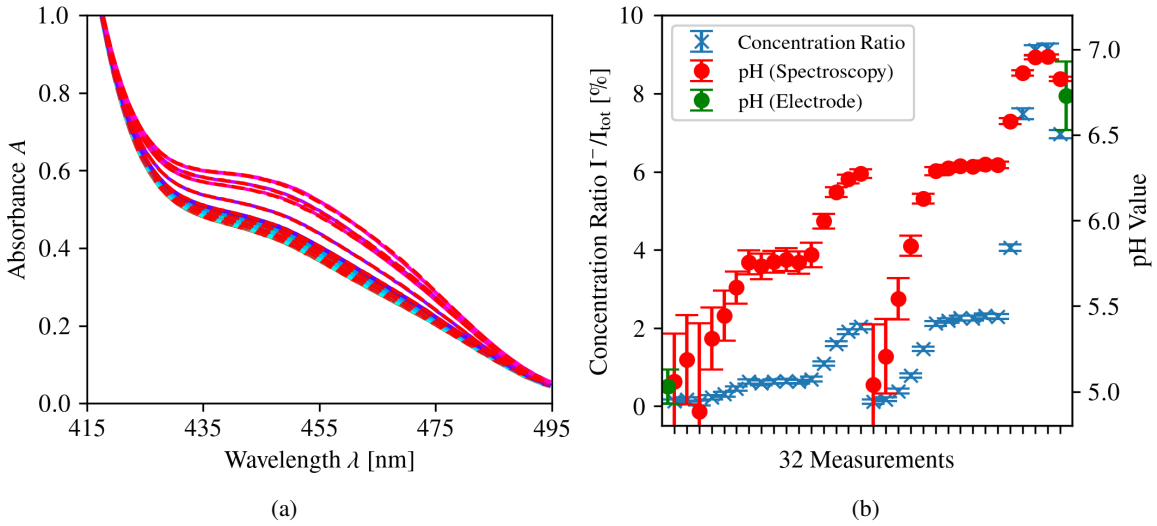

Figure 5.6: Processing of the water-side UV-VIS spectroscopic data. (a) Fits of the absorption spectra of one measurement day. Only the region of the absorption peak of I^- and the declining flank of IH are fitted. An increase in absorbance due to the increasing pH value with increasing I^- concentration can be seen over the course of the measurement day. (b) Extracted concentrations and pH values over the course of a measurement day with a total of 32 spectral acquisitions. After the first half of the measurement day, the pH value is reduced to 5 again by adding hydrochloric acid. Error bars are larger at low pH values, as smaller concentration ratios have to be detected. Green data points correspond to pH values measured with the pH electrode at the beginning and end of the measuring day.

5.3.4 Validation of the Chemical System

At this point, we can revisit the comparison between the simulated chemical system with and without consideration of carbonate equilibrium, as introduced in Sec. 3.4.1. Previously, it was assumed that simulations incorporating carbonate equilibrium would give a more accurate representation of experimental reality. Now, with dye concentrations determined from UV-VIS spectroscopic data, this assumption can be verified.
To validate the model, we consider the final spectroscopically determined pH value for each gas exchange experiment and plot it against the cumulative total concentration of methylamine injected into the system. For sequentially performed experiments, the cumulative amount of methylamine from

all previous steps must naturally be taken into account. The conversion from the weighed methylamine input to the concentration in the water follows Eq. (5.1), except using the total volume of water instead of the total volume of the system. Note that this is based on the assumption that the total injected methylamine volume dissolves completely in the water, with negligible losses due to leakage. As the leakage rates in the gas exchange experiments carried out here typically account for around 1 % of the air-side gas transfer velocities, this assumption is justified. As part of this simplification, an input uncertainty of 0.1 g per measurement is considered instead, which accumulates over successive experiments.

The resulting dataset is shown in Fig. 5.7 accompanied by the two simulated curves, one with and one without consideration of carbonate buffer system. An agreement is found between the measured data and the simulation with carbonate equilibrium. This gives direct evidence that the carbonate equilibrium plays a crucial role in the fluorescence response of the chemical system and must therefore always be taken into account. While the simulation agrees better with the experimental

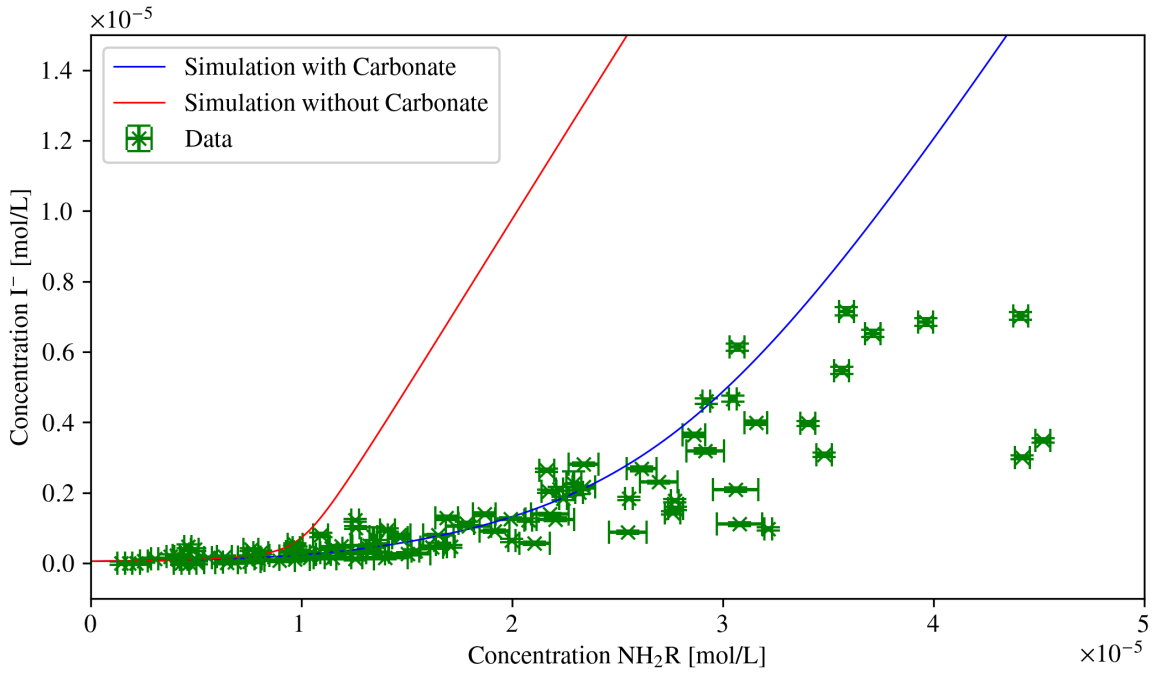

Figure 5.7: Simulation results of the chemical system with and without consideration of the carbonate buffer in comparison to the measured dye concentrations.

data at low methylamine concentrations below $2.5 \cdot 10^{-5}\,\mathrm{mol\,L^{-1}}$, the deviation increases at higher concentrations, where the measured pH values tend to be consistently lower than the predicted values. This indicates that an additional process not considered in the simulation could influence the results, namely the ongoing invasion of atmospheric CO_2 during the experiment. In the simulation, it is assumed that the equilibrium concentration of CO_2 in the water is set once by equilibration with the atmosphere and is only changed by internal chemical reactions within the carbonate system. In practice, however, additional CO_2 from the atmosphere can continuously dissolve in the water. As the pH value increases with rising methylamine concentration, the proportion of protonated carbonic acid species in the water decreases, creating favorable conditions for further CO_2 uptake. This newly

dissolved CO_2 then forms additional carbonic acid, which counteracts the pH increase caused by methylamine and reduces the enrichment of I^-. Since both the physical absorption of CO_2 and the subsequent chemical reactions forming carbonic acid are relatively slow processes, this effect may occur with a certain delay. Importantly, the additional invasion of CO_2 is not a speculative explanation but is supported by experimental observations. Sequential measurements usually show a gradual increase in background fluorescence due to the accumulation of I^-. However, in the period between measurements when only a homogeneous background fluorescence should be visible, dark streaks are occasionally observed on the water surface. These appear to result from a local CO_2 invasion, leading to a transient local acidification of the system and a reversion of I^- to the acidic form. This causes a decrease in fluorescence in these regions. As this CO_2 invasion effect only becomes significant at higher methylamine concentrations which are rarely reached in the experiments, the application of the simulation model with carbonate buffer is not invalid. In fact, for the vast majority of experimental conditions, this model provides a robust and accurate representation of the chemical processes at play.

5.4 Image Data

The gas exchange experiments conducted in this study generate a substantial amount of image data, primarily due to the use of high temporal resolution imaging with a frame rate of 500 Hz. Thus, each camera records approximately 3 GB of image data per second, resulting in a total raw data volume of up to 20 TB per camera over the whole measurement campaign. Basically, this immense amount of data necessitates compression approaches and the implementation of efficient algorithms when analyzing the images. The initial processing of the image data presented here involves several preprocessing steps, supplemented by a brightness calibration and a geometric calibration. All image sequences are stored in an 8-bit grayscale format. For each measurement series, the available image data consists of the actual image sequence with a typical duration between 5 min to 14 min. In addition to this main sequences, for each measurement day there is one dark sequence, recorded under dark conditions, and a zero sequence, recorded in the acidic initial state of the water surface before gas injection. These reference sequences are an integral part of the data set and are necessary to correct the raw image data. The analysis of image data in this work is restricted to the sequences recorded by the central camera of the array, as the full 3D reconstruction via data fusion from all cameras has not yet been implemented within the scope of this study.

5.4.1 Preprocessing

The preprocessing of image data covers both data compression and image correction steps. Image correction itself comprises an inverse gamma transformation, a flat field correction, and a removal of image defects. These correction processes serve to compensate for the nonlinear response of the image sensor to light intensity, correct for inhomogeneous illumination across the image field, and eliminate artifacts, respectively. A representative result of this image preprocessing is shown in Fig. 5.8. The individual successive processing steps are explained in detail in the following. For clarification, the image correction workflow is illustrated in Fig. 5.9.

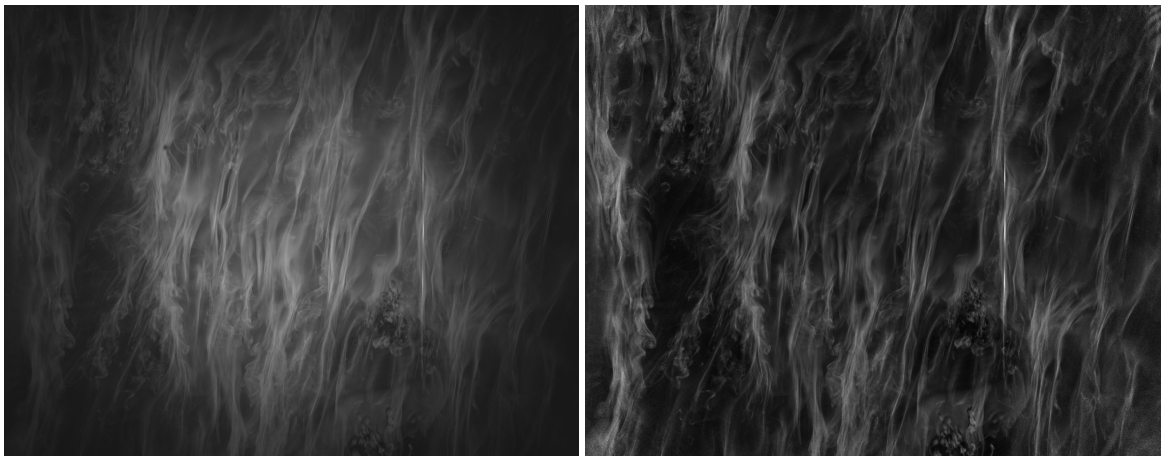

(a) (b)

Figure 5.8: Comparison of the image data (a) before and (b) after preprocessing steps. Before preprocessing, there are differences in fluorescence intensity due to inhomogeneous illumination.

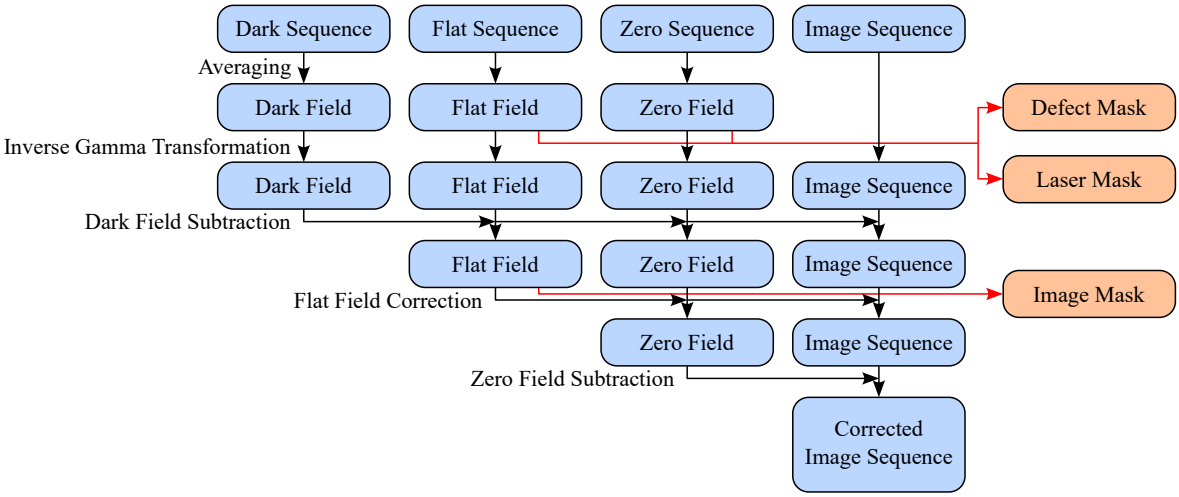

Figure 5.9: Workflow of image preprocessing. Compression step is not shown, but is the very first step. The schema is done separately for the fields of each measurement day. All preprocessing steps are applied to each individual image of the measurement image sequence.

Compression

As the recorded image sequences of all experiments require an enormous amount of data storage space, it is advisable to compress them in the first processing step.

An initial compression operation to reduce the image data involves converting the 8-bit images into a 7-bit format via bit-shifting. This transformation removes one bit, leading to a slight increase of noise and a degradation of image quality, which is nevertheless acceptable in view of the memory reduction achieved.

In the next compression step, we make use of the fact that successive images in the sequences change only minimally due to the high frame rate. Therefore, it is usually advantageous to store only the differences between adjacent images. All image sequences are generally organized in stacks of 1000 frames each. Specifically, the first image of each stack is stored in its original format, while all

subsequent images are stored as pixel-wise differences to their previous image. This technique, known as delta encoding, does not lead directly to a reduction in data volume, but helps to enhance the effectiveness of the subsequent compression.
Finally, the bit-shifted and delta-encoded data are further compressed using LZW compression and saved in TIFF format. This multi-stage compression pipeline achieves a data reduction of approximately 70 % compared to the original raw image format. While the initial bit-shifting step is lossy, the subsequent compression steps are lossless. This provides a good compromise between reducing storage requirements and maintaining image quality.

Creation of Dark Field, Zero Field, and Flat Field

The first step in image correction is to create three reference images: the dark field, the zero field, and the flat field. For each measurement day, the dark field and the zero field are obtained by calculating the pixel-wise average of 2000 individual frames from the respective dark and zero sequences. This averaging keeps the background noise to a minimum. In contrast, generating the flat field is more challenging. A flat field represents the normalized illumination field across the entire image area. It is created by averaging selected raw image sequences over an extended time interval, whereby the inhomogeneous structures on the water surface are averaged out in the fluorescence signal. Typically, the image data from the last or penultimate acquisition of a measurement day is used, when the background illumination is maximal. Averaging is done over a period from 60 s to 260 s after the start of the measurement, when the gas flux is typically at its highest, resulting in the strongest fluorescence signal and more reliable statistics. As the measurement conditions can vary on a daily basis, the flat fields calculated for individual measurement days may differ significantly in intensity. To compensate for these fluctuations, we select the brightest flat field of each measurement week and apply it uniformly throughout that week, while disregarding the remaining flat fields from the same week. This approach guarantees consistency within a week and accommodates any optical variations between different weeks with respect to the flat field. Overall, we obtain a dark field and a zero field for each measurement day, and a single representative flat field for each measurement week used for all corresponding measurements. A representative set of these averaged reference fields is shown in Fig. 5.10.

Creation of Defect Mask and Laser Mask

After averaging, both the zero fields and flat fields exhibit artifacts. These artifacts comprise, on the one hand, black spots arising from defects in the bottom window of the Aeolotron and, on the other hand, the bright laser line projected onto the water surface. As these exceptionally dark or bright pixels would affect the flat field correction, it is necessary to identify and remove the artifacts in this step.
Despite averaging, both features stand out due to intensity changes and can therefore be easily extracted with a Canny edge detector. This image operation is performed with a lower threshold value of 6 and an upper threshold value of 12. After edge detection, the identified pixel regions are enlarged by a dilation operation with a window size of $(15, 15)$, followed by creating a defect mask (Fig. 5.12(a))

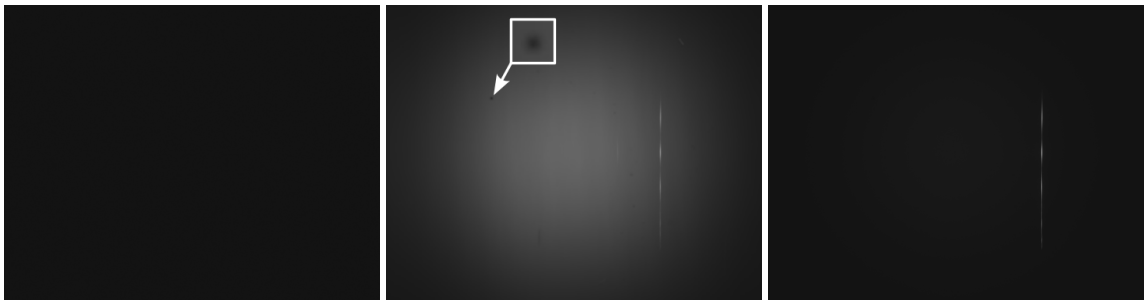

(a) (b) (c)

Figure 5.10: Averaged (a) dark field, (b) flat field, and (c) zero field. Both flat field and zero field show artifacts due to defects on the bottom window of the Aeolotron and the laser line. Defect is zoomed in the flat field and cannot be seen in the zero field due to the low contrast. Both artifacts must be removed before flat field correction.

and a laser mask (Fig. 5.12(b)). The separation of the detected pixels into defect mask and laser mask is done by a contour analysis. According to this, the largest detected pixel contour is assigned to the laser line and the remaining ones to the defects. Furthermore, as the laser line may shift slightly on the water surface due to water wave movements, we define a rectangular frame around the detected laser contour. Specifically, this frame extends 20 pixels to the left and right of the laser contour and covers the maximum horizontal displacement. By doing so, a fixed region is defined in which the laser line remains completely enclosed during the entire image sequence despite its possible movement.
The purpose of this processing step is twofold. First, the defect mask enables fast and reliable identification and correction of defective pixels in all images. Second, the laser mask defines a precise region where the laser line is expected to appear, simplifying its subsequent accurate localization. This extraction of both masks is applied independently to the zero field and the flat field. The results are then combined to create a unified defect mask and a unified laser mask. In general, the defect mask is derived more reliably from the flat field, as the dark defect pixels are more clearly visible against the bright background. In contrast, the laser mask is extracted more effectively from the zero field, where the bright laser line stands out against the darker background.

Inverse Gamma Transformation

Since a gamma correction with a factor of $\gamma = 0.5$ is applied during image acquisition, the recorded grayscale values do not correspond to the actual light intensities. To restore the original intensities, an inverse gamma transformation is executed according to the following formula

$$I_{\text{out}} = I_{\text{in}}^{\frac{1}{\gamma}}. \tag{5.18}$$

This transformation follows a quadratic relationship between recorded and actual intensities and is implemented using a lookup table (LUT) approach. Rather than recalculating the transformation for each pixel, an LUT contains the precomputed results for all 256 possible 8-bit grayscale levels. Thus, the LUT directly maps each input value to its corresponding transformed intensity value, allowing an efficient pixel-wise transformation. The inverse gamma transformation is applied to all raw image

sequences as well as to the created dark fields, zero fields, and flat fields.

Defect Correction in Zero Field and Flat Field

After applying inverse gamma correction, defect correction is performed on both the zero field and the flat field using a combined mask of the precomputed defect and laser masks. This combined mask identifies both the artifacts due to defects and the area of the laser line. Then, the masked regions are interpolated using radial basis function (RBF) interpolation (Powell, 1987). In this method, a random sample of 20000 unmasked pixels is chosen as sampling points. Based on a set of radially symmetric basis functions centered on these sampling points, the masked regions are interpolated. These basis functions are designed to approximate the intensity profile with a single, dominant peak, producing a smooth and uniform profile. The RBF interpolation is particularly effective for our application because both the zero field and the flat field exhibit approximate radial symmetry in their illumination profiles. So, this method accurately reconstructs even the extensive masked region associated with the laser line. Hence, this step yields a uniform and continuous intensity distribution of the zero and flat fields.

Flat Field Correction

With the defect-corrected, smoothed zero and flat fields available, a flat field correction can be applied to compensate for illumination inhomogeneities in the images. Initially, the dark field (Fig. 5.11(a)) is subtracted pixel-wise from all individual frames of the image sequences as well as from zero field and flat field to remove dark current noise. Next, the flat field is normalized to the range [0, 1] by dividing each pixel by the field's maximum grayscale value. Both the image sequences and the zero field are then divided by this normalized flat field (Fig. 5.11(b)) to compensate for any non-uniform illumination. To prevent division by zero, a tiny numerical offset is added to the denominator. Finally, the corrected zero field (Fig. 5.11(c)) is subtracted from the images to remove residual background contributions of the fluorescence signal from the bulk water. All steps of this flat field correction can be summarized by the following equation

$$I_{\text{corr}}(x, y) = \frac{I_{\text{raw}}(x, y) - D(x, y)}{F(x, y) - D(x, y)} - \frac{Z(x, y) - D(x, y)}{F(x, y) - D(x, y)}, \tag{5.19}$$

whereby $I_{\text{raw}}(x, y)$ refers to the individual frames of the image sequences, $D(x, y)$ the dark field, $Z(x, y)$ the zero field, and $F(x, y)$ the flat field. This correction procedure is applied individually for each measurement day, using the corresponding daily dark and zero fields as well as the flat field chosen for this measurement week.

Defect Correction in Image Data

In the final correction step, all defects in the flat field-corrected image data are addressed. Using the defect mask, the affected pixels are identified and then reconstructed by an inpainting method (Telea, 2004) with an inpaint radius of 8 pixels. In contrast to the previous correction steps, the laser line is deliberately retained in the final images. The reason for this is that reconstructing the structures

(a) (b) (c)

Figure 5.11: Corrected (a) dark field, (b) flat field, and (c) zero field. All fields are gamma corrected. The flat field is additionally corrected by subtracting the dark field and normalized to the range [0, 1]. The zero field is also dark field corrected and divided by the flat field. For better representation of dark and zero fields, their grayscale values are multiplied by 100. The irregularities in the zero field are artifacts resulting from the division with the flat field. However, this is ignored as the grayscale values of the zero field are in any case negligibly small.

covered by the laser line is both technically challenging and error-prone. In addition, the laser line can serve as a useful brightness reference in subsequent analyses.

Creation of Image Mask

Since not all regions of the corrected image sequences exhibit the same level of quality, an image mask (Fig. 5.12(c)) is defined in this supplementary step to allow subsequent image analysis to be focused on areas with a high signal-to-noise ratio (SNR). In particular, the image corners tend to have a lower SNR, which is due to the reduced illumination. This causes a noise amplification when dividing the image during the flat field correction. As the illumination spot of the image area is approximately circular, this motivates the creation of a mask that covers the best illuminated circular area of each image. To create this mask, the 80th percentile of the brightest pixels is identified for the normalized flat field image. Then, the centroid of this region is calculated and a circular mask is defined around this centroid covering exactly 80 % of the image area. Such a circular shape guarantees that the image mask is radially symmetric in the same way as the light spot and represents a single connected region of interest. This procedure is applied to the flat field from each measurement day, producing an image mask that restricts attention to the 80 % of pixels with the highest signal-to-noise ratio.

Laser Line Correction

In certain evaluations, the laser line must be precisely removed from the image sequences, as its presence would interfere with the respective image analysis. To begin with, the predefined laser mask is used to restrict the search area to the expected region for the laser line. Within this area, the horizontal position of the laser line is determined by identifying the brightest pixel in each image row and calculating the average x-coordinate across all rows. This averaging yields a reliable estimate of the laser line's lateral position. A vertical line of masked pixels is then drawn at the calculated position, extending over the entire height of the search area. To ensure complete coverage of the laser line, we subsequently perform a dilation operation with an $(8, 8)$ kernel. This step takes into account

(a) (b) (c)

Figure 5.12: Constructed (a) defect mask, (b) laser mask, and (c) image mask. The defect mask covers the image defects in the white areas resulting from defects of the bottom window, the laser mask shows the area in which the laser line is expected to move and the image mask marks the 80 % of the pixels with the highest SNR.

that the laser line extends over more than one single pixel width. As a result of this preprocessing step, we obtain a precise binary mask of the laser line for each frame of an image sequence. This area can be excluded from evaluation in subsequent image processing.

5.4.2 Brightness Calibration

The purpose of brightness calibration is to establish a quantitative relationship between the grayscale values in the captured images, representing the image brightness, and the underlying fluorescence signal intensity. This is accomplished by creating calibration data that maps the image brightness to known concentrations of pyranine. By separately simulating the fluorescence signal based on constant pyranine concentration profiles, it is possible to obtain a calibration factor from the comparison with the measured image brightness. This factor enables a conversion between the two scales.
In order to create calibration data, we analyze the image brightness of the sequences in the initial phase of each gas exchange experiment. During this phase, only the background fluorescence is visible in the images as no gas input has yet been applied. Specifically, the first 2000 images of each sequence are averaged pixel by pixel, and the mean brightness is determined by further averaging over the resulting mean image. To improve the accuracy of the brightness values, the laser line is removed from the images before averaging. The procedure for this has already been described in Sec. 5.4.1. Given that no gas exchange takes place during the averaging interval, it is assumed that the background fluorescence originates from a constant concentration depth profile of pyranine in the water. The obtained mean brightness values are assigned to these constant pyranine concentrations based on the UV-VIS spectroscopy data. Since spectroscopic data are not yet available in this initial phase, we estimate the pyranine concentration based on the final spectrum of the previous measurement. For the initial phase of a day's first measurement, the pyranine concentration is determined from the zero spectrum. This approach is justified by the expectation that the dye composition should remain stable between successive runs.
To ensure the reliability of the calibration, only the two highest mean image brightnesses per measurement day are included in the calibration data, as these correspond to the highest pyranine concentrations. In addition, the image brightness must exceed a grayscale value of 2. At lower brightness levels, the associated pH values are usually very low, making the spectral fitting less robust. As described

in Sec. 5.3, the resulting pyranine concentration estimates can be significantly inaccurate under these conditions. Along with the acquisitions from gas exchange experiments, we also include the brightness data from images of the flat water surface taken separately at the end of selected measurement days in the calibration. These sequences play a crucial role for defining the higher brightness range of the calibration curve, as these are typically acquired at raised pH values where the deprotonated form of pyranine dominates the fluorescence signal.
All calibration data are fitted to a simulated fluorescence curve using the simulation results from Sec. 3.4.2. In this simulation, the fluorescence signal has already been modeled for constant dye depth profiles with increasing pH values, assuming a total pyranine concentration of $5 \cdot 10^{-5}\,\mathrm{mol\,L^{-1}}$ and a tartrazine concentration of $2 \cdot 10^{-5}\,\mathrm{mol\,L^{-1}}$. The application of this single simulation curve across all measurements is justified by the fact that the tartrazine concentration is found to be approximately constant with a mean value of $2.02 \cdot 10^{-5}\,\mathrm{mol\,L^{-1}}$ in all measurements throughout the campaign. Furthermore, the different pyranine concentrations used during the measurement campaign do not affect the simulation curve, as the fluorescence signal depends solely on $\mathrm{I^-}$, and the acidic component of pyranine does not contribute to any absorption or fluorescence in the relevant spectral excitation range. Consequently, any given concentration of $\mathrm{I^-}$ results in the same fluorescence signal for all measurements, ensuring consistency of the calibration curve. It is important to note that the measurements in weeks 1, 2, 5, and 6 are performed with 4 laser array units, while in weeks 3 and 4 only two laser units are available for excitation. This leads to only about half the excitation intensity for these measurements. When calculating the calibration factor, it is therefore necessary to consider the calibration data of the two configurations separately, which also gives two different values. The relationship between the observed image brightness I_{Image} and the simulated fluorescence intensity $I_{F,\mathrm{tot}}$ is finally expressed by the following equation

$$I_{\mathrm{Image}} = \sigma I_{F,\mathrm{tot}}, \tag{5.20}$$

where σ denotes the desired calibration factor. The calibration factor is determined by fitting the simulated curve to the measured brightness data, which is illustrated in Fig. 5.13 and gives the values

$$\sigma_{4\,\mathrm{Laser}} = 166.95 \pm 2.13, \tag{5.21}$$

$$\sigma_{2\,\mathrm{Laser}} = 66.88 \pm 2.71. \tag{5.22}$$

These calibration factors allow for an accurate conversion of grayscale image data into physically meaningful fluorescence intensity values, expressed in terms of the reference excitation intensity at the water surface.

5.4.3 Geometric Calibration

In a last procedure, a geometric calibration of the image data is applied to extract the relationship between image coordinates and world coordinates, which allows a size estimation of the image dimensions. This calibration is made using image sequences of a calibration target. The method involves identifying the image coordinates of distinct reference points on the calibration target and

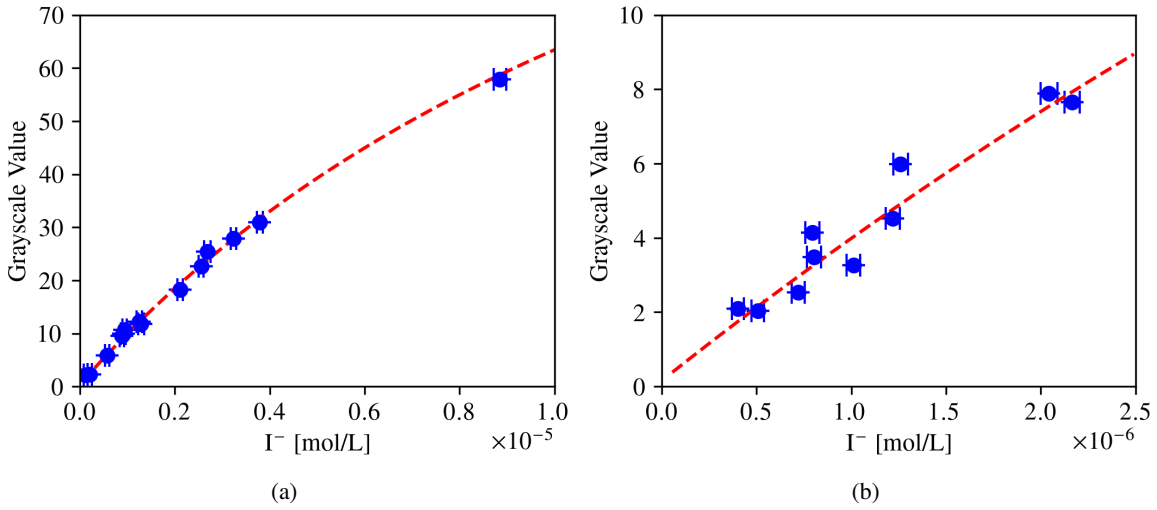

Figure 5.13: Brightness calibration curves for laser array illumination setup with (a) 4 laser units and (b) 2 laser units. The fit curves correspond to the simulated data from Fig. 3.8. Note that only data points with significantly lower I^- concentrations are available for the setup with 2 laser units.

relating them to the physical distances. In our case, the calibration target consists of a regular grid of circles with varying sizes. For the purpose of geometric calibration, the centers of these circles serve as reference points to establish the correspondence between image and world coordinates. How the center points of the circles are detected is explained in more detail in the following.
First, a Gaussian filter with a kernel of $(3, 3)$ is applied to smooth the image and prevent individual pixels from being falsely recognized as circular features. Next, the smoothed image is thresholded using Otsu's method (Otsu, 1979), which separates the calibration pattern from the background and converts it into a binary mask (Fig. 5.14(a)). With this binary mask, the contours of the pattern are extracted along with a filtering process to select only the desired circles. Among all circles, only the largest ones are chosen for calibration, as their position is the easiest and most accurate to detect. The selection criteria of the detected contours according to these circles are as follows:

- The area of the contour must lie between 450 and 600 pixels.
- The contour perimeter must deviate by no more than 5 % from that of the corresponding minimal enclosing circle.
- The aspect ratio of the bounding box must not exceed 0.9.

These conditions make sure to find only sufficiently circular and appropriately sized contours, effectively isolating the largest circles in the calibration grid for further processing. The center coordinates of each detected circle, representing the image coordinates, are identified using contour moments. Based on the known geometry of the calibration target, the corresponding world coordinates are assigned, where the exact spacing between adjacent circle centers is 6 cm in both the x- and y-directions. A typical calibration image sequence displays a grid of 48 fully visible and detectable circles arranged in a 8×6 pattern (Fig. 5.14(b)). However, not all 48 circles are always recognized in each frame. To correct for this, an additional verification step is necessary. This involves calculating the distances

between all neighboring detected image coordinates, and if any irregularity suggests a missing circle, the corresponding world coordinate is also removed. In this way, the number of image and world coordinates always matches, allowing for accurate mapping.

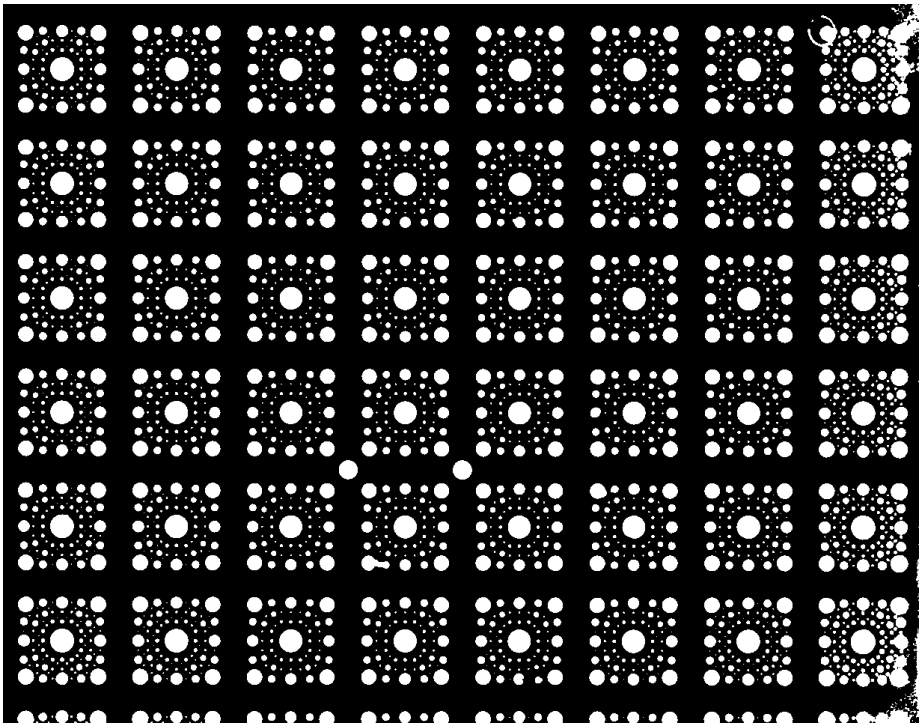

(a)

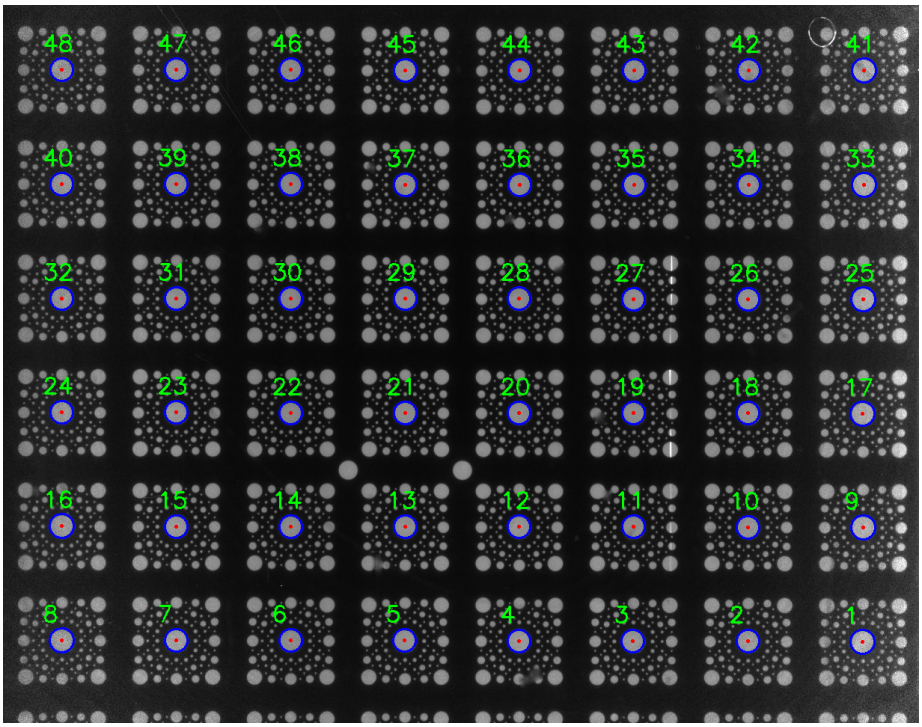

(b)

Figure 5.14: Geometric calibration. (a) Binary mask of the calibration target after Otsu's threshold operation. (b) Detected circles and circle centers drawn into the raw calibration image.

Using the extracted correspondence between image and world coordinates, the magnification factor of the optical setup can be derived. Assuming negligible perspective distortion, this factor is given by the ratio between pixel distances measured in the image and the corresponding distances in physical space. To ensure consistency between the two coordinate systems, a common origin must be defined. By default, the world coordinate system is centered on the position of the upper left circle in the calibration grid, which is assigned the coordinates $(0, 0)$. Aligning the image coordinate system accordingly requires to shift all image coordinates in such a way that this first detected circle also corresponds to the origin. This is achieved by subtracting the pixel coordinates of this reference circle from all other detected image coordinates. Since both coordinate systems now coincide in the same origin, all coordinates correspond directly to the distance to the origin. The magnification factor is obtained by dividing the image coordinates by the world coordinates according to

$$M = \frac{X_{\text{Image}}}{X_{\text{World}}}. \tag{5.23}$$

An individual magnification factor is determined for each detected image coordinate, followed by averaging all values of all frames to obtain a single magnification factor for the respective calibration sequence. This procedure is repeated for several calibration sequences. Overall, this gives an average magnification factor of

$$M \approx 2.54 \, \frac{\text{px}}{\text{mm}} \tag{5.24}$$

for the standard measurement configuration, meaning for a water level of 1 m. Given this magnification factor, the recorded image area of each sequence, with a standard resolution of $1224\,\text{px} \times 960\,\text{px}$, covers a physical area of $48.2\,\text{cm} \times 37.8\,\text{cm}$.

6 Image Analysis

After preprocessing the raw image data, the actual image analysis is carried out. This begins with a general description of the fluorescent image structures as part of a qualitative analysis. At this stage, initial results are already presented, as the turbulent fluorescence patterns reveal first indications of near-surface transport processes relevant to gas exchange. These observations serve as a basis for interpretation, which will be revisited in the results chapter. Subsequently, a simple quantitative analysis of the fluorescence intensity is presented using grayscale histograms. The last section introduces an advanced image processing algorithm that enables the detection of a key phenomenon: microscale wave breaking. While the data processing steps described in the previous chapter are applied to the raw data of all experiments, the following chapters focus on selected measurements. This prioritization is necessary due to the enormous volume of data.

6.1 Characterization of Fluorescent Structures

The Fluorescence Imaging show impressively the near-surface transport processes involved in gas exchange. For a first idea of how the imaging of gas exchange at a water surface looks in two dimensions, Fig. 6.1 shows representative snapshots of the measurement campaign under different conditions. Here, various fluorescent structures are visible on the water surface, exhibiting high variability and extending over several spatial scales. This first observation, that fluorescence intensity is not homogeneously distributed but shows a structured pattern, is direct evidence that gas exchange does not occur uniformly across the water surface, as one might naively assume. Instead, it is modulated by a structured turbulence field, leading to spatial inhomogeneities. Despite their variability, the fluorescence structures observed in the image sequences can be generally categorized into two distinct types: elongated, streak-like structures with preferential orientation and cloud-like, unordered structures. At low wind speeds, the water surface is mainly dominated by streaks, whereas at higher wind speeds, the presence of cloud-like structures becomes more pronounced. In this section, we provide an initial qualitative description of the various near-surface fluorescence structures observed during the measurement campaign. The discussion remains purely descriptive, without quantitative analysis, and results solely from visual inspection of the image sequences. In all images, the wind direction is oriented from bottom to top.

6.1.1 Streak Patterns

As reported in earlier studies (Kräuter, 2015; Schnieders et al., 2013), streak-like patterns on a water surface arise due to Langmuir circulation or small-scale turbulent vortices that establish convergence and divergence zones within the turbulent flow field. An image sequence of these streak structures

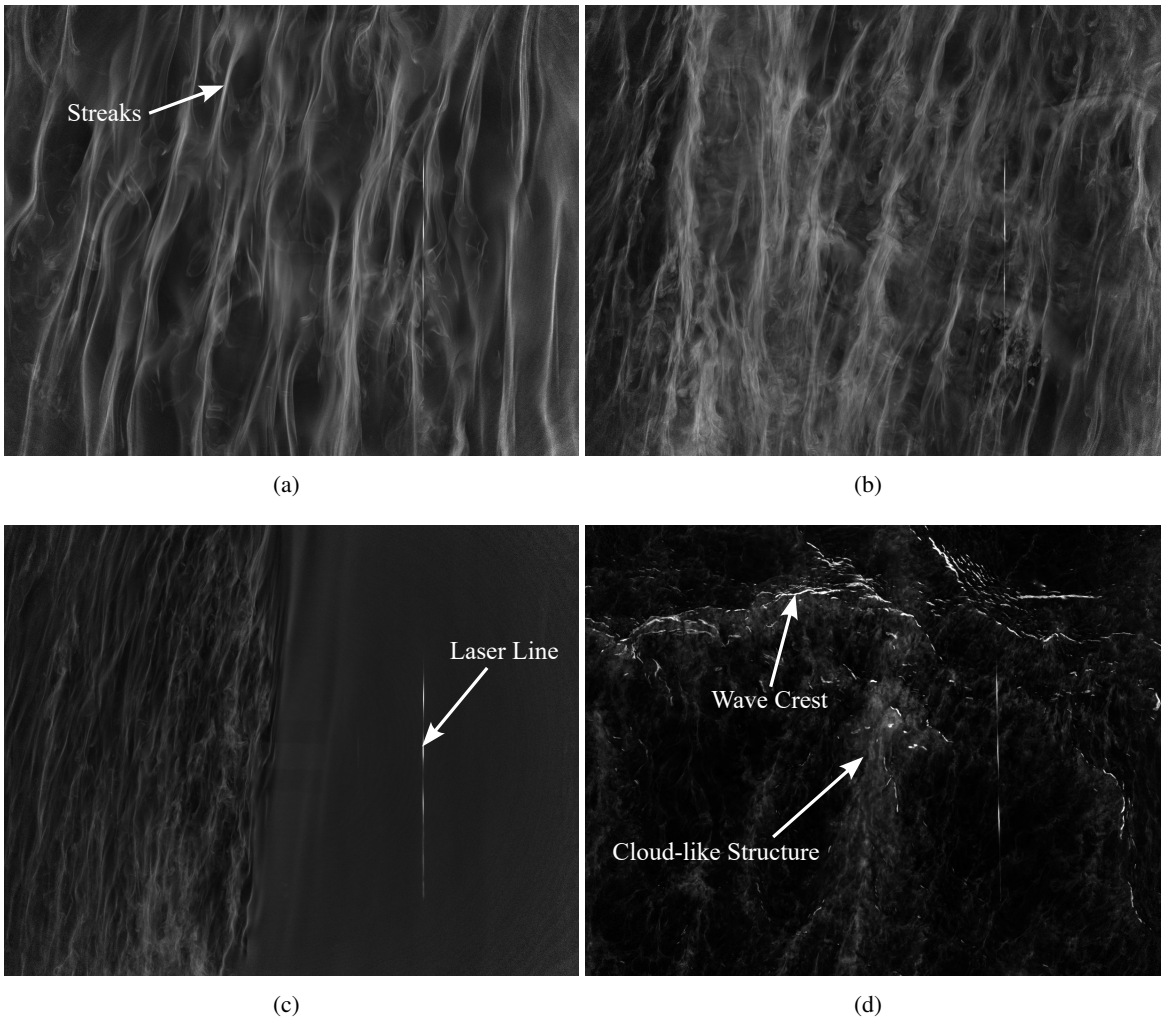

Figure 6.1: Variability of fluorescence patterns observed with Fluorescence Imaging. (a) Streak-like patterns at low wind speed (5.0 Hz). (b) More turbulent patterns at increased wind speed (10.0 Hz). (c) Hexadecanol film-covered water surface (14.1 Hz). The film is stable on the water surface, yet turbulent patterns form on the left side while no patterns appear on the right side. (d) Cloud-like structures at high wind speeds (25.2 Hz). Wave crests create reflections in the images.

can be viewed in the video provided by Hofmann (2025c), illustrating their spatial and temporal dynamics. In particular, convergence zones are associated with enhanced downward transport leading to vertical accumulation of the fluorescent component of pyranine. Consequently, these regions exhibit higher integrated fluorescence intensity, appearing as streaks in the convergence zones shaped by the existing cross-flows. In contrast, divergence zones are characterized by an upward transport leading to a depletion of pyranine near the surface. This leads to a locally reduced fluorescence intensity. Consequently, this spatial variability of the fluorescence signal directly reflects the heterogeneity of gas exchange. Importantly, both the convergence and divergence zones as well as the resulting orientation of the streaks are generally aligned with the wind direction. This also reveals the directional characteristics of the underlying turbulent flow structures. To further investigate the formation and properties of the streaks, we analyze their behavior in more detail by means of measurements with surface films and with variable fetch. These two conditions provide additional insights into the

prevailing turbulence mechanisms and their development over time.

Influence of Surface Films

Surface film experiments provide an approach to isolate the influence of wave-induced dynamics on near-surface turbulence structures. By effectively suppressing surface waves, they allow a clear separation of shear- and wave-driven mechanisms that contribute to the formation of surface streaks. Our measurements show that surface films of hexadecanol suppress wave formation up to wind speeds of 15.8 Hz, while Triton X-100 and olive oil extend this suppression up to 20.0 Hz. So under almost all measured conditions the water surface remains completely smooth in film measurements. Only at the highest tested wind speed (28.3 Hz) the surface film breaks down allowing waves to develop.
An exemplary comparison of the surface structures on a clean and a hexadecanol film-covered water surface is given in Fig. 6.2. Despite the absence of surface waves, Fluorescence Imaging reveals streak-like structures that are very similar to those visible on a clean water surface. However, there are important differences in their spatial organization. On film-covered surfaces, the streaks are densely packed, nearly equidistant, and comparatively straight. In contrast, the streaks observed under clean surface conditions are often curved, irregularly spaced, and exhibit local clustering. These differences imply two different mechanisms responsible for the formation of streaks: Langmuir circulations and quasi-streamwise vortices, as already reported in numerical simulations (Tsai & Lu, 2023). LCs result from the nonlinear interaction between wind-induced shear and the Stokes drift of surface waves. They generate large-scale convergence and divergence zones that manifest as streaks organized into regular, large-scale patterns over the surface. In contrast, QSVs are generated exclusively by shear-induced turbulence near the surface and produce aligned, small-scale vortex structures that self-organize into regular streaks. Another known contributor to small-scale surface patterns, namely fish-scale vortices, can be excluded here as they form hexagonal or honeycomb-like patterns that are not observed in our image sequences.

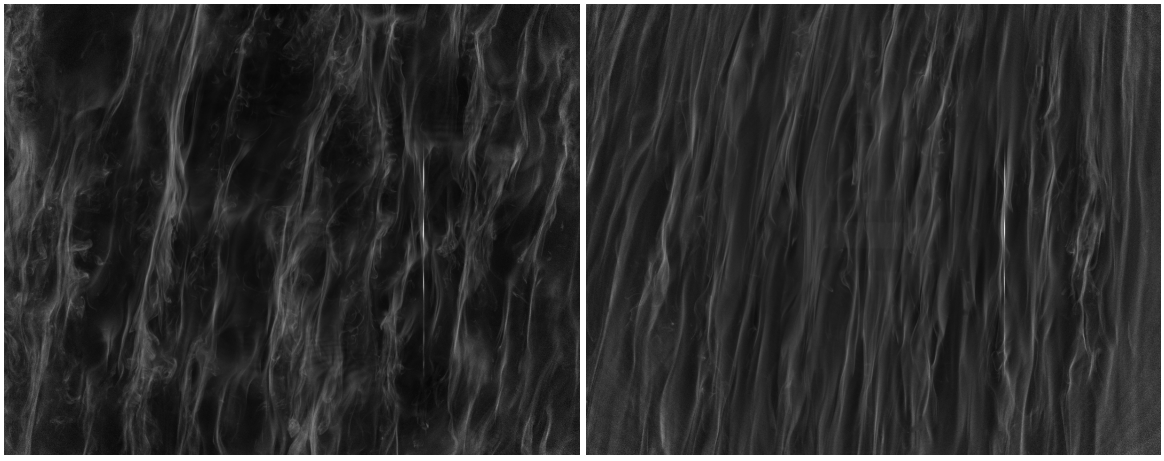

(a) (b)

Figure 6.2: Comparison of the streak-like patterns on a (a) clean and a (b) film-covered water surface. Streaks on a film-covered water surface are more orderly as in the case of QSVs. On a clean water surface, the streaks are more disordered due to the additional effect of the LCs.

Since LCs are inherently dependent on the presence of surface waves, their influence under film-covered conditions can be ruled out. The presence of regular, equidistant streaks under smooth surface conditions therefore confirms that QSVs alone are capable of generating such patterns. The high degree of spatial regularity observed in these cases is consistent with the expected behavior of QSVs when undisturbed by large-scale crossflows. Accordingly, the QSVs appear extremely regular in the absence of LCs. In contrast, in the presence of waves, as under clean water conditions, LCs introduce large-scale motions perpendicular to the wind direction. These secondary currents bend the streaks generated by QSVs and divert them into convergence zones, resulting in locally increased streak density and more irregular spacing. This shows that under clean surface conditions, both QSVs and LCs coexist and interact, resulting in the observed complex streak geometry. The coexistence of both mechanisms becomes particularly evident in transient cases when the surface film is temporarily disrupted. During brief intervals when the wind resumes after a break, small waves can re-emerge due to localized breaks in the film. In these areas, the streaks immediately transition from a regular, QSV-dominated arrangement to a curved and irregular configuration typical of an LC-dominated flow. Once the film reforms, the streaks quickly return to the regular QSV pattern. These rapid transitions emphasize the local, instantaneous, and reversible nature of the two turbulence mechanisms.
Finally, no significant differences in the fluorescence patterns are observable between the different types of tested films hexadecanol, Triton X-100, and olive oil (Fig. 6.3). This suggests that surface films primarily influence near-surface dynamics through their ability to suppress surface waves rather than through specific physicochemical properties. Although it is often assumed that surface films act as molecular barriers to gas exchange, our results suggest that their dominant effect is hydrodynamic by suppressing wave formation (Frew et al., 1995).

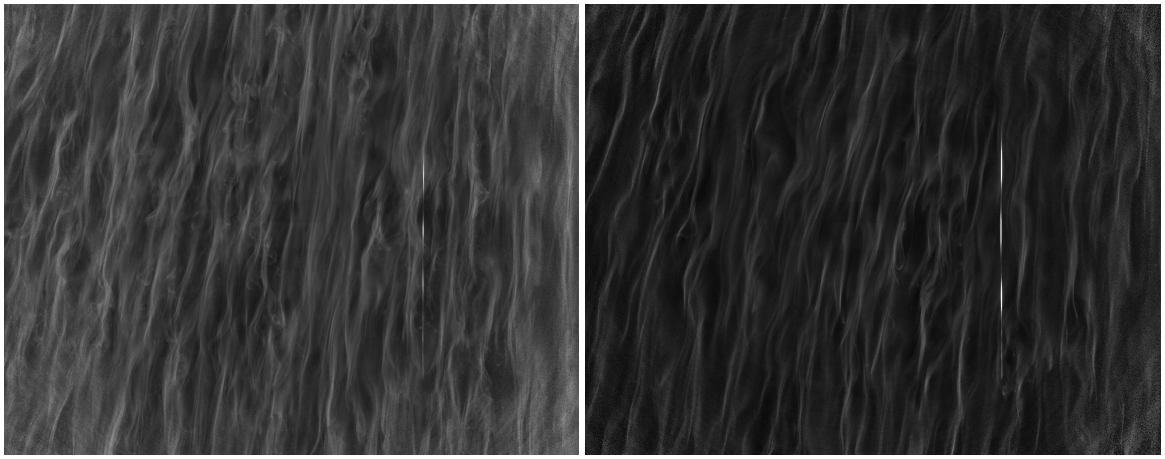

(a) (b)

Figure 6.3: Comparison of streak structures on film-covered water surface for (a) Triton X-100 and (b) olive oil. The pattern of fluorescent footprints is similar for the different films. In (b), the grayscale values are multiplied by 2 to compensate for the reduced illuminance caused by the loss of two laser units.

Influence of Fetch

Measurements with variable fetch are particularly relevant for understanding the temporal evolution of turbulent structures during the development of a wave field. A representative sequence of such an experiment is shown in Fig. 6.4, with the corresponding video available in Hofmann (2025d), taken shortly after the onset of the wind. Initially, the water surface shows a homogeneous fluorescence intensity without any recognizable structures. Accordingly, gas exchange occurs homogeneously. Shortly after the first capillary waves appear, this uniform distribution is broken, leading to the progressive formation of streak-like patterns. In the initial phase, these streaks appear elongated, well organized, and clear. After a further short period, however, the system undergoes a sudden transition in which additional turbulent structures are created. Once this transition has occurred, the fluorescence pattern corresponds to that of the equilibrium state, in which wind and wave fields are in balance. This temporal evolution can be observed at all low wind speeds where the streak-like patterns dominate.
A key observation here is that streaks become visible only after the initial appearance of capillary waves. However, considering the results of surface film experiments, in which streaks are observed even in the absence of waves, the question arises why these structures do not form in the initial fetch phase. One plausible explanation is that the near-surface shear flow is initially laminar and does not have sufficient turbulent energy for the formation of QSVs, which are known to be generated by turbulent shear. The initial streaks are therefore likely caused by LCs triggered by interactions between the newly forming capillary waves and the still laminar shear flow. As the fetch increases, the shear flow turns into a turbulent state, allowing the development of QSVs. Simultaneously, the increasing turbulence disrupts the coherence of LCs. Consequently, an equilibrium turbulence regime emerges, characterized by the simultaneous presence of both LCs and QSVs.
An open question remains regarding the precise nature of the observed transition with increasing fetch. Specifically, the sudden appearance of additional small-scale turbulent structures could indicate a genuine transition from laminar to turbulent shear flow. Alternatively, these structures could have already been present at greater depths and only become visible when the gas exchange extends into deeper layers of the water column. A comparison of the initial phase from measurements under equilibrium conditions, where the flow is expected to be fully turbulent from the outset, provides more insights. Shortly after the start of the gas input under such conditions, the turbulence field also appears relatively orderly, with elongated streaks. However, smaller vortices occur gradually over time in the case of a fully developed turbulence field, rather than appearing abruptly. The sudden transition observed during increasing fetch therefore likely marks the actual development from laminar to turbulent shear flow.
Additionally, the comparison with equilibrium turbulence structures suggests two potential explanations for the emergence of small-scale vortices in the fetch case. Either they emerge in deeper layers and only become visible when the turbulence propagates downwards, or the turbulent energy is transferred from large to small scales over time. On the one hand, the former is consistent with the classical theory of mass boundary layers, which states that turbulence and eddy fragmentation increase with the depth. On the other hand, the latter is in accordance with Kolmogorov's theory of turbulence, which describes a cascade of turbulent energy from larger to smaller scales. However, the exact origin cannot be determined from the image data.

In summary, these results clarify the sequence in which turbulent structures such as LCs and QSVs develop in a growing wave field. First, LCs develop due to interactions between capillary waves and a still laminar shear flow. This is followed by a transition to a turbulent shear flow during which QSVs become prominent. With increasing turbulence, the coherence of the LCs is disturbed, leading to the fully developed turbulence regime observed under equilibrium conditions.

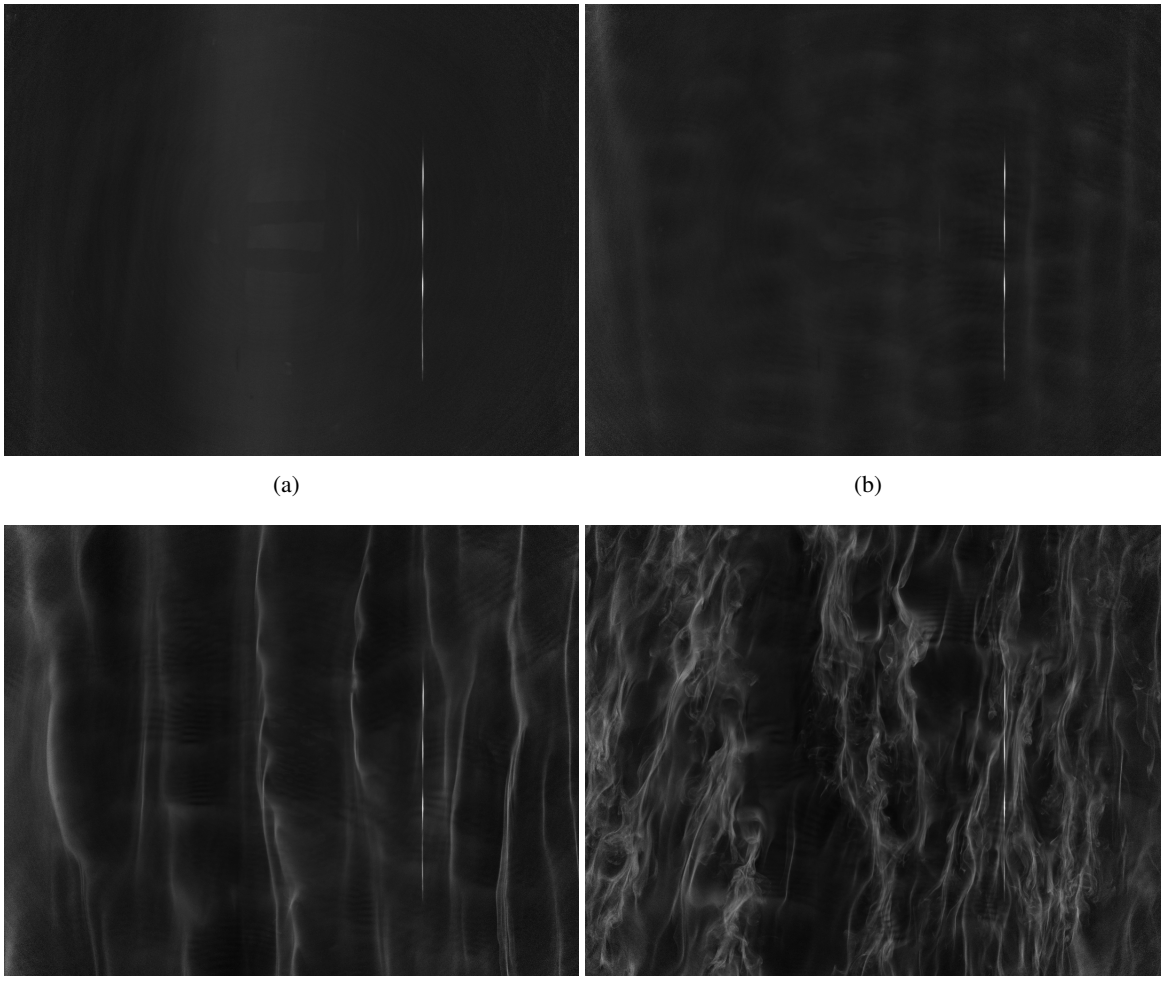

(a) (b)

(c) (d)

Figure 6.4: Creation of streaks with increasing fetch (7.1 Hz). (a) Homogeneous fluorescence intensity. (b) Appearance of the first capillary waves. (c) Formation of ordered streaks. (d) Transition of the initially ordered patterns to a turbulent fluorescence signal. The time interval between successive images is approximately 6 s.

6.1.2 Microscale Wave Breaking

A particularly important phenomenon, especially at low wind speeds, is microscale wave breaking (Jessup et al., 1997). This effect becomes clearly observable from wind speeds of about 6.3 Hz and is only absent at the lowest tested wind speed of 5.0 Hz as well as in the case of film-covered water surfaces.

An MWB event typically begins with a dominant wave crest, followed by intense swirling turbulence behind it, which visibly renews the water surface (Fig. 6.5). At low wind speeds, this process is

particularly pronounced as coherent streak-like structures are visibly disrupted by the passage of the wave, which leaves behind cloud-like turbulence patterns. As wind speed increases, both the frequency of MWB events and the surface area affected by each event grows. When comparing the fluorescent footprints of MWB with those resulting from the breaking of larger waves at higher wind speeds, there is no obvious visual difference, except that the turbulent regions appear darker at high wind speeds. This may be due to deeper penetration of turbulent energy, resulting in lower fluorescence intensity in the near-surface layers. In contrast, MWB tends to remain confined to the uppermost layer, resulting in stronger fluorescence signals. Finally, at high wind speeds, the MWB footprints can no longer be identified, as the large-scale wave breaking obscures all other structures.
It remains an open question whether MWB and large-scale wave breaking contribute to gas exchange in a similar way. However, given that MWB leads to clearly visible surface renewal even at low wind speeds, it is plausible that it plays a particularly important role in gas exchange under such conditions. For this reason, this effect is analyzed in more detail in the last section of this chapter.

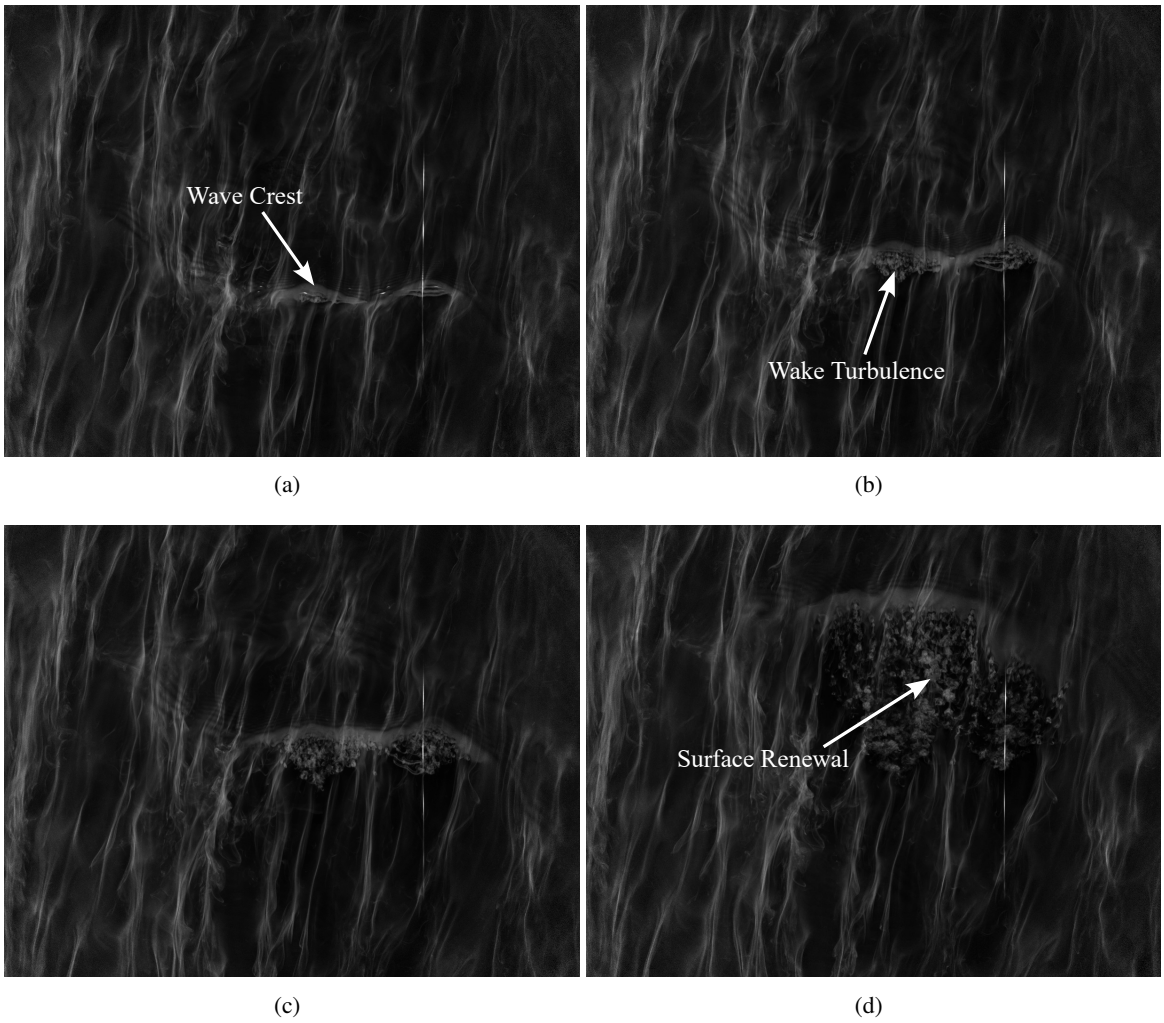

Figure 6.5: Temporal sequence of an MWB event (7.9 Hz). A dominant wave crest generates turbulent eddies behind it, which cause the ordered streaks to break up into cloud-like structures. The time interval between successive images is approximately 0.1 s.

6.1.3 High-Turbulence Patterns

At higher wind speeds, the Fluorescence Imaging reveals a distinct shift in the dominant fluorescent patterns. While elongated streaks remain characteristic at lower wind speeds, these structures become increasingly chaotic and less coherent with growing wind speed. Instead, irregular, cloud-like fluorescence patterns appear, which eventually dominate the near-surface signature at above 20.0 Hz. This structural change is illustrated in Fig. 6.6 by comparing scenarios with moderate and high wind speeds. While the streaks are still partially visible at moderate wind speeds, they are completely obscured at high wind speeds and replaced by the more diffuse, turbulent patterns.
The cloud-like structures are indicative of small-scale, disordered vortices that locally mix the concentration field and renew the water surface. A video showing these cloud-like structures in action is available at Hofmann (2025e), illustrating their dynamics at higher wind speeds. Their formation is closely linked to wave breaking, which introduces intense turbulence into the upper water layers. At low wind speeds, such structures may occur sporadically as a result of MWB, typically in isolated patches. However, with increasing wind speed, larger and more frequent wave breaking appears, producing widespread turbulent renewal and leading to the dominance of these cloud-like structures. Two complementary mechanisms can explain the observed transition from ordered streaks to chaotic, cloud-like patterns. First, increasing wind speeds lead to greater turbulent energy input into the water. This increases the intensity of the near-surface turbulence, which further destabilizes and eventually destroys the coherent flow structures responsible for the streak formation. The resulting turbulent field becomes more isotropic and disordered, which manifests itself in cloud-like fluorescence distributions. Second, according to Kolmogorov's theory of turbulence, the energy injected at larger scales is transferred to smaller scales through a cascade process. This leads to the formation of numerous small-scale vortices that obscure the streaks and create the diffused cloud-like patterns.
Although these cloud-like patterns dominate under conditions of high turbulence states, their description is not yet correctly captured by existing theoretical models.

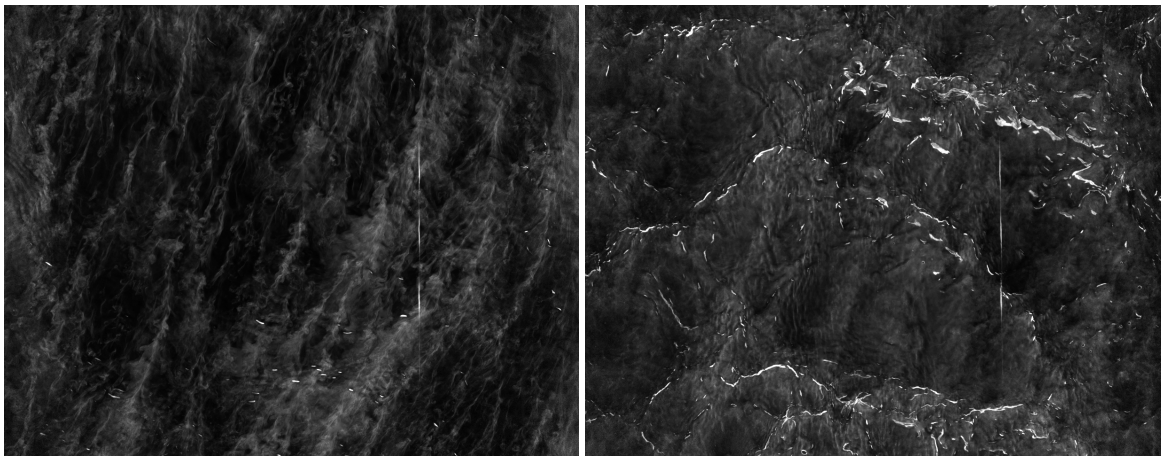

(a) (b)

Figure 6.6: Comparison of fluorescent structures at (a) medium (20.0 Hz) and (b) high wind speeds (35.6 Hz). While streaks are still visible at medium wind speeds, they are completely broken up at high wind speeds.

6.1.4 Summary

In summary, the qualitative analysis of the Fluorescence Imaging sequences identifies three different types of fluorescent surface patterns, each associated with a different mechanism contributing to gas exchange:

- Quasi-Streamwise Vortices
- Langmuir Circulations
- Cloud-like Structures

While QSVs reflect the contribution of turbulence generated by the turbulent shear flow, LCs represent transport processes arising from the interaction of surface waves and shear flow. Last, the cloud-like structures are the result of wave breaking, which can be further subdivided into MWB and visible wave breaking at higher wind speeds. A key difference between these two is the size and spatial impact of the resulting turbulence. On the one hand, MWB produces localized, surface renewal, on the other hand, wave breaking at high wind speeds generates broader, deeper-reaching fields of turbulence. Despite these differences, their visual signatures in the fluorescence images appear remarkably similar.

6.2 Fluorescence Intensity Analysis

A simple yet efficient approach for quantitatively evaluating the fluorescence footprints in the image sequences is to analyze the fluorescence intensity. The most efficient way to achieve this is to calculate image histograms over the entire sequence. These histograms provide information about the statistical distribution of pixel intensities and offer a memory-efficient method for analyzing the extensive image data.

6.2.1 Image Statistics

A grayscale histogram is computed for each individual frame of the preprocessed image sequence by adding up the frequency of each grayscale value. To ensure reliable results, the histogram is only calculated over image areas with a sufficiently high SNR. This is achieved by applying the binary image mask, which excludes low-signal regions in the image corners. Furthermore, the laser line is also excluded from the calculation by means of the laser mask. Based on these histograms, the mean fluorescence intensity and the standard deviation are extracted. Since the evaluation is carried out over the entire image sequence, all statistical parameters are obtained as time series.
Of particular interest is the time-resolved evolution of the mean fluorescence intensity. Notably, this temporal development matches approximately the course of the methylamine gas concentration in the air (cf. Sec. 5.2) and thus reflects the dynamic gas flux into the water (Fig. 6.7). This correspondence demonstrates that fluorescence intensity provides an indirect but effective means of accessing vertical transport processes at the air-water interface. In the following chapter, we show how these observations can be used to infer water-side gas transfer velocities.

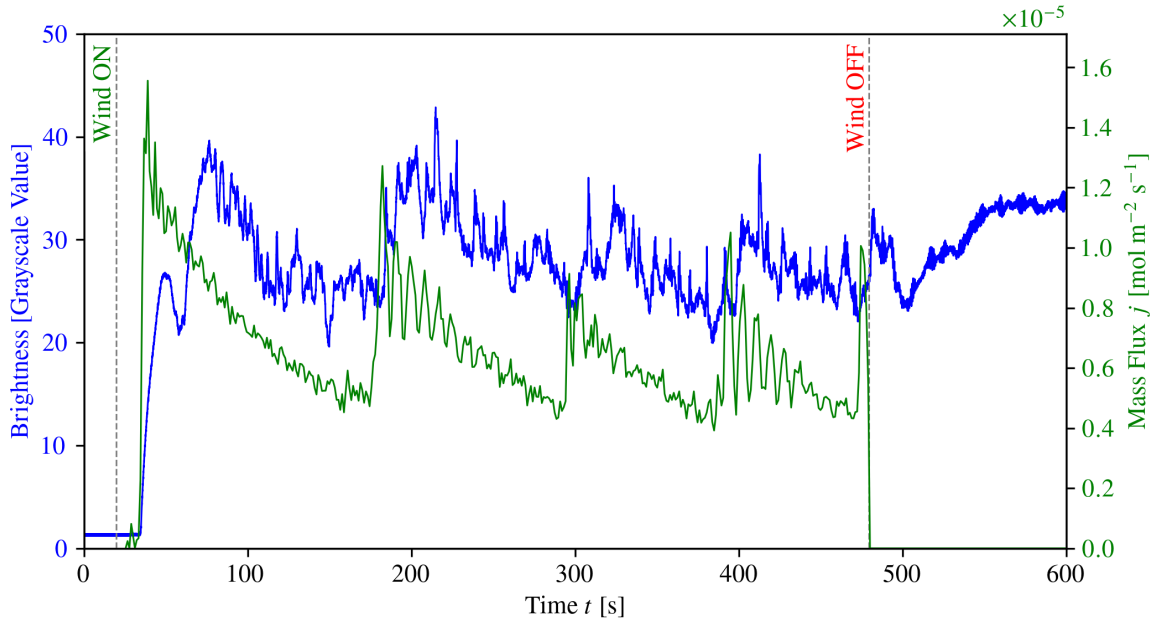

Figure 6.7: Comparison of the time series of the spatially averaged fluorescence brightness with the mass flux. The temporal variations of the gas flux are mirrored in the fluorescence brightness. After switching off the wind, the mass flux is no longer determinable.

6.2.2 Probability Density Function

To put the observed intensity distributions of the histograms into a mathematical framework, we try to describe them with a probability density function. In this case, we make use of a log-normal distribution, which is commonly used to model variables that are the result of multiplicative random processes. The probability density function of a log-normal distribution defined by the parameters mean μ and standard deviation σ is given by

$$f(x;\mu,\sigma) = \frac{1}{x\,\sigma\sqrt{2\pi}} \exp\left(-\frac{(\ln x - \mu)^2}{2\sigma^2}\right), \quad x > 0. \tag{6.1}$$

In order to fit this distribution to the image data, each histogram is first normalized by dividing all bin numbers by the total number of pixels to ensure that the total probability is 1. A lognormal curve is then fitted to the normalized histogram for each frame in the sequence.

It is found that the grayscale intensity distributions of the fluorescence signal are well described by this log-normal distribution, particularly under conditions of sufficient brightness. This is illustrated in Fig. 6.8. Although the underlying physical model for this good agreement is unclear, some possible explanations can be proposed. The log-normal distribution often occurs in systems where one variable is influenced by the multiplicative interaction of many independent random processes. In the context of Fluorescence Imaging, the observed intensity at each pixel may be the result of a complex interaction between turbulent transport, diffusion, and optical propagation. All of these processes may contribute multiplicatively to the final signal. The statistical nature of the fluorescence distribution may therefore reflect the cumulative effect of these processes. Similar statistical behavior has also been observed in other physical systems involving turbulence transport. For example, numerical simulations show

a lognormal distribution of turbulent kinetic energy on large horizontal scales of the ocean surface (B. Pearson & Fox-Kemper, 2018).

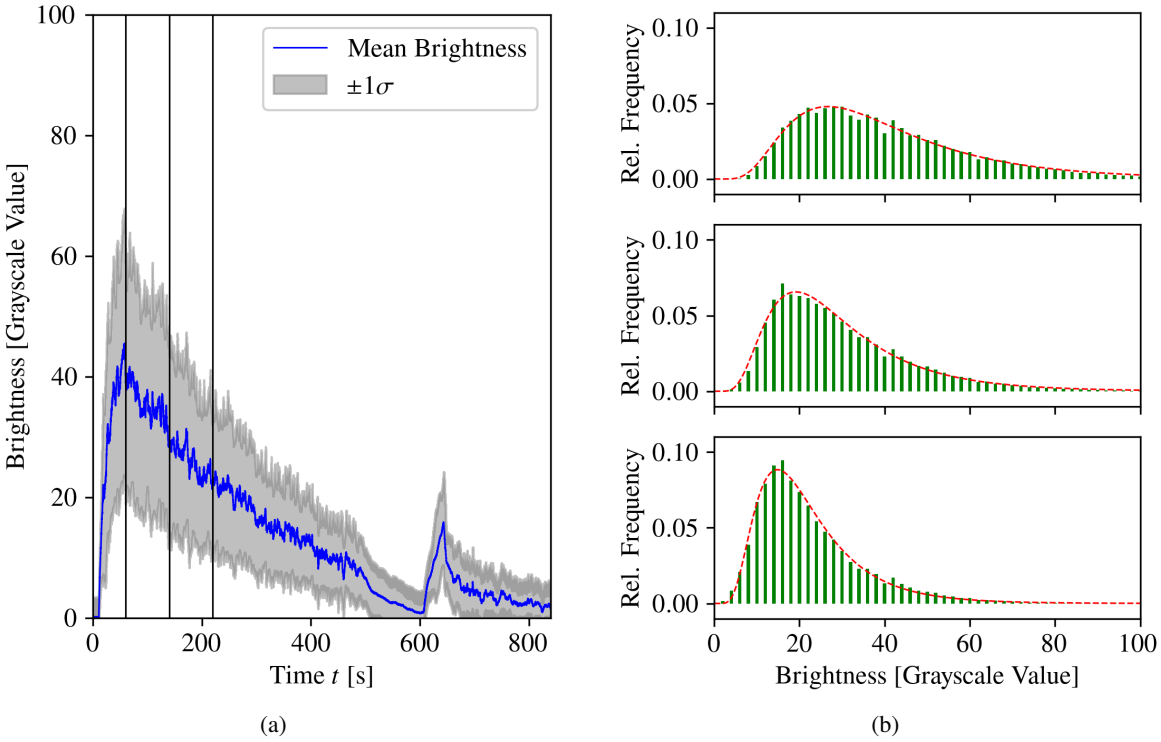

Figure 6.8: Analysis of the image histograms over time. (a) Spatially averaged fluorescence brightness over time. (b) Associated grayscale histograms at three different time points, indicated by the black lines in (a). The grayscale histograms are well described by a logarithmic normal distribution (red).

6.3 Microscale Wave Breaking Analysis

One of the most striking effects observed in the image sequences is MWB. This phenomenon is suspected to contribute significantly to gas exchange, especially at low wind speeds (Zappa et al., 2004). Accordingly, its analysis is of particular importance within this study. The MWB events are visually recognizable in the images due to the turbulence that forms behind the wave crest. These turbulent regions disrupt the previously ordered, streak-like structures and creates a rather chaotic, cloud-like pattern. While MWB events are associated with visible surface renewal, where structures are transported to deeper layers, they do not necessarily lead to a reduction in brightness behind the wave crest. In fact, the turbulent eddies caused by MWB often appear brighter overall compared to the more localized, ordered streaks. This characteristic pattern emphasizes the need for a detection algorithm capable of identifying such events that goes beyond simple thresholding techniques used in previous studies (Klein, 2019; Kräuter, 2015; Zappa et al., 2004). The following section introduce an advanced detection algorithm that utilizes spatio-temporal image features to robustly identify MWB events. This allows the derivation of a spatially and temporally resolved surface renewal rate afterwards.

6.3.1 Detection Algorithm

The MWB detection algorithm integrates elements of structure tensor and optical flow analysis. Its core idea is to identify regions with a high density of corner-like features, indicating the visual chaos caused by MWB-induced turbulence. The algorithm operates frame-by-frame across the entire image sequence. However, due to the relatively slow temporal evolution of MWB compared to the high frame rate of the acquisition, the analysis is only performed on every fourth frame, corresponding to an effective frame rate of 125 Hz. This temporal downsampling is sufficient to reliably detect MWB events and simultaneously reduce the computational cost. An illustrative example of the step-by-step application of the algorithm is shown in Fig. 6.9. The visualization steps shown do not correspond directly to the numbered procedure, but are intended to illustrate the overall process. A full demonstration of the algorithm in practice is provided in the accompanying videos Hofmann (2025f) and Hofmann (2025g).

Step 1 - Keypoint Detection

The initial step involves applying an Oriented FAST and Rotated BRIEF (ORB) detector to an image to identify salient keypoints (Fig. 6.9(b)). This detector integrates the feature detection capabilities of the FAST algorithm with the feature description of the BRIEF algorithm in a modified rotation-invariant form. Its detailed functionality is reported in Rublee et al. (2011). The FAST detector identifies potential corner candidates by comparing the intensity of each pixel with the intensities of the 16 neighboring pixels located on a circular ring with a radius of 3 pixels. A pixel is classified as a corner candidate if at least 9 neighboring pixels differ significantly in brightness compared to the central pixel. The sensitivity of this comparison is controlled by a brightness threshold, which is set to 20 by default. This FAST detection is performed across eight levels of an image pyramid with a scale factor of 1.2, enabling the detection of scale-invariant keypoints. To further achieve rotation invariance, ORB computes the orientation of each keypoint using the intensity centroid method, which estimates the direction of the local intensity gradient. The BRIEF descriptor is then rotated accordingly, ensuring that the resulting feature vector remains stable under in-plane rotations. Since the previous steps tends to detect an extensive number of keypoints, including both corners and edges, an additional filtering step is introduced using a Harris corner response. This approach evaluates the intensity gradients in different directions, similar to the structure tensor, and assigns a quality score to each pixel indicating the likelihood of it being a corner. The detected keypoints are ranked based on their Harris score, and only the high-scoring points are retained. Here, the selection threshold is set to 1000 keypoints. Although the keypoints identified by the ORB detector do not exclusively belong to MWB events, as other turbulent processes can also produce corner-like structures, the ORB detector has proven to be the most reliable option among several tested feature detectors (FAST, SIFT, SURF). The subsequent steps are designed to specifically minimize the number of false keypoints.

Step 2 - Clustering

At this stage, a number of candidate keypoints have been identified but have not yet been assigned to an MWB event. A visual analysis of the detected keypoints reveals that MWB events are typically

characterized by a high local density of such features. Based on this observation, the next step is to cluster the keypoints to identify regions of interest. Clustering is performed using the DBSCAN algorithm (Ester et al., 1996), which groups keypoints that lie in a certain spatial proximity and occur in sufficient density. Specifically, a cluster must consist of at least 20 keypoints and the maximum allowable distance between neighboring points is set to 20 pixels. As a result, the previously detected keypoints are grouped into coherent clusters, while those that do not meet this threshold criteria are discarded (Fig. 6.9(c)). Typically, an MWB event begins with a pronounced wavefront at which a significant number of keypoints can be detected and clustered. As this wavefront propagates, turbulent vortices typically detach behind it, forming a characteristic visual feature of an MWB event. The temporal development of these features will be investigated in the next step.

Step 3 - Tracking

To analyze the dynamic evolution of the identified clusters throughout the image sequence, a tracking step is implemented. This algorithm relies on the correlation method described in Sec. 2.4.2. For each keypoint within a cluster, a $32\,\mathrm{px} \times 32\,\mathrm{px}$ patch is defined, with the keypoint positioned in the center (Fig. 6.9(d)). This image patch serves as a template for the correlation method. In the subsequent frame, the image region with the highest correlation to the template is identified, allowing the shift of each keypoint to be determined. The search area for the displacement is constrained to a region that does not extend more than 20 pixels in any direction around the template's current boundaries. This restriction represents a compromise between computational efficiency and physically plausible motion. A smaller search area reduces the number of possible cross-correlation calculations, while a sufficiently large search area ensures that the keypoint remains trackable between successive frames. Naturally, as the frame rate would decrease, the required search area has to increase, leading to a sublinear rise in computational effort. In addition, a minimum correlation threshold of 0.2 is imposed. If the peak correlation between the template and candidate regions falls below this value, it is assumed that no reliable correspondence could be found for that keypoint in the subsequent frame. This ensures that only confidently matched displacements are used for tracking. By applying this tracking approach to each keypoint, the joint movement of the keypoint-containing clusters within the image sequence is traced (Fig. 6.9(e)).

Step 4 - Motion Threshold

So far, we have identified potential MWB events solely based on the local density of keypoints, without yet verifying their dynamic character. To establish a clear link to MWB events, an additional criterion is applied in terms of movement. As previously mentioned, the early phase of an MWB event is characterized by a prominent wave crest that propagates faster than the underlying turbulent structures. To isolate clusters that exhibit this dynamic behavior, a velocity threshold is applied. Specifically, the mean velocity is calculated for each cluster using the temporal displacement of the individual keypoints determined in the tracking step. A cluster is then classified as an MWB event if its average velocity exceeds a threshold of 5 pixels per frame for at least five consecutive frames. This threshold corresponds to a phase speed of approximately $25\,\mathrm{cm\,s^{-1}}$, which is a suitable value

for delimiting the transition from the capillary to the gravity wave regime. It is therefore consistent with the dynamics of MWB, which occur with short gravity waves. Clusters that do not fulfill this condition are discarded as non-MWB-related features. With this step, the selection of valid keypoints and their assignment to MWB-related clusters is completed. The final stage focuses on analyzing the temporal evolution of these validated clusters.

Step 5 - Iteration

The steps 1 to 4 are now applied iteratively across the entire image sequence for each individual frame. However, if there are already existing clusters in the current image, the workflow is adjusted accordingly. Newly detected clusters are checked whether they overlap with existing clusters or are within 50 pixels of an existing cluster. If this condition is met, it is assumed that the registered keypoints of the new cluster belong to a turbulent pattern of an ongoing MWB event. Consequently, these keypoints are assigned to the existing cluster, bypassing the velocity threshold verification from step 4. A further refinement addresses the growing number of keypoints that can accumulate over time for a single MWB event. This may significantly increase the computing costs, as numerous motions have to be tracked. To counteract this, only keypoints that contribute to an informational gain are retained. Specifically, during each iteration step, a mask is used that represent the current coverage of all keypoints' templates. Each newly clustered keypoint is evaluated to determine whether its associated template patch extends this coverage. Thus, keypoints whose patches lie entirely within already covered regions are discarded, as they do not provide any new information about the spatial extent of the MWB event. In addition, the laser line mask extracted during preprocessing is integrated into the overall mask. This prevents the detection of keypoints in the laser line region, where strong intensity gradients create bright, high-contrast features in the image. These artificial contrasts often trigger keypoint detections by the ORB detector, even though they are unrelated to any turbulent flow structures.
This iterative approach, combined with the outlined modifications, provides a visual representation of the temporal evolution of MWB events. It captures both the growth of these events by accumulating keypoints in an expanding turbulent zone behind the wave crest as well as the continuous tracking of their movement over time.

Step 6 - Characterization of MWB Events

The characterization of MWB events is not a conventional sequential step but occurs in parallel with the iteration process for each registered cluster. The primary metric used for event characterization is the convex hull enclosing the detected keypoints, which is updated for each frame. This convex hull defines the spatial extent of the MWB event. Over the image sequence, this detected area is accumulated using a binary mask. To avoid overcounting, only the union of newly added regions is taken into account ensuring that overlapping areas between consecutive images of one single event are not counted multiple times. Tracking the temporal evolution of an event's area also helps to establish when an MWB event has been concluded. During the active phase, turbulence usually leads to a steady increase in the affected area. Based on this, a termination criterion is implemented. When the

area of an event increases by less than 10 % of its current size in each of five consecutive frames, the event is considered as completed (Fig. 6.9(f)). At this point, it is assumed that the event no longer contributes significantly to surface renewal. From then on, only the motion of the event is tracked, while its region is excluded from further keypoint detection. This exclusion is done by including the final event region in the detection mask, discarding all newly detected keypoints within this region. Once an event is classified as complete, its accumulated surface renewal area is enclosed by a final convex hull. This step helps to close potential gaps in the renewal mask caused by the discrete nature of the frame-by-frame keypoint detection. Finally, the mask of each completed event is added to a cumulative map that summarizes all detected MWB events. This final output of the detection algorithm is a spatial distribution showing the number of MWB events that have occurred at each pixel within the observed area.

6.3.2 Post-Processing of Surface Renewal Map

Although the detection algorithm accurately identifies areas exposed by an ongoing MWB event, it tends to overestimate the number of events. Specifically, certain regions are falsely classified as MWB events when bright structures are present and a capillary wave propagates over them, despite the absence of actual wave breaking and surface renewal. The primary reason for these false detections is that the strong intensity variations of the existing structures lead to the detection of a sufficient number of keypoints, which are then clustered together. Additionally, since the passing wave momentarily exceeds the velocity threshold for the same pixels, both detection criteria are fulfilled independently rather than through a single unified process, as is the case with MWB events. These false detections predominantly occur under conditions of high gas flow, where the contrast of streaks is more pronounced. In such scenarios, the modified quality assessment of the ORB detector results in the detection of a large number of keypoints along the streaks. Consequently, to ensure that only genuine MWB events are considered in subsequent analyses, a post-processing correction step is necessary. This correction involves a manual visual inspection of the detected clusters. Each cluster is assigned a unique ID during detection, which is displayed in the processed image sequence for easy identification. In this way, the entire sequence can now be reviewed retrospectively by assigning each cluster whether it is a genuine MWB event or a false detection. Based on the assigned IDs, a refined surface renewal map is created that includes only the cluster areas identified as true MWB events.

6.3.3 Determination of Surface Renewal Rate

The MWB detection algorithm yields a surface renewal map indicating for each pixel how often it is affected by MWB events. This cumulative map of surface renewal calculated over the entire image sequence provides valuable insight into the spatial distribution and homogeneity of these events (Fig. 6.10(a)). However, it is not suitable for a direct quantification of the surface renewal rate, as it lacks temporal resolution. Additionally, variations in the wind speed schedule throughout the image acquisition are not considered. So, further processing steps are required to derive a meaningful estimate of the average surface renewal rate. The following steps are performed individually for each surface renewal map generated from batches of 250 images. Each batch results from MWB detection

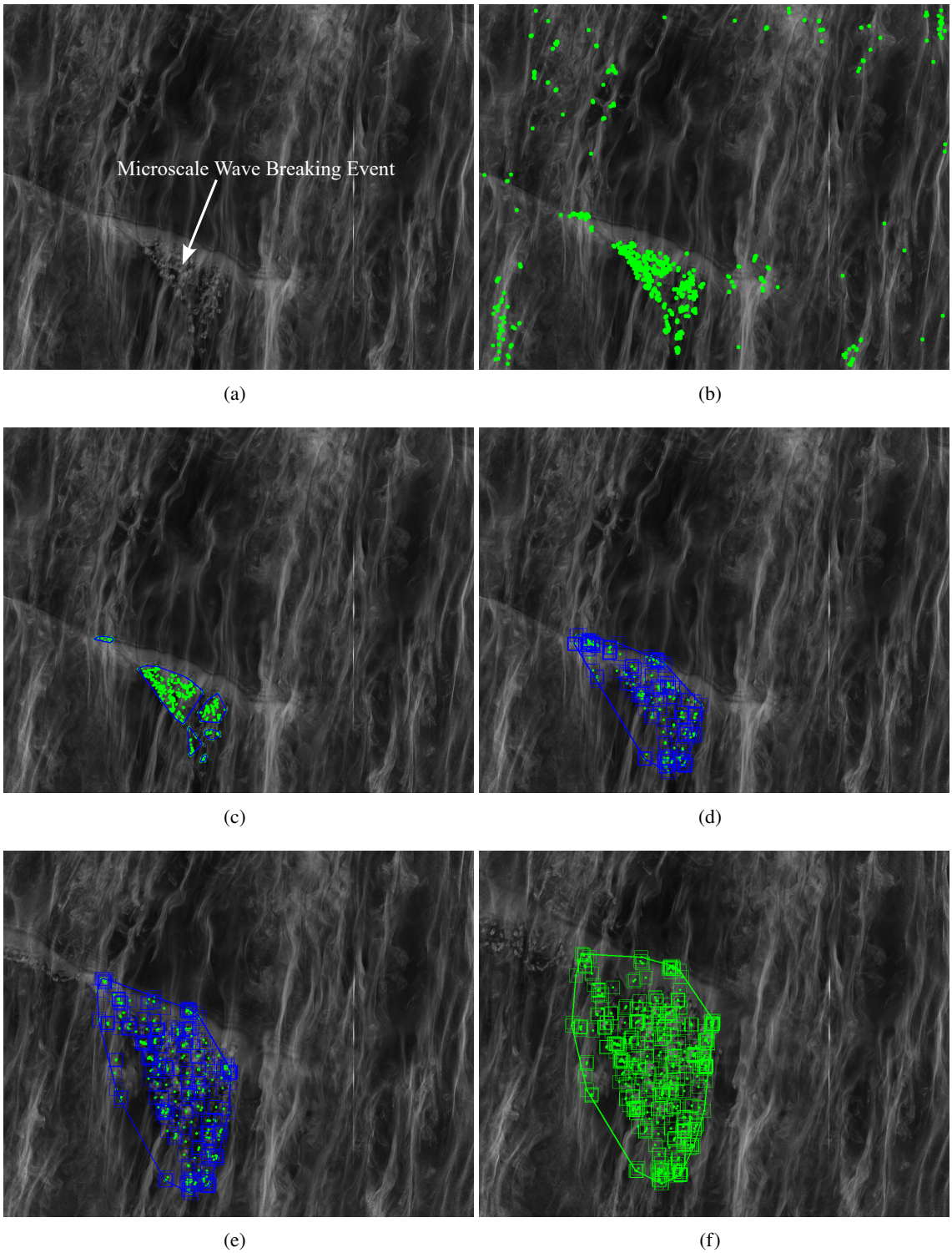

Figure 6.9: MWB Detection Algorithm. (a) Formation of an MWB event. (b) Application of an ORB detector identifies potential keypoints of corner-like structures. (c) DBSCAN clustering extracts keypoints with sufficient density. (d) Creation of template patches in a (32, 32) window around the keypoints. (e) Tracking of template patches of all keypoints by correlation method. (f) Completion of an MWB event if the convex hull area increases no more than 10 % for 5 images. Active events are shown with blue templates and convex hull, completed events with green.

of every 4th image of the original batches with 1000 raw images. With this approach, the temporal evolution of surface renewal can be reconstructed.

First of all, image regions at the edges must be cropped, as the surface renewal is always zero in these areas. These inactive areas result as artifacts from the limitations of the keypoint tracking method. A keypoint can only be tracked reliably as long as its surrounding template patch remains completely within the image domain. Since MWB convex hull areas are bounded by the central keypoint position in the template window, the edges of the image remain inaccessible to the event's surrounding area. To correct this, 16 pixels are cut off from each edge of the image, which corresponds to the half width of the template tracking patch. In addition, only the image regions lying within the binary image mask are included in the analysis (cf. Sec. 5.4.1). This ensures that MWB events detected in the corners, where the SNR is usually lower, are excluded due to their potentially lower reliability. Next, to compute the average renewal rate, the cropped surface renewal map is averaged over its spatial domain. This spatial averaging provides a measure of how often the entire imaged area is renewed within the specified time interval. Since each image batch corresponds to a 2-second interval, division gives the renewals of the surface per second.

By plotting the development of the average surface renewal rate over the duration of the entire image sequence (Fig. 6.10(b)), the statistical character of MWB becomes obvious. In particular, the temporal fluctuations under non-equilibrium conditions are also observed. This is especially evident during phases when the wind is turned off, as the MWB vanishes completely. In order to determine a representative value for the surface renewal rate, it is therefore crucial to average over a well-chosen time interval in which quasi-stationary conditions prevail. The criteria for selecting this time window are twofold. First, the image brightness must be sufficient, as MWB detection is more robust under high-contrast conditions. Second, the interval must be long enough to ensure the statistical reliability of the observed MWB frequency. It was found in the experiments that averaging over a period of 3 min, starting 30 s after the beginning of the acquisition, fulfills both conditions. The resulting average serves as a representative surface renewal rate for the equilibrium state associated with the respective wind condition.

The corresponding equilibrium renewal rates for different wind conditions are shown in Fig. 6.10(c). Only the measurements from measurement week 1 are included, as these were conducted under equilibrium conditions and so the selected averaging interval fulfills the criterion of a quasi-stationary state. For experiments with variable fetch, the averaging interval would have to be selected differently. In order to allow a better comparison, the data are plotted against the measured friction velocity corresponding to the respective wind condition, as this parameter provides a more meaningful representation of the wind profile than the Aeolotron-specific wind control frequency (cf. Sec. 4.2.5). An uncertainty of 10 % is assumed for the renewed surface area, as the use of a convex hull does not allow a more accurate determination of this quantity. In general, the delimitation of the area renewed by an MWB event can only be estimated. Even with a manual assessment, it would be difficult to determine exactly which part of the surface is affected by an event. Plotting the surface renewal rate against the friction velocity shows the expected increase in renewal processes with increasing shear stress for the clean water surface. Furthermore, for the lowest wind setting and the film-covered water surface, no surface renewal processes can be detected.

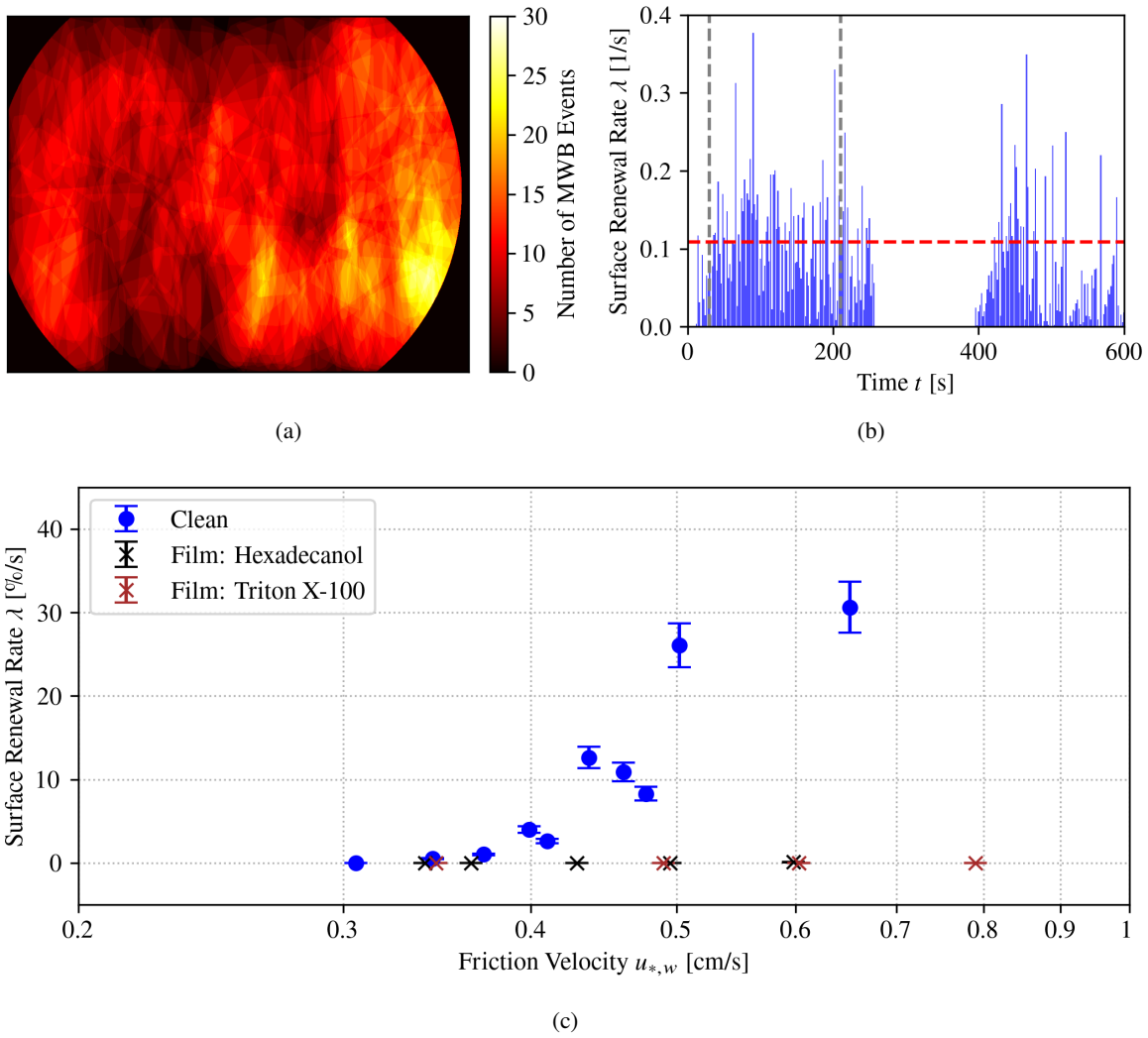

Figure 6.10: Surface renewal data of MWB. (a) Cumulative surface renewal map of the image domain. The image corners with low SNR are masked with the image mask. (b) Time-resolved surface renewal rate over the time course of a measurement. The wind is switched off between 260 s and 380 s. Averaging over the selected interval (gray lines) results in a representative mean surface renewal rate (red line). (c) Average surface renewal rate as a function of friction velocity. The values correspond to the respective mean value (red line) determined from (b). Note that the renewal rate in (c) is given in percentage of the image area.

6.3.4 Determination of Schmidt Number Exponents

Based on the surface renewal rate, an estimate can be made of the total area continuously affected by MWB events. This in turn provides access to the Schmidt number exponent. The determination of the Schmidt number exponent is carried out here using the facet model and the total surface area obtained by MWB detection (cf. Sec. 2.2.3). It is assumed that, on the one hand, the surface area renewed by MWB events exhibits the boundary condition of a rough water surface associated with a Schmidt number exponent of $n_w = \frac{1}{2}$, and, on the other hand, only this area fulfills this condition. Conversely, the remaining surface area unaffected by MWB is assumed to behave like a smooth water surface, related to a Schmidt number exponent of $n_s = \frac{2}{3}$. These assumptions only apply at low wind speeds, where MWB is the dominant surface renewal mechanism and large-scale wave breaking is negligible.

Fortunately, a transition of the Schmidt number exponent is theoretically expected under these wind conditions, making this regime particularly suitable for studying the effects of MWB.
The most challenging step in this analysis is the conversion of the surface renewal rate into a fractional surface area a_w. This is only possible by defining a recovery time, which describes how long a pixel renewed by MWB maintains the characteristics of a rough surface. The fractional area permanently affected by MWB is then estimated by multiplying the surface renewal rate by the average recovery time of the surface. Based on the facet model in Eq. (2.62), the Schmidt number exponent is calculated from the resulting fractional area a_w. The calculation employs experimentally evaluated values for the dimensionless scaling factors $\beta_s = 12.2$ and $\beta_w = 6.7$ (Krall, 2013), together with the Schmidt number for methylamine given in Sec. 3.3.3. In Fig. 6.11 the resulting Schmidt number exponents are shown which are derived from the surface renewal data presented in Fig. 6.10(c). For clean water surface conditions, different recovery times are assumed to estimate the fractional area a_w. Each recovery time leads to a unique estimate of the Schmidt number exponent via the facet model. In addition to this, the plot is complemented with the data of the film-covered water surface conditions. Due to the absence of observable surface renewal under these conditions, a constant Schmidt number exponent of $n = \frac{2}{3}$ is predicted. As a reference, gas exchange data measured in 2017 by K. Krall (unpublished, personal communication), which are the most accurate Aeolotron measurements to date, are also included. The transition of the Schmidt number exponent is parameterized as a function of

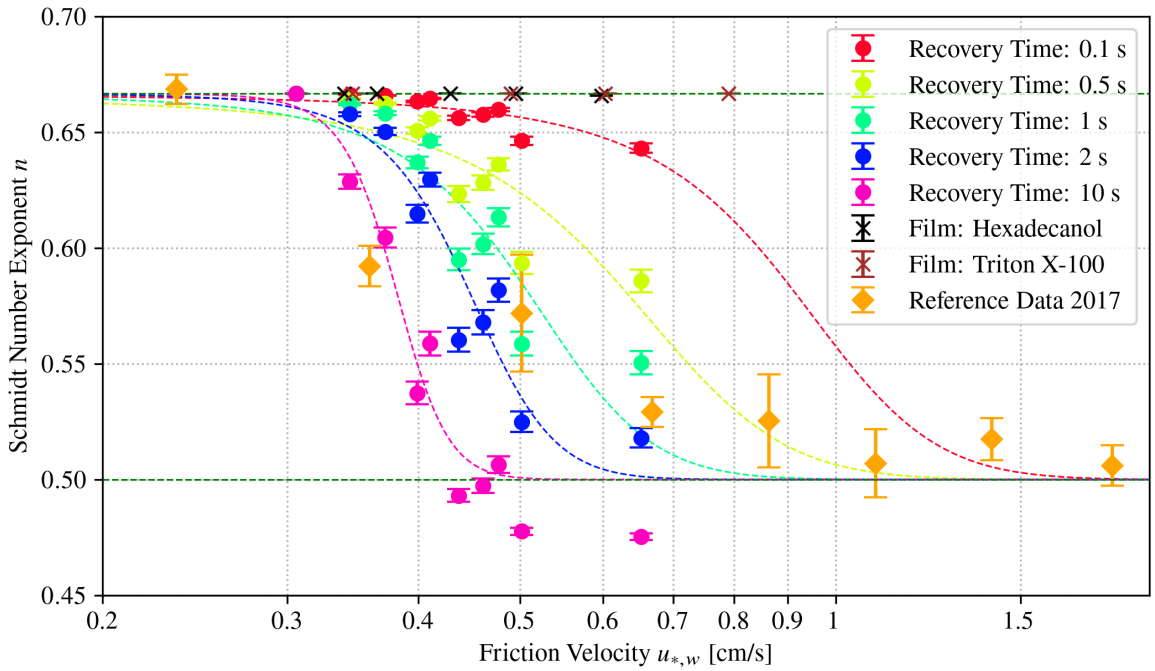

Figure 6.11: Schmidt number exponent in dependence on the friction velocity extracted from the surface renewal rates of MWB. The values for a clean water surface are calculated assuming the facet model with different recovery times of an MWB event. Each curve with clean water surface is fitted with a sigmoid function.

the friction velocity for all data points with a clean water surface at different recovery times. While previous parameterizations are theoretically motivated only in terms of mean square slope, we propose

a parameterization based on friction velocity using the following sigmoid function

$$n(u_{*,w}, a, b) = \frac{2}{3} + \left(\frac{1}{2} - \frac{2}{3}\right) \frac{1}{1 + \exp\left(-\frac{u_{*,w} - a}{b}\right)}, \tag{6.2}$$

with the free parameters a and b. This choice ensures that the function asymptotically approaches $n = \frac{2}{3}$ for low wind speeds and $n = \frac{1}{2}$ for high wind speeds, providing a smooth transition without local extrema. The sigmoid function allows a convincing fit to the observed Schmidt number transition.

It becomes evident that the recovery time strongly influences both the position of the inflection point along the x-axis and the steepness of the transition. Increasing the recovery time shifts the transition to lower friction velocities and leads to a steeper slope, as a longer recovery time implies that renewed pixels retain the boundary conditions of a rough surface for a longer period. This leads to a larger effective fraction of the renewed surface and thus causes an earlier transition towards the exponent $n = \frac{1}{2}$. However, a comparison with the reference measurements shows that no single recovery time provides consistently good agreement. Each recovery time intersects the reference data at different friction velocities, and no curve completely reproduces the overall shape of the reference trend. Notably, the three intermediate data points in the reference data set between $u_{*,w} = 0.3\,\mathrm{cm\,s^{-1}}$ and $u_{*,w} = 0.7\,\mathrm{cm\,s^{-1}}$ that are furthest from the boundary exponents appear to be best represented by a recovery time between 1 s and 10 s. The discrepancy between all fitted curves and the reference data is most plausibly explainable by the oversimplified assumption of a constant recovery time. A more realistic approach would consider the recovery time as a function of renewed area size itself as larger MWB events may have longer recovery times than smaller MWB events. Furthermore, the recovery time would probably decrease with increasing wind speed, as stronger wind-induced transverse currents accelerate the reformation of the surface structures. This would explain the observed discrepancies, as at low friction velocities longer recovery times would decrease the Schmidt number exponent, while at higher velocities shorter recovery times would increase it. As a result, the overall transition would appear more gradual and better match the reference trend.

Since no single recovery time gives a sufficient match, its estimation remains a key uncertainty. A conceptual method to determine the recovery time would be to track the reformation of coherent surface streaks after the detection of MWB and thus identify the time at which the renewed surface transitions back to a smooth, undisturbed state. Visual inspection of the image sequences suggests a plausible recovery time range between 1 s and 10 s, which corresponds well with the most appropriate interval of the fitting curves.

Attempts to determine recovery times more precisely using image processing techniques did not yield reliable results. First, it is challenging to define a consistent criterion for when the original surface structure is restored, especially when no coherent patterns re-emerge after renewal and the renewed region remains dark. Second, tracking the renewed region becomes increasingly difficult as the surface changes structurally. Last, in most wind conditions, the recovery time exceeds the residence time of the renewed surface regions within the image due to advection, so that a reliable image-based estimate is not possible.

Given these limitations, we rely on the reference data from 2017 for robust Schmidt number values. The sigmoid parameterization is refitted to match the reference dataset and to generate a smooth,

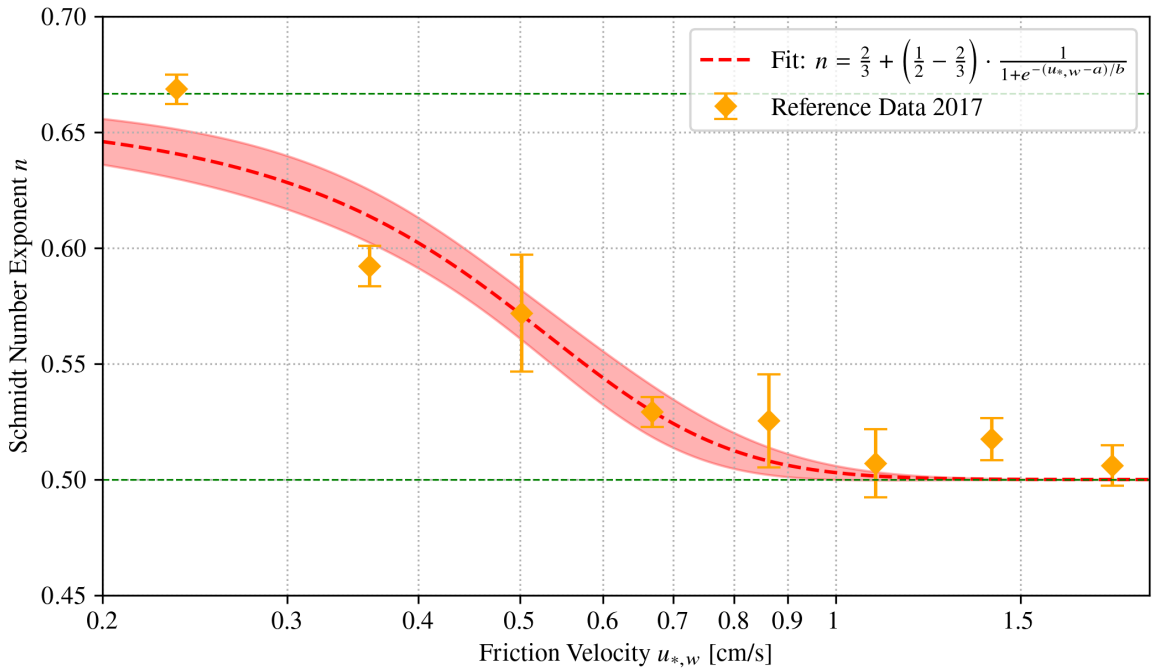

Figure 6.12: Fit of the Schmidt number exponent based on the reference data from 2017 as a function of the friction velocity.

continuous Schmidt number exponent as a function of friction velocity (Fig. 6.12). The uncertainty associated with this fit is also taken into account to provide a realistic estimate of the Schmidt number exponent. These parameterized Schmidt number exponents, including their associated uncertainty, are used in the subsequent chapter for the accurate determination of the water-side gas transfer velocity.

7 Simulation of Gas Transfer

As one of the most important aspects of this study, the current chapter presents the determination of water-side gas transfer velocities from the fluorescence signal. Its approach is based on the mass transport simulation described in Sec. 3.4.3 and builds on several results from the previous data analyses. First, the general simulation framework for determining the gas transfer velocities is explained, followed by an uncertainty analysis of the modeling procedure. Basically, the analyses presented here are applied exclusively to experimental data obtained under equilibrium conditions. This includes measurements with a clean water surface and with surface films from measurement week 1 as well as equilibrium measurements at high wind speeds from weeks 5 and 6, both with and without the artificial saltwater model.

7.1 Determination of Gas Transfer Velocities

The calculation of water-side gas transfer velocities incorporates data on the measured gas flux from Sec. 5.2.3, histogram data from Sec. 6.2.1, and the estimate of the Schmidt number exponent from Sec. 6.3.4. In addition, the calibrated diffusion coefficient of pyranine (Sec. 5.1.3) and brightness calibration factor (Sec. 5.4.3) are required. So, this procedure requires almost all results from previous data analyses. The core idea is to simulate the mass transport using the temporal gas flux as input parameter over different turbulence profiles and to determine the profile that best fits the measured fluorescence data. For clarity, the workflow of this methodology is shown in Fig. 7.1.

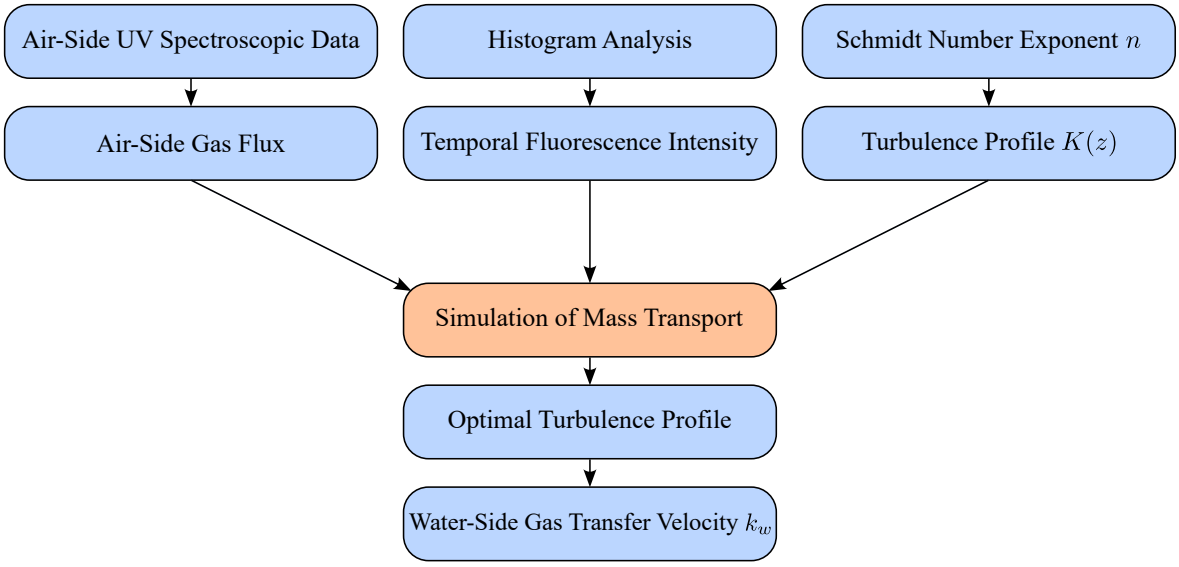

Figure 7.1: Workflow of the gas exchange simulation for calculating the water-side gas transfer velocities.

7.1.1 Simulation Input Variables

In order to set up the simulation, all relevant input parameters along with the objective function must be defined. The first step involves selecting the time interval over which the gas exchange simulation is to be performed. This period usually extends from the start of the gas exchange measurement to the first change in wind speed, typically when the wind is switched off (cf. Sec. 4.2.2). Over this time interval, equilibrium conditions are assumed to prevail, ensuring that the gas flux into the water remains well-defined.

The core of the simulation relies on the temporal evolution of the fluorescence intensity, derived from the histogram data of the image sequences (cf. Sec. 6.2.1). As the model assumes a horizontally uniform gas flux, the mean fluorescence intensity, calculated as the average grayscale value over the entire image domain, is used as the objective function. To convert these grayscale values into physically meaningful fluorescence intensities, they are normalized with the brightness calibration factor σ_{Laser} (cf. Sec. 5.4.2).

The simulation is formulated as an optimization problem in which different vertical turbulence profiles $K(z)$ are tested to determine the best fit to the measured fluorescence time series. Its underlying assumption follows the Small Eddy model (cf. Sec. 2.2.3), where the vertical profile of turbulent diffusivity takes the form

$$K(z) = a \cdot z^m. \tag{7.1}$$

Optimization over both parameters a and m is computationally intensive and leads to a high-dimensional parameter space. To handle this complexity, the exponent m is fixed to $m = \frac{1}{1-n}$ using the prior estimates n from the Schmidt number analysis (Sec. 6.3.4). Of course, this exponent varies greatly at low wind speeds and must therefore be adjusted accordingly for each data set. Consequently, the optimization reduces to a single-parameter problem focused on determining the prefactor a for the turbulence intensity that best explains the recorded fluorescence signal.

7.1.2 Optimization Scheme

The parameter optimization is performed using an adaptive, sequential search strategy tailored to the high computational costs and the non-differentiable structure of the simulation. Given this "black box" nature of the simulation, gradient-based methods for optimization to the objective function are unsuitable. Instead, a search approach inspired by the grid refinement method is used to balance computational efficiency and accuracy.

It begins by defining an initial parameter space comprising 20 logarithmically distributed values spanning a plausible range for the turbulence prefactor between $a = 10^{-2}$ and $a = 10^{1}$. For each value in this initial parameter space, the mass transport simulation is run and the resulting temporal fluorescence profiles are compared with the experimental time series of the spatially averaged fluorescence intensities. The goodness of match is quantified by the mean absolute temporal deviation between simulated and measured fluorescence intensities. We consider the parameter with the lowest mean absolute temporal deviation as the optimal candidate within the current search range.

After this first scan, the parameter space is adaptively refined by means of a grid refinement strategy. Normally, if the optimal value lies within the boundaries of the initial range, a narrower parameter

interval is constructed around the best fitting parameter, bounded by its two closest neighbors. Within this refined interval, 20 linearly distributed parameter values are generated, and the simulation is rerun to obtain a more accurate estimate of the optimal prefactor. The parameter a yielding the smallest deviation between simulated and measured fluorescence in this second scan is taken as the final result of the optimization procedure.

In the rare cases when the best fitting parameter of the first run is at the boundary of the initial search range, the parameter space is extended by an order of magnitude in the appropriate direction to ensure that the true optimum has not been truncated. A new set of 20 linearly distributed parameter values between the extended boundary and the initial boundary value is then generated and the process is repeated. Once the optimal parameter is found within the interior of the defined interval, the final refinement step proceeds as described above. This extension option is implemented primarily as protection against boundary errors and not as a routine requirement, as such boundary optima only occur in exceptional cases. Nevertheless, if the final optimized parameter lies outside the physically meaningful range between $a = 10^{-2}$ and $a = 10^{1}$, its validity has to be checked anyway before accepting it. An exemplary result of this simulation method with different turbulence profiles is shown in Fig. 7.2. Obviously, the optimized parameter a determines the turbulence depth profile that best represents the measured mean fluorescence signal extracted from the image data.

Although this optimization scheme does not allow for continuous parameter adjustment via gradient-based methods and instead works with discrete parameter sets, it provides a practical balance between accuracy and computational efficiency. Here, the distance between adjacent parameter values corresponds to approximately 2 % of the respective parameter value while the simulation's total runtime when run in parallel on multiple processors is approximately 2 h for one gas exchange experiment.

7.1.3 Calculation of Gas Exchange Quantities

Since the optimized parameter a uniquely defines the turbulence depth profile $K(z)$, we can derive further gas exchange parameters from it. A key quantity is the thickness of the mass boundary layer z_*, defined as the depth at which molecular diffusion and turbulent transport are equal. This corresponds to the point where the turbulence profile intersects with the constant molecular diffusion coefficient, expressed as

$$K(z_*) = a \cdot z_*^m \stackrel{!}{=} D. \tag{7.2}$$

Solving for z_*, the boundary layer thickness is obtained from the parameter a given by

$$z_* = \sqrt[m]{\frac{D}{a}}, \tag{7.3}$$

where m is the respective exponent of turbulent diffusivity profile and D is the diffusion constant of NH_2R. Finally, this gives the gas transfer velocity k by numerical integration according to Eq. (2.34) from the surface to the mass boundary layer thickness z_*

$$k = -\left(\int_0^{z_*} \frac{1}{D + a \cdot z^m} \, dz \right)^{-1}. \tag{7.4}$$

So, each simulated fluorescence curve corresponds to a unique gas transfer velocity derived from the optimized turbulence profile.

7.1.4 Improvements of Mass Transport Simulation

In its current implementation, the mass transport simulation in conjunction with gas flux and fluorescence data has proven to be very effective for determining the water-side gas transfer velocities. However, simulation results from initial trials suggest that in many cases the gas flux into the water may exceed the transport of the species through the mass boundary layer. This leads to a depletion of the acidic reactants for the methylamine reaction and saturation of the reaction products at the surface. As a result, NH_2R may not react immediately upon entering the water surface, but penetrates deeper into the mass boundary layer before reacting with the acidic dye component. This raises the question of whether the gas exchange remains fully controlled on the air side and whether Eq. (5.15) is still valid.

To address this, the simulation framework is slightly modified to dynamically adjust the gas flux based on surface concentrations. The approach is to back-calculate the air-side concentrations at the surface from the water-side concentration fields. Specifically, at the end of each time step n, the current surface concentration of NH_2R on the water side $c_{w,s}$, in the top cell of the simulation grid, i.e. $c_{w,s} = C^n_{0,NH_2R}$, is used to estimate the air-side surface concentration $c_{a,s}$ using Henry's law in Eq. (2.27). Here, the solubility value from Sec. 3.3.3 is used. Comparing this value with the current air-side NH_2R bulk concentration $c_{a,b}$ reveals whether the invasion remains air-side controlled. If the resulting concentration gradient indicates a deviation from the assumption of air-side control, the gas flux for the subsequent time step $n + 1$ is corrected using

$$J^{n+1}_{NH_2R} = k_a \left(c_{a,b} - \frac{C^n_{0,NH_2R}}{\alpha} \right), \tag{7.5}$$

which is equivalent to Eq. (5.13). This correction ensures that the simulation remains valid even if the air-side control is compromised. Although this modification introduces an additional feedback loop into the simulation, it is computationally efficient and does not significantly increase the simulation time. So, to ensure consistency and robustness, this correction is applied in all simulations, regardless of whether a deviation from air-side control is explicitly identified.

7.2 Uncertainty Analysis of the Simulation

The calculation of gas transfer velocities relies on several experimentally determined quantities that are subject to measurement uncertainties and are all incorporated into the mass transport simulation. In the actual simulation of the fluorescence curves, these include the gas flux j, the Schmidt number exponent n, as it determines the exponent of the turbulent diffusivity profile $K(z)$, and the experimentally verified diffusion coefficient D of pyranine. In addition, uncertainties in the brightness calibration factor σ play a role when comparing the target fluorescence signal with the simulation data. In this uncertainty analysis, the effects of uncertainties in the input parameters on the simulation curves itself are first

examined, followed by an investigation of how uncertainties in the target function affect the selection of the best-matching simulation curve.

7.2.1 Uncertainty Analysis of Simulation Input Parameters

Because the relationship between the input parameters and the simulation output behaves like a black box, meaning it cannot be analytically described or differentiated, the impact of parameter uncertainties on the simulation outcome itself must be assessed numerically. This is further complicated by the fact that not all uncertainties propagate in the same direction through the simulation.

To determine the sign and direction of the resulting uncertainty in the gas transfer velocity, the influence of each individual parameter is first analyzed. In this step, one parameter of gas flux j, Schmidt number exponent n, or diffusion coefficient D is varied either to its upper or lower bound within the uncertainty range, while the other two parameters are kept at their mean values. Note that the gas flux is a time-dependent function $j(t)$, whose entire temporal profile must be adjusted pointwise within its uncertainty envelope $\Delta j(t)$. In contrast, the Schmidt number exponent and the diffusion coefficient are scalar quantities and are treated as single values.

The mass transport simulation is run for all upper and lower limits of these three parameters to assess the directional effect of uncertainties on the overall gas transfer velocity. It is found that reducing the gas flux to its lower uncertainty bound $j(t) - \Delta j(t)$ results in a decreased gas transfer velocity. Conversely, lowering the Schmidt number exponent to $n - \Delta n$ leads to an increase in the gas transfer velocity. Variations in the diffusion coefficient of pyranine within its uncertainty range have a negligible impact on the result. This is because the resulting curve shifts are smaller than the resolution of the simulation, which is constrained by the discrete nature of the parameter space for the prefactor a.

To estimate the overall uncertainty of the gas transfer velocity, a combined uncertainty analysis is performed in the form of a worst-case scenario. This assumes that simultaneously setting all parameters to their respective upper or lower limits leads to the maximum deviation in the simulation outcome. Here, the directionality of the effects must be taken into account. Specifically, the simulations are repeated with parameter combinations set to the extreme limits $j(t) \pm \Delta j(t)$ and $n \mp \Delta n$ to calculate the maximum and minimum possible values of the gas transfer velocity. The diffusion coefficient is omitted in this combined uncertainty scenario, as it has been found to have a negligible influence.

The individual uncertainty contributions and the results of the worst-case scenario analysis are listed in Tab. A.4 (see Appendix A.5). These results indicate that despite the non-analytical nature of the system, the total uncertainty in gas transfer velocity Δk_{tot} scales approximately linearly with the relative uncertainties of the input parameters. Thus, a simplified relationship of the form

$$\frac{\Delta k_{\text{tot}}}{k} \approx \frac{\Delta k_j}{k} + \frac{\Delta k_n}{k}, \tag{7.6}$$

holds, where $\frac{\Delta k_j}{k}$ represents the relative contribution from uncertainty in the gas flux $j(t)$, and $\frac{\Delta k_n}{k}$ corresponds to the contribution from uncertainty in the Schmidt number exponent n. In addition, it is observed that the uncertainties of both the Schmidt number exponent and the gas flux have comparatively sized effects on the gas transfer velocity, i.e. $\frac{\Delta k_j}{k} \approx \frac{\Delta k_n}{k}$. However, this conclusion

only applies under clean surface conditions and at low wind speeds. Under conditions with surface films or high wind speeds, the Schmidt number exponent is known, meaning the exponent of the turbulent diffusivity profile is fixed to a value of 2 or 3 without uncertainty, leaving the gas flux as the only relevant source of uncertainty in such cases. Consequently, experiments performed with film-covered surfaces have lower overall uncertainties due to the absence of this additional uncertainty. In contrast, the uncertainty remains large for measurements at high wind speeds despite only one uncertain parameter, as the uncertainty of the gas flux increases significantly with wind speed. This is primarily because higher wind speeds lead to higher gas input rates.

7.2.2 Uncertainty Analysis of Target Function

The uncertainty of the target fluorescence signal stems from the uncertainty of the brightness calibration factor σ. Since its uncertainty is small and comparable to the resolution of the parameter space, its impact on the gas transfer velocity is expected to be minor.
Nevertheless, to capture its contribution, the worst-case uncertainty scenario is extended by this factor. For this purpose, the target fluorescence curve is adapted according to the lower and upper uncertainty limits of the brightness calibration factor and the optimal simulation parameter a is extracted by comparing with the previously calculated worst-case simulation results. The resulting total uncertainties of the gas transfer velocity, comprising the uncertainties of the simulation input parameters and the objective function, are summarized in Tab. A.4 (see Appendix A.5). It is found that including the uncertainty of the brightness calibration factor changes the overall uncertainty of the gas transfer velocity by a maximum of only 2 % in both directions.
The results of the worst-case analysis, which includes the uncertainties of both the input parameters and the target function, represent the final result of the uncertainty analysis for the water-side gas transfer velocities.

7.3 Discussion of the Simulation

Although the simulation of mass transport is based on a highly simplified model, it has proven to be an effective tool for estimating gas transfer velocities from Fluorescence Imaging data. A key advantage of this approach is that the mean fluorescence intensity alone is sufficient to compute gas transfer velocities.

7.3.1 Quality of Simulation Results

A comparison between the simulated curves and the fluorescence data shows that in most cases there is overall good agreement. This is especially true for the quasi-stationary state in the later parts of the curves. However, discrepancies arise during the initial phase of gas injection. It is important to distinguish between three characteristic types of curve progressions. In general, distinct curve profiles can be identified for low wind speeds under clean conditions, for film-covered water surfaces, and for high wind speeds, as exemplified in Fig. 7.2. When interpreting these differences, it must also be taken into account that the gas injection procedure varied between experiments. Specifically, measurements

at low wind speeds involved a relatively short initial gas injection, while those at high wind speeds used a continuous, regulated gas input over a longer time period.

It can be observed that the discrepancy between simulated and measured fluorescence during the initial gas injection phase, which begins about 10 s after the start of the measurement and lasts about 30 s to 50 s, occurs mainly at low wind speeds and is particularly pronounced by the presence of a surface film. In these cases, the initial rise in fluorescence occurs more rapidly in the experimental data than predicted by any of the simulation curves.

Tests with varying simulation parameters indicate that a better fit to the target fluorescence curve is achieved when the grid cells in the simulation are made larger. In such cases, the invasive methylamine penetrates deeper into the water column, promoting faster formation of the alkaline form of pyranine at greater depths, which in turn manifests as a stronger integrated fluorescence signal. As a result, the simulated fluorescence curves increase more rapidly over time and better match the measured fluorescence signal. However, this raises the question of how deep methylamine penetration into the water column can realistically be allowed. It is also found that, with increasing grid cell size, the rise in the fluorescence signal at the beginning of gas input becomes more stepwise rather than smooth. This is an indication of non-physical behavior in the simulation.

Nevertheless, these tests suggest that the faster rise in the measured fluorescence signal requires a faster formation of I^- at deeper layers, implying that transport should be faster than predicted by the current simulation implementation. While the initial increase in fluorescence cannot be fully explained with this model, experimental results show that this has a negligible impact on the final simulation results. Accordingly, increasing the grid cell size within a physically reasonable range does not alter the optimal value of the parameter a within the accuracy limits of the parameter space.

In the course of analyzing the initial phase of gas injection, the simulation also reveals that the alkaline form of pyranine reaches saturation at the water surface within just a few seconds after starting the gas input, even at the lowest gas fluxes used in the experiments. This saturation typically extends over the maximum thickness of the mass boundary layer of 300 µm within about 10 s to 20 s. Despite this saturation, the simulated fluorescence signal increases significantly slower than the measured signal. This discrepancy is direct evidence that a substantial part of the observed fluorescence does not originate directly from the mass boundary layer, but from concentration fields located below it. More precisely, the maximum fluorescence intensity that can be emitted from a fully I^--saturated mass boundary layer of this thickness is estimated to $I_{F,\mathrm{tot}} \approx 0.1 \cdot I_{\mathrm{ref}}$. Since this estimate is significantly lower than the experimentally observed fluorescence intensities, the contribution of the mass boundary layer to the overall signal appears to be small. This underlines the importance of the fluorescence-emitting structures located below the mass boundary layer.

Furthermore, in simulations of measurements conducted at high wind speeds, the initial rise of the fluorescence data corresponds very well with the simulated curves. Overall, there is a very good agreement, as evidenced by oscillations in the fluorescence curves, which appear in both the simulations and the measurements. The reason for this is that, in order to maintain gas flux at high wind speeds, the gas input must be tightly regulated. Localized injection of methylamine into the channel sometimes leads to delays in the mixing of the air space, resulting in quasi-periodic oscillations in the gas input.

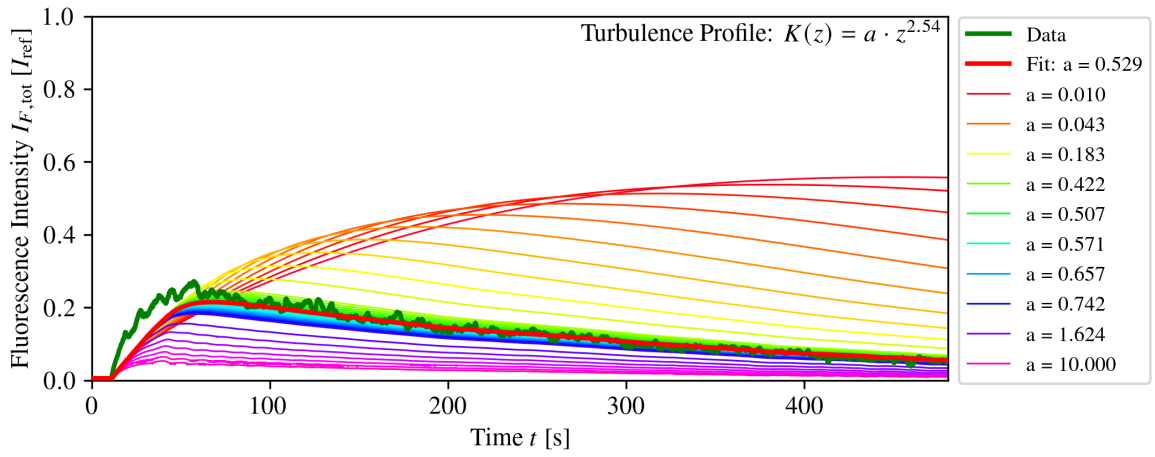

(a)

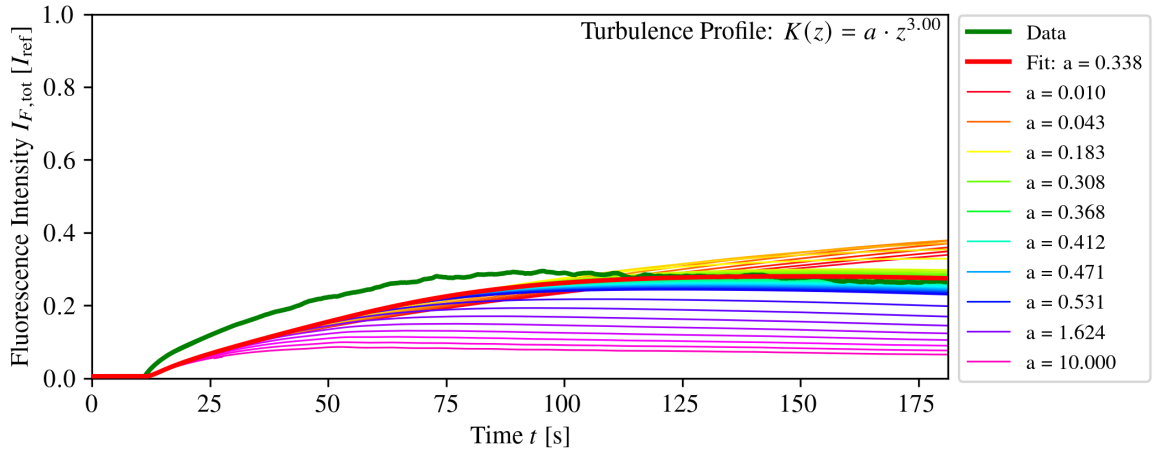

(b)

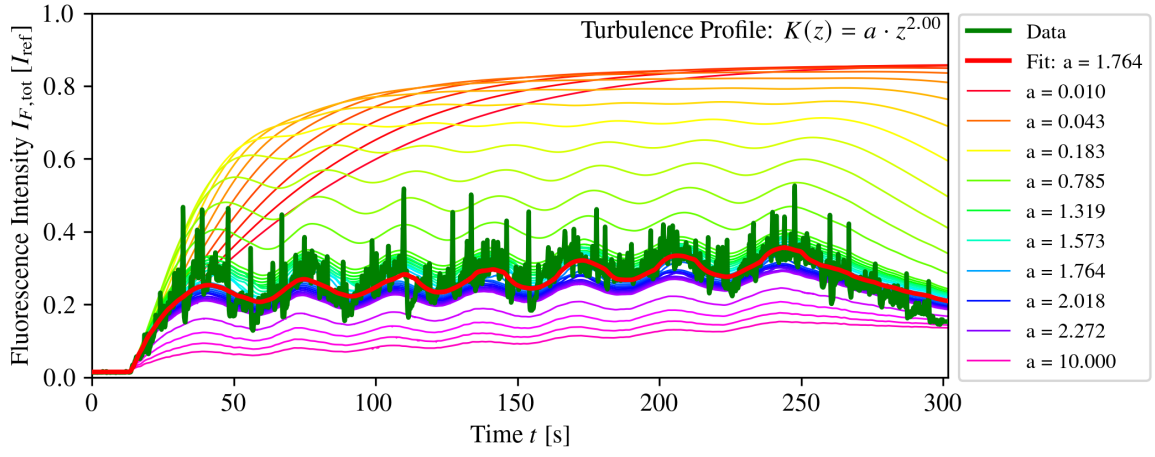

(c)

Figure 7.2: Exemplary temporal fluorescence curves of the mass transport simulation for (a) low wind speeds and clean conditions, (b) low wind speeds and film conditions, and (c) high wind speeds. All measurements with the same conditions show similar curve progressions.

A potential issue with simulations at high wind speeds is that the measured fluorescence intensity exhibits stronger fluctuations, which can overlay the oscillations of the gas input. These fluctuations are caused by reflections from wave crests (cf. Fig. 6.6(b)). Specifically, waves of a certain height produce saturated brightness levels at the wave crests in the images. The exact cause of these reflections cannot be conclusively determined, but a plausible explanation is that increasing wave amplitude leads to increased curvature of the wave crests, which at a certain point acts as a lens. This lensing effect focuses the fluorescence signal onto specific pixels, producing image artifacts that systematically increase brightness. Such a bias toward higher brightness results in a systematic underestimation of the gas transfer velocities. At low wind speeds, this effect is minimal due to the smaller wave heights and overall smoother water surface and can be neglected. However, at high wind speeds this effect is frequently observed, both in terms of occurrence and affected area. Nevertheless, when considering these reflections relative to the overall image size and their frequency, the only significant increase in overall image brightness can be observed for large breaking waves. These are identifiable as dominant peaks in the measured fluorescence signal. Given their low frequency, they are expected to have only a minimal effect on the overall agreement between simulated and measured fluorescence. Thus, it is reasonable to conclude that the effect of reflections on the total simulation results is minor compared to the uncertainty in the input parameters.
Overall, it is found that discrepancies in the initial gas input phase or optical artifacts have only a limited impact on the accuracy of the final results. Thus, the simulation method provides robust and consistent estimates of gas transfer velocities over a wide range of conditions.

7.3.2 Potential Improvements and Extensions

The main limitation of the simulation method lies in its reliance on a known Schmidt number exponent. This exponent directly influences the shape of the initialized turbulent depth profile, and inaccuracies in its estimation can significantly affect the simulation output. Therefore, a precise knowledge of this value is critical for the reliability of the method.
One possible alternative is to treat the exponent of the turbulent depth profile as a free parameter, performing the simulation over a two-dimensional parameter space defined by the scaling factor a and the exponent m. However, this approach faces two major challenges. First, the large parameter space increases computational cost substantially. Second, preliminary attempts reveal that different parameter combinations often yield similarly small deviations from the measured fluorescence data. This arises because both parameters affect the shape of the simulation curve in similar ways, leading to an overparameterized model. Depending on the chosen combination, different time intervals in the data may be better or worse represented. These findings challenge the physical validity of the optimized parameters. For example, the optimized exponent m does not necessarily exhibit the expected decrease from 3 to 2 with increasing wind speed. To constrain the optimization, additional conditions could be introduced, such as enforcing a monotonic decrease of the exponent with wind speed. However, this would require a global optimization over all measurements at different wind speeds, further increasing computational demand.
A further potential extension of the method would involve not only the mean fluorescence intensity but also the full distribution of pixel intensities. This would allow for the derivation of local gas transfer

velocities by associating each grayscale value in the image sequence with a corresponding vertical transport rate. However, this concept introduces a contradiction between the simulation model and the characteristics of the observed turbulent streaks. The streaks consistently show higher fluorescence than the image mean. A typical simulation curve that explains such high-intensity regions would require a lower parameter a, implying weaker vertical transport. This conflicts with the interpretation presented in Sec. 6.1.1, where the bright streaks are linked to convergence zones that accumulate tracers from surrounding flow due to enhanced vertical mixing. The resolution of this contradiction lies in the fact that the simulation currently only describes vertical transport in one dimension. A realistic representation of the convergence and divergence zones driven by turbulent vortices would require a two- or three-dimensional model. Such a model could incorporate lateral transport perpendicular to the wind direction, allowing for a more physically consistent interpretation in which high local fluorescence corresponds to enhanced vertical transport. Implementing a higher-dimensional mass transport simulation would substantially increase the model complexity. It would require abandoning the simplified turbulent depth profile in favor of an explicit treatment of hydrodynamic structures such as vortices and Langmuir circulation.

Nevertheless, while this discrepancy limits the physical interpretability of local intensities within the simulation framework, it does not affect the use of mean fluorescence for determining gas transfer velocities. The horizontal variability introduced by convergence and divergence zones averages out in the mean signal, meaning that the lateral flows have negligible impact on the mean intensity. Thus, the current simulation remains methodologically valid when applied to the mean fluorescence signal.

8 Results and Discussion

This chapter presents the main findings of the previous analyses in their entirety. Initially, the results of the air- and water-side gas transfer velocities are presented. This is followed by a combined analysis of the water-side gas transfer velocities together with the results of MWB analysis. In particular, an attempt is made to quantify the contribution of MWB to gas exchange. The chapter concludes with a discussion of the results. While the methodological and technical discussion of the gas transfer simulation as well as the MWB detection algorithm has already been presented in Secs. 6.3.4 and 7.3, this section provides a broader interpretation of the results and their implications for gas exchange. As friction velocity data is not yet available for all measurements considered in this chapter, the parameterization of gas transfer velocities is primarily based on the wind control frequency. However, in those cases where friction velocity data is available, particularly at low wind speeds, an additional parameterization is showed by means of the friction velocity. This representation enables better comparability of the data with existing or future gas exchange measurements in other wind-wave channels or field measurements.

8.1 Air-Side Gas Transfer Velocities

The results of the air-side gas transfer velocities are derived from the analysis of the air-side UV spectroscopy data, as described in Sec. 5.2. Although these are not central to the objectives of this study, since the primary resistance for the air-side controlled methylamine lies on the air side, they are briefly presented here for completeness.

When plotting the gas transfer velocities as a function of wind control frequency (Fig. 8.1), a clear increase in transfer velocity is observed, as expected. The nearly linear trend in the double-logarithmic plot indicates that the increase can be described by a power law. A distinct difference is evident between the transfer velocities measured with clean water surfaces and those with film-covered surfaces. In the presence of surface films, a reduction in transfer velocity of approximately 20 % is observed at identical wind speeds. This finding is similar to the results reported by Patkai (2024).

Furthermore, the results obtained for the two different films, hexadecanol and Triton X-100 do not show significant differences and can therefore be considered as one combined data set. This finding supports the previously proposed hypothesis that the effect of surface films on gas exchange is primarily governed by their wave-damping properties, which are similar for both films, rather than their differing chemical compositions.

In addition, no significant difference can be identified between the gas transfer velocities on clean water and those on the saltwater model. However, these data are limited to high wind speeds, where greater variability in the measured values is observed. A noteworthy outlier from a film-covered

measurement at high wind speed falls within the cluster of transfer velocities typically associated with clean water. This suggests that the reduction in transfer due to the film was eliminated in this case, which aligns with visual observations during the experiment indicating that the film was disrupted by the high wind speed and wave formation. This supports the assumption that once the film is broken, it no longer has a significant impact on gas exchange.

Last, it is important to address the final data point at the highest wind control frequency of 50.0 Hz, which falls significantly below the value predicted by the linear model. This deviation is attributed to wave-induced spray formation at wind speeds above 40.0 Hz, which led to water droplets entering the optical path of the UV measurement setup. The resulting additional absorption by these droplets is evident in the UV spectra, particularly as a negative offset, which makes reliable determination of gas concentrations impossible. Although a correction could be applied by weighting the concentration data during the fitting process to determine the transfer velocity, this is not pursued here. Due to the observed spray formation, the accuracy of the gas concentration measurements above 40.0 Hz is considered questionable.

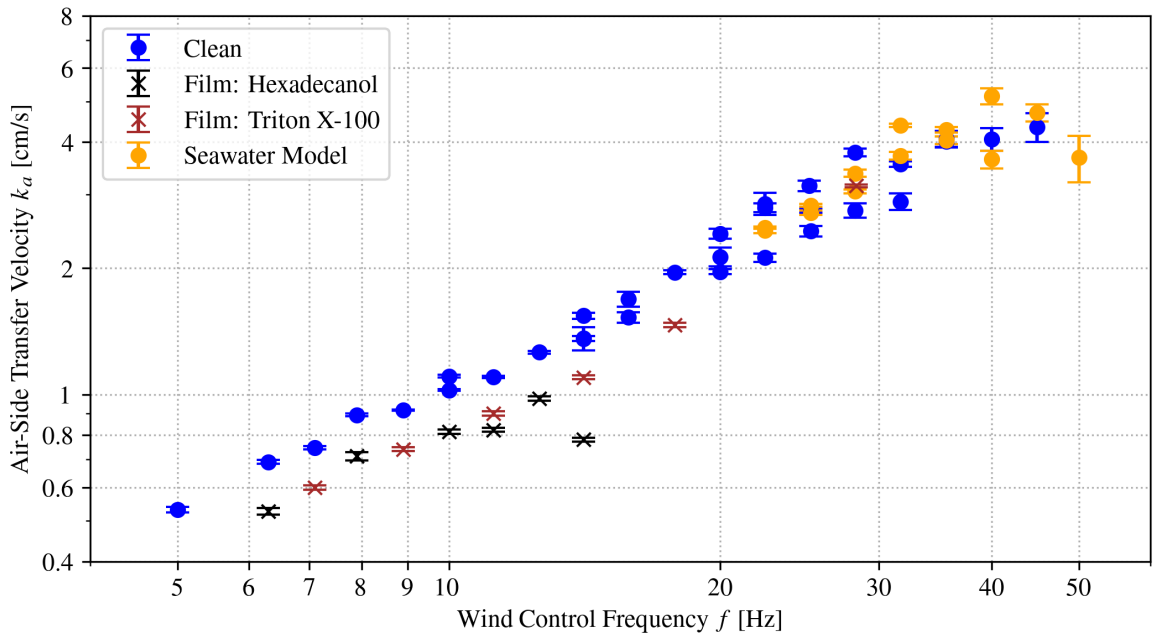

Figure 8.1: Results of air-side gas transfer velocities determined from the analysis of UV spectroscopic data as a function of wind control frequency.

8.2 Water-Side Gas Transfer Velocities

This section presents the water-side gas transfer velocities calculated using the mass transport simulation introduced in Sec. 7.1. As previously noted, these results are limited to experiments conducted under equilibrium conditions.

The results including the respective uncertainties derived from the uncertainty analysis are shown in Fig. 8.2. Similar to the results for air-side gas transfer velocities, the data exhibit an approximately linear increase with wind control frequency when plotted on a double-logarithmic scale across the

various measurement series. Notably, the slopes of these linear trends differ substantially between the dataset acquired with a clean water surface and those collected in the presence of surface films. In contrast, the gas transfer velocities for both hexadecanol and Triton X-100 follow a similar trend.
Overall, a significantly stronger reduction of gas transfer velocities due to surface films is observed on the water side compared to the air side. It is likely that the damping of surface waves by the film more strongly affects the near-surface turbulence on the water side than on the air side. Furthermore, it can be observed that at high wind speeds, the gas transfer velocities are considerably lower than would be expected based on the linear trend derived from low wind speed data with a clean surface. Finally, it is again evident that during film measurements at high wind speeds, where the film was disrupted, the gas transfer velocities are of the same order of magnitude as those observed under clean conditions.

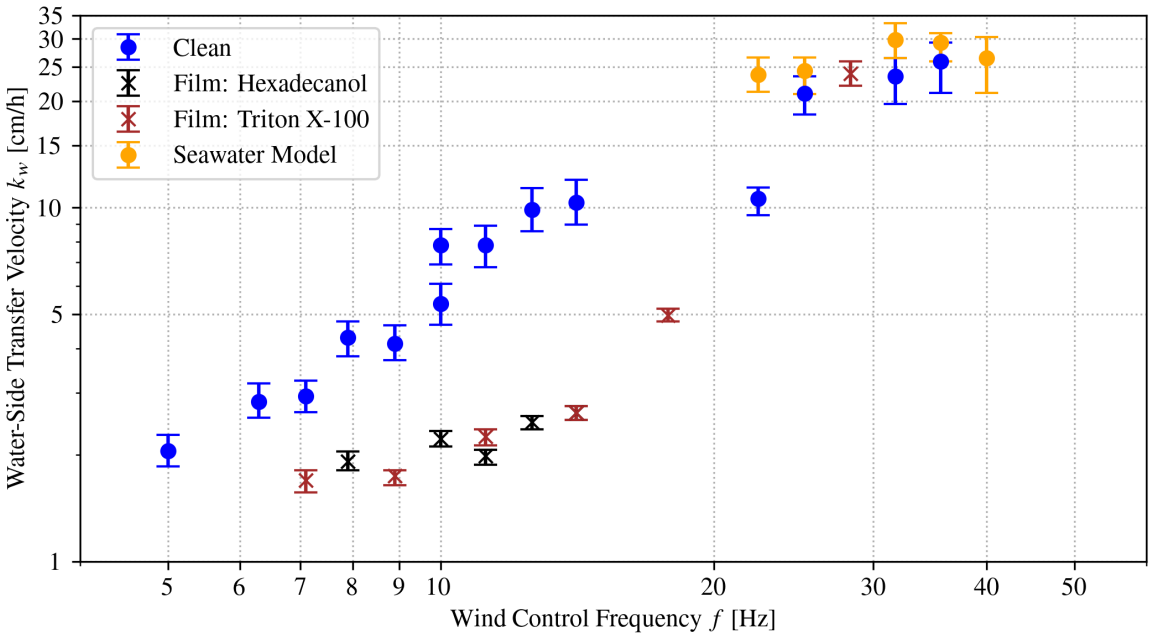

Figure 8.2: Results of water-side gas transfer velocities determined from the fluorescence intensity using the mass transport simulation as a function of the wind control frequency.

In addition to the representation as a function of wind control frequency, Fig. 8.3 provides a complementary view of the water-side gas transfer velocities plotted against the friction velocity. This is shown for the subset of measurements at low wind speeds, where friction velocity data were available. Plotting the gas transfer velocities against friction velocity also allows a comparison of the experimental data with the general parameterization of gas transfer velocity based on the theoretical gas exchange model in Eq. (2.59). For this purpose, the model predictions for both a smooth water surface using the parameters $n = \frac{2}{3}$ and $\beta = 12.2$ as well as for a rough water surface using the parameters $n = \frac{1}{2}$ and $\beta = 6.7$ are included in the plot. The Schmidt number used is again the value documented in Sec. 3.3.3.
This comparison reveals that the data points corresponding to the film-covered water surface agree well with the theoretical prediction for a smooth surface, with the exception of the data point at the friction velocity $u_{*,w} = 0.8\,\mathrm{cm\,s^{-1}}$. This outlier may be due to the fact that the condition of a smooth

water surface is no longer completely fulfilled at this increased wind speed. In contrast, the data points for the clean water surface are between the model predictions for smooth and rough surfaces, as expected. They show a gradual transition from the smooth surface behavior at low wind speeds to the rough surface behavior as the wind speed increases. This is consistent with the expected shift of the Schmidt number exponent from $n = \frac{2}{3}$ to $n = \frac{1}{2}$ in this wind speed regime (cf. Sec. 6.3.4). Overall, the results show that the water-side gas transfer velocities derived from the mass transport simulation provide physically plausible values that are consistent with established theoretical models.

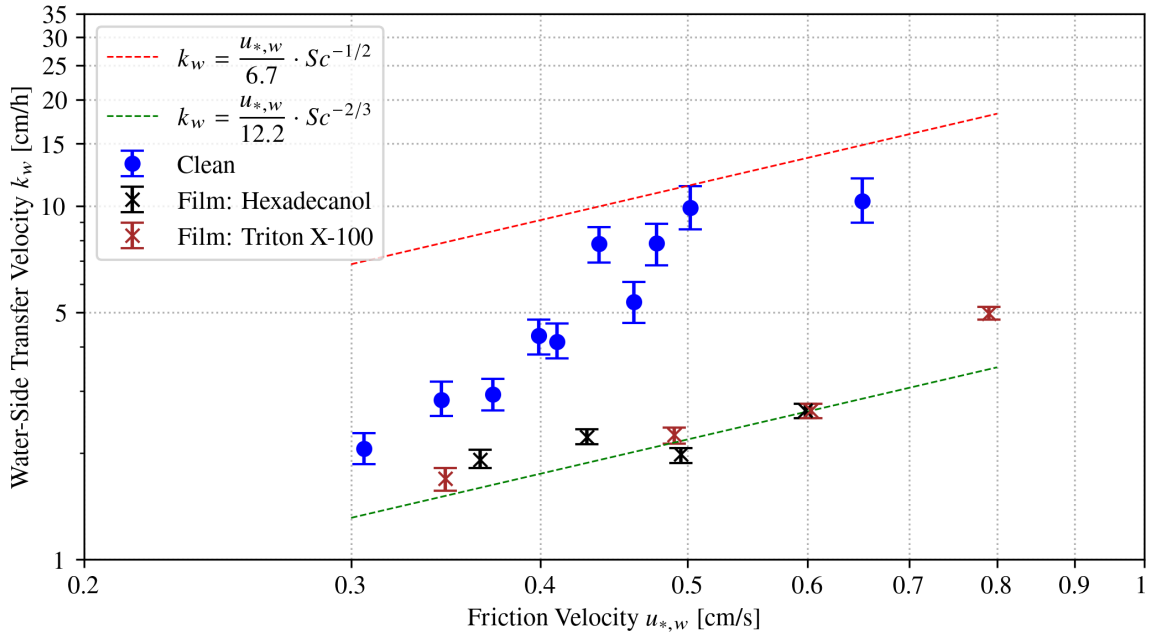

Figure 8.3: Results of water-side gas transfer velocities analogous to Fig. 8.2 but as a function of the friction velocity. Friction velocities are only available for measurements at low wind speeds. The gas exchange model predictions for a smooth (green) and a rough (red) water surface are plotted.

8.3 Quantification of Gas Exchange Mechanisms

Based on the previously presented results of water-side gas transfer velocities (cf. Sec. 8.2) and qualitatively identified turbulence structures (cf. Sec. 6.1), an estimate of the contribution of different mechanisms to gas exchange can be made. The primary objective is to quantify the effect of MWB on gas exchange using the calculated surface renewal rates (cf. Sec. 6.3.3). To simplify this analysis, we conceptually divide gas exchange into two additive contributions. The rationale for this division will become clearer at the end of this section. Specifically, we distinguish between a contribution we refer to as the *Turbulent Vortices Effect*, which encompasses all transport mechanisms associated with the turbulent streaks, such as convergence and divergence zones driving vertical exchange, and a second contribution, the *Surface Renewal Effect*, which accounts for directly observable surface renewal events linked to MWB. Due to the complex potential interactions, additional effects such as large-scale wave breaking are excluded, restricting the analysis to low wind speed conditions.

8.3.1 Turbulent Vortices Effect

To quantify the contribution of mechanisms related to the formation of turbulent streaks, we refer to the measurement results obtained under surface film conditions. As previously discussed in Sec. 6.1.1, the presence of surface films suppresses both LCs and visible surface renewal events. Instead, regularly spaced streak-like patterns, identified as QSVs, are observed. All turbulence phenomena associated with these QSVs are here considered as a single mechanism. Since the gas transfer velocities over film-covered surfaces increase nearly linearly with wind forcing on a logarithmic scale (cf. Fig. 8.2), the effect of turbulent vortices on water-side gas transfer velocity can be empirically parameterized as

$$k_{\mathrm{res}}(f) = a f^{m}. \tag{8.1}$$

By fitting the this function to the data, we obtain $m = 0.96$ for the data with surface films, indicating an approximately linear increase of gas transfer velocity with wind control frequency (Fig. 8.4). In the image sequences with surface films, the appearance of the turbulent QSVs does not change substantially with increasing wind speed, unlike the fluorescent structures on clean surfaces. This suggests a reduced sensitivity of the underlying dynamics to wind forcing, which is consistent with the weak wind dependence observed in the fitted gas transfer velocities. A more detailed theoretical description beyond this simple parameterization is not currently feasible.

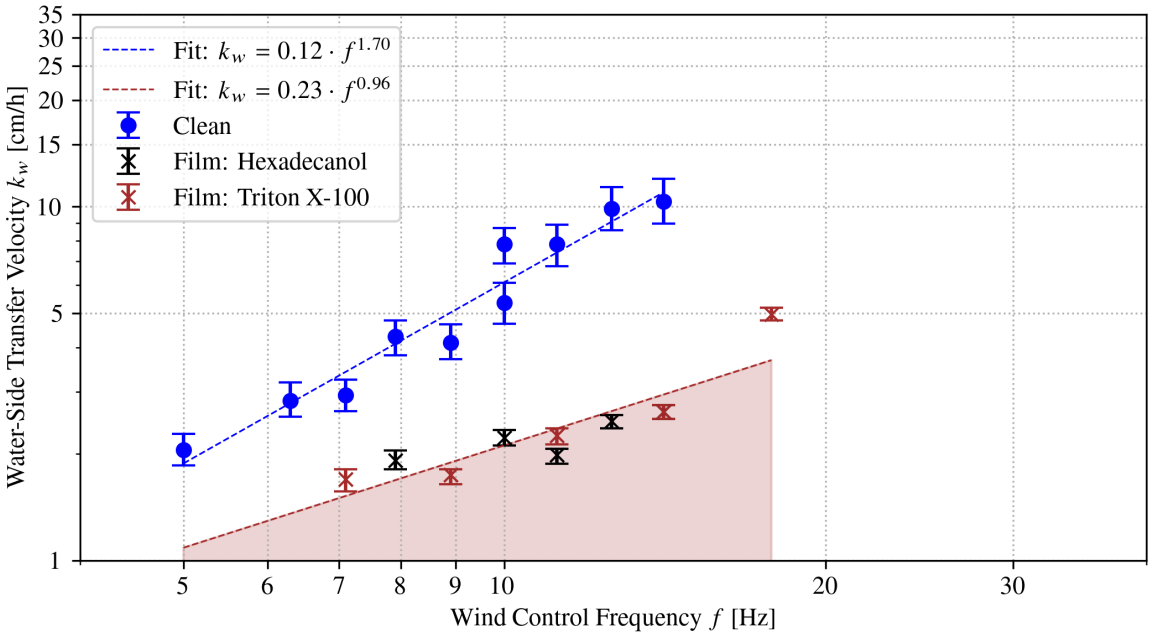

Figure 8.4: Separation of the contribution of Turbulent Vortices Effect to gas exchange. The contribution of the Turbulent Vortices Effect to the water-side gas transfer velocity corresponds to the brown shaded area.

8.3.2 Surface Renewal Effect

The second mechanism to quantify is surface renewal driven by MWB. This phenomenon was analyzed in detail in Sec. 6.1.2, where a surface renewal rate was extracted for each equilibrium wind condition.

It was also shown that no MWB occurs on a film-covered surface and thus no surface renewal is present. According to the classical surface renewal model of gas exchange (cf. Sec. 2.2.3), the relationship between gas transfer velocity and surface renewal rate is

$$k = \sqrt{\lambda D}. \tag{8.2}$$

When plotting water-side gas transfer velocities against surface renewal rates derived from MWB detection, a discrepancy with the model becomes evident (Fig. 8.5). A log-log plot reveals that the data are best described by a power law with an exponent of 0.34.

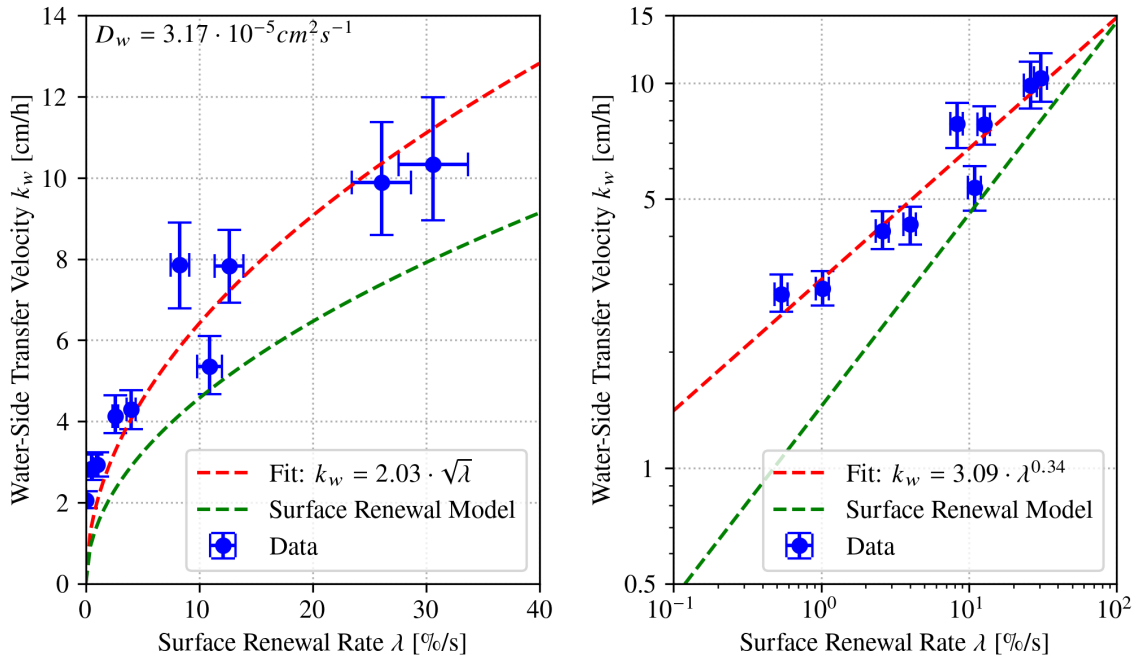

Figure 8.5: Results of the water-side gas transfer velocities as a function of the surface renewal rate from detection of the MWB (without correction of the film contribution) as (a) linear plot and (b) log-log plot. The fit shows the deviation from the surface renewal model. Note that both plots use different fit functions. While the fit in the linear plot requires a square root function, the fit in the log-log plot uses a free exponent. At the top left of (a), the value for the diffusion constant D_w derived from squaring the fitted prefactor is shown.

This deviation from the classical surface renewal model can be explained by recognizing that the model implicitly includes not only clearly visible MWB-induced renewal events but also renewal driven by bulk-phase turbulence reaching the interface. Otherwise, the model would predict vanishing gas transfer in the absence of MWB, such as over a film-covered surface. This leads to the proposition of a combined model given by

$$k = \sqrt{\lambda D} = \sqrt{\lambda_{\mathrm{MWB}} D} + k_{\mathrm{res}}(f). \tag{8.3}$$

Here, λ_{MWB} accounts for MWB-driven surface renewal, and $k_{\mathrm{res}}(f)$ includes all remaining mechanisms contributing to exchange between surface and bulk water. This is intended to represent a

generalized surface renewal framework. It also clarifies the use of the term k_{res}, as it refers to the residual term, encompassing all processes that contribute to gas exchange but are not associated with observable surface renewal.

To test this model, we subtract the fitted $k_{\mathrm{res}}(f)$ contribution based on film measurements from the water-side gas transfer velocities in case of clean water, isolating the MWB contribution according to Eq. (8.3). These corrected values are then plotted against the MWB surface renewal rate (Fig. 8.6). The result shows a significantly better agreement with the surface renewal model than in Fig. 8.5. In particular, a log-log fit yields an exponent of 0.44, indicating improved consistency with the theoretically expected square-root dependence. A linear representation using a fixed square-root fit further demonstrates a clear agreement between the measured values and the surface renewal model. According to Eq. (8.2), the diffusion coefficient can be obtained by squaring the fitted prefactor in the appropriate units. This back-calculating yields a value of $D = 1.53 \cdot 10^{-5}\,\mathrm{cm^2\,s^{-1}}$, which is indeed close to the literature value for methylamine $D_{\mathrm{NH_2CH_3}} = 1.61 \cdot 10^{-5}\,\mathrm{cm^2\,s^{-1}}$.

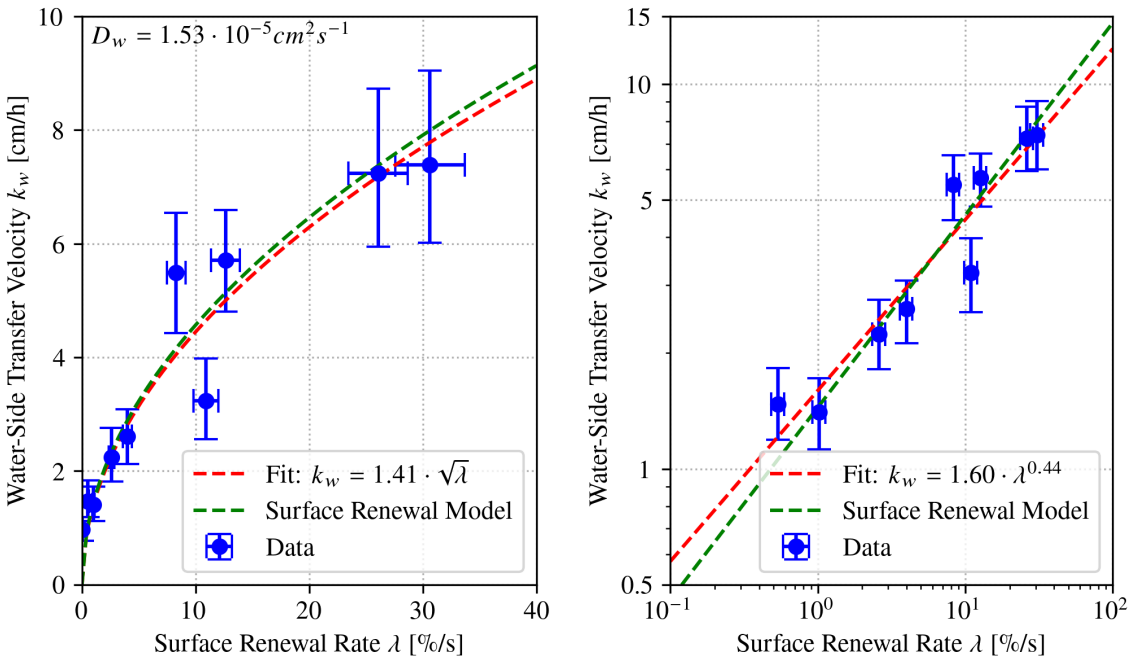

Figure 8.6: Results of the water-side gas transfer velocities as a function of the surface renewal rate from detection of the MWB (with correction of the film contribution) as (a) linear plot and (b) log-log plot. Analogous to Fig. 8.5.

These findings support the conclusion that the observed increase in gas exchange over a clean water surface, compared to a film-covered surface, can be attributed solely to additional MWB-induced surface renewal (Fig. 8.7). This conclusion holds for the low wind speed range up to 17.8 Hz, where MWB is dominant and easily detectable. However, at higher wind speeds MWB becomes masked by large-scale wave breaking, which prevents the derivation of meaningful values for the surface renewal rate in this regime.

Assuming that MWB accounts for the observed increase in gas exchange, its relative contribution can

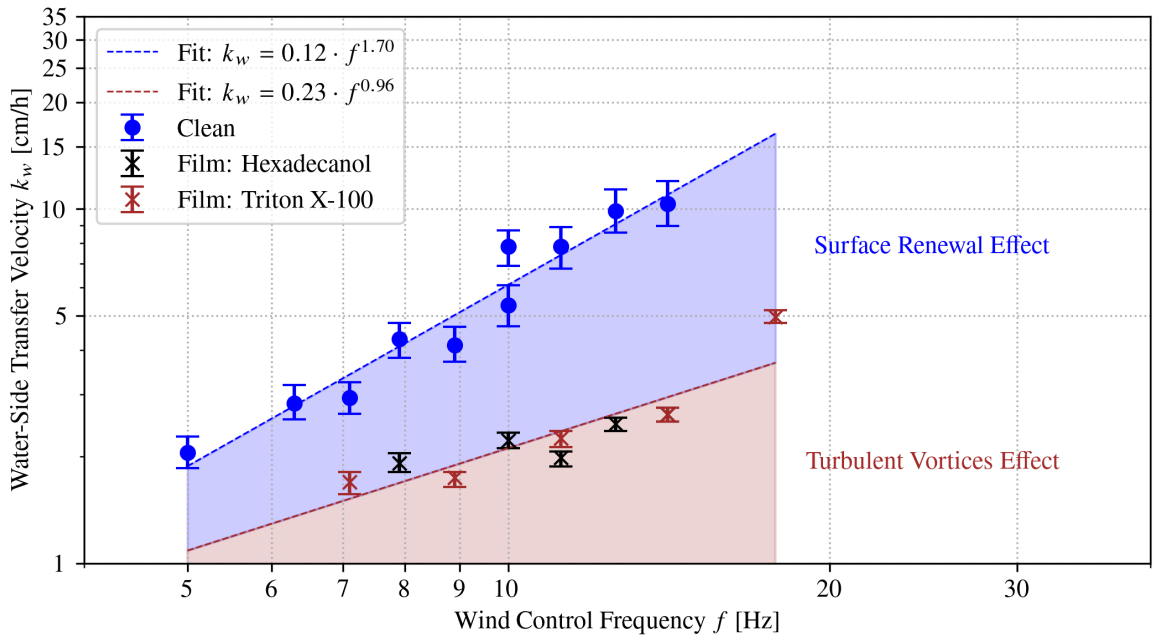

Figure 8.7: Separation of the contribution of Surface Renewal Effect to gas exchange. The contribution of the Surface Renewal Effect to the water-side gas transfer velocity corresponds to the blue shaded area.

be estimated. This is achieved by calculating the ratio of the linear fits from both data sets in the double-logarithmic plot shown in Fig. 8.7, whereby the friction velocity is used for parameterization. This ratio provides an estimate of the Surface Renewal Effect due to MWB on the measured water-side gas transfer velocity under varying wind forcing, as illustrated in Fig. 8.8. The resulting plot shows that the MWB contribution increases from approximately 35 % at $u_{*,w} = 0.3\,\mathrm{cm\,s^{-1}}$ to around 80 % at $u_{*,w} = 0.8\,\mathrm{cm\,s^{-1}}$. Accordingly, under these assumptions, MWB significantly influences gas exchange even at low wind speeds, becoming the dominant mechanism for gas transfer at approximately $u_{*,w} = 0.35\,\mathrm{cm\,s^{-1}}$. Its impact continues to rise steadily up to the transition into the moderate wind speed regime at $u_{*,w} = 0.8\,\mathrm{cm\,s^{-1}}$.

8.4 Discussion

The results presented here are based on two newly developed analysis methods: the derivation of water-side gas transfer velocities from fluorescence intensity using a mass transport simulation, and the quantification of surface renewal rates through the detection of MWB. Since both methods are applied in this form for the first time, the results should primarily be viewed as a validation of these novel approaches.

Due to the lack of reference measurements from established techniques, the validity of the results must be assessed through their physical plausibility. For the mass transport simulation, good agreement is found between simulated and measured fluorescence time series (cf. Sec. 7.3). The credibility of the method is further supported by the fact that the resulting gas transfer velocities follow physically expected power-law relationships with wind forcing. In particular, the obtained gas transfer velocities yield plausible absolute values when compared with theoretical model predictions for gas exchange

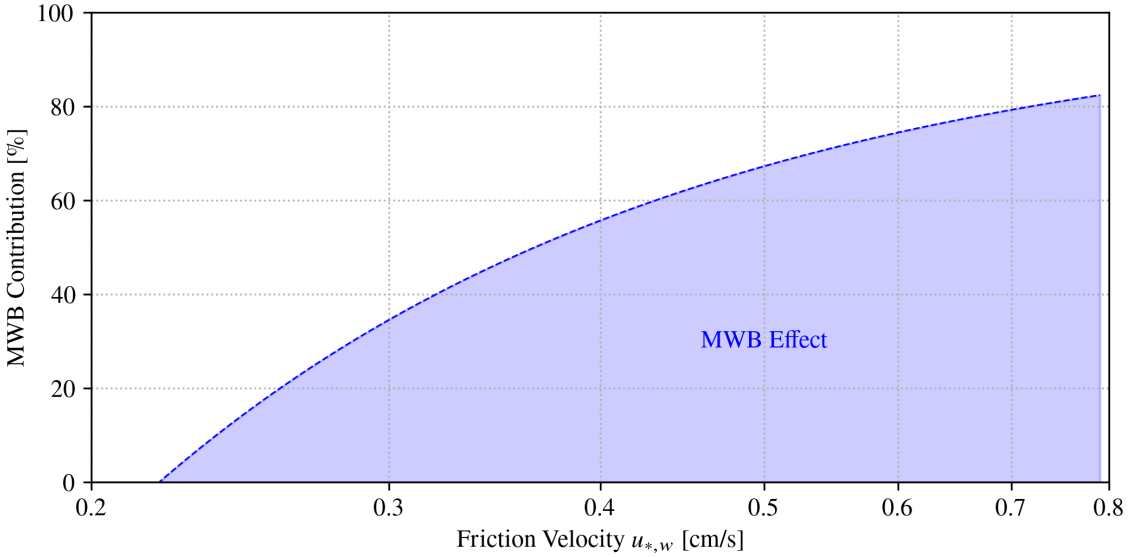

Figure 8.8: Estimated contribution of MWB to the water-side gas transfer velocity. Calculated by dividing the two fits from Fig. 8.7.

over smooth and rough water surfaces, further providing the validity of the method. This is notable given the simplifications underlying the model, specifically, the assumption of a one-dimensional turbulent diffusivity profile derived from horizontally averaged fluorescence data. Nevertheless, this approach yields gas transfer velocities with uncertainties in the range of 5–20 %, with a median uncertainty of approximately 12 %. Additionally, the method yields a vertical diffusivity profile as part of the simulation process. However, a definitive validation, will require direct comparison with independent measurement techniques as thermography or mass balance methods.

One unresolved issue is that, at higher wind speeds, the measured gas transfer velocities fall below the extrapolated trend established at lower wind speeds. While systematic errors, such as optical reflections on the steep slopes of surface waves, were previously identified and assessed as minor, they may still introduce a slight underestimation of gas exchange rates. This is unusual as experimental gas exchange experiments usually report an increased gas transfer at higher wind speeds compared to the extrapolated trend from moderate wind speed data, which is probably primarily due to additional bubble-mediated exchange processes. Of course, the determination of gas transfer velocity from fluorescence intensity performed here also completely neglects bubble effects. It is therefore to be expected that the gas transfer velocities cannot be methodically determined correctly at high wind speeds with this simulation approach. However, it remains unclear why the data are nevertheless lower than the extrapolated trend.

The MWB detection algorithm similarly demonstrated good performance. The extracted surface renewal rates increase with wind forcing, as expected. In contrast to the simulation, the MWB events identified by the algorithm can be visually verified, providing a more direct means of validation. The primary source of uncertainty lies in accurately defining the spatial extent of MWB events. To account for this, a conservative uncertainty of 10 % was assigned to the surface renewal rates.

By combining the results of both methods, an estimate of the MWB contribution to total gas exchange can be made. Although the additive separation of gas transfer velocity into a turbulent vortices

component and an MWB-driven surface renewal component is a strong simplification, the results align remarkably well with classical surface renewal theory. Still, this conceptual model inherently neglects certain transport processes. For instance, the turbulent vortices effect is inferred from measurements over film-covered surfaces, where QSVs dominate, but LCs are suppressed. Thus, the contribution of Langmuir-driven transport, known from other studies (Schnieders et al., 2013) to significantly enhance gas exchange, is not explicitly captured in the current model.

Moreover, it is assumed that the turbulent vortices contribution under film-covered conditions is comparable in magnitude to that under clean-surface conditions. While this assumption allows for a pragmatic estimation, it is not guaranteed. A more accurate quantification of the turbulent vortices effect under clean conditions is currently not possible, as QSVs co-exist with LCs and cannot be observed independently on clean surfaces. Observations suggest a nonlinear interaction between these structures, as LCs lead to a visible clustering and redistribution of QSVs, changing the pattern of the turbulent surface (cf. Sec. 6.1.1). This is also not captured in the present simplified model. As a result of these oversimplifications, the model of surface renewal presented here must be viewed cautiously and serves more as an initial estimate of the gas exchange mechanisms than as a well-founded theory.

Despite the simplifications and neglected effects, the present analysis demonstrates that the gas exchange data found from Fluorescence Imaging experiments at low wind speeds can be well described by an additive model in which MWB-induced surface renewal is the main contributor to the observed increase in transfer velocity. Similar findings have been reported in Zappa et al. (2004), where a significant contribution of MWB to total gas transfer was found. Here, MWB contributions of about 25 % were observed at a reference wind speed of $u_{10} = 4.2\,\mathrm{m\,s^{-1}}$ and up to 75 % at $u_{10} = 9.3\,\mathrm{m\,s^{-1}}$. It was also detected that the fraction of the surface renewed by MWB is between 0.25 and 0.40 at wind speeds between $u_{10} = 4.2\,\mathrm{m\,s^{-1}}$ and $u_{10} = 9.3\,\mathrm{m\,s^{-1}}$. To allow a direct comparison with our data, the measured friction velocities in the Aeolotron are converted to reference wind velocities over the open ocean using $u_{10}^2 = C_D u_*^2$ (Krall & Jähne, 2025) with a parameterization for C_D from Edson et al. (2013). In this way, equivalent reference wind speeds are obtained that would generate the same wind stress over the open ocean as measured in the laboratory. Based on this conversion, our results show an MWB contribution of about 35 % at a reference wind speed of $u_{10} = 2.8\,\mathrm{m\,s^{-1}}$ and up to 80 % at $u_{10} = 7.1\,\mathrm{m\,s^{-1}}$. In addition, the proportion of surface area renewed by MWB increases from about 10 % at $u_{10} = 4.3\,\mathrm{m\,s^{-1}}$ to about 30 % at $u_{10} = 6.0\,\mathrm{m\,s^{-1}}$. Although the data sets show some quantitative differences, both studies demonstrate a consistent trend indicating that MWB contributes significantly to gas exchange towards moderate wind speeds. This agreement in magnitude supports the conclusion that MWB-induced surface renewal plays a crucial role under these conditions. Further insight into the relative contributions of the different turbulence mechanisms could be gained by a more detailed analysis of the streak population and its dynamics. This could allow a more accurate quantification of the transport processes associated with these structures.

In conclusion, the quantification presented here should be considered as a first-order estimate. It provides a first basis for future investigations aiming at a more comprehensive understanding of the complex interactions between the various fluorescent surface patterns that give insight into air-water gas exchange dynamics.

9 Conclusion and Outlook

9.1 Conclusion

In investigating gas exchange between atmosphere and ocean, various imaging techniques have been developed to capture the dynamics of small-scale turbulence structures beneath the water surface. Among these, a range of Fluorescence Imaging methods have emerged that can directly make gas exchange visible in the laboratory. However, these methods often reach their limits under high wind speeds and strong wave activity. This work, building upon Papst (2019), demonstrates how a Fluorescence Imaging method can be experimentally implemented in a large wind-wave facility to image gas exchange dynamics horizontally with high spatial and temporal resolution across a wide range of wind speeds, including high-wind conditions. Specifically, an imaging setup was realized at the Heidelberg Aeolotron (cf. Sec. 4.1), consisting of a high-power illumination system with approximately 256 W radiation power and a multi-camera array. This setup enables the detection of gas exchange processes on a wave-affected surface of 48.2 cm × 37.8 cm at a frame rate of 500 fps. The high light intensity in combination with the temporal resolution of the cameras and the adaptation of a height tracking system for the imaging array, was essential to enable measurements at high wind speeds. This ensures sufficient fluorescence intensity even under thinning mass boundary layers at increasing wind speeds and allows the rapid dynamics of the wave field to be accurately resolved.
A comprehensive measurement campaign was carried out across the full range of possible wind speeds between 5 Hz and 50 Hz (cf. Sec. 4.2). In addition to measurements under standard conditions, tests were conducted with the two insoluble surface films hexadecanol and olive oil as well as with the water-soluble film Triton X-100. Further measurements were performed under reduced surface tension, in a heavy atmosphere, and with a seawater model. Data were collected under both equilibrium conditions and variable fetch scenarios. However, due to the large amount of data and the associated computation time, it was not possible to cover all measurements in this study.
An initial qualitative image analysis enabled the identification of various mechanisms such as QSVs, LCs, and MWB, and revealed their presence under different experimental conditions (cf. Sec. 6.1). At low wind speeds, QSVs appear to be isolated on film-covered water surfaces, whereas clean water surfaces exhibit additional LCs, which lead to more variability in the spatial distribution of streaks. Consequently, wind-aligned streaks on film-covered surfaces tend to show more ordered structures, while those on clean surfaces appear more irregular. Surface signatures did not vary significantly between different surface films. MWB events were observed from wind speeds of approximately 6.3 Hz, with increasing frequency and surface area as wind speeds rose. These events are easily recognizable, as the wake turbulence manifests in dominant, cloud-like patterns. At higher wind speeds, a breakdown of the streak-like structures occurs, and the cloud-like structures of the highly

turbulent regions dominate. Additionally, a simple quantitative histogram analysis showed that the mean fluorescence intensity of surface structures over time roughly follows the temporal evolution of the invasive gas flux (cf. Sec. 6.2.1). This provides a first step towards calculating gas transfer velocities from the fluorescence signal. Moreover, the grayscale statistics of the fluorescence structures appear to follow a log-normal distribution reflecting the multiplicative interaction of various stochastic processes, although a concrete physical model is still lacking (cf. Sec. 6.2.2).

A key outcome of this study is the demonstration of how gas transfer velocity can be derived from the fluorescence intensity in image sequences (cf. Sec. 7.1). A direct simulation of one-dimensional mass transport based on the Small Eddy Model forms the core of this method. The simulation uses the invasive gas flux and various turbulence depth profiles. By comparing the simulated temporal fluorescence signal with the measured data, the turbulence profile that best matches the fluorescence response can be extracted. This enables the estimation of both the turbulence depth profile and the water-side gas transfer velocity. A critical point in the simulation is the requirement for a known Schmidt number, which defines the exponent of the turbulent diffusivity profile. A comprehensive uncertainty analysis based on a worst-case scenario shows that, despite the simplified transport assumptions and the reduction to a one-dimensional model, this method provides robust estimates of water-side gas transfer velocities, with uncertainties ranging between approximately 5 % and 20 % (cf. Sec. 7.2). The resulting gas transfer velocities exhibit physically plausible values and fall within the expected range predicted by theoretical models for both smooth and rough water surfaces (cf. Sec. 8.2).

Furthermore, this work introduces the development of an algorithm for detecting MWB events and tracking renewed surface areas (cf. Sec. 6.3.1). This algorithm combines structural tensor concepts using an ORB detector with cluster analysis to identify regions with high vortex density, along with optical flow techniques to track the dynamics of the renewed regions. Although the algorithm reliably identifies MWB regions, it also detects false positives, necessitating manual verification (cf. Sec. 6.3.2). The resulting data provide insights into the spatial and temporal statistics of MWB events in the context of surface renewal (cf. Sec. 6.3.3). By including the surface renewal in the facet model, an important step has been made towards calculating the Schmidt number exponent (cf. Sec. 6.3.4). However, the exact determination of the recovery time of the renewed surface remains a challenge for the precise recording of the boundary conditions, which must be solved for a reliable determination of the Schmidt number exponent.

By combining the results from water-side gas transfer velocity and surface renewal rates, the relevance of MWB to gas exchange could be evaluated. This was done via an additive decomposition of the water-side gas transfer velocity into a term describing transport via turbulent vortices and a surface renewal term attributed to MWB (cf. Sec. 8.3). It was found that the difference in gas transfer velocities between clean and film-covered surfaces, when plotted against the corresponding surface renewal rates, agrees well with the classical surface renewal model. This additive decomposition predicts that the MWB contribution rises from around 35 % at a friction velocity of $u_{*,w} = 0.3\,\mathrm{cm\,s^{-1}}$ to approximately 80 % at $u_{*,w} = 0.8\,\mathrm{cm\,s^{-1}}$. Due to strong simplifications and the neglect of interactions between different transport mechanisms, this should be considered a rough estimate rather than a quantitatively definitive result (cf. Sec. 8.4).

9.2 Outlook

Since this work primarily focused on the methodological development of the Fluorescence Imaging technique and corresponding analysis tools, rather than a full evaluation of the results, the logical next step is to apply the developed methods to the entire dataset collected during the measurement campaign. Particularly, the analysis of fetch-dependent measurements would be of interest. Until now, the mass transport simulation for determining gas transfer velocity is limited to equilibrium conditions. An extension of this simulation framework to incorporate time-dependent gas transfer velocities and temporally variable turbulence profiles would enable the evaluation of fetch-dependent data as well. Another possible direction is the implementation of two- or three-dimensional mass transport simulations (cf. Sec. 7.3) to describe the fluorescence intensity of microscale structures. Both approaches aim at resolving the gas transfer velocity in both time and space. Additionally, a final validation of the implemented method is required. This should involve a comparison of the calculated gas transfer velocities with the outstanding results from complementary thermographic measurements or mass balance methods.

With the current analysis method for detecting MWB events, a specific transport mechanism can already be reliably captured. However, other transport processes, particularly those related to the surface signatures of turbulent vortices, cannot yet be reliably quantified. The main challenge here is that the structures are difficult to separate using image processing algorithms, as they often overlap and deform rapidly over time. As a result, fluorescence signals from different structures are superimposed. A more detailed investigation of the fluorescence signal of the streaks would likely only be possible through a 3D reconstruction of the near-surface turbulence dynamics. However, an algorithm for fusing the multi-camera data from the array does not yet exist and represents a completely new challenge in the field of image processing. Such a 3D reconstruction could also lead to a reevaluation of the results related to gas exchange mechanisms, as transport mediated by turbulent vortices could be more accurately extracted.

Another promising direction lies in further methodological development of the technique itself. While Fluorescence Imaging offers unique insights into the small-scale structure of gas exchange, its application is currently limited to wind-wave channels under controlled conditions and deionized water. To broaden its applicability, initial tests were conducted at the Aeolotron and at the Large Air-Sea Interaction Facility (LASIF) in Marseille, a linear wind-wave tank, using a spray method. In this approach, the fluorescent dye pyranine is directly sprayed onto the water surface, and surface signatures are recorded with a setup similar to Fluorescence Imaging. These tests have shown that, even without the use of a trace gas, similar fluorescent footprints can be observed. This simplified version of Fluorescence Imaging offers a promising opportunity to image the near-surface turbulence driving gas exchange even in open-ocean field experiments.

Bibliography

Anthony, K. R. N., Kline, D. I., Diaz-Pulido, G., Dove, S., & Hoegh-Guldberg, O. (2008). Ocean acidification causes bleaching and productivity loss in coral reef builders. *Proceedings of the National Academy of Sciences*, *105*(45), 17442–17446. https://doi.org/10.1073/pnas.0804478105

Asher, W. E., & Pankow, J. F. (1986). The interaction of mechanically generated turbulence and interfacial films with a liquid phase controlled gas/liquid transport process. *Tellus B*, *38*(5), 305–318. https://doi.org/10.3402/tellusb.v38i5.15139

Banner, M. L., & Phillips, O. M. (1974). On the incipient breaking of small scale waves. *J. Fluid Mech.*, *65*(4), 647–656. https://doi.org/10.1017/S0022112074001583

Bird, R. B., Stewart, W. E., & Lightfoot, E. N. (2002). *Transport phenomena* (2nd ed.). John Wiley & Sons.

Bopp, M. (2014). *Luft- und wasserseitige Strömungsverhältnisse im ringförmigen Heidelberger Wind-Wellen-Kanal (Aeolotron)* [Master's thesis]. Institut für Umweltphysik, Universität Heidelberg, Germany. https://doi.org/10.11588/heidok.00017151

Brox, T., van den Boomgaard, R., Lauze, F., van de Weijer, J., Weickert, J., Mrázek, P., & Kornprobst, P. (2006). Adaptive structure tensors and their applications. In J. Weickert & H. Hagen (Eds.), *Visualization and Processing of Tensor Fields* (pp. 17–47). Springer. https://doi.org/10.1007/3-540-31272-2_2

Burkholder, J. B., Sander, S. P., Abbatt, J., Barker, J. R., Huie, R. E., Kolb, C. E., Kurylo, M. J., Orkin, V. L., Wilmouth, D. M., & Wine, P. H. (2015). Chemical kinetics and photochemical data for use in atmospheric studies, Evaluation No. 18. *JPL Publication 15-10*. http://jpldataeval.jpl.nasa.gov

Coantic, M. (1986). A model of gas transfer across air-water interfaces with capillary waves. *J. Geophys. Res.*, *91*(C3), 3925–3943. https://doi.org/10.1029/JC091iC03p03925

Craik, A. D. D., & Leibovich, S. (1976). A rational model for Langmuir circulations. *J. Fluid Mech.*, *73*(3), 401–426. https://doi.org/10.1017/S0022112076001420

Cussler, E. L. (2009). *Diffusion - Mass transfer in fluid systems* (3rd ed.). Cambridge University Press.

Danckwerts, P. V. (1951). Significance of liquid-film coefficients in gas absorption. *Ind. Eng. Chem.*, *43*(6), 1460–1467. https://doi.org/10.1021/ie50498a055

Deacon, E. L. (1977). Gas transfer to and across an air-water interface. *Tellus A*, *29*(4), 363–374. https://doi.org/10.3402/tellusa.v29i4.11368

Degreif, K. (2006). *Untersuchungen zum Gasaustausch - Entwicklung und Applikation eines zeitlich aufgelösten Massenbilanzverfahrens* [Dissertation]. Institut für Umweltphysik, Fakultät für Physik und Astronomie, Heidelberg University. https://doi.org/10.11588/heidok.00006120

Doney, S. C., Fabry, V. J., Feely, R. A., & Kleypas, J. A. (2009). Ocean acidification: The other CO_2 problem. *Annu. Rev. Marine Sci.*, *1*, 169–192. https://doi.org/10.1146/annurev.marine.010908.163834

Dong, Y., Yang, M., Bakker, D. C. E., Kitidis, V., & Bell, T. G. (2021). Uncertainties in eddy covariance air-sea CO_2 flux measurements and implications for gas transfer velocity parameterisations. *Atmos. Chem. Phys.*, *21*(10), 8089–8110. https://doi.org/10.5194/acp-21-8089-2021

Edson, J. B., Jampana, V., Weller, R. A., Bigorre, S. P., Plueddemann, A. J., Fairall, C. W., Miller, S. D., Mahrt, L., Vickers, D., & Hersbach, H. (2013). On the exchange of momentum over the open ocean. *J. Phys. Oceanogr.*, *43*(8), 1589–1610. https://doi.org/10.1175/JPO-D-12-0173.1

Ester, M., Kriegel, H., Sander, J., & Xu, X. (1996). A density-based algorithm for discovering clusters in large spatial databases with noise. *Knowledge Discovery and Data Mining*. https://api.semanticscholar.org/CorpusID:355163

Fick, A. (1855). Ueber Diffusion. *Annalen der Physik*, *170*(1), 59–86. https://doi.org/10.1002/andp.18551700105

Ford, D. J., Blannin, J., Watts, J., Watson, A. J., Landschützer, P., Jersild, A., & Shutler, J. D. (2024). A comprehensive analysis of air-sea CO_2 flux uncertainties constructed from surface ocean data products. *Global Biogeochem. Cycles*, *38*(11). https://doi.org/10.1029/2024gb008188

Franklin, B., Brownrigg, W., & Mr. Farish. (1774). XLIV. Of the stilling of waves by means of oil. Extracted from sundry letters between Benjamin Franklin, LL. D. F. R. S. William Brownrigg, M. D. F. R. S. and the Reverend Mr. Farish. *Phil. Trans. R. Soc.*, *64*, 445–460. https://doi.org/10.1098/rstl.1774.0044

Frew, N. M., Bock, E. J., McGillis, W. R., Karachintsev, A. V., Hara, T., Münsterer, T., & Jähne, B. (1995). Variation of air-water gas transfer with wind stress and surface viscoelasticity. In B. Jähne & E. C. Monahan (Eds.), *Air-Water Gas Transfer, Selected Papers from the Third International Symposium on Air-Water Gas Transfer* (pp. 529–541). AEON. https://doi.org/10.5281/zenodo.10405

Frew, N. M., Bock, E. J., Schimpf, U., Hara, T., Haußecker, H., Edson, J. B., McGillis, W. R., Nelson, R. K., McKenna, S. P., Uz, B. M., & Jähne, B. (2004). Air-sea gas transfer: Its dependence on wind stress, small-scale roughness, and surface films. *J. Geophys. Res.*, *109*(C8), C08S17. https://doi.org/10.1029/2003JC002131

Friedl, F. (2013). *Investigating the transfer of oxygen at the wavy air-water interface under wind-induced turbulence* [Dissertation]. Institut für Umweltphysik, Fakultät für Physik und Astronomie, Heidelberg University. https://doi.org/10.11588/heidok.00014582

Friedlingstein, P., O'Sullivan, M., Jones, M. W., Andrew, R. M., Gregor, L., Hauck, J., Quéré, C. L., Luijkx, I. T., Olsen, A., Peters, G. P., Peters, W., Pongratz, J., Schwingshackl, C., Sitch, S., Canadell, J. G., Ciais, P., Jackson, R. B., Alin, S. R., Alkama, R., . . . Zheng, B. (2022). Global carbon budget 2022. *Earth Syst. Sci. Data*, *14*(11), 4811–4900. https://doi.org/10.5194/essd-14-4811-2022

Friman, S. I., & Jähne, B. (2019). Investigating SO_2 transfer across the air-water interface via LIF. *Exp. Fluids*, *60*, 65. https://doi.org/10.1007/s00348-019-2713-6

Garbe, C. S., Rutgersson, A., Boutin, J., Delille, B., Fairall, C. W., Gruber, N., Hare, J., Ho, D., Johnson, M., de Leeuw, G., Nightingale, P., Pettersson, H., Piskozub, J., Sahlee, E., Tsai, W.-T., Ward, B., Woolf, D. K., & Zappa, C. (2014). Transfer across the air-sea interface. In P. S. Liss & M. T. Johnson (Eds.), *Ocean-Atmosphere Interactions of Gases and Particles* (pp. 55–112). Springer. https://doi.org/10.1007/978-3-642-25643-1_2

Handler, R. A., Smith, G. B., & Leighton, R. I. (2001). The thermal structure of an air-water interface at low wind speeds. *Tellus A*, *53*(2), 233–244. https://doi.org/10.1034/j.1600-0870.2001.00158.x

Harned, H. S., & Davis, R., Jr. (1943). The ionization constant of carbonic acid in water and the solubility of carbon dioxide in water and aqueous salt solutions from 0 to 50°. *Journal of the American Chemical Society*, *65*(10), 2030–2037. https://doi.org/10.1021/ja01250a059

Harned, H. S., & Scholes, S. R., Jr. (1941). The ionization constant of HCO_3^- from 0 to 50°. *Journal of the American Chemical Society*, *63*(6), 1706–1709. https://doi.org/10.1021/ja01851a058

Harriott, P. (1962). A random eddy modification of the penetration theory. *Chem. Eng. Sci.*, *17*(3), 149–154. https://doi.org/10.1016/0009-2509(62)80026-8

Haußecker, H. (1996). *Messung und Simulation von kleinskaligen Austauschvorgängen an der Ozeanoberfläche mittels Thermographie* [Dissertation]. Institut für Umweltphysik, Fakultät für Physik und Astronomie, Heidelberg University. https://doi.org/10.5281/zenodo.14789

Herlina & Jirka, G. H. (2008). Experiments on gas transfer at the air-water interface induced by oscillating grid turbulence. *J. Fluid Mech.*, *594*, 183–208. https://doi.org/10.1017/S0022112007008968

Herzog, A. (2010). *Imaging of water-sided gas-concentration fields at a wind-driven, wavy air-water interface* [Dissertation]. Institut für Umweltphysik, Fakultät für Physik und Astronomie, Heidelberg University. https://doi.org/10.11588/heidok.00011220

Hiby, J. W., Braun, D., & Eickel, K. H. (1967). Eine Fluoreszenzmethode zur Untersuchung des Stoffübergangs bei der Gasabsorption im Rieselfilm. *Chemie Ingenieur Technik*, *39*(5–6), 297–301. https://doi.org/10.1002/cite.330390517

Higbie, R. (1935). The rate of absorption of a pure gas into a still liquid during short periods of exposure. *Trans. Am. Inst. Chem. Eng.*, *31*, 365–389.

Ho, D. T., Wanninkhof, R., Schlosser, P., Ullman, D. S., Hebert, D., & Sullivan, K. F. (2011). Toward a universal relationship between wind speed and gas exchange: Gas transfer velocities measured with $^3He/SF_6$ during the Southern Ocean Gas Exchange Experiment. *J. Geophys. Res.*, *116*(C4), C00F04. https://doi.org/10.1029/2010JC006854

Hofmann, D., & Jähne, B. (2023). Fluorescence imaging of concentration fields of dissolved gases at water interfaces. In J. Beyerer, T. Längle, & M. Heizmann (Eds.), *OCM 2023 - Optical Characterization of Materials: Conference Proceedings* (pp. 149–157). KIT Scientific Publishing. https://doi.org/10.58895/ksp/1000155014-12

Hofmann, D. (2025a, May 6). *Simulation of mass transport during gas exchange - Low gas flux* [Video]. YouTube. https://youtu.be/nnzHhz53naQ

Hofmann, D. (2025b, May 6). *Simulation of mass transport during gas exchange - High gas flux* [Video]. YouTube. https://youtu.be/hNPmhW8gQ-E

Hofmann, D. (2025c, May 6). *Fluorescence Imaging - Streak-like structures* [Video]. YouTube. https://youtu.be/jIGL8UjCQHM

Hofmann, D. (2025d, May 6). *Fluorescence Imaging - Formation of streaks* [Video]. YouTube. https://youtu.be/ENdmFwFIRPU

Hofmann, D. (2025e, May 6). *Fluorescence Imaging - Cloud-like structures* [Video]. YouTube. https://youtu.be/D9ZpKfkX9NU

Hofmann, D. (2025f, May 6). *Microscale wave breaking detection algorithm - Condition 1* [Video]. YouTube. https://youtu.be/VclZLDd46mY

Hofmann, D. (2025g, May 6). *Microscale wave breaking detection algorithm - Condition 2* [Video]. YouTube. https://youtu.be/Rgc8abMaPwg

Hühnerfuss, H., Walter, W., Lange, P. A., & Alpers, W. (1987). Attenuation of wind waves by monomolecular sea slicks and the Marangoni effect. *J. Geophys. Res.*, *92*(C4), 3961–3963. https://doi.org/10.1029/JC092iC04p03961

Hühnerfuss, H. (2006). Basic physicochemical principles of monomolecular sea slicks and crude oil spills. In M. Gade, H. Hühnerfuss, & G. M. Korenowski (Eds.), *Marine Surface Films* (pp. 21–35). Springer. https://doi.org/10.1007/3-540-33271-5_4

IPCC. (2013). *Climate change 2013 - The physical science basis. Contribution of Working Group I to the Fifth Assessment Report of the Intergovernmental Panel on Climate Change* (T. F. Stocker, D. Qin, G.-K. Plattner, M. Tignor, S. K. Allen, J. Boschung, A. Nauels, Y. Xia, V. Bex, & P. M. Midgley, Eds.). Cambridge University Press. https://doi.org/10.1017/CBO9781107415324

Jähne, B. (1980). *Zur Parametrisierung des Gasaustauschs mit Hilfe von Laborexperimenten* [Dissertation]. Institut für Umweltphysik, Fakultät für Physik und Astronomie, Heidelberg University. https://doi.org/10.11588/heidok.00016796

Jähne, B. (2007). Complex motion in environmental physics and live sciences. In B. Jähne, R. Mester, E. Barth, & H. Scharr (Eds.), *Complex Motion* (pp. 91–103, Vol. 3417). Springer. https://doi.org/10.1007/978-3-540-69866-1_8

Jähne, B., & Haußecker, H. (1998). Air-water gas exchange. *Annu. Rev. Fluid Mech.*, *30*, 443–468. https://doi.org/10.1146/annurev.fluid.30.1.443

Jähne, B., Libner, P., Fischer, R., Billen, T., & Plate, E. J. (1989). Investigating the transfer process across the free aqueous boundary layer by the controlled flux method. *Tellus B*, *41*(2), 177–195. https://doi.org/10.3402/tellusb.v41i2.15068

Jähne, B. (1985). *Transfer processes across the free water interface* [Habilitation thesis]. Institut für Umweltphysik, Fakultät für Physik und Astronomie, Heidelberg University. https://doi.org/10.11588/heidok.00016798

Jähne, B. (2012). *Digitale Bildverarbeitung und Bildgewinnung* (7th ed.). Springer. https://doi.org/10.1007/978-3-642-04952-1

Jähne, B. (2013). *Compression by noise equalization* (HCI Technical Report No. 1). Heidelberg Collaboratory for Image Processing (HCI), IWR, Heidelberg University. https://doi.org/10.5072/zenodo.12761

Jähne, B. (2019). Air-sea gas exchange. In J. K. Cochran, H. J. Bokuniewicz, & P. L. Yager (Eds.), *Encyclopedia of Ocean Sciences* (3rd ed., pp. 1–13, Vol. 6). Academic Press. https://doi.org/10.1016/B978-0-12-409548-9.11613-6

Jähne, B. (2020). What controls air-sea gas exchange at extreme wind speeds? Evidence from laboratory experiments. In P. Vlahos & E. Monahan (Eds.), *Recent Advances in the Study of Oceanic Whitecaps* (pp. 133–150). Springer. https://doi.org/10.1007/978-3-030-36371-0_10

Jähne, B., & Bock, E. (2000). *Physically-based modeling of air-sea gas transfer* [Unpublished Manuscript], Institut für Umweltphysik, Fakultät für Physik und Astronomie, Heidelberg University.

Jessup, A. T., Zappa, C. J., & Yeh, H. (1997). Defining and quantifying microscale wave breaking with infrared imagery. *J. Geophys. Res.*, *102*(C10), 23145–23153. https://doi.org/10.1029/97JC01449

Jones, M., Jr., & Fleming, S. A. (2014). *Organic chemistry* (5th ed.). W. W. Norton & Company.

Klein, A. (2019). *The fetch dependency of small-scale air-sea interaction processes at low to moderate wind speeds* [Dissertation]. Institut für Umweltphysik, Fakultät für Physik und Astronomie, Heidelberg University. https://doi.org/10.11588/heidok.00026559

Kolmogorov, A. N. (1941). The local structure of turbulence in incompressible viscous fluid for very large Reynolds numbers. *Dokl. Akad. Nauk SSSR*, *30*(4), 301–305.

Krall, K. E., & Jähne, B. (2025). Annular wind-wave tanks [in press]. In B. Jähne, K. E. Krall, & C. Marandino (Eds.), *Air-Water Gas Exchange: Cross-linking Field Measurements, Laboratory Measurements and Modeling*. Heidelberg University Publishing.

Krall, K. E. (2013). *Laboratory investigations of air-sea gas transfer under a wide range of water surface conditions* [Dissertation]. Institut für Umweltphysik, Fakultät für Physik und Astronomie, Heidelberg University. https://doi.org/10.11588/heidok.00014392

Kräuter, C., Trofimova, D., Kiefhaber, D., Krah, N., & Jähne, B. (2014). High resolution 2-D fluorescence imaging of the mass boundary layer thickness at free water surfaces. *J. Eur. Opt. Soc.-Rapid Publ.*, *9*, 14016. https://doi.org/10.2971/jeos.2014.14016

Kräuter, C. (2015). *Visualization of air-water gas exchange* [Dissertation]. Institut für Umweltphysik, Fakultät für Physik und Astronomie, Heidelberg University. https://doi.org/10.11588/heidok.00018209

Kühn, P. E. (2022). *Evaluierung von Tracern für schnelle Gasaustauschmessungen im Aeolotron mittels UV-Absorptionsspektroskopie* [Bachelor's thesis]. Institut für Umweltphysik, Universität Heidelberg, Germany.

Kundu, P. K., & Cohen, I. M. (2008). *Fluid mechanics* (4th ed.). Academic Press.

Kunz, J. (2017). *Active thermography as a tool for the estimation of air-water transfer velocities* [Dissertation]. Institut für Umweltphysik, Fakultät für Physik und Astronomie, Heidelberg University. https://doi.org/10.11588/heidok.00022903

Lakowicz, J. R. (2006). *Principles of fluorescence spectroscopy* (3rd ed.). Springer. https://doi.org/10.1007/978-0-387-46312-4

Lamb, H. (1975). *Hydrodynamics* (6th ed.). Cambridge University Press.

Langmuir, I. (1938). Surface motion of water induced by wind. *Science*, *87*(2250), 119–123. https://doi.org/10.1126/science.87.2250.119

Leibovich, S. (1983). The form and dynamics of Langmuir circulations. *Annu. Rev. Fluid Mech.*, *15*, 391–427. https://doi.org/10.1146/annurev.fl.15.010183.002135

Levin, I., & Hesshaimer, V. (2000). Radiocarbon - A unique tracer of global carbon cycle dynamics. *Radiocarbon*, *42*(1), 69–80. https://doi.org/10.1017/S0033822200053066

Lide, D. R. (2004). *CRC Handbook of chemistry and physics* (85th ed.). CRC Press.

Liss, P. S., & Slater, P. G. (1974). Flux of gases across the air-sea interface. *Nature*, *247*, 181–184. https://doi.org/10.1038/247181a0

Marmorino, G. O., Smith, G. B., & Lindemann, G. J. (2005). Infrared imagery of large-aspect-ratio Langmuir circulation. *Cont. Shelf Res.*, *25*(1), 1–6. https://doi.org/10.1016/j.csr.2004.08.002

Mesarchaki, E. (2014). *Volatile organic compounds at the air-sea interface: Gas exchange rates, oceanic emissions and the effect of ocean acidification* [Dissertation]. University of Mainz. https://doi.org/http://doi.org/10.25358/openscience-4252

Nagel, L. (2014). *Active thermography to investigate small-scale air-water transport processes in the laboratory and the field* [Dissertation]. Institut für Umweltphysik, Fakultät für Chemie und Geowissenschaften, Heidelberg University. https://doi.org/10.11588/heidok.00016831

Neukermans, G., Harmel, T., Galí, M., Rudorff, N., Chowdhary, J., Dubovik, O., Hostetler, C., Hu, Y., Jamet, C., Knobelspiesse, K., Lehahn, Y., Litvinov, P., Sayer, A. M., Ward, B., Boss, E., Koren, I., & Miller, L. A. (2018). Harnessing remote sensing to address critical science questions on ocean-atmosphere interactions. *Elementa: Science of the Anthropocene*, *6*, 71. https://doi.org/10.1525/elementa.331

Otsu, N. (1979). A threshold selection method from gray-level histograms. *IEEE Transactions on Systems, Man, and Cybernetics*, *9*(1), 62–66. https://doi.org/10.1109/TSMC.1979.4310076

Papst, M. (2019). *Development of a method for quantitative imaging of air-water gas exchange* [Master's thesis]. Institut für Umweltphysik, Universität Heidelberg, Germany. https://doi.org/10.11588/heidok.00027271

Patkai, L. (2024). *Untersuchung des Einflusses von Oberflächenfilmen auf den luftseitig kontrollierten Gasaustausch am Heidelberg Aeolotron* [Bachelor's thesis]. Institut für Umweltphysik, Universität Heidelberg, Germany. https://doi.org/10.11588/heidok.00036311

Pearson, B., & Fox-Kemper, B. (2018). Log-normal turbulence dissipation in global ocean models. *Phys. Rev. Lett.*, *120*, 094501. https://doi.org/10.1103/PhysRevLett.120.094501

Pearson, K. (1905). The problem of the random walk. *Nature*, *72*, 342. https://doi.org/10.1038/072342a0

Peirson, W. L. (1997). Measurement of surface velocities and shears at a wavy air-water interface using particle image velocimetry. *Exp. Fluids*, *23*, 427–437. https://doi.org/10.1007/s003480050131

Phillips, O. M. (1958). The equilibrium range in the spectrum of wind-generated waves. *J. Fluid Mech.*, *4*(4), 426–434. https://doi.org/10.1017/S0022112058000550

Powell, M. J. D. (1987). Radial basis functions for multivariable interpolation: A review. In J. C. Mason & M. G. Cox (Eds.), *Algorithms for Approximation* (pp. 143–167). Clarendon Press.

Prandtl, L. (1957). *Führer durch die Strömungslehre* (5th ed.). Vieweg.

Reichardt, H. (1951). Vollständige Darstellung der turbulenten Geschwindigkeitsverteilung in glatten Leitungen. *Journal of Applied Mathematics and Mechanics*, *31*(7), 208–219. https://doi.org/10.1002/zamm.19510310704

Reynolds, O. (1883). XXIX. An experimental investigation of the circumstances which determine whether the motion of water shall be direct or sinuous, and of the law of resistance in parallel channels. *Philosophical Transactions of the Royal Society of London*, *174*, 935–982. https://doi.org/10.1098/rstl.1883.0029

Riedel, E., & Janiak, C. (2011). *Anorganische Chemie* (8th ed.). De Gruyter.

Robinson, S. K. (1990). A review of vortex structures and associated coherent motions in turbulent boundary layers. In A. Gyr (Ed.), *Structure of Turbulence and Drag Reduction* (pp. 23–50). Springer.

Roedel, W., & Wagner, T. (2017). *Physik unserer Umwelt: Die Atmosphäre* (5th ed.). Springer Spektrum. https://doi.org/10.1007/978-3-662-54258-3

Rose, B. E. J., & Rayborn, L. (2016). The effects of ocean heat uptake on transient climate sensitivity. *Current Climate Change Reports*, *2*, 190–201. https://doi.org/10.1007/s40641-016-0048-4

Rublee, E., Rabaud, V., Konolige, K., & Bradski, G. (2011). ORB: An efficient alternative to SIFT or SURF. *International Conference on Computer Vision*, 2564–2571. https://doi.org/10.1109/ICCV.2011.6126544

Sander, R. (2023). Compilation of Henry's law constants (version 5.0.0) for water as solvent. *Atmos. Chem. Phys.*, *23*(19), 10901–12440. https://doi.org/10.5194/acp-23-10901-2023

Satish, U., Mendell, M. J., Shekhar, K., Hotchi, T., Sullivan, D., Streufert, S., & Fisk, W. J. (2012). Is CO_2 an indoor pollutant? Direct effects of low-to-moderate CO_2 concentrations on human decision-making performance. *Environmental Health Perspectives*, *120*(12), 1671–1677. https://doi.org/10.1289/ehp.1104789

Schlichting, H., & Gersten, K. (2006). *Grenzschicht-Theorie* (10th ed.). Springer. https://doi.org/10.1007/3-540-32985-4

Schnieders, J., Garbe, C. S., Peirson, W. L., Smith, G. B., & Zappa, C. J. (2013). Analyzing the footprints of near-surface aqueous turbulence: An image processing-based approach. *J. Geophys. Res.*, *118*(3), 1272–1286. https://doi.org/10.1002/jgrc.20102

Smith, C. R., & Paxson, R. D. (1983). A technique for evaluation of three-dimensional behavior in turbulent boundary layers using computer augmented hydrogen bubble-wire flow visualization. *Exp. Fluids*, *1*, 43–49. https://doi.org/10.1007/BF00282266

Soloviev, A., Donelan, M., Graber, H., Haus, B., & Schlüssel, P. (2007). An approach to estimation of near-surface turbulence and CO_2 transfer velocity from remote sensing data. *J. Marine Syst.*, *66*(1–4), 182–194. https://doi.org/10.1016/j.jmarsys.2006.03.023

Syms, R. (2017). Rapid evaporation-driven chemical pre-concentration and separation on paper. *Biomicrofluidics*, *11*(4), 044116. https://doi.org/10.1063/1.4989627

Szeliski, R. (2011). *Computer vision - Algorithms and applications*. Springer. https://doi.org/10.1007/978-1-84882-935-0

Telea, A. (2004). An image inpainting technique based on the fast marching method. *Journal of Graphics Tools*, *9*(1), 23–34. https://doi.org/10.1080/10867651.2004.10487596

Thorpe, S. A. (2004). Langmuir circulation. *Annu. Rev. Fluid Mech.*, *36*(1), 55–79. https://doi.org/10.1146/annurev.fluid.36.052203.071431

Trofimova, D. (2015). *Towards four dimensional visualization of air-water gas exchange* [Dissertation]. Institut für Umweltphysik, Fakultät für Physik und Astronomie, Heidelberg University. https://doi.org/10.11588/heidok.00019066

Tsai, W.-T., Chen, S.-M., & Moeng, C.-H. (2005). A numerical study on the evolution and structure of a stress-driven, free-surface turbulent shear flow. *J. Fluid Mech.*, *545*, 163–192. https://doi.org/10.1017/S0022112005007044

Tsai, W.-T., & Lu, G.-H. (2023). A numerical study on Langmuir circulations and coherent vortical structures beneath surface waves. *J. Fluid Mech.*, *969*, A30. https://doi.org/10.1017/jfm.2023.577

Valeur, B., & Berberan-Santos, M. N. (2013). *Molecular fluorescence: Principles and applications*. John Wiley & Sons.

Veron, F., & Melville, W. K. (2001). Experiments on the stability and transition of wind-driven water surfaces. *J. Fluid Mech.*, *446*, 25–65. https://doi.org/10.1017/S0022112001005638

Voigt, P. I. (2021). *Investigation of the water-sided shear layer at a wind-driven wavy surface by active thermography* [Master's thesis]. Institut für Umweltphysik, Universität Heidelberg, Germany. https://doi.org/10.11588/heidok.00030834

Wanner, S., & Goldluecke, B. (2014). Variational light field analysis for disparity estimation and super-resolution. *IEEE Trans. Pattern Analysis Machine Intelligence*, *36*(3), 606–619. https://doi.org/10.1109/TPAMI.2013.147

Wanninkhof, R., Park, G. H., Chelton, D. B., & Risien, C. M. (2011). Impact of small-scale variability on air-sea CO_2 fluxes. In S. Komori, W. McGillis, & R. Kurose (Eds.), *Gas Transfer at Water Surfaces 2010* (pp. 431–444). http://hdl.handle.net/2433/156156

Wanninkhof, R., Asher, W. E., Ho, D. T., Sweeney, C., & McGillis, W. R. (2009). Advances in quantifying air-sea gas exchange and environmental forcing. *Annu. Rev. Marine Sci.*, *1*, 213–244. https://doi.org/10.1146/annurev.marine.010908.163742

Whitman, W. G. (1923). The two-film theory of gas absorption. *Chemical and Metallurgical Engineering*, *29*(4), 146–148.

Wolfbeis, O. S., Fürlinger, E., Kroneis, H., & Marsoner, H. (1983). Fluorimetric analysis - 1. A study on fluorescent indicators for measuring near neutral ("physiological") pH-values. *Fresenius Journal of Analytical Chemistry*, *314*, 119–124. https://doi.org/10.1007/BF00482235

Wolff, L. M., & Hanratty, T. J. (1994). Instantaneous concentration profiles of oxygen accompanying absorption in a stratified flow. *Exp. Fluids*, *16*(6), 385–392. https://doi.org/10.1007/BF00202063

Wong, K.-L., Bünzli, J.-C. G., & Tanner, P. A. (2020). Quantum yield and brightness. *Journal of Luminescence*, *224*, 117256. https://doi.org/https://doi.org/10.1016/j.jlumin.2020.117256

Woolf, D. K., Shutler, J. D., Goddijn-Murphy, L., Watson, A. J., Chapron, B., Nightingale, P. D., Donlon, C. J., Piskozub, J., Yelland, M. J., Ashton, I., Holding, T., Schuster, U., Girard-Ardhuin, F., Grouazel, A., Piolle, J.-F., Warren, M., Wrobel-Niedzwiecka, I., Land, P. E.,

Torres, R., ... Paul, F. (2019). Key uncertainties in the recent air-sea flux of CO_2. *Global Biogeochem. Cycles*, *33*(12), 1548–1563. https://doi.org/10.1029/2018GB006041

Wurl, O., Wurl, E., Miller, L., Johnson, L., & Vagle, S. (2011). Formation and global distribution of sea-surface microlayers. *Biogeosciences*, *8*(1), 121–135. https://doi.org/10.5194/bg-8-121-2011

Wurl, O., Stolle, C., Thuoc, C. V., Thu, P. T., & Mari, X. (2016). Biofilm-like properties of the sea surface and predicted effects on air–sea CO_2 exchange. *Prog. Oceanogr.*, *144*, 15–24. https://doi.org/10.1016/j.pocean.2016.03.002

Xiao, M.-J., & She, Z.-S. (2019). Symmetry-based description of laminar-turbulent transition. *Science China Physics, Mechanics & Astronomy*, *62*(9), 994711. https://doi.org/10.1007/s11433-018-9377-0

Yaws, C. L. (1995). *Handbook of transport property data*. Gulf Publishing Company.

Zappa, C. J., Asher, W. E., Jessup, A. T., Klinke, J., & Long, S. R. (2004). Microbreaking and the enhancement of air-water transfer velocity. *J. Geophys. Res.*, *109*(C8), C08S16. https://doi.org/10.1029/2003JC001897

A Appendix

A.1 Diffusion Constants

Table A.1: Diffusion coefficient of chemical species

Species	Diffusion coefficient [$cm^2\ s^{-1}$]	Source
H_3O^+	$9.31 \cdot 10^{-5}$	Cussler, 2009
OH^-	$5.28 \cdot 10^{-5}$	Cussler, 2009
NH_2R	$1.61 \cdot 10^{-5}$	Yaws, 1995
NH_3R^+	$1.56 \cdot 10^{-5}$	Lide, 2004
IH	$5.71 \cdot 10^{-6}$	measured
I^-	$5.71 \cdot 10^{-6}$	measured
TH	$4.9 \cdot 10^{-6}$	Syms, 2017
T^-	$4.9 \cdot 10^{-6}$	Syms, 2017
CO_2	$1.92 \cdot 10^{-5}$	Cussler, 2009
$HCO_3{}^-$	$1.19 \cdot 10^{-5}$	Lide, 2004
$CO_3{}^{2-}$	$9.2 \cdot 10^{-6}$	Lide, 2004

A.2 Measurements

Table A.2: Overview of all performed Fluorescence Imaging measurements

Date	Series	Wind [Hz]	Gas Input [g]	pH Start	pH End	Mode / Condition
Measurement Week 1						
03-11-2023	A_01	7.9	1.4	5.15	5.80	Equilibrium / Clean
	A_02	6.3	1.4			
	A_03	5.0	1.4			
	A_04	7.1	1.2			
	A_05	8.9	1.4			
04-11-2023	A_01	10.0	1.0	5.02	5.85	Equilibrium / Clean
	A_02	11.2	1.8			
	A_03	12.6	1.4			
	A_04	14.1	1.6			
	A_05	10.0	1.6			

Table A.2: Overview of all performed Fluorescence Imaging measurements (continued)

Date	Series	Wind [Hz]	Gas Input [g]	pH Start	pH End	Mode / Condition
05-11-2023	A_01	7.9	1.2	4.95	5.50	Equilibrium / Surface Film: Hexadecanol
	A_02	10.0	1.2			
	A_03	12.6	1.2			
	A_04	14.1	1.4			
	A_05	11.2	1.4			
	A_06	6.3	1.4			
	A_07	6.3	0.0			
06-11-2023	A_01	17.8	0.8	5.00	5.85	Equilibrium / Surface Film: Triton X-100
	A_02	14.1	1.8			
	A_03	11.2	1.2			
	A_04	8.9	1.6			
	A_05	7.1	1.6			
	A_06	28.3	1.4			
Measurement Week 2						
02-01-2024	A_01	10.0	4.43	4.98	6.32	Fetch / Clean
	A_02	10.0	3.43			
	A_03	10.0	2.57			
03-01-2024	A_01	7.9	2.46	5.08	6.24	Fetch / Clean
	A_02	6.3	3.70			
	A_03	5.6	2.88			
	A_04	7.1	2.72			
	A_05	8.9	2.47			
	A_06	11.2	2.97			
04-01-2024	A_01	7.9	2.11	5.00	6.40	Fetch / Surface Tension: Hexanol (low Concentration)
	A_02	8.9	2.39			
	A_03	10.0	1.87			
	A_04	11.2	4.33			
	A_05	5.6	1.61			
	A_06	15.9	4.78			
05-01-2024	A_01	5.6	2.57	5.28	–	Fetch / Surface Tension: Hexanol (high Concentration)
	A_02	7.9	3.52			
	A_03	8.9	3.34			
	A_04	10.0	5.17			
	A_05	11.2	1.69			
	A_06	28.3	17.87			

Table A.2: Overview of all performed Fluorescence Imaging measurements (continued)

Date	Series	Wind [Hz]	Gas Input [g]	pH Start	pH End	Mode / Condition
Measurement Week 3						
06-05-2024	A_01	7.1	0.00	4.98	5.49	Equilibrium / Clean
	A_02	7.1	5.44			
	A_03	8.9	1.93			
07-05-2024	A_01	7.1	2.29	4.90	6.04	Equilibrium / Atmosphere: Argon
	A_02	7.1	1.25			
	A_03	7.1	0.89			
	A_04	8.9	1.25			
	A_05	11.2	1.70			
	A_06	14.1	2.63			
08-05-2024	A_01	7.9	2.26	5.00	6.15	Equilibrium / Surface Film: Olive Oil
	A_02	6.3	1.98			
	A_03	10.0	2.39			
	A_04	12.6	2.58			
	A_05	15.8	2.96			
09-05-2024	A_01	7.1	2.75	5.25	6.35	Equilibrium / Surface Film: Olive Oil
	A_02	8.9	2.66			
	A_03	11.2	2.76			
	A_04	14.1	2.95			
	A_05	17.8	3.93			
Measurement Week 4						
03-06-2024	A_01	14.05	3.10	4.90	6.60	Fetch / Clean
	A_02	17.8	4.26			
	A_03	22.4	5.70			
	A_04	28.2	0.00			
04-06-2024	A_01	14.1	5.27	5.00	6.50	Fetch / Clean
	A_02	15.8	2.92			
	A_03	20.0	7.80			
05-06-2024	A_01	20.0	7.02	5.25	6.50	Fetch / Clean
	A_02	22.4	5.12			
	A_03	25.1	5.49			
06-06-2024	A_01	15.8	7.00	5.35	6.40	Fetch / Clean
	A_02	28.2	5.08			

Table A.2: Overview of all performed Fluorescence Imaging measurements (continued)

Date	Series	Wind [Hz]	Gas Input [g]	pH Start	pH End	Mode / Condition
Measurement Week 5						
02-09-2024	A_01a	20.0	12.42	4.97	6.60	Fetch / Clean
	A_02a	28.2	7.61			
	A_03a	40.0	16.31			
03-09-2024	A_01a	22.4	7.58	5.04	6.65	Fetch / Clean
	A_01b	22.4	2.37			
	A_02a	31.7	9.25			
	A_02b	31.7	7.88			
04-09-2024	A_01a	25.2	7.49	5.12	5.12	Fetch / Clean
	A_01b	25.2	5.31			
	A_02a	50.0	1.69			
05-09-2024	A_01a	35.6	12.94	5.02	6.91	Fetch / Clean
	A_01b	35.6	7.79			
	A_02a	44.9	17.02			
	A_02b	44.9	8.22			
Measurement Week 6						
17-09-2024	A_01a	28.2	14.26	4.97	6.65	Fetch / Seawater Model
	A_01b	28.2	7.87			
	A_02a	40.0	12.52			
	A_02b	40.0	7.38			
18-09-2024	A_01a	31.7	11.16	4.92	6.35	Fetch / Seawater Model
	A_01b	31.7	8.28			
	A_02a	44.9	17.96			
	A_02b	44.9	6.73			
19-09-2024	A_01a	25.2	8.60	4.90	6.50	Fetch / Seawater Model
	A_01b	25.2	6.82			
	A_02a	50.0	11.59			
	A_02b	50.0	7.42			
20-09-2024	A_01a	22.4	9.54	5.03	6.73	Fetch / Seawater Model
	A_01b	22.4	5.96			
	A_02a	35.6	15.48			
	A_02b	35.6	9.17			

A.3 Friction Velocities

Table A.3: Friction velocities of all experiments from measurement week 1

ID	Wind Control Frequency f [Hz]	Friction Velocity $u_{*,w}$ [cm s^{-1}]	Condition
231103_A_03	5.0	0.306	Clean
231103_A_02	6.3	0.344	
231103_A_04	7.1	0.372	
231103_A_01	7.9	0.399	
231103_A_05	8.9	0.410	
231104_A_01	10.0	0.437	
231104_A_05	10.0	0.461	
231104_A_02	11.2	0.477	
231104_A_03	12.6	0.502	
231104_A_04	14.1	0.652	
231105_A_06	6.3	0.340	Surface Film: Hexadecanol
231105_A_01	7.9	0.365	
231105_A_02	10.0	0.429	
231105_A_05	11.2	0.495	
231105_A_04	14.1	0.598	
231106_A_05	7.1	0.346	Surface Film: Triton X-100
231106_A_03	11.2	0.490	
231106_A_02	14.1	0.603	
231106_A_01	17.8	0.790	

A.4 Leakage Rates

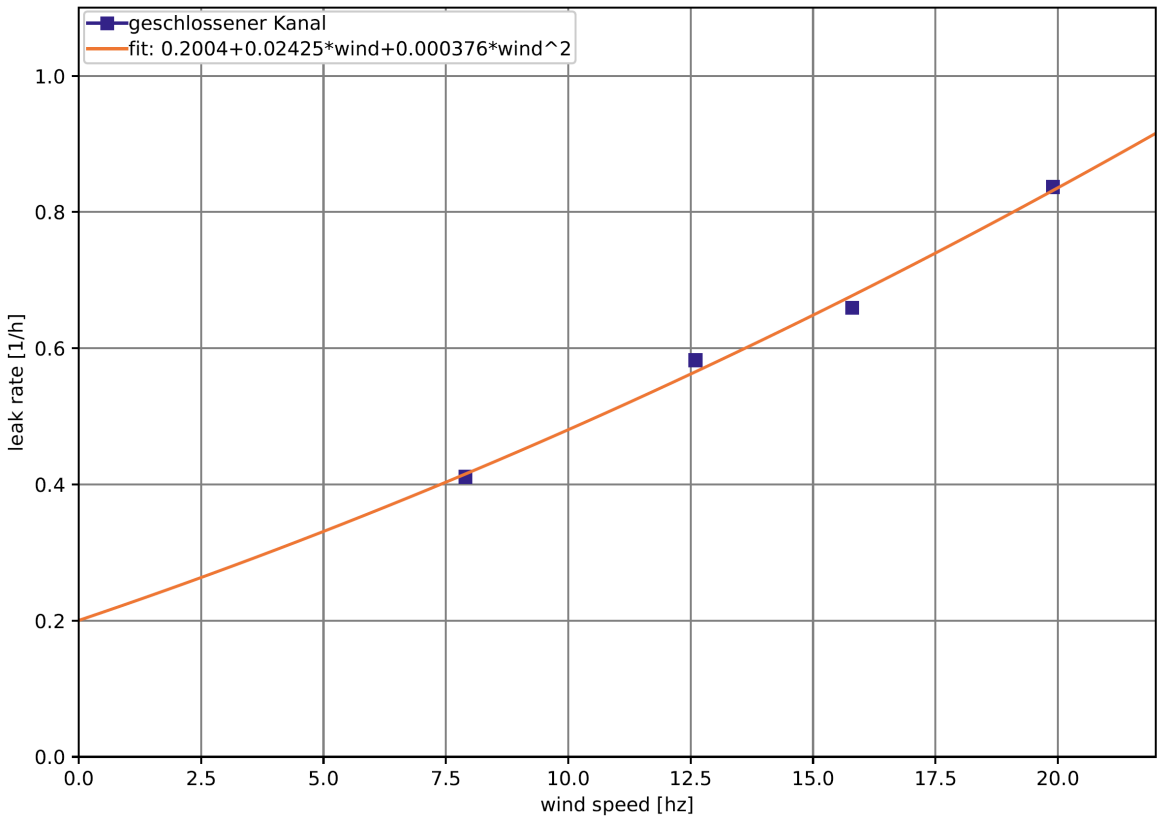

Figure A.1: Leakage rates of the Aeolotron, measured by K. Krall (personal communication) using the insoluble gas CF_4. A quadratic fit of the four discrete data points allows to interpolate values over the entire range of wind control frequencies.

A.5 Uncertainty Analysis

Table A.4: Uncertainty analysis of water-side gas transfer velocities. Relative uncertainties of the water-side gas transfer velocities with variations of the different simulation parameters n, j, σ. For the individual parameters, min and max mean setting the parameters n or j to their respective minimum and maximum values within the uncertainty range. Note the sign effect of the Schmidt number on the final result. For the worst-case scenarios, min and max mean the minimum and maximum deviations achieved in k. Additional listing of the exponent m of the turbulent diffusivity profile $K(z)$ and the water-side gas transfer velocity k.

ID	Exponent m	k [cm h^{-1}]	Effect of Schmidt Number $\frac{\Delta k}{k}(n)$ [‰]		Effect of Gas Flux $\frac{\Delta k}{k}(j)$ [‰]		Worst-Case Scenario Input Parameter $\frac{\Delta k}{k}(n, j)$ [‰]		Worst-Case Scenario Input Parameter + Target Function $\frac{\Delta k}{k}(n, j, \sigma)$ [‰]	
			min	max	min	max	min	max	min	max
231103_A_01	2.54	4.29	5.45	-5.95	-5.62	4.61	-11.41	11.10	-11.41	11.10
231103_A_02	2.70	2.83	6.95	-5.73	-4.70	4.70	-9.85	12.75	-11.30	12.75
231103_A_03	2.80	2.06	4.96	-4.27	-5.21	4.74	-9.62	10.66	-10.76	12.00
231103_A_04	2.62	2.93	5.70	-4.91	-4.44	5.46	-9.70	10.74	-10.97	12.34
231103_A_05	2.43	4.13	5.24	-5.58	-5.77	5.87	-10.38	12.42	-11.64	12.42
231104_A_01	2.32	7.82	3.94	-5.50	-6.48	5.31	-11.55	11.31	-11.55	11.31
231104_A_02	2.22	7.85	7.17	-8.67	-7.77	5.28	-13.51	13.46	-15.21	15.47
231104_A_03	2.13	9.88	7.06	-6.98	-7.30	6.74	-13.15	15.00	-13.15	15.00
231104_A_04	2.08	10.33	8.94	-6.24	-7.28	8.04	-13.29	16.06	-13.29	17.86
231104_A_05	2.32	5.35	8.31	-6.59	-5.79	5.26	-12.70	13.97	-12.70	14.38
231105_A_01	3.00	1.91	0.00	0.00	-5.35	6.84	-5.35	6.84	-7.68	8.11
231105_A_02	3.00	2.22	0.00	0.00	-4.77	5.12	-4.77	5.12	-5.81	6.32
231105_A_03	3.00	2.47	0.00	0.00	-4.51	4.04	-4.51	4.04	-5.59	5.32
231105_A_04	3.00	2.64	0.00	0.00	-4.87	4.42	-4.87	4.42	-6.17	5.92
231105_A_05	3.00	1.99	0.00	0.00	-5.77	4.02	-5.77	4.02	-7.85	6.38
231105_A_06	3.00	3.15	1.38	1.38	-5.59	6.57	-5.59	6.57	-7.83	8.98
231106_A_01	3.00	4.97	0.00	0.00	-3.93	4.40	-3.93	4.40	-5.09	5.50
231106_A_02	3.00	2.64	0.00	0.00	-4.87	4.42	-4.87	4.42	-6.17	5.92
231106_A_03	3.00	2.25	0.00	0.00	-5.47	4.93	-5.47	4.93	-5.47	6.09
231106_A_04	3.00	1.74	0.00	0.00	-5.81	3.88	-5.81	3.88	-6.88	6.32
231106_A_05	3.00	1.69	0.00	0.00	-7.68	6.84	-7.68	6.84	-8.89	8.11
231106_A_06	2.00	23.97	0.10	-0.10	-7.77	8.16	-7.86	8.27	-9.91	8.27
240903_A_01b	2.00	10.63	0.74	-0.74	-9.58	8.42	-10.24	7.17	-10.24	9.23
240903_A_02b	2.00	23.53	0.03	-1.99	-16.96	15.19	-16.64	12.77	-18.28	15.22
240904_A_01b	2.00	21.04	0.31	-1.99	-12.54	11.58	-12.80	11.93	-12.80	14.08
240905_A_01b	2.00	25.94	0.01	-0.01	-18.56	10.89	-18.56	12.95	-18.56	12.95
240917_A_02b	2.00	26.53	0.00	-0.00	-20.37	14.55	-20.37	14.55	-22.31	17.27
240918_A_01b	2.00	29.82	0.03	-0.03	-9.10	9.02	-11.06	11.32	-11.06	11.32
240919_A_01b	2.00	24.37	0.31	-0.31	-13.67	8.60	-13.93	8.95	-13.93	8.95
240920_A_01b	2.00	23.81	0.86	-0.85	-9.81	10.60	-10.56	11.56	-12.64	13.99
240920_A_02b	2.00	29.30	0.06	-0.06	-11.46	6.19	-11.46	6.20	-11.46	10.97

Danksagung

Hiermit möchte ich allen danken, die mich während meiner Dissertation begleitet und unterstützt haben. Mein besonderer Dank gilt Prof. Dr. Bernd Jähne für die engagierte Betreuung meiner Arbeit. Durch seine Unterstützung durfte ich 3,5 spannende Jahre in einem abwechslungsreichen und interdisziplinären Forschungsfeld verbringen. Ich danke ihm insbesondere für die finanzielle Förderung, die Teilnahme an Konferenzen und Messkampagnen sowie die Möglichkeit, wertvolle Erfahrungen in der internationalen Gasaustausch-Community zu sammeln. Darüber hinaus konnte ich mich durch unsere zahlreichen gemeinsamen Experimente intensiv im experimentellen Arbeiten weiterentwickeln.
Mein Dank gilt ebenfalls Prof. Dr. Ulrich Platt für sein Interesse an meiner Forschung und seine Bereitschaft, als Zweitgutachter mitzuwirken. Ebenso bedanke ich mich bei den weiteren Mitgliedern meines Prüfungskomitees, Prof. Dr. Markus Oberthaler und Prof. Dr. Matthias Bartelmann, für ihre Zeit und Bereitschaft, meine Forschung zu begutachten.
Ein besonderer Dank geht an Kerstin Krall, die mir im Laufe meiner Promotionszeit bei nahezu jeder Frage zum Thema Gasaustausch weiterhelfen konnte. Ich danke Ihr außerdem für Ihre Fähigkeit, im Windkanallabor alles zu finden, sowie das präzise Korrekturlesen meiner Dissertation. Auch Günther Balschbach danke ich für seine schnelle und kompetente Unterstützung bei allen EDV-Problemen.
Als letzter Doktorand der Arbeitsgruppe möchte ich mich bei allen ehemaligen Windis bedanken, die mich in dieser Zeit begleitet und bei Experimenten tatkräftig unterstützt haben. Besonders danken möchte ich hier Roman Stewig, Lukas Warmuth, Pernilla Kühn und Rada Beronova, für die gemeinsame Zeit auf dem Gasaustausch-Symposium in Plymouth. Mein Dank gilt außerdem Yuanxu Dong für sein unermüdliches Interesse an meiner Forschung, viele anregende Gespräche und seine Unterstützung bei den finalen Messkampagnen im Aeolotron.
Ebenso danke ich der SOLAS-Community für die Organisation einer unvergesslichen Summer School in Mindelo, Kap Verde. Diese bot eine einmalige Gelegenheit, internationale Zusammenarbeit zu erleben und zahlreiche Kontakte mit Forschenden aus aller Welt zu knüpfen.
Zum Schluss danke ich meiner Familie für ihre langjährige Unterstützung während meines Studiums. Ein ganz besonderer Dank gilt meiner Freundin, die mich in stressigen Phasen stets motiviert und gestärkt hat.